FRAMEWORK FOR NATURAL AND ANTHROPOGENIC CHANGES TO THE URBAN VADOSE ZONE: CASE STUDIES

Matthys A. Dippenaar

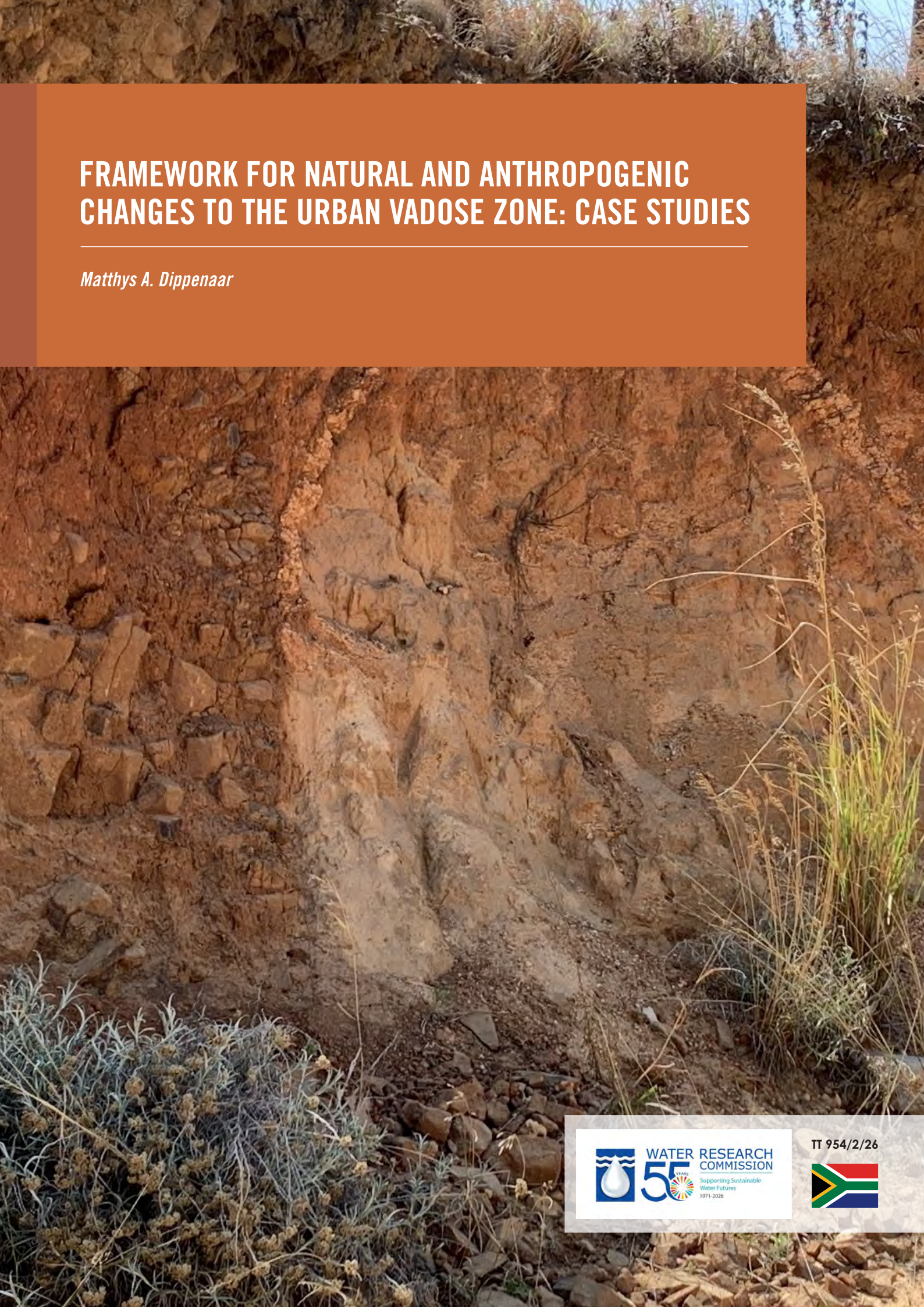

WATER RESEARCH COMMISSION
55 YEARS
Supporting Sustainable Water Futures
1971-2026

TT 954/2/26

Framework for Natural and Anthropogenic Changes to the Urban Vadose Zone: Case Studies

Report
to the Water Research Commission

by

Matthys A. Dippenaar[1] (Editor)

[1] Department of Geology, University of Pretoria

WRC report no. TT 954/2/26
ISBN 978-0-6392-0797-1

May 2026

This is the final report for WRC project no. C2020/2021-00581.

ACKNOWLEDGEMENTS

The project team wishes to thank the Reference Group members for their contributions to the project that included peer review of the work and continuous input during meetings to improve the quality of these project outcomes that include this book and the accompanying case studies book.

Reference Group	Affiliation
Prof Seifu Gurmessa	University of KwaZulu-Natal
Prof Kai Witthüser	DeltaH
Prof Jan van Tol	University of the Free State
Mr Kwazikwakhe Majola	Department of Water and Sanitation
Dr Kirsty Carden	University of Cape Town
Prof Nebo Jovanovic	University of the Western Cape
Dr Anna Taylor	University of Cape Town
Prof Molla Demlie	University of KwaZulu-Natal

ORCID (Online Researcher and Contributor ID)

Matthys Alois Dippenaar	https://orcid.org/0000-0002-6807-1353
Jan Louis van Rooy	https://orcid.org/0000-0003-4708-6991
Mampho Maoyi	https://orcid.org/0000-0003-0737-6548
Duan Swart	https://orcid.org/0009-0003-7803-0066
Yazeed van Wyk	https://orcid.org/0009-0001-5324-5576

BOOK COVER CREDITS

The book covers were taken from the case studies of the three PhD students:

1. For the book (WRC report no. TT 954/1/26), the cover shows the quarry used in the case studies of Dr Mampho Maoyi and Dr Yazeed van Wyk. The photograph was taken by Mampho Maoyi in 2023.
2. For the case studies book (WRC report no. TT 954/2/26), the cover shows the weathered granitic profile around Magoebaskloof of Dr Duan Swart. The photograph was taken by Duan Swart in 2020.

CONTENTS

LIST OF FIGURES

LIST OF TABLES

CHAPTER 1: INTRODUCTION

1.1 BACKGROUND AND SOUTH AFRICAN CONTEXT

This book is composed of the case studies referenced in Dippenaar et al. (2026) titled *Framework for Natural and Anthropogenic Changes to the Urban Vadose Zone* which is published as TT 954/1/26 by the Water Research Commission. All the authors were part of the Geology Department of the Faculty of Natural and Agricultural Sciences of the University of Pretoria at the time of writing.

The case studies are placed here to provide the background information, large data sets, and elaborate methodology that are not necessary for the book. This can be used to understand where the data come from and how it was interpreted to eventually contribute to the new findings, and the relevant theses, dissertations, and articles are provided for each. The case studies are very important, seeing that they provide the first data points in the field and that continue in the laboratory.

All case studies are in South Africa, where the geology, topography, and climate are all highly variable, given our coastlines to the west, south, and southeast. This caused a lot of weathering and erosion, causing the Great Escarpment around a plateau with the arid Fish River Canyon to the west in Namibia, the humid Blyde River Canyon to the east in South Africa, and the Cape Fold Mountains to the south. This caused denudation of South Africa's soils, exposing very old rocks and preserved mineral deposits that make South Africa one of the countries with the oldest exposed geology in Barberton, and some of the richest mineral deposits of minerals, for instance gold, diamonds, platinum, coal, chromium, and vanadium, all in proximity to the administrative capital city Pretoria, and the economic hub Johannesburg.

Weathering in South Africa is related in terms of engineering geology (geotechnical work) based on Weinert's N-value, which is determined as follows: dividing twelve times the evaporation in January (E_J) by the annual precipitation (P). At N = 5, there is no preferential weathering, and the smaller it gets the more towards 2, the stronger decomposition (chemical weathering) dominates due to the moisture surplus (Weinert 1980). The greater it gets toward 10, disintegration (physical or mechanical weathering) dominates due to a moisture deficit. Figure 1-1 shows the Great Escarpment and the N-values related to the predominant type of weathering with the neighbouring countries and some cities for reference (Dippenaar et al. 2025).

There is no glossary or list of abbreviations in this document. Each case study will define each term and write out each abbreviation in the appropriate chapter, even if there is repetition between the chapters.

The case studies were selected keeping the following in mind:

- Accessibility of sites and sample localities is important since those determine the acquisition of field data.
- Different methods should be used on similar sites or in different laboratory techniques to relate the correlation between different methods.
- Different case studies relate to different soils, rocks, and water conditions that are affected in different ways by climate and topography.
- Human impacts exacerbate problems associated with many natural problems, given that the hydraulic and mechanical properties of the materials are altered.

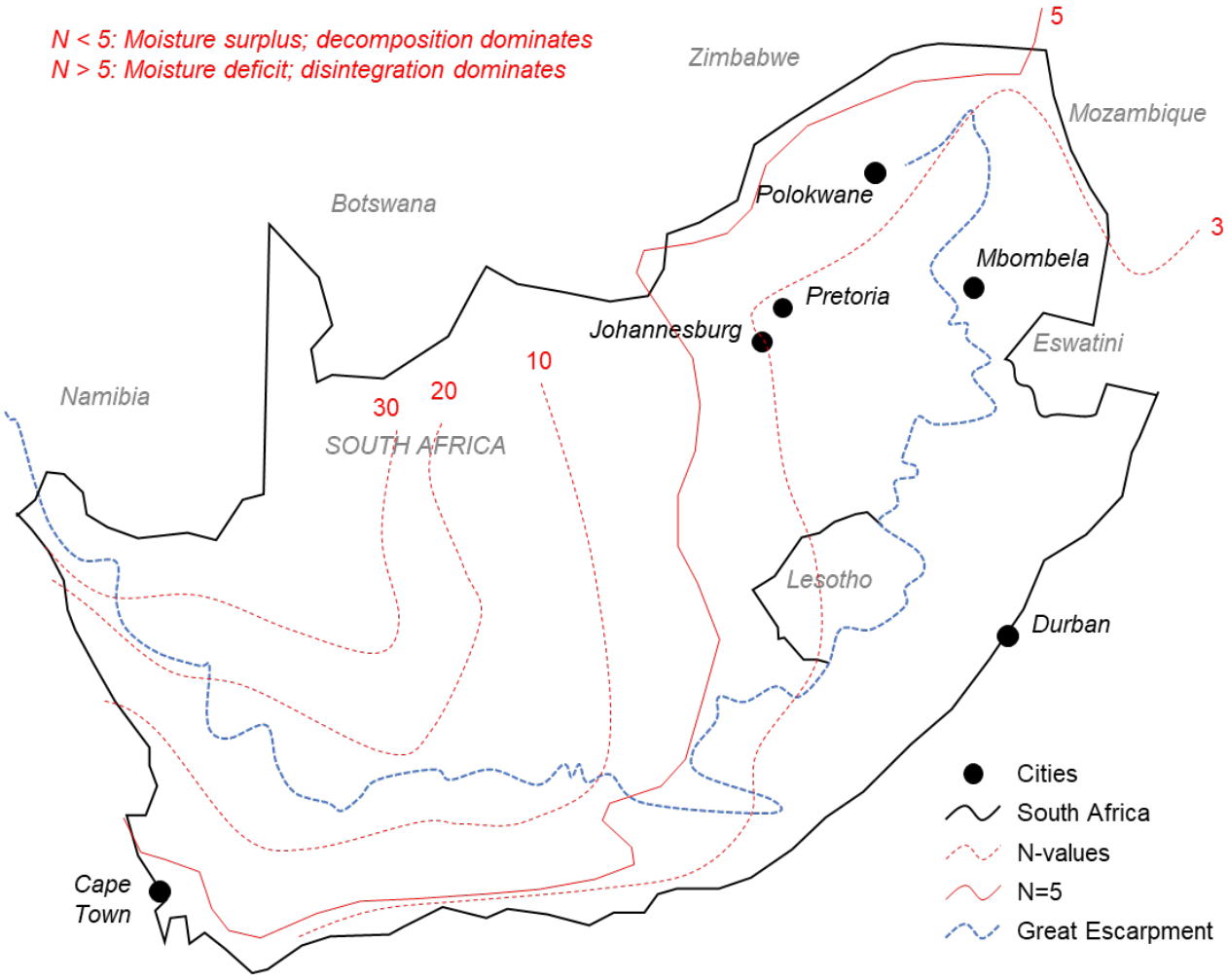

Figure 1-1 South Africa with its Great Escarpment and the areas more prone to different types of weathering (Dippenaar et al. 2025).

1.2 VADOSE ZONE STUDY AREAS

The different projects had case studies that were labelled Vadose Zone Study Area (VZSA), and all of these prior to this project are summarised in Dippenaar et al. 2022 together with all the relevant publications and qualifications. The details and references of the individual reports, including those incorporated into this project, are provided in Table 1.

Table 1-1 Vadose Zone Study Areas (VZSAs)

Number	Title	Reference
VZSA 01	Ephemeral Inland Wetlands (Midrand, Gauteng)	Dippenaar et al. 2014
VZSA 02	Platinum Tailings Storage Facility (Bushveld Complex)	Dippenaar et al. 2014
VZSA 03	Peri-urban Cemeteries (Temba, City of Tshwane)	Dippenaar et al. 2014
VZSA 04	Corrosion of Accessory Burial Materials	Dippenaar et al. 2018
VZSA 05	Flow along the Soil-rock Interface	Dippenaar et al. 2018
VZSA 06	Fontein Street Cemetery (Steve Tshwete Local Municipality)	Dippenaar et al. 2018
VZSA 07	Cape Town Cenozoic Sand Cemeteries	Dippenaar et al. 2018

VZSA 08	Microbial Contamination of Selected Burial Sites	Dippenaar et al. 2018
VZSA 09	Hydrology and Geochemistry of a Dolomite Mine	Dippenaar et al. 2019
VZSA 10	Dolomite Bedrock	Dippenaar et al. 2019
VZSA 11	Residual Dolomite and Wad	Dippenaar et al. 2019
VZSA 12	Facilitated Karst Dialogues	Dippenaar et al. 2019
VZSA 13	Intermediate Vadose Zone of Fractured Rock Mass	Jones et al. 2016
VZSA 14	Variably Saturated Fracture Flow	Jones et al. 2016
VZSA 15	Permeable Pavements	Dippenaar et al. 2022
In this book: Dippenaar (ed.) 2026		
VSZA16	Hydraulic and Mechanical Properties of Completely Weathered Bedrock (Eastern Escarpment)	Swart 2026a
VSZA 17	Weathering Profiles of Mn-Rich Dolomite in Humid to Sub-Arid Environments	Swart 2026b
VSZA18	Contaminant Transport in a Fractured Rock System using Tracers and Isotopes	Van Wyk 2026
VSZA 19	Analysis of Unsaturated Flow Behaviour through Discontinuities in Rock Mass	Maoyi & van Rooy 2026
VSZA 20	Fresh Rock Granite Weathering Rims	Bruyns 2026
VSZA 21	Urban Water related to Roodeplaat Dam and Hartbeespoort Dam	Visagie & Smith 2026
VSZA 22	Timbavati Goundwater and Surface Water Quality	Raible 2026

The case studies presented in this book were written by the authors, and the final formatting and editing were done by the editor to ensure that everything has the same overall feeling. The case studies were handled individually, and all relate to the MSc and PhD research of the single or main authors.

1.3 REFERENCES

Dippenaar MA, Maoyi M, Swart D, van Wyk Y, van Rooy JL (2026) Framework for Natural and Anthropological Changes to the Urban Vadose Zone. Report TT 954. Water Research Commission. Pretoria. www.wrc.org.za

Dippenaar MA, Jones BR, Van Rooy JL, Maoyi M, Swart D (2022) The Vadose Zone: from Theory to Practise. Report TT 869/21. Water Research Commission. Pretoria. ISBN 978-0-6392-0313-3. www.wrc.org.za (155 pages)

Dippenaar MA, Olivier J, Lorentz S, Ubomba-Jaswa E, Abia ALK, Diamond RE (2018) Environmental Risk Assessment, Monitoring and Management of Cemeteries. Report 2449/18/1. Water Research Commission. Pretoria. ISBN 978-1-4312-0978-1. www.wrc.org.za (94 pp)

Dippenaar MA, Swart D, Van Rooy JL, Diamond RE (2019) The Karst Vadose Zone: Influence on Recharge, Vulnerability and Surface Stability. Report TT 779/19. Water Research Commission. Pretoria. ISBN 978-0-6392-0080-4. www.wrc.org.za (91 pages)

Dippenaar MA, Van Rooy JL, Breedt N, Huisamen A., Muravha SE, Mahlangu S, Mulders JA (2014) Vadose Zone Hydrology: Concepts and Techniques. Water Research Commission. ISBN 978-1-4312-0507-3. www.wrc.org.za (174 pp)

Dippenaar MA, Van Rooy JL, Davis G, A'Bear. (eds.) 2025. Engineering Geological Soil and Rock Description Guideline. South African Institute for Engineering and Environmental Geologists (SAIEG). Pretoria. South Africa. www.saieg.co.za. 56 pages.

Jones BR, Van Rooy JL, Dippenaar MA, Brouwers LB, Roux JI, Joubert A, Segole KP (2016) Advances in the Understanding of Variably Saturated Fracture Flow. Report 2326/16/1 Water Research Commission. Pretoria. ISBN 978-1-4312-0794-7. www.wrc.org.za

Weinert HH. 1980. The Natural Road Construction Materials of Southern Africa. Academica. Cape Town.

CHAPTER 2: HYDRAULIC AND MECHANICAL PROPERTIES OF COMPLETELY WEATHERED BEDROCK (EASTERN ESCARPMENT)

Author: Duan Swart

This chapter emanates from the following project-related outcomes:

- Swart D. (2025). Evaluating hydraulic and mechanical properties of weathered intrusive and chemical sedimentary bedrock in South Africa. PhD (specialising in Engineering Geology) Thesis. University of Pretoria
- Swart D, Dippenaar MA, Van Rooy JL. (2023) Field tests for the identification of silts. Bulletin of Engineering Geology and the Environment. 82:425. https://doi.org/10.1007/s10064-023-03442-7
- Swart D, Dippenaar MA. (2025). Weathering profile of completely weathered rock from the Dullstroom Formation, South Africa. Bulletin of Engineering Geology and the Environment. https://doi.org/10.1007/s10064-025-04224-z

2.1 INTRODUCTION

2.1.1 Overview

Understanding the weathering bedrock profile within the complex vadose zone is essential for accurate geotechnical and hydrological site assessments. This chemically decomposed zone plays a critical role in governing near-surface unsaturated moisture flow, water storage, filtration, and the movement of water through the soil-rock interface. Traditional methods for pore geometry and moisture flow analysis have primarily relied on two-dimensional (2D) assessments, simplified pore pressure measurements and models, and empirical volume and density calculations. However, a deeper understanding of pore geometry and size distribution is required, particularly in unsaturated weathered geological materials, where moisture flow and other characteristics are strongly influenced by the internal pore structure, which evolves throughout the weathering process. The relict rock structure in completely weathered rock also provides stiffness, a crucial characteristic for engineering stability. However, natural or anthropogenic actions that destroy this structure will led to a loss of stiffness and alter the natural pore geometry.

In completely weathered rock, moisture flow follows a dual-porosity system, where fractures originating from the parent rock structure serve as primary pathways for moisture movement in the early stages of weathering. As weathering intensifies, primary pores within the rock matrix continually develop along mineral grain boundaries, defects, and cleavage breaks, forming pore orientations determined by the rock's stress history.

This case study demonstrates that X-Ray Computed Tomography (XRCT) is the most effective technique for characterizing metastable materials like completely weathered rock. By combining traditional soil classification methods with advanced imaging technologies, this study provides a more robust framework for understanding the behaviours of residual soils and weathered rock. This study highlights the importance of characterizing pore geometry and size distribution to better understand how moisture percolates through these materials under unsaturated conditions, offering practical

applications for early-stage site investigations and long-term monitoring of geotechnical engineering projects.

2.2 SITE DESCRIPTION

2.2.1 Locality

The study area is located along the eastern escarpment and the eastern Highveld in both the Mpumalanga and Limpopo provinces. The top of the eastern escarpment represents an area where intensive chemical weathering and low erosion rates take place, and it is covered by a thin surficial transported horizon (Makhubela et al. 2021). This ground profile allows for accessibility to completely weathered rock material for sampling and logging in freshly dug trial pits. The specific sample locations were chosen for the expected bedrock geology and weathering profile. The objective of the sampling was to retrieve completely weathered rock that grades as a silt when broken down and sieved. The field identification methods used to confirm the presence of silt is discussed in Swart et al. (2023). The sample locations are presented in Figure 2-12. The sample locations are named after the closest town to the site of interest.

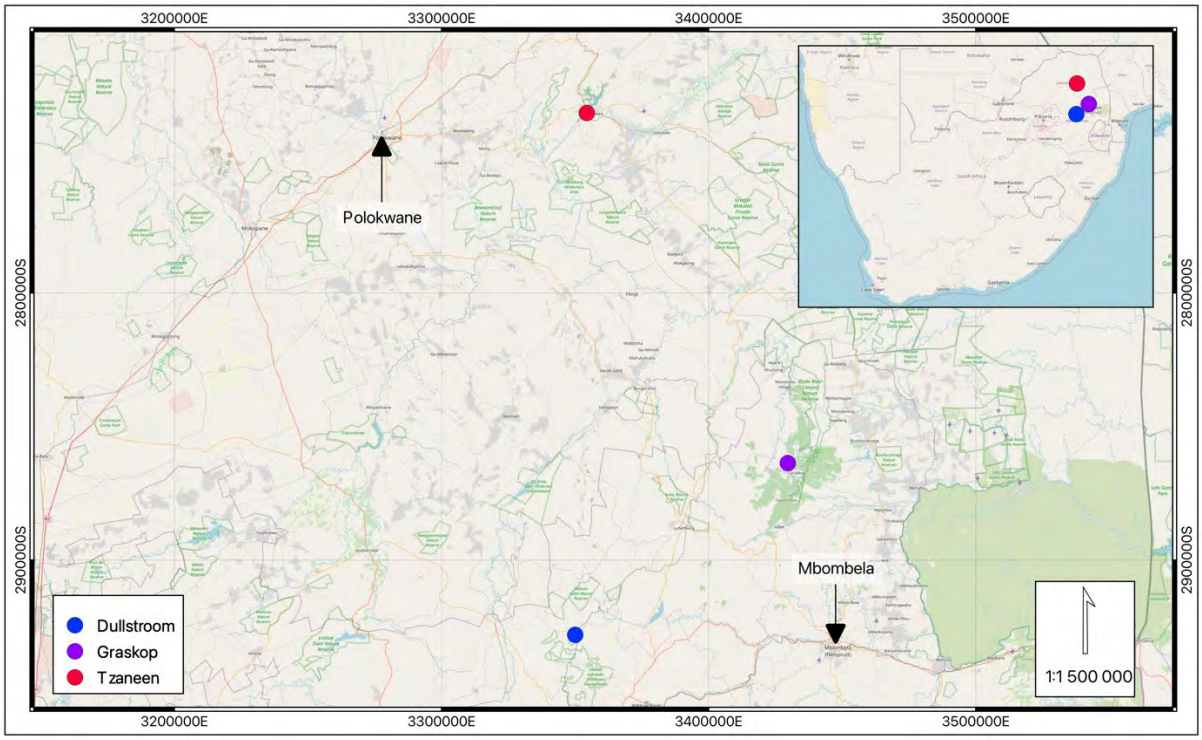

Figure 2-1 Locality of retrieve samples.

2.2.2 Geology

2.2.2.1 Dullstroom

The specific site on which the samples were successfully retrieved is underlain by the Dullstroom Formation of the Rooiberg Group, commonly referred to as the *Dullstroom lavas* or *Dullstroom diabase* (Schweitzer et al. 1995; Bunchanan 2006). This geological unit comprises basaltic to andesitic lavas,

as well as dacites and rhyolites, formed by a fine-grained groundmass with variable proportions of phenocrysts, porphyroblasts and amygdales.

2.2.2.2 Tzaneen

Mafic intrusions in South Africa, comprising dykes and sills of dolerite and diabase, are widespread throughout the Kaapvaal Craton (Anhaeusser, 2006). Weinert (1980) stated the term dolerite is used to differentiate the Karoo-aged diabase from the older Proterozoic and Archean intrusions. However, these two terms are given to the same rock with similar chemical compositions and is only used to emphasise the expected difference in engineering behaviour due to the generally more deeply weathered, and possibly altered, diabase.

The sampled diabase material forms part of the Proterozoic (~1.90 Ga) NE-trending mafic dyke swarm occurring in the granitoid intrusions near Tzaneen. Klausen et al. (2010) found that these intrusions are basaltic tholeiites and have undergone very little alteration, resulting in pristine doleritic textures which are typically ophitic to sub-ophitic. The chemical composition of these intrusions is typically a series of Ca-rich plagioclase (anorthite and labradorite) and pyroxene minerals (mainly augite), and lesser to no olivine.

2.2.2.3 Graskop

The Malmani Subgroup dolomites are replacement products of limestone alternation through the process of dolomitization and chertification during the late Archean and early Proterozoic (Obbes, 1995). The precursor carbonates that formed in the Transvaal Supergroup Epeiric Sea some 2550 Ma ago are stromatolitic deposits or the direct result of erosion and weathering of stromatolites (Eriksson and Altermann, 1998). Dolomite rock contains more than 90% dolomite (mineral) and less than 10% calcite, secondary silica (chert) and detrital minerals. The best representation of the range of the dolomite compositions that forms, namely calcian to magnesian dolomites, is Ca(1+x)Mg(1-x)(CO3)2 as dolomites are rarely stoichiometric (CaMg(CO3)2) (Warren, 2000). Dolomite can be “enriched” in iron (Fe) or manganese (Mn), but these are usually minor amounts in the overall rock (Buttrick, 1986). Buttrick (1986) states “the fabric developed in the wad is determined by the nature of the fabric inherent in the parent dolomite”; therefore, the diagenesis and especially the stress history of dolomite influences the properties of wad.

All site areas are characterised as having a Weinert N-value less than 2, and deep weathering profiles are expected to exist.

2.3 METHODOLOGY

2.3.1 Fieldwork

The site areas were investigated to find and expose weathering profiles presenting completely weathered rock of the desired bedrock type by means of excavating machine-dug trial pits, or locating existing borrow pits or excavation faces. Existing excavation faces were dug back by hand and shovel until the moisture content was such that the soil was not desiccated, and the in-situ structure was preserved. The objective of the sample placement strategy was to assess the impact of chemical weathering on the relict rock structure and resultant porosity of the completely weathered rock and

residual soil. To achieve this, one sample was obtained within the residual soil, and one within the completely weathered rock. At the Dullstroom site, four samples were taken, one in the residual and three in the completely weathered rock at varying depths.

The sampling comprised undisturbed block and tube samples, and disturbed bag samples. The tube samples were retrieved by pushing a PVC pipe (30.0 mm x 10.0 mm) into the soil profile, which were taken at the Graskop and Dullstroom sites. Only block samples were taken at the Tzaneen site. Undisturbed samples were wrapped and capped appropriately to ensure moisture loss was minimal before being tested in the laboratory.

2.3.2 Laboratory work

The tube samples were scanned at X-Sight X-Ray Services by means of a Nikon XT H225 ST system. The tube samples required no preparation or drying as the scanner can scan at any moisture and sample shape, if small enough. The scans were conducted at 180 kV and 330 uA where approximately 2985 (no.) images were acquired of each sample while the samples rotated a full 360 degrees. Two-dimensional (2D) and three-dimensional (3D) slices were constructed using the Phoenix Datos acquisition and reconstruction software. The software processing focused on the sample material only and excluded a 2.00 mm space between the sample material and the tube's inner wall and 2.00 mm at the top and bottom portions of the sample. This was done to exclude areas where displacement and density alteration would have occurred at the sample and tube interface during sample retrieval. The density contrast and pore space analyses were performed with the use of VOLUME GRAPHICS (VG) STUDIO MAX software.

2.4 RESULTS

A schematic of the sample positions as well as photographs and sample details of the Dullstroom, Tzaneen and Graskop samples are shown in Figure 2-2, Figure 2-14, and Figure 2-15, respectively. According to the calculated density and moisture content of the Dullstroom and Tzaneen samples, there is generally a decrease in dry density and increase in moisture content with an increase in weathering. Graskop shows the inverse, with an increase in dry density and decrease in moisture higher up the weathering profile. The continued leaching of the wad and pedogenic activity causes the extremely low-density material to densify.

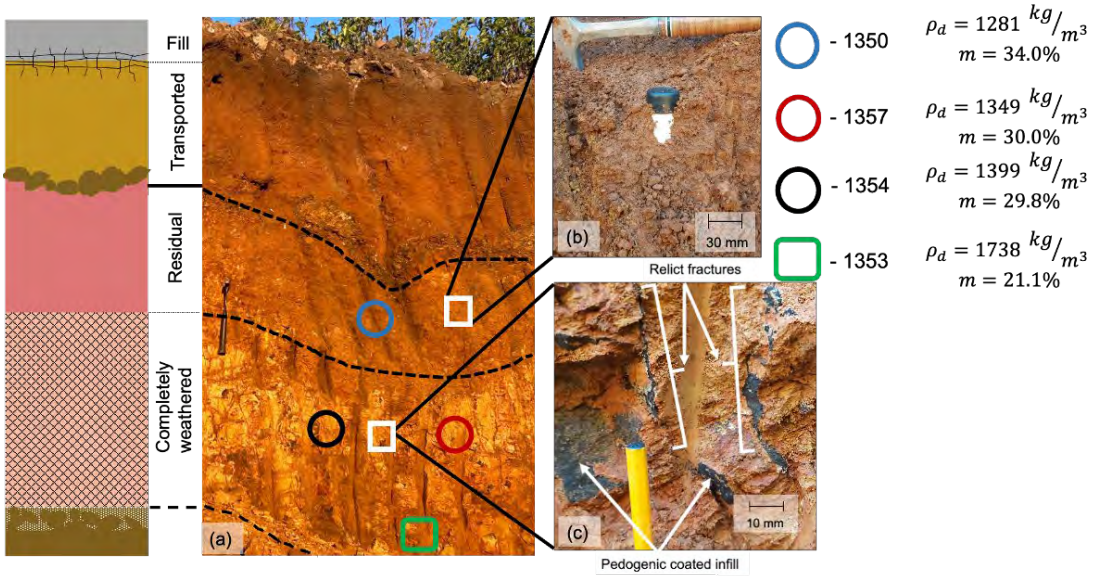

Figure 2-2 (a) Existing excavation face at Dullstroom (photograph taken by MA Dippenaar); (b) Macro soil structure in residual soil with tube sample (c) Macro soil structure indicating relict rock structure and pedogenic infill.

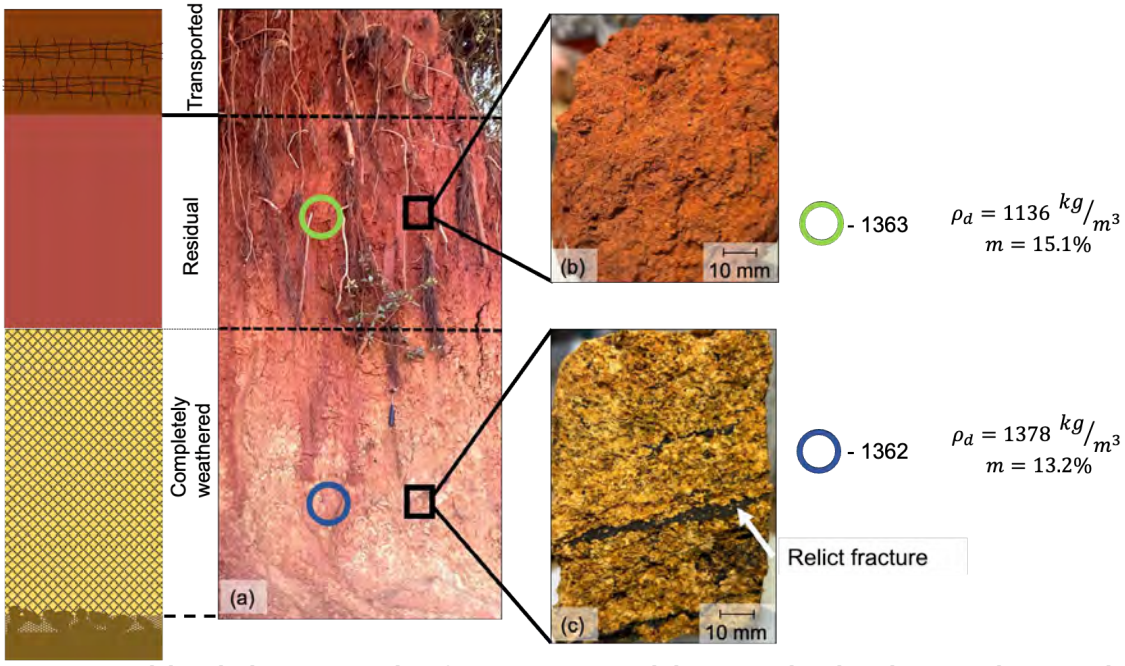

Figure 2-3 (a) Existing excavation face at Tzaneen (photograph taken by MA Dippenaar); (b) Macro soil structure in residual soil (c) Macro soil structure indicating relict rock structure and pedogenic infill.

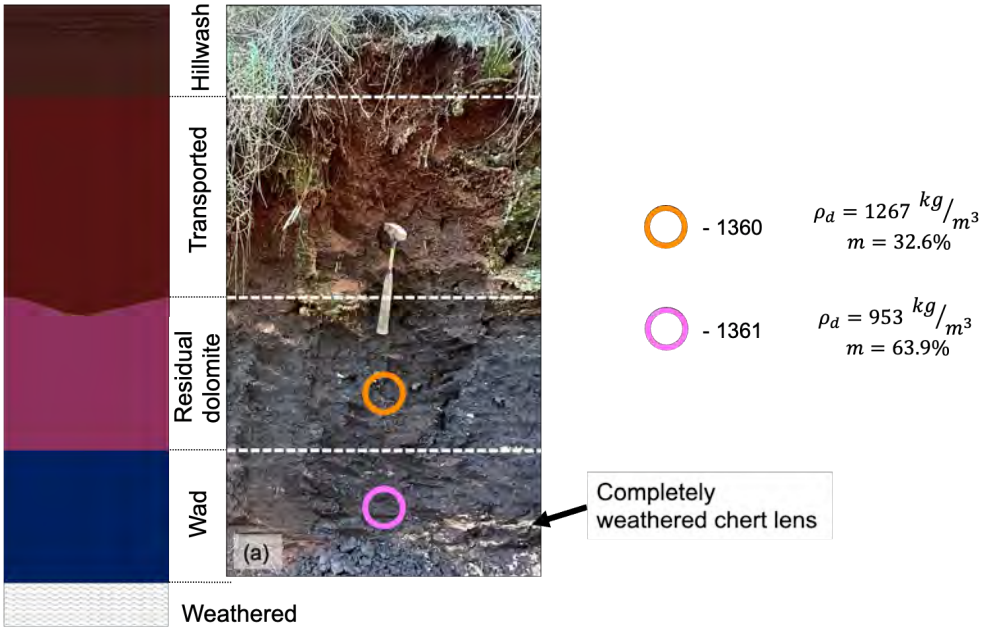

Figure 2-4 (a) Existing excavation face at Graskop (photograph taken by MA Dippenaar).

2.4.1 Dullstroom

As shown in Figure 2-5, the porosity of sample 1357 is largely controlled by its relict rock structure and texture, with the open pores being elongated and aligned parallel to the vertical structures identified on-site (Figure 2-2(c)). In contrast, the oriented pores in sample 1350 have been lost. The largest void in sample 1350, marked in red, appears to be a root channel that has penetrated the matrix, creating an open pathway. The remaining pores in sample 1350 are generally non-effective and lack a clear orientation.

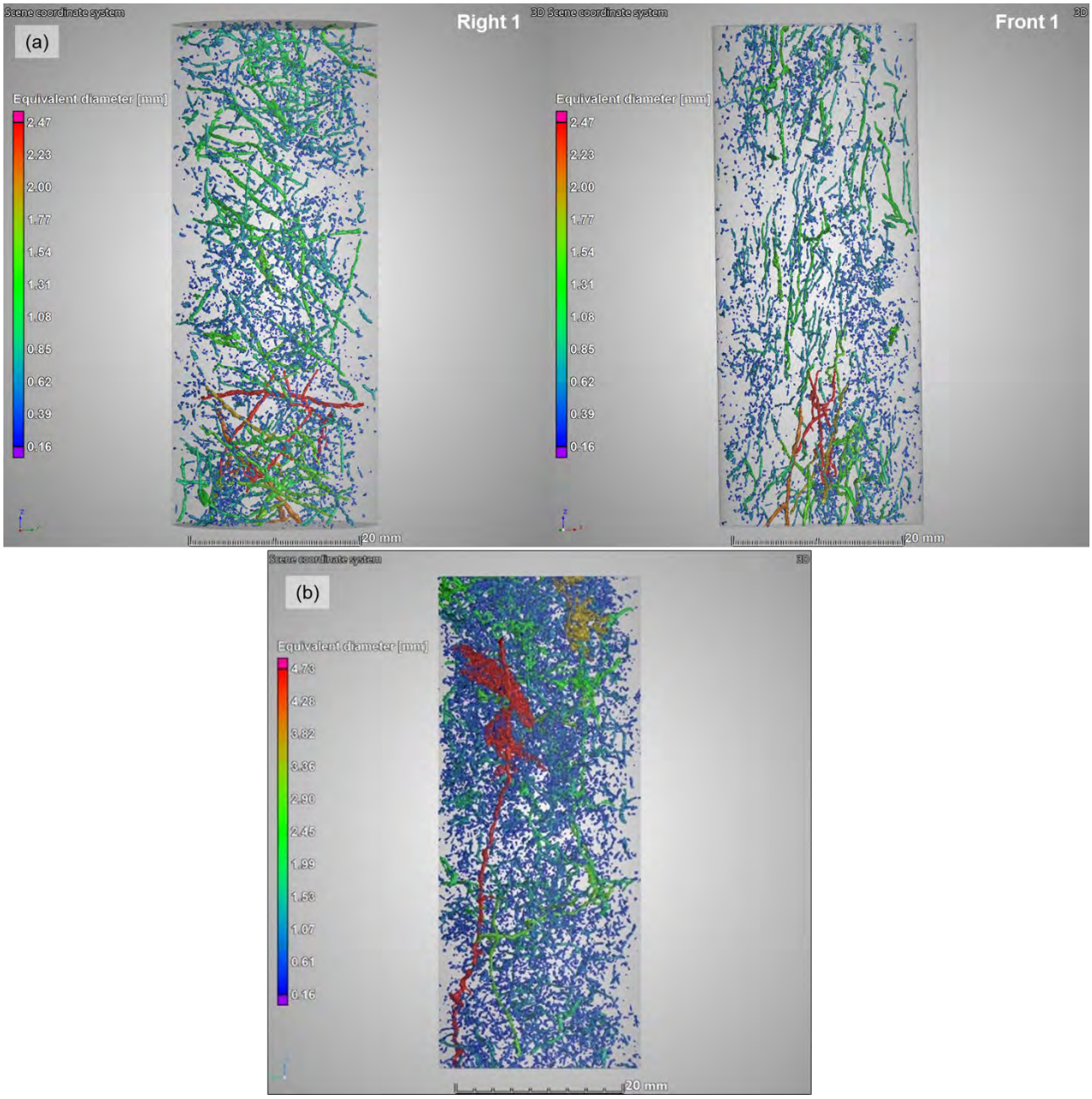

Figure 2-5 (a) Sample 1357 3D porosity model with right view (left) and front view (right); (b) Sample 1350 3D porosity model.

2.4.2 Tzaneen

Figure 2-17 presents a 2D scan of the completely weathered diabase, showing both top and front views. The densest portion of the material is shaded in red, while lighter shaded areas represent pyroxene minerals that have survived weathering. Black-shaded regions indicate open pores. Pyroxene minerals decompose through surface reactions starting at the edges and progressing inward, often altering into secondary products like various clay minerals and Fe-oxides, or completely decomposing without leaving a weathering product, resulting in open pores (Colman, 1982; Wilson, 2004).

The surrounding grey portions represent the weathering products of plagioclase. Although both pyroxene and plagioclase are susceptible to chemical weathering, pyroxenes are more resistant than

Ca-rich plagioclase (Schaetzl & Anderson, 2005). It is hypothesised that most feldspars have weathered into kaolinite and halloysite, losing their original structure, whereas the pyroxene has only weathered at the surface edges, with the inner portions remaining intact and forming the densest part of the material.

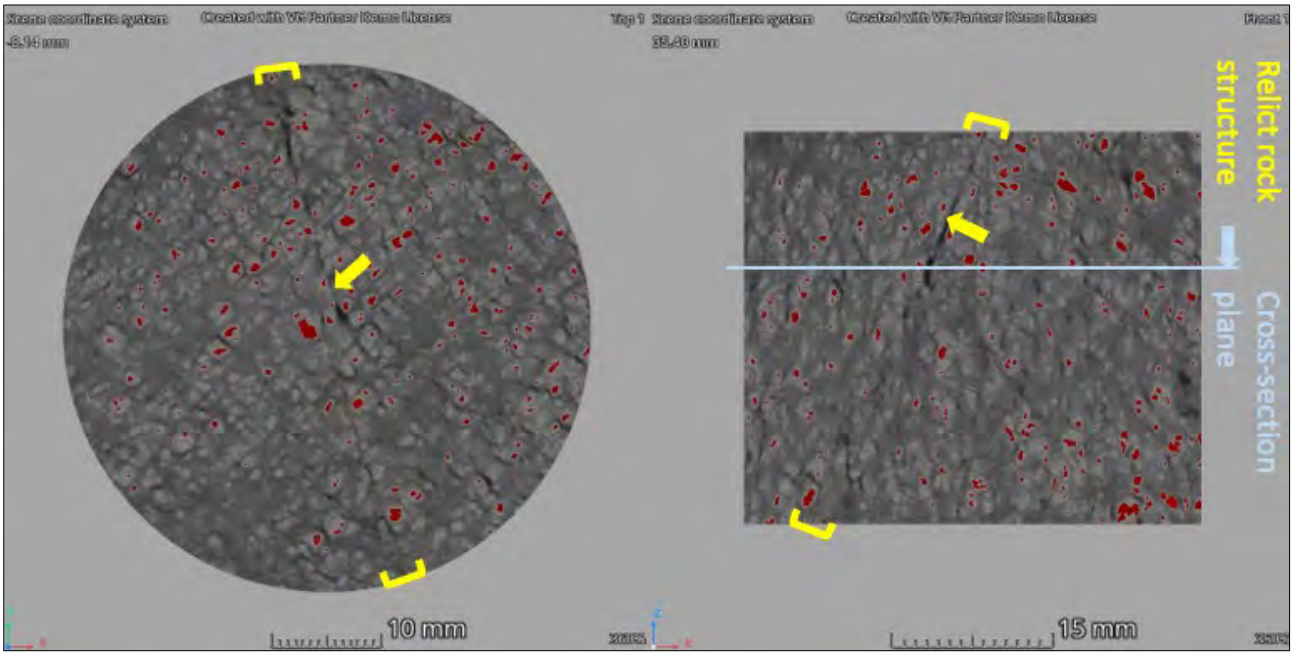

Figure 2-6 Sample 1362 2D slices from top view (left) and front view (right) with density colour contrast.

According to Wilson and Jones (1983), the dissolution of pyroxene and amphibole minerals is strongly influenced by the relict structure of the mineral grain, leading to surface etching and cleavage breaks that govern pore orientation during weathering. This is clearly seen in the near-perpendicular pore orientations within the moderately decomposed pyroxene, which has two cleavage planes intersecting at approximately a 90° angle, as shown in Figure 2-18. This indicates that the geometry of the initial porosity formed during the early stages of weathering is governed by the rock mineral's structure, chemical defects, and stress history. Most of the modelled pores are located near or on the mineral grain boundary. It is expected that the pores within the kaolinite portion of the sample are smaller than the voxel size and thus could not be detected.

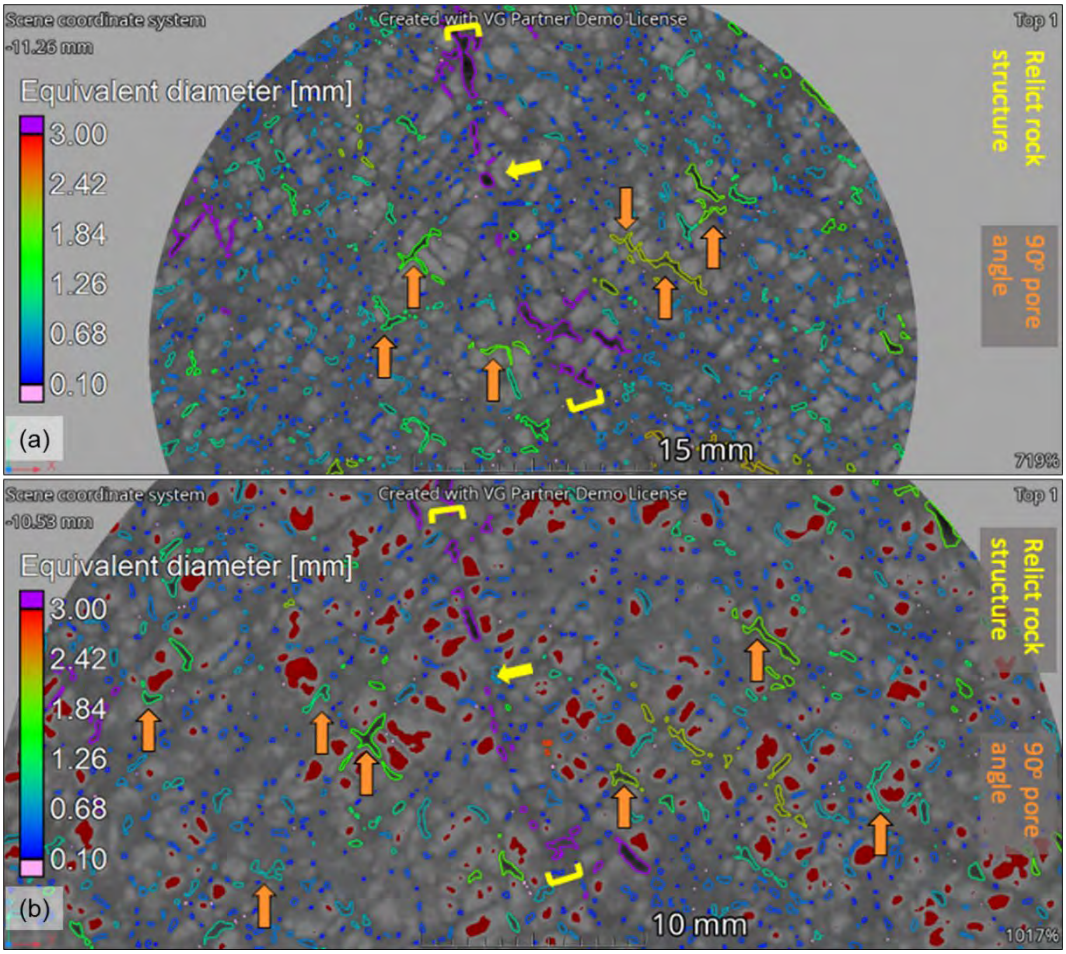

Figure 2-7 (a) Sample 1362 2D slices from top view with pore modelling; (b) Sample 1362 top view with pore modelling and density colour contrast.

2.4.3 Graskop

Dowding (2004) investigated the same profile and found both the wad and residual dolomite to be enriched in lithiophorite ($MnO_2(OH)_2$) with a relative increase in Fe content and pedogenic nodules in the residual dolomite. The residual dolomite has a minor to abundant amount of weakly to strongly cemented Fe and Mn nodules which are typically sand size, as presented in Figure 2-19.

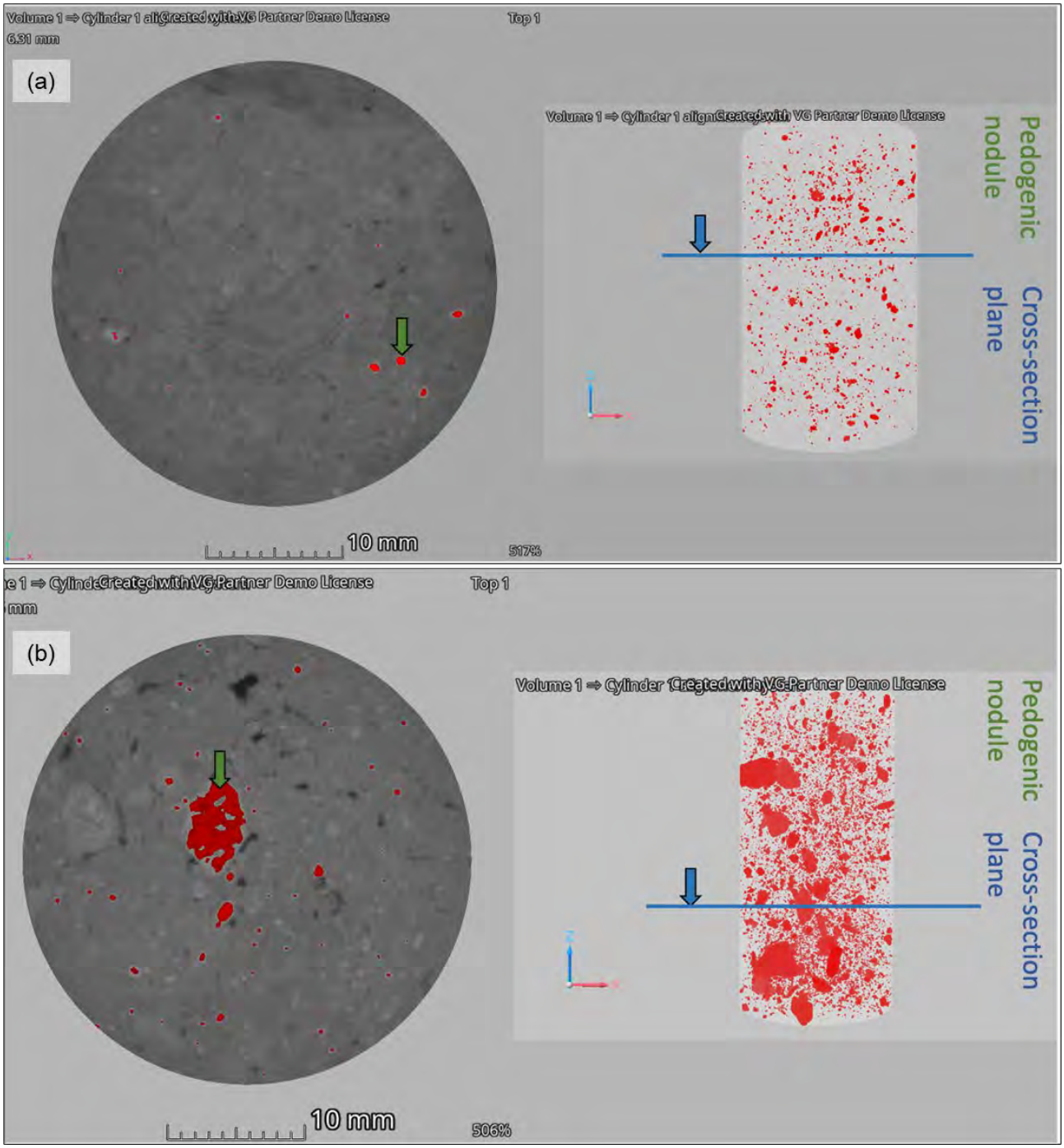

Figure 2-8 (a) Sample 1361 2D slice top view (left) and 3D density contrast (right); (b) Sample 1360 top view (left) and 3D porosity distribution (right).

Figure 2-20 presents the top view of the two tube samples with the modelled pore spaces and density contrast applied. The wad (sample 1361) has scatter pores that are less than 1.00 mm in diameter and a few pore sizes between 1.50 mm and 1.00 mm in diameter. It is expected that the majority of the pore spaces in the wad will be smaller than 0.06 mm in diameter, which could not be identified and modelled by the XRCT equipment as this exceeds the smallest measurable voxel size. Swart et al (2019) identified pore spaces of 100.0 nm in diameter within silt-sized grains of birnessite (MnO_2). The residual dolomite (sample 1360) has generally larger pores which are frequently greater than 1.00 mm and elongated in shape.

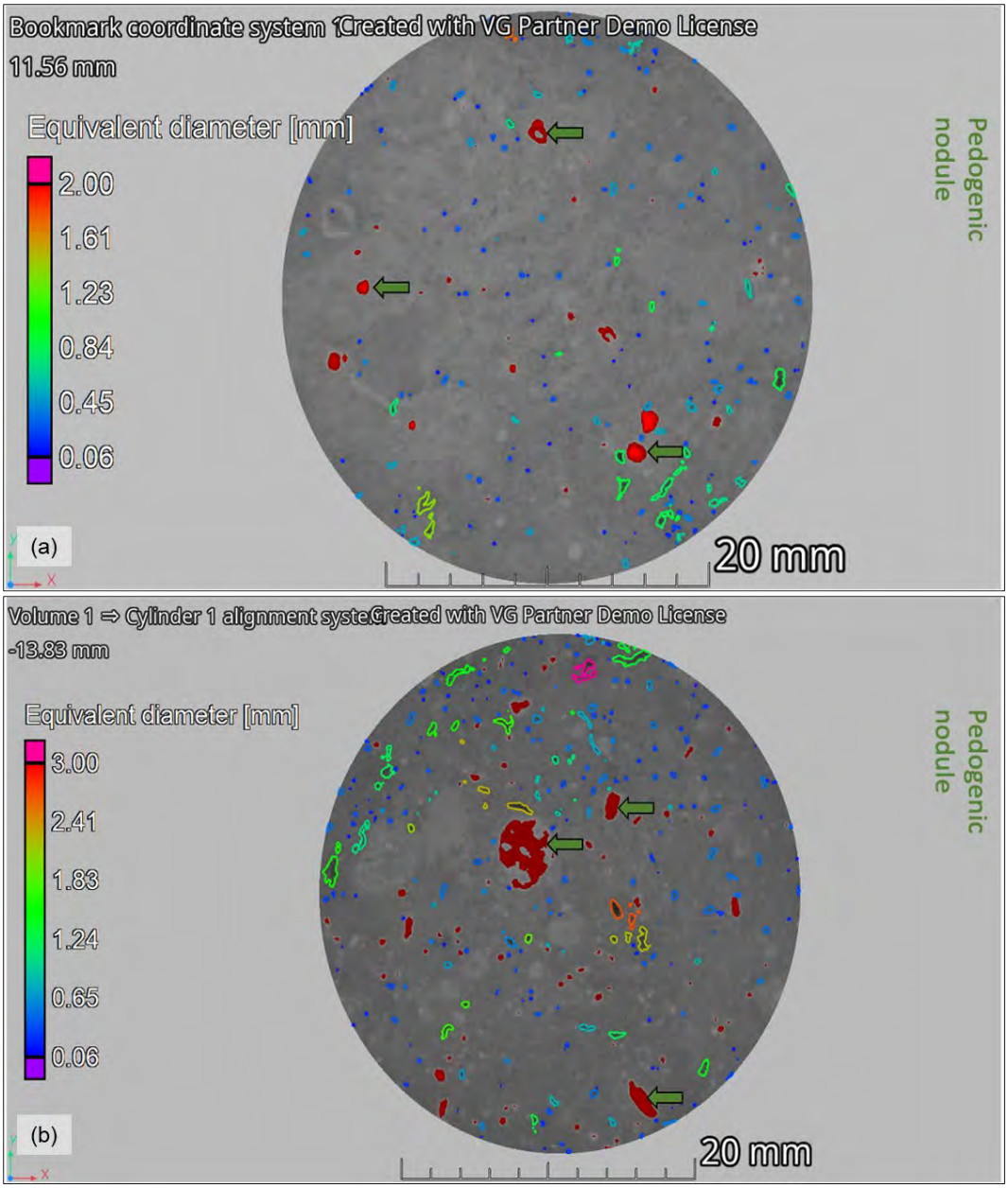

Figure 2-9 (a) Sample 1361 2D slice top view with pore modelling and density colour contrast; (b) Sample 1360 top view with pore modelling and density colour contrast.

2.5 DISCUSSION

The structural change due to weathering of the completely weathered rock is evident in the sample photographs, 2D slices, the 3D porosity models and density calculations. Weathering occurs with water moving through the profile and causes chemical reactions that release ions from minerals and leach them away. The removal of material will result in a decrease in the dry density and an increase in the void ratio. Volume change is expected to occur during weathering with opening of fissures.

In competent rock, water will often flow in open secondary pores such as rock fractures. In completely weathered rock, water flows through the preferred, initially open, pathways, reaching a high flow rate; erosion is expected to take place and remove material from the weathered fracture face. The erosion may increase with the further opening of the fracture, or the material may lodge in a narrow opening

and reduce flow, thereby terminating the erosion process. The resulting clay and silt infill are typically stained black from pedogenic deposits coating the surface as can be seen in the Dullstroom and Tzaneen completely weathered rock samples. The pedogenic coatings are typically goethite and hematite, which are Fe-oxides and have high density values (5.26 g/m^3). The denser material is highlighted in the 2D slices due to X-ray attenuation and represented in density contrast in the Graskop samples. The pedogenic staining on the fracture faces in the Tzaneen completely weathered rock (sample 1362) is not highlighted by the density contrast as it is very thin and smaller than the voxel size of the scan; therefore, not able to be recorded.

Figure 2-10 summarises the different structural profiles determined in the completely weathered rock for the Dullstroom and Tzaneen sites. The primary porosity formed during the initial stages of weathering is determined by the rock mineral properties. The secondary porosity is determined by the presence of the relic rock structure, such as fractures and discontinuities. As weathering occurs, much of the relict rock structure is destroyed and porosity becomes ever more governed by the primary porosity, which gradually forms from pedogenic processes. The residual soil loses the relict rock structure and therefore the secondary structure tends to zero. According to Hencher (2012), the upper portion of the residual soil will eventually collapse through continued weathering, whereby increasing dry density and reducing void ratio.

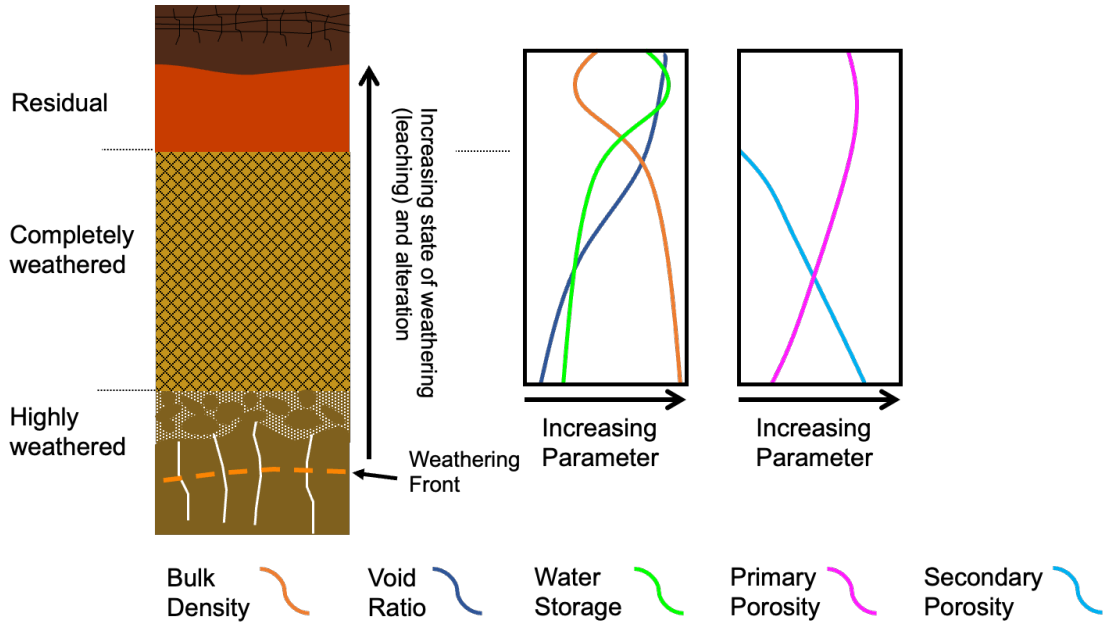

Figure 2-10 Vertical anisotropy profiles in completely weathered rock for intrusive igneous rock.

The reworking and external forces, be it natural or anthropogenic, seemingly impact both the chemical and structural parameters and subsequently the colour and expected grading. The weathering, structural, and chemical profiles of Mn-rich dolomite bedrock are shown in Figure 2-22. It must be noted that the alteration between the wad and residual dolomite is usually controlled by a densification of the wad and a reduction in water holding capacity within the more weathered profiles. This trend of bulk density agrees with Hencher (2012); however, this differs from the structural profile shown Figure 2-10, where there is a continuous decrease of bulk density into the residual soil before the densification occurs near the residual soil / transported soil boundary.

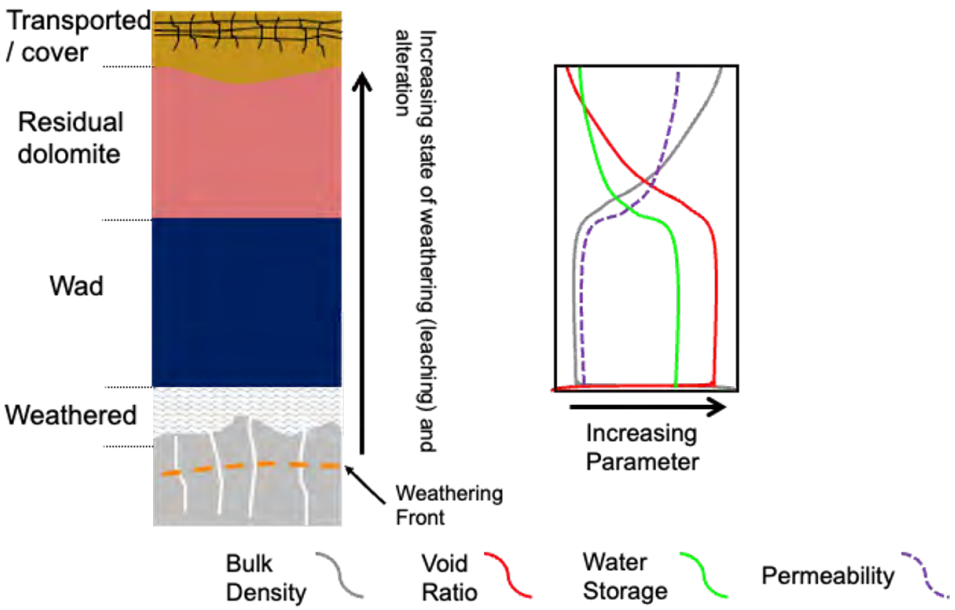

Figure 2-11 Vertical anisotropy profiles on weathered Mn-rich dolomite.

2.6 OUTCOME AND WAY FORWARD

Understanding the weathering bedrock profile within the complex vadose zone is essential for accurate geotechnical and hydrological site assessments. This chemically decomposed zone plays a critical role in governing near-surface unsaturated moisture flow, water storage, filtration, and the movement of water through the soil-rock interface. Traditional methods for pore geometry and moisture flow analysis have primarily relied on two-dimensional (2D) assessments, simplified pore pressure measurements and models, and empirical volume and density calculations. However, a deeper understanding of pore geometry and size distribution is required, particularly in unsaturated weathered geological materials, where moisture flow and other characteristics are strongly influenced by the internal pore structure, which evolves throughout the weathering process.

This research demonstrates that XRCT is the most effective technique for characterizing metastable materials like completely weathered rock, as it preserves their natural pore structures and moisture flow characteristics. By combining traditional soil classification methods with advanced imaging technologies, this study offers a more robust framework for understanding the behaviour of residual soils and weathered rock. The findings improve the accuracy of soil classification, moisture flow assessment, and dual-porosity modelling, providing practical applications for early-stage site investigations and long-term monitoring of geotechnical engineering projects.

One limitation of XRCT in this study was its inability to differentiate between minerals with similar densities in close proximity, as well as distinguishing air from water within pores. To address this, sample preparation through the use of additives that stain specific soil features or pore water is necessary, depending on the application. Staining alters the density, enhancing contrast between minerals, liquids, or soil structures (Li & Tang, 2019; Terribile et al., 2022). However, the main aim of this study was to characterize the in-situ soil structure and mineral relationships at different weathering stages, and sample preparation could have affected these characteristics.

The intensity of weathering in the samples influences the material's characteristics, impacting rock fabric, primary and secondary porosities, and chemical composition. The geometry of the initial porosity formed during the early stages of weathering is governed by the rock mineral's structure, chemical defects, and stress history. In completely weathered rock, pore geometry tends to follow the preferred rock structure rather than the texture determined by grading analyses. In contrast, the residual soil has lost its relict rock structure due to intense weathering, with porosity and pedogenic formations controlled by typical soil-forming processes and biotic activity.

The XRCT scans show that most pores in less-weathered rock are non-effective and exist within the relict structure. As weathering progresses, primary porosity increases, leading to greater total porosity. However, secondary porosity decreases as relict structures are destroyed, reaching near-zero in the residual soil. There appears to be volume change during the weathering process, with fissures opening that later become flow paths before clogging with pedogenic material.

Pedogenic deposits form along relict structures as stains and coatings on infill, suggesting that water flow primarily occurs along these relict openings in less-weathered rock. As weathering intensifies, the distribution of pedogenic material increases within the matrix, indicating that flow occurs through both primary and secondary pores, making completely weathered rock a dual-porosity system. This reinforces the idea, as suggested by various authors, that using pedological classifications in engineering can be beneficial for understanding water flow in the unsaturated zone.

2.7 REFERENCES

Anhaeusser, C. R., 2006. Ultramafic and Mafic Intrusions of the Kaapvaal Craton. In: M. R. Johnson, C. R. Anhaeusser & R. J. Thomas, eds. The Geology of South Africa. s.l.:Geological Society of South Africa, Johannesburg/Council for Geoscience, Pretoria, pp. 95-134.

Buchanan, P., 2006. The Rooiberg Group. In: The geology of South Africa. s.l.: Council for Geoscience, pp. 283-290.

Buttrick, D. B. (1986). Wad and Ferroan Soil Developed in the Dolomitic Area South of Pretoria. MSc (University of Pretoria).

Colman, S. (1982). Chemical Weathering of Basalts and Andesites: Evidence from Weathering Rinds. Washington: Geological Survey Professional.

Eriksson, P., & Altermann, W. (1998). An overview of the geology of the Transvaal Supergroup dolomites (South Africa). Environmental Geology, 36, 179-188.

Hencher, S., 2012. Practical Engineering Geology. NY: Spon Press.

Klausen, M., Söderlund, U., Olsson, J., Ernst, R., Armoogam, M., Mkhize, S., & Petzer, G. (2010). Petrological discrimination among Precambrian dyke swarms: Eastern Kaapvaal craton (South Africa). Precambrian Research, 183, 501-522.

Li, Z. & Tang, L., 2019. Using Synchrotron-Based X-ray Microcomputed Tomography to Characterize Water Distribution in Compacted Soils. Advances in Materials Science and Engineering

Makhubela, T. et al., 2021. Erosion rates and weathering timescales in the eastern Great Escarpment, South Africa. Chemical Geology, Volume 580.

Obbes, A. (1995). The Structure, Stratigraphy and Sedimentology of the Black Reef-Malmani-Rooihoogte Succession of the Transvaal Supergroup South-West of Pretoria. Master Thesis, Rand Afrikaans University

Schaetzl, R., & Anderson, S. (2005). Soils Genesis and Geomorphology. Cambridge University Press.

Schweitzer, J., Hatton, C. & de Waal, S., 1995. Regional lithochemical stratigraphy of the Rooiberg Group, upper Transvaal Supergroup: A proposed new subdivision. S.Afr.J.Geol, 98(3), pp. 245-255.

Swart D, Dippenaar MA, Van Rooy JL. (2023) Field tests for the identification of silts. Bulletin of Engineering Geology and the Environment. 82:425. https://doi.org/10.1007/s10064-023-03442-7

Terribile, F. et al., 2022. Soil Sampling and Preparation for X-ray Imaging. In: S. Mooney, I. Young, R. Heck & S. Peth, eds. X-ray Imaging of the Soil Porous Architecture. s.l.: Springer, pp. 19-38.

Weinert, H. (1980). The Natural Road Construction Materials of Southern Africa. Pretoria: CSIR.

Wilson, M. (2004). Weathering of the primary rock-forming minerals: processes, products and rates. Clay Minerals, 39, 233-266.

Wilson, M., & Jones, D. (1983). Lichen weathering of minerals: Implications for pedogenesis. Residual Deposits: Surface Related Weathering Processes and Materials. Special issue of the Journal of the Geological Society, 5-12.

CHAPTER 3: WEATHERING PROFILES OF MN-RICH DOLOMITE IN HUMID TO SUB-ARID ENVIRONMENTS

Author: Duan Swart

This chapter emanates from the following project-related outcomes:

- Swart D. 2019. Mechanical and hydraulic properties of residual dolomite and wad found in the Malmani Subgroup in South Africa. MSc (specialising in Engineering Geology) Dissertation. Geology Department. University of Pretoria.
- Swart D. 2025. Evaluating hydraulic and mechanical properties of weathered intrusive and chemical sedimentary bedrock in South Africa. PhD (specialising in Engineering Geology) Thesis. Department of Geology. University of Pretoria
- Swart D, Dippenaar, M. & Van Rooy, J., 2019. Mechanical and hydraulic properties of residual dolomite and wad. South African Journal of Geology, pp. 1-10.
- Swart D, Gaspar TAV, Dippenaar MA (2021) Testing of hydromechanical properties of the variably saturated residual dolomite (wad). In: Proceedings of the 20th Conference on Soil Mechanics and Geotechnical Engineering. Sydney.

3.1 FORMATION OF RESIDUAL DOLOMITE AND WAD

Dolomite residuum (including wad and residual dolomite) is formed from leaching of a calcium-magnesium-rich carbonate rock called dolomite. Dolomite rock contains more than 90% dolomite (mineral) and less than 10% calcite, secondary silica (chert) and detrital minerals. The best representation of the range of the dolomite compositions that forms, namely calcian to magnesian dolomites, is Ca(1+x)Mg(1-x)(CO3)2, as dolomites are rarely stoichiometric (CaMg(CO3)2) (Warren 2000). Dolomite can be *enriched* with iron (Fe) or manganese (Mn), but these are usually minor amounts, less than 2%, in the overall rock (Buttrick 1986).

Beukes et al. (1999) concluded that the dolomite residuum seen in weathering profiles today formed after the break-up of Gondwanaland (~180 ma.), where conditions were humid and warm, resulting in moderately acidic to weakly alkaline and oxidising conditions. These conditions allow for deep chemical weathering to form typical wad material from dolomite. The dolomite bedrock outcropping on the Eastern Escarpment near Graskop is exposed to a similar humid environment, which is forming wad and residual dolomite close to the surface. Rainwater that precipitates, infiltrates, and eventually percolates through dolomite bedrock becomes slightly acidic due to the partial pressure of carbon dioxide in the atmosphere and the soil, forming a weak carbonic acid (H2CO3). The meteoric water flowing through the discontinuities in the dolomite rock mass causes leaching of the soluble carbonate minerals, resulting in a bicarbonate-rich water that leaves behind the insoluble material. The insoluble material is described as wad when dark blue to purple, very porous, Mn-rich soil. Continued weathering of the profile will typically form red, silty to clayey, Fe-rich soil termed residual dolomite, as shown in Figure 3-1.

The movement of manganese (Mn) in a weathering profile has been investigated by many authors from various backgrounds (van der Merwe 1942; Buttrick 1986; Dowding et al. 2005; Dowding & Fey 2007; Bourgault & Rabenhorst 2011). Mn can exist in multiple different oxidation states in soil but can only be dissolved if Mn (III) or Mn (IV) is reduced to Mn (II) or Mn (II) is released from the crystal lattice. This process is controlled by the pH value and the oxidation-reduction equilibrium of the soil. Mn compounds are much more soluble in acid soils than in neutral or alkaline soils, and much more soluble in reducing

than in oxidising soils. The greater susceptibility of Mn to undergo different forms of oxidation, compared to iron (Fe), makes the Mn oxides readily dissolve into solution when exposed to further leaching and acidic environments. This can be seen in weathering profiles where Mn oxides, typically birnessite and lithiophorite, which form wad, in highly weathered soils are normally confined to the C horizon, or completely weathered rock, in which the pH may be more alkaline and reduction subdued enough to allow precipitation. Above the wad, the Mn oxides have dissolved, and the Mn redistributes to form nodules in the residual dolomite, whereby the red colour of the Fe oxides is exposed. This reworking process reduces the influence the Mn oxides have on the hydromechanical properties of the weathered profile.

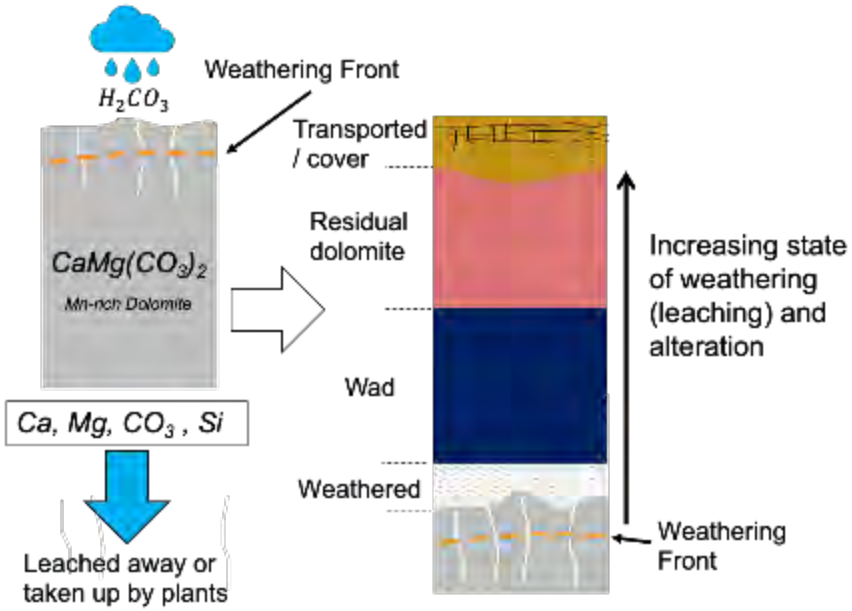

Figure 3-1 Vertical chemical profile in completely weathered rock.

3.2 ROLE OF MANGANESE OXIDES IN DOLOMITE RESIDUUM

Metal (Fe and Mn) oxides in wad have recently been thought to influence the variable and high liquid limits to a much greater extent than previously thought, especially the presence of certain Mn oxides (Swart et al. 2019). Jenne (1968) stated that the chemical influences that Mn oxides have on the surrounding environment and aqueous solutions far outweigh their concentrations. The type of Mn mineral is usually difficult to identify due to the poor crystallinity of the material. This is further complicated due to Mn minerals having similar X-ray diffraction (XRD) diagnostic peaks to common clay minerals (Dowding 2004). The typical Mn oxides found in wad are birnessite (MnO_2), lithiophorite ($MnO_2(OH)_2$), and todorokite. Birnessite is the simplest form of the Mn oxides in nature and the most common. It has a coral to sponge type structure, has a surface area of 300 m^2/g and can hold 15% to 25% of its weight in water (Buser & Graf 1955; Post 1999; Swart et al. 2019).

The dissolution of this mineral greatly reduces the liquid limit of this material, as shown in Figure 3-2 and Figure 3-3. The redistribution of Mn typically forms nodules or coatings on soil grains that do not possess the same water-holding capabilities. The physical appearance changed during the reworking process is shown in Figure 9-4. The type of reworking is dependent on the surrounding environment but will typically result in a decrease in Mn oxides, the fines component, and liquid limit, and an increase in SiO_2 content in the form of quartz, and a relative increase in Fe-oxides and an increase in nodules. Note the abundance of sand-size nodules in Figure 3-4(c).

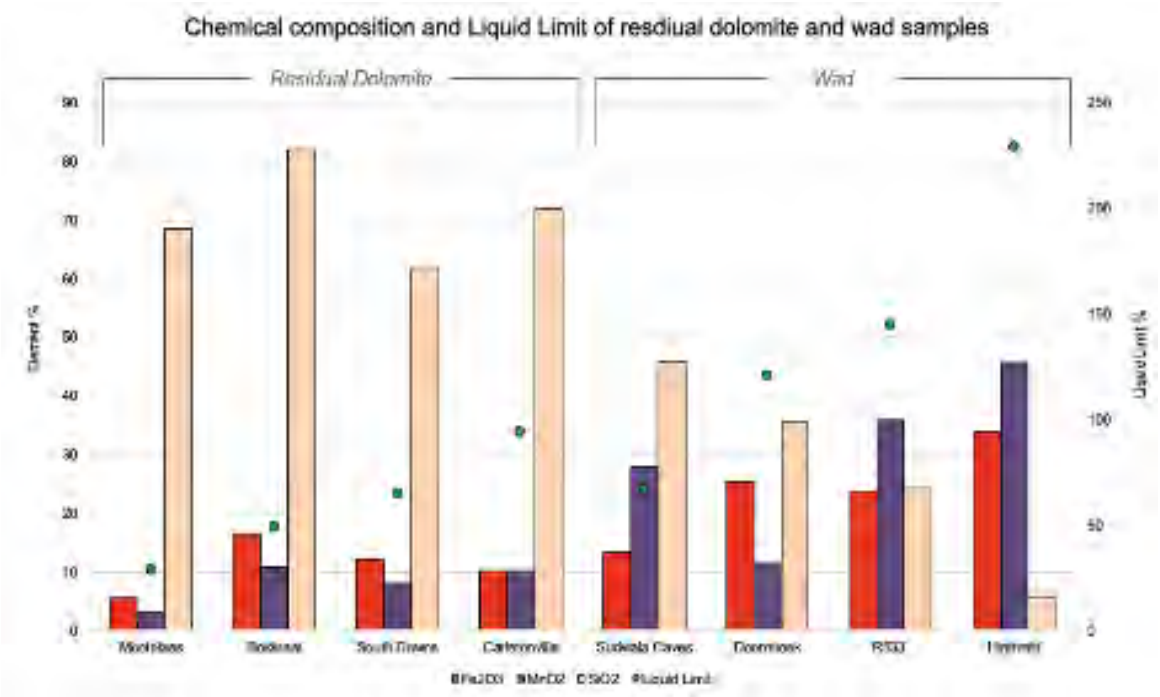

Figure 3-2 Major chemical components and liquid limits of residual dolomite and wad samples (Swart 2019).

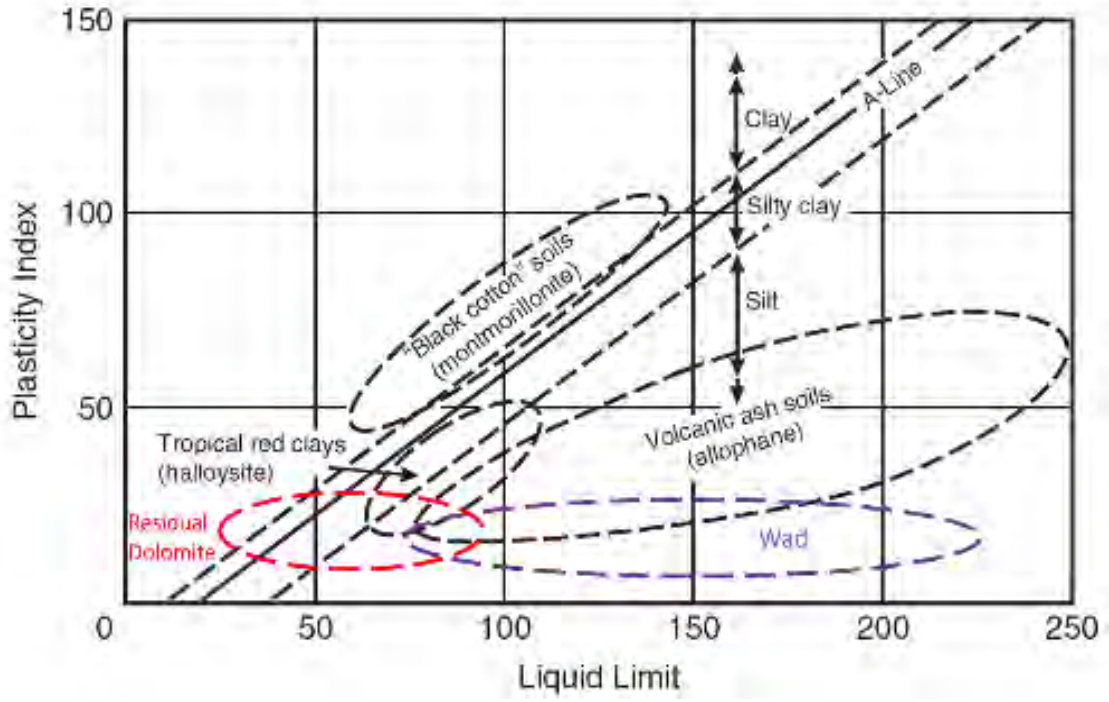

Figure 3-3 Atterberg limits of residual and weathered soils (Adapted from Wesley 2010).

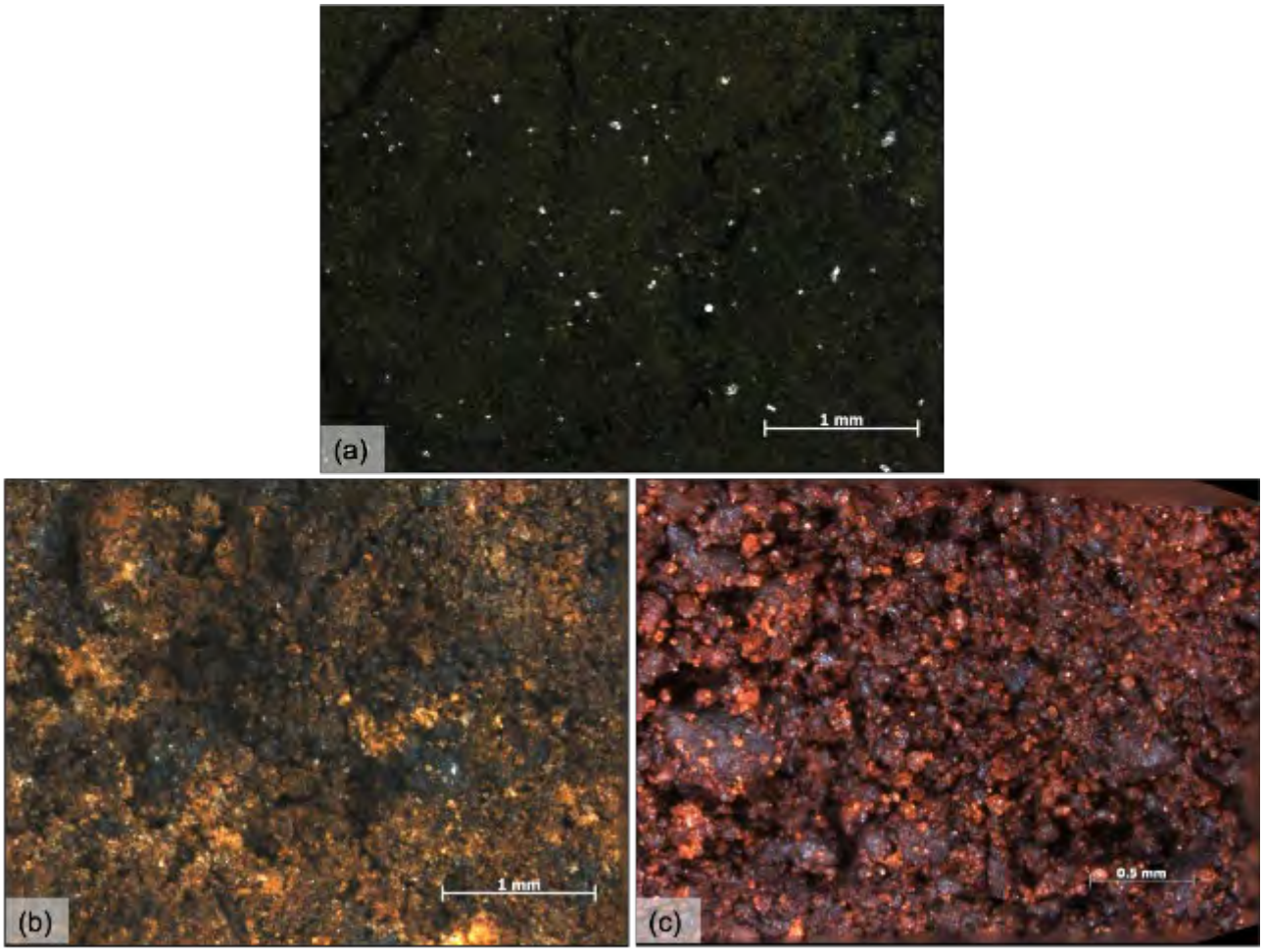

Figure 3-4 Stereo microscope photographs taken of (a) Highveld, (b) Sudwala Caves, and (c) Bokkraal samples.

3.3 RELICT PARENT ROCK STRUCTURE IN WAD

Wad is divided into two groups based on the structure, either structured wad or non-structured wad. Structured wad is the insoluble residue that occupies a similar volume to the parent rock after the soluble rock leaches away, resulting in a high porosity and low permeability material. The structure observed in the wad is inherited from the parent rock, and it could be said wad is a form of completely weathered rock. Structured wad possesses more than double the average void ratio value than non-structured wad. The void ratios are generally greater than 1 and have been found to be as high as 16. The natural moisture content of structured wad usually exceeds the liquid limit (Buttrick 1986; Wagener 1982; De Beer 1985; Brink 1979). Breaking down of the structure through external factors, much like the reworking previously discussed, results in a decrease of water holding capabilities and may cause the material to liquify in-situ without a change in moisture content. Photographs taken of the structured wad are shown in Figure 3-5.

Soil Water Retention Curves (SWRC) were conducted on the Highveld sample using the *Tuks Tensiometer* at the University of Pretoria. The methodology and equipment for this test have been discussed in Swart et al. (2021) and Jacobsz (2018). The influence of the relict rock structure was tested by measuring the suctions of a drying curve from full saturation on an undisturbed sample and repeating the test on the same material after it has been remoulded, thereby breaking down the structure and

slightly densifying the material. The resultant SWRCs for two tests are presented in Figure 3-6. The material properties are presented in Table 3-1.

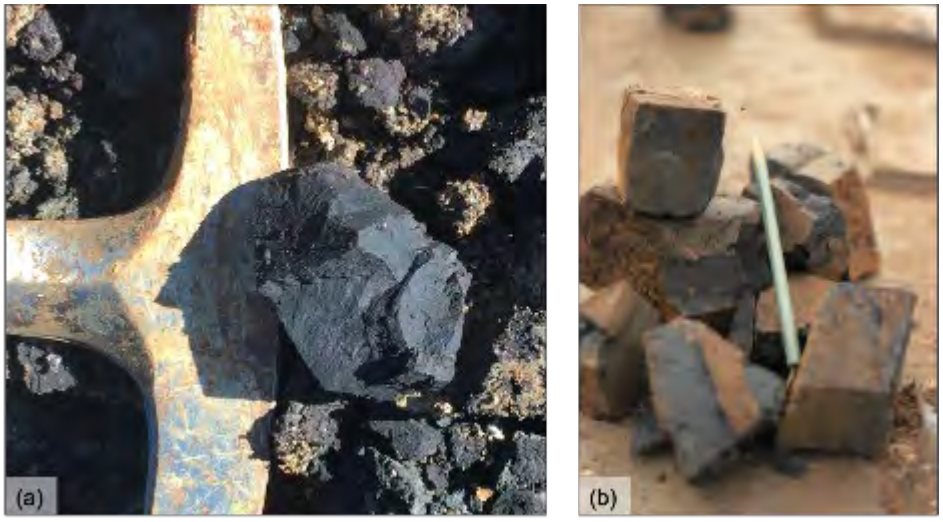

Figure 3-5 Photographs taken of (a) Highveld sample (taken by Swart 2019) and (b) structured wad from Buttrick (1986).

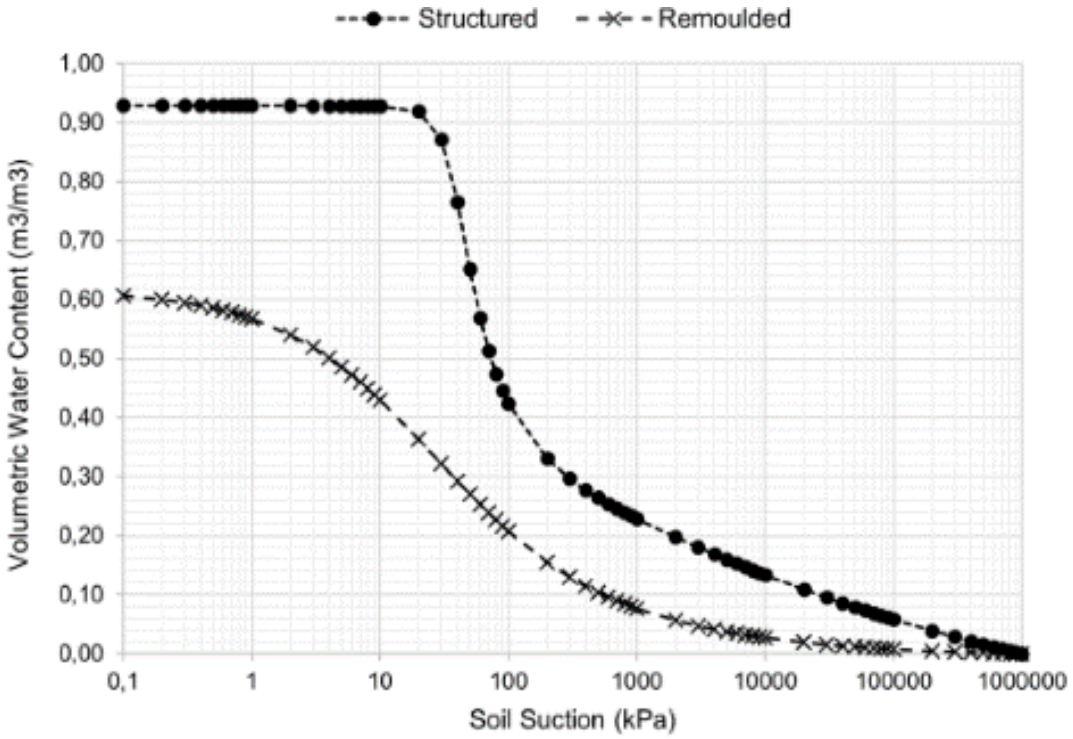

Figure 3-6 SWRCs for an undisturbed Highveld sample (structured) and remoulded Highveld sample.

Table 3-1 Summary of SWRC test results

Sample	Dry Density (kg/m^3)	Saturated moisture content (%)	Void Ratio
Highveld structured	309	300	8.32
Highveld remoulded	700	88	2.18

It is expected for the SWRC to change with a change in void ratio and density; however, the change in the air entry value (AEV) and suction levels between 1 kPa and 1000 kPa indicate the remoulding

process destroys critical porosity characteristics for the material to retain high suctions at a given moisture content. Field observations show the importance of recognising structure in this type of soil where no visible water is seen in the material until the structure is broken down. Thereafter, free water is present in the palm of the hand and the remaining soil texture will be in a liquefied state. This behaviour could indicate the critical role wad has in the formation of sinkholes. If wad near the throat of a receptacle experiences an external force, environmental change, or continuous weathering, and the structure is lost, the material will liquify and move into the receptacle, either forming a void or initiating a sinkhole depending on the blanketing material.

3.4 WEATHERING PROFILE OF MN-RICH DOLOMITE

The definitions and differentiation of wad and residual dolomite are based firstly on the chemical composition of the material, be it Mn- or Fe-rich, and secondly on the presence of structure. The behaviour that the chemical composition and structure provide has been discussed in this chapter. Figure 3-7 presents a photograph and a schematic of the tube sample positions taken in a weathering profile exposed in a road cut near the town of Graskop, Mpumalanga. The dry density and in-situ moisture content are presented of the residual dolomite and wad, respectively. There is an abrupt increase in dry density and decrease in moisture content with an increase in weathering when comparing the wad and residual dolomite samples. The non-structured wad was described as moist, with free water present in the palm of a hand when the material was broken down and remoulded. The relict rock structure in wad forms a low-density material, typically less than water, and allows the material to have a large water-holding capacity that often exceeds the liquid limit (Buttrick 1986; Swart 2019). Occasional lenses of completely weathered chert occurred within the wad.

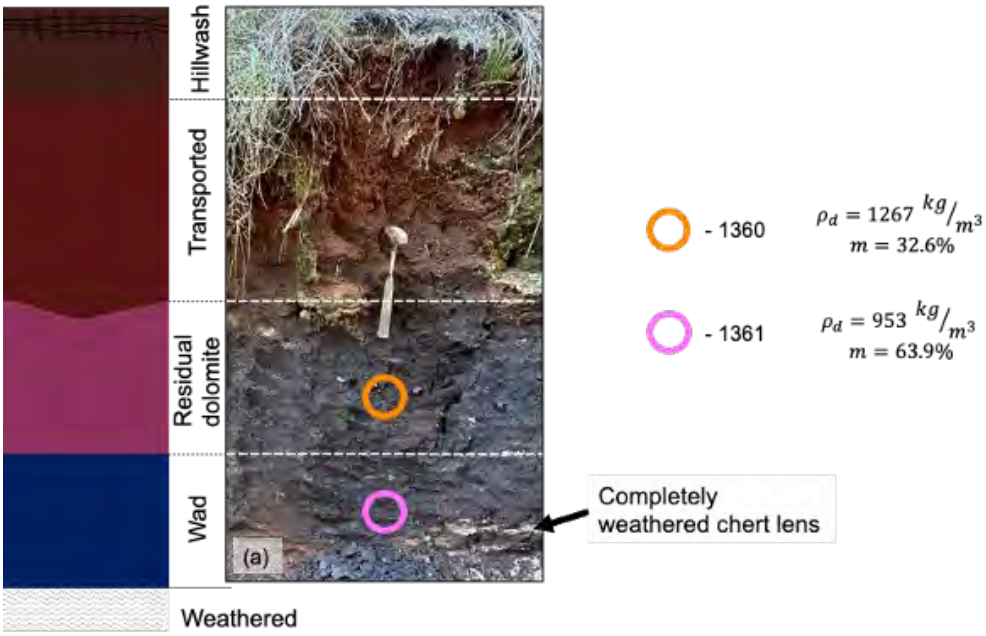

Figure 3-7 (a) Photograph of weathering profile formed on Mn-rich dolomite and tube sample locations and details (photograph taken by MA Dippenaar).

Dowding (2004) investigated the same profile and found both the wad and residual dolomite to be enriched in lithiophorite ($MnO_2(OH)_2$) with a relative increase in Fe content and pedogenic nodules in the residual dolomite. The residual dolomite has a minor to abundant amount of weakly to strongly cemented Fe and Mn nodules which are typically sand size, as presented in Figure 3-8.

Figure 3-9 presents the top view of the two tube samples with the modelled pore spaces and density contrast applied. The wad (sample 1361) has scattered pores that are less than 1.00 mm in diameter and a few pore sizes between 1.50 mm and 1.00 mm diameter. It is expected that the majority of the pore spaces in the wad will be smaller than 0.06 mm in diameter, which could not be identified and modelled by the XRCT equipment, as this exceeds the smallest measurable voxel size. Swart et al (2019) identified pore spaces of 100.0 nm in diameter within silt-sized grains of birnessite (MnO_2). The residual dolomite (sample 1360) has generally larger pores which are frequently greater than 1.00 mm and elongated in shape.

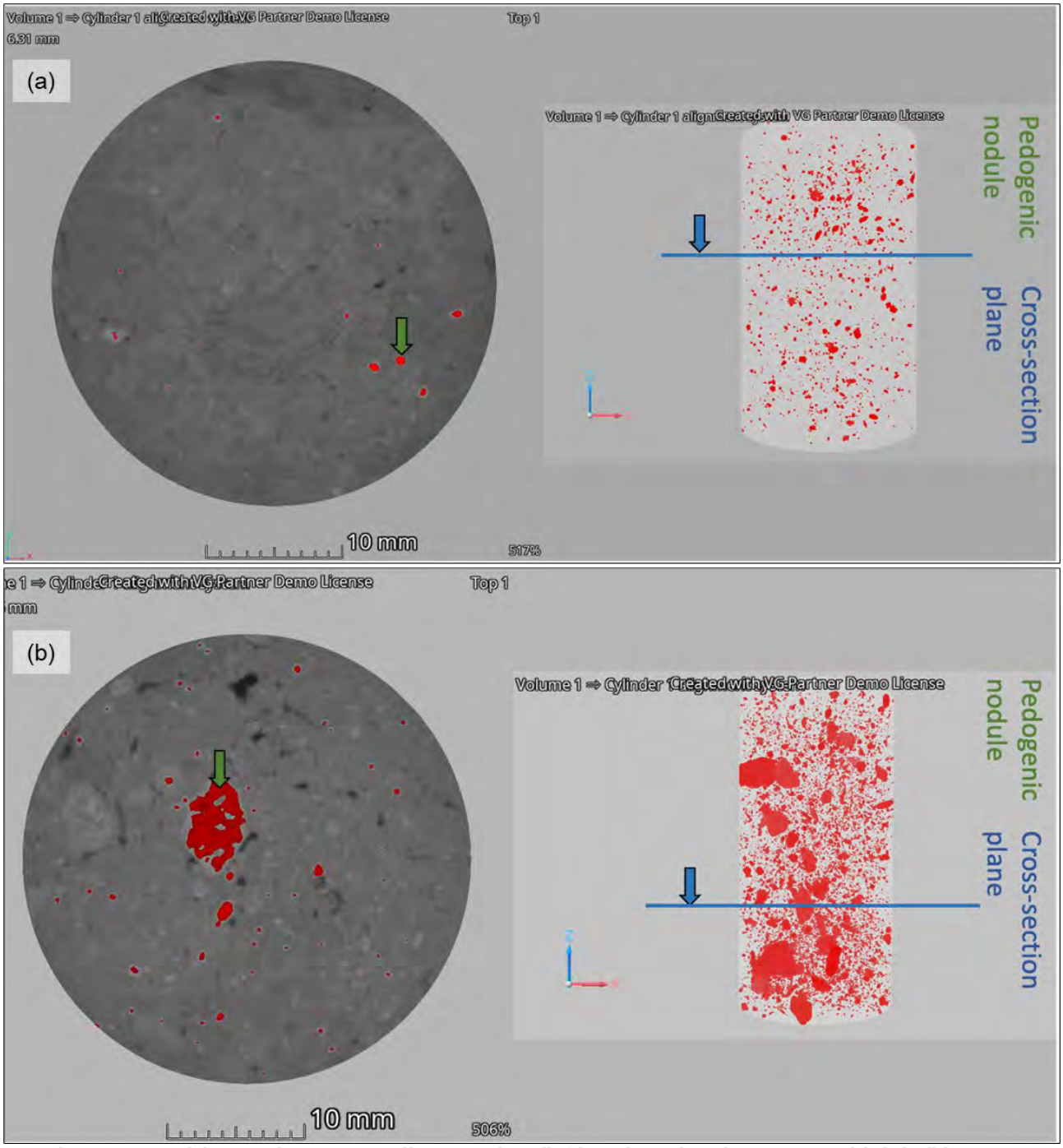

Figure 3-8 (a) Sample 1361 2D slice top view (left) and 3D density contrast (right); (b) Sample 1360 top view (left) and 3D porosity distribution (right).

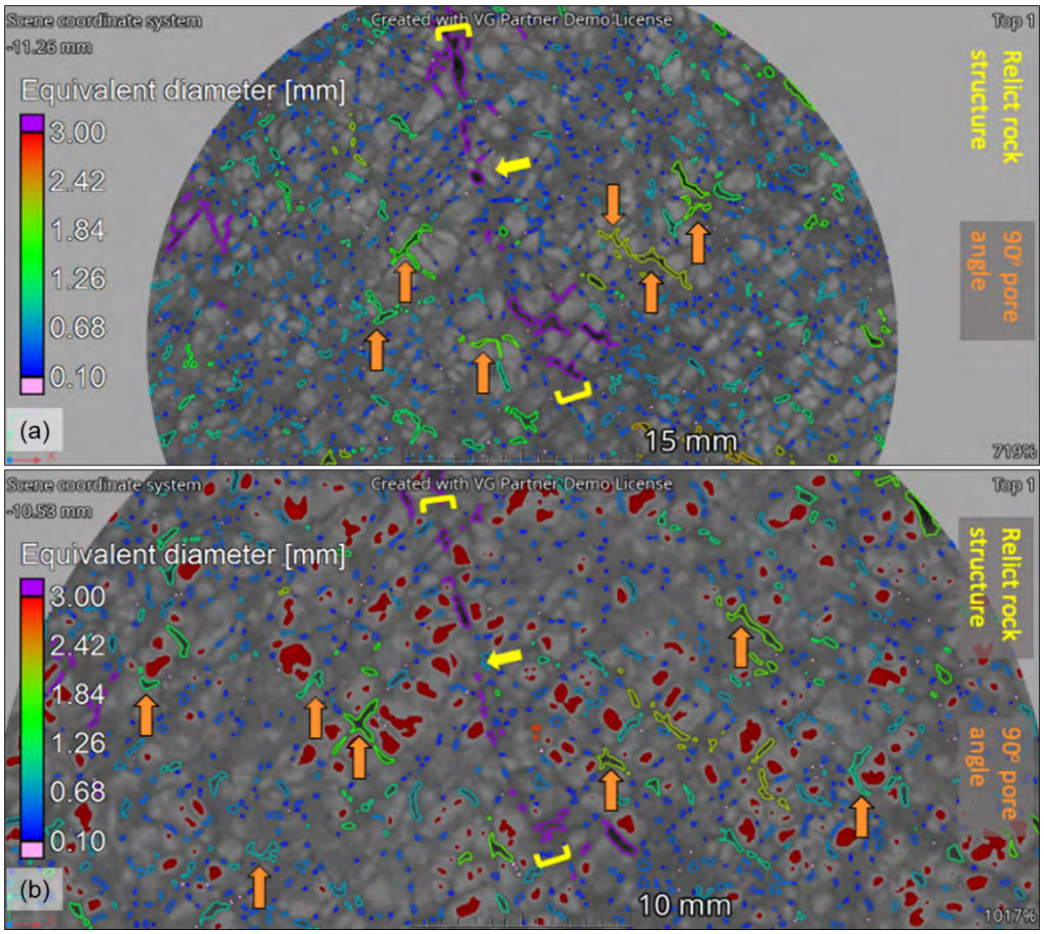

Figure 3-9 (a) Sample 1361 2D slice top view; (b) Sample 1360 top view.

The reworking and external forces, be it natural or anthropogenic, seemingly impact both the chemical and structural parameters and subsequently the colour and expected grading. Considering the above discussion in this Chapter, the weathering, structural, and chemical profiles of Mn-rich dolomite bedrock are shown in Figure 3-10.

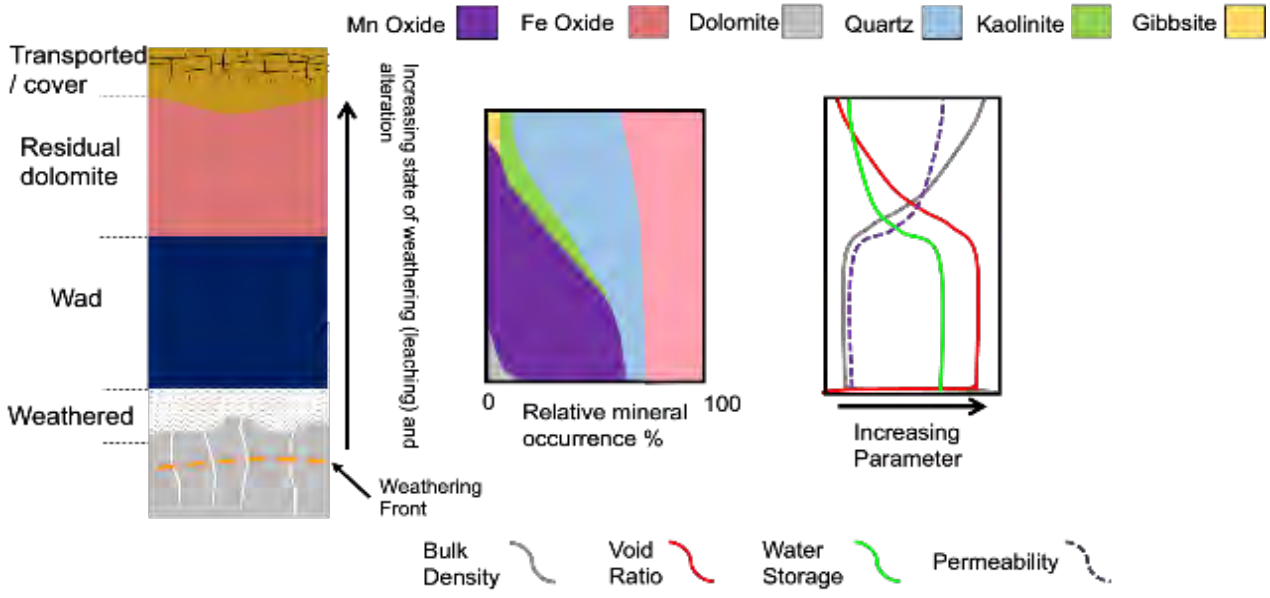

Figure 3-10 Vertical anisotropy profiles on weathered Mn-rich dolomite (a) Sample 1361 2D slice top view; (b) Sample 1360 top view.

It must be noted that the alteration between the wad and residual dolomite is usually controlled by a densification of the wad and a reduction in water holding capacity within the more weathered profiles. This trend of bulk density agrees with Hencher (2012); however, this differs from the structural profile discussed in Chapter 8, where there is a continuous decrease of bulk density into the residual soil before the densification occurs near the residual soil / transported soil boundary.

CHAPTER 4: CONTAMINANT TRANSPORT IN A FRACTURED ROCK SYSTEM USING TRACERS AND ISOTOPES

Author: Yazeed van Wyk

This comes from the following project-related outcomes:

- Van Wyk Y. 2024. Combined use of environmental and artificial tracers to characterise the anthropogenically altered vadose zone. PhD (specialising in Hydrogeology) Thesis. Department of Geology. University of Pretoria.
- Van Wyk, Y., Ubomba-Jaswa, E., (2024). Enhancing hydrological analysis by incorporating environmental and artificial tracers of an altered vadose zone: A systematic review, Journal of African Earth Science. Volume 212, 105209, https://doi.org/10.1016/j.jafrearsci.2024.105209

4.1 INTRODUCTION

Groundwater systems associated with mining environments are often highly complex due to the interaction between geological structures, mining activities, and hydrological processes. Open-pit quarrying in fractured rock environments can significantly alter the natural vadose zone and groundwater flow system by creating new fracture networks, modifying existing structures, and changing hydraulic gradients. Understanding groundwater flow pathways and contaminant transport in such altered environments is essential for sustainable mine closure planning and groundwater management. Traditional hydrogeological investigations often rely on hydraulic testing and water chemistry; however, these methods may not adequately capture the heterogeneity of fractured rock systems. Environmental and artificial tracers provide an effective means of investigating groundwater recharge, flow paths, and solute transport mechanisms in fractured aquifers.

This case study presents the results of tracer investigations conducted in an open-pit quarry located east of Pretoria, South Africa. The study integrates geological observations, tracer experiments, hydrochemical analysis, stable isotopes, and analytical modelling to improve understanding of groundwater flow dynamics within the altered vadose zone. This work forms part of a broader investigation into the use of environmental and artificial tracers to characterise anthropogenically altered hydrogeological systems.

4.2 STUDY AREA DESCRIPTION

4.2.1 2.2.1 Locality and prevailing conditions / land use

The study site is an open-pit quartzite and sandstone quarry located approximately 20 km east of Pretoria, South Africa. The quarry covers an area of approximately 84 hectares within Portions 46, 47, and 180 of the Farm Zwavelpoort 373 JR. Mining operations began in the 1960s and continued until the quarry closed in November 2023, following decades of aggregate extraction.

The quarry is situated on the north-eastern slope of the Bronberg Ridge and is characterised by steep slopes typical of hard-rock open-pit mining operations. These operations have substantially modified the landscape and subsurface hydrogeological conditions. Figure 4-1indicates the location of the study area. The mining right authorised the quarry to extract quartzitic sandstone, which was crushed on site to produce aggregates and sand of various sizes.

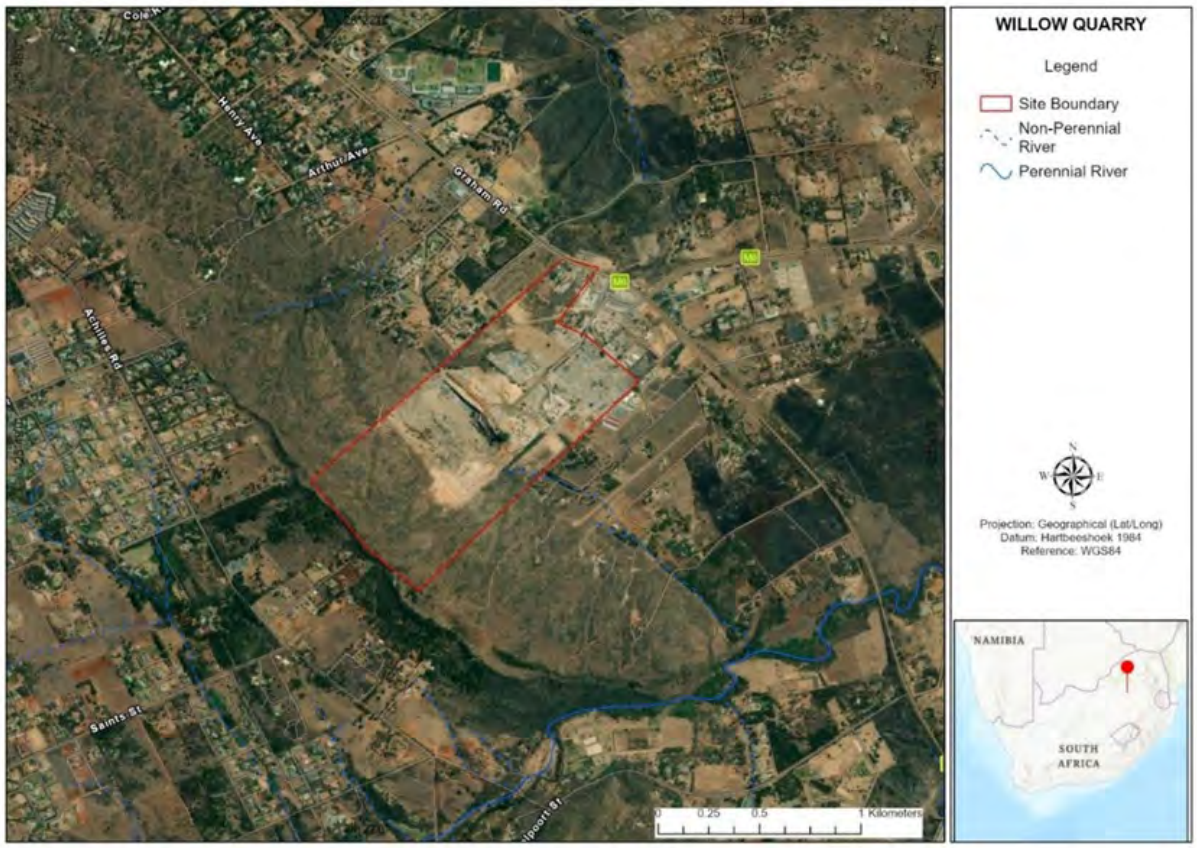

Figure 4-1 Locality map of the open-pit quarry on the Bronberg Ridge, east of Pretoria, South Africa.

4.2.2 Geology

The local geology is dominated by the quartz arenites of the Daspoort Formation, underlain by the shales and hornfels of the Silverton Formation. The ore deposit consists of a competent quartzitic rock mass intruded by several sub-vertical diabase dykes and sills of Bushveld age. The general dip of the bedding planes is 10°–15° to the north-east, and a prominent sub-vertical joint set strikes north-west. In addition, two faults occur to the north-west of the existing pit, while another fault trends north-east in the western section of the mine, as shown in the geological map (Figure 4-2).

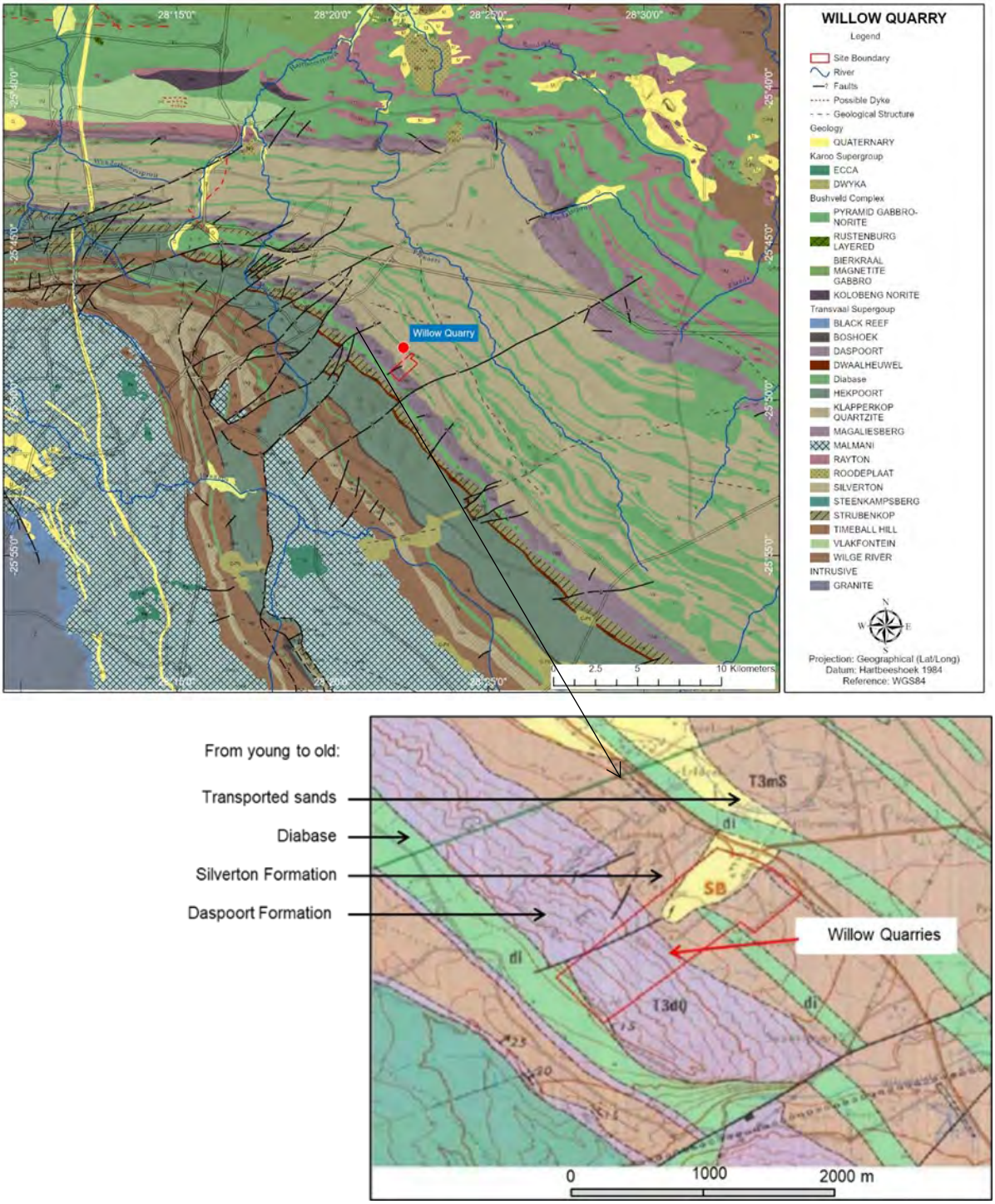

Figure 4-2 Regional and site-specific geology of the study area.

4.2.3 Climate and topography

The quarry site is located within quaternary catchment A23A, which forms part of the Crocodile West and Marico Catchment in Gauteng Province. The area contains several drainage lines, seepage zones, and an artificial dam, all of which drain eastward into the Pienaars River, approximately 6 km from the site. Some drainage lines flow into the quarry pit, where water was used for dust suppression and processing. The site characteristics of the quaternary catchment are outlined in Table 4-1.

Table 4-1 Quaternary catchment characteristics (after Herold & Bailey, 2016)

Quaternary Catchment	Area	Mean Annual Precipitation (MAP)	Mean Annual Run-Off (MAR)	Mean Annual Evaporation (MAE)
A23A	682 km^2	698 mm	4 2mm	1750 mm

Elevations range from 1,420 m in the north-east to 1,560 m in the south-west (Figure 4-3), reflecting a drop of approximately 120 m over a distance of 800 m, sloping north-eastward.

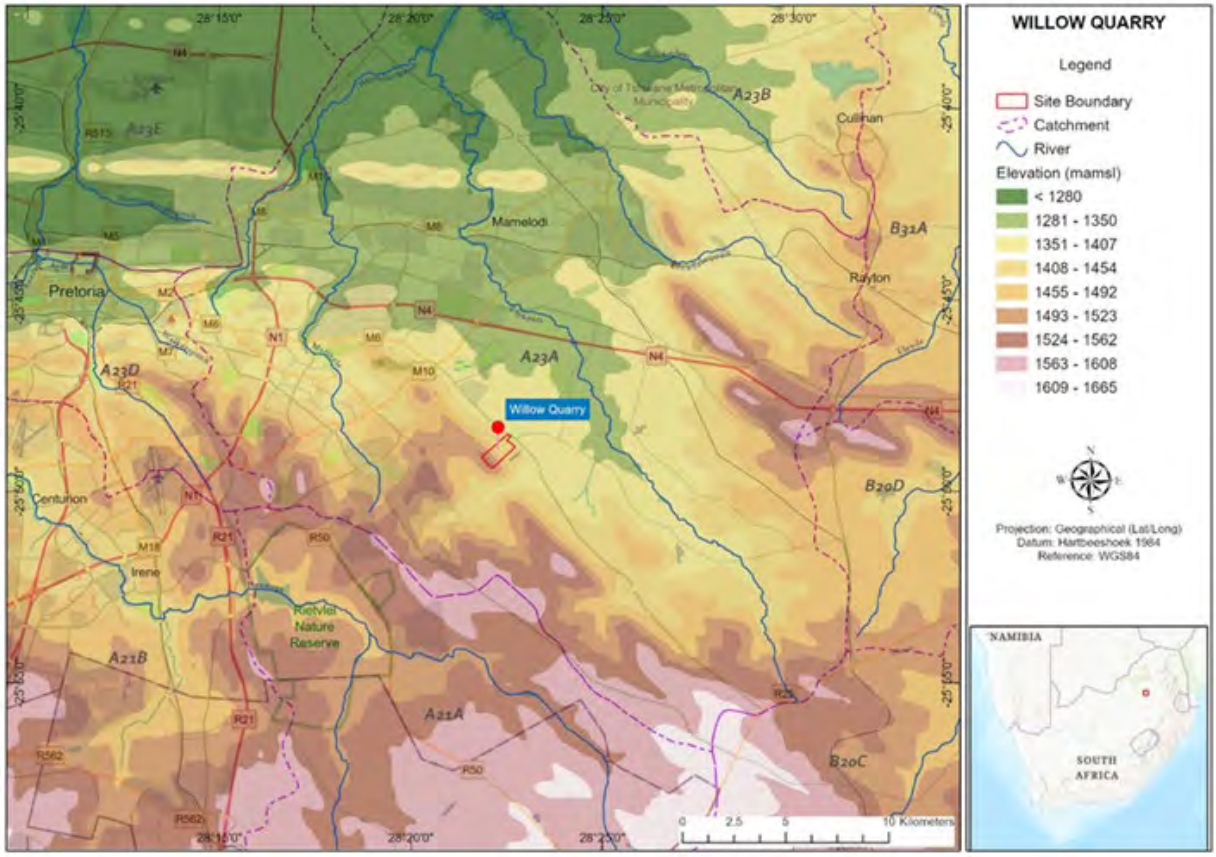

Figure 4-3 Map showing the regional surface drainage features, topography, and study area.

Mining activities have substantially altered the topography, creating steep gradients, particularly along the pit edges and stockpiles. Consequently, runoff mostly infiltrates into the excavated areas and contributes to groundwater recharge, rather than flowing into external drainage lines. The mine area has been largely cleared of natural vegetation, with bare soil, compacted surfaces, and limited paved areas dominating the landscape. Most of the site is inward-draining and therefore contributes minimally to stormwater runoff.

4.2.4 Fracture characterisation

4.2.4.1 Present-day stress regime

The stress regime surrounding the study area was determined using six earthquake focal mechanisms from the national seismic network (Dhansay, 2021). The analysis reveals two distinct faulting regimes: normal faulting and strike-slip faulting (Figure 4-4). The orientation of the principal stresses for these

regimes suggests a substantial influence on the fracture network, with normal faulting characterised by a vertical σ1, and strike-slip faulting dominated by horizontal σ1 and σ3 stresses.

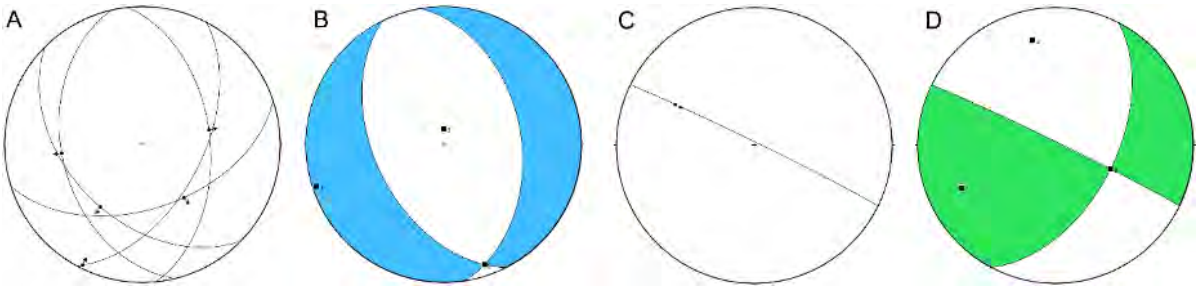

Figure 4-4 Present-day stress regimes as derived from earthquake focal mechanisms for normal and strike-slip faulting, A and C, respectively. Principal stress orientations for both faulting regimes are shown in (B) and (D), with beach ball diagrams representing σ1 (blue) and σ3 (green).

4.2.4.2 Present-day stress magnitude

Present-day stress magnitudes were estimated following (Dhansay et al., 2017), using a bulk rock density of 2 550 kg/m³, pore fluid density of 1 080 kg/m³, and a reservoir depth of no greater than 1 000 m. Pore fluid pressure at these depths is estimated at 10.46 MPa. With a friction coefficient (μ) of 0.85 and an R-ratio of 0.5, stress magnitudes for normal and strike-slip regimes were calculated. The results are summarised in Table 4-2.

Table 4-2 Present-day stress regime orientation and magnitude for normal and strike-slip faulting near the study area.

Regime	Stress	Trend	Plunge	Magnitude (MPa)
Normal	σ1	251.6	2.9	25.02
	σ2	161.2	8.5	19.35
	σ3	1.0	81.0	13.68
Strike-slip	σ1	245.6	26.1	34.36
	σ2	113.2	54.0	25.02
	σ3	347.6	23.0	15.68

4.2.4.3 Fault kinematics

Twenty fault kinematic measurements from the study area reveal predominantly NE-SW and NW-SE orientations, which correlate with regional fracture patterns (Dhansay, 2021). These faults are typically steeply inclined between 75° and 90°, although some shallowly inclined faults were also observed (Figure 4-5).

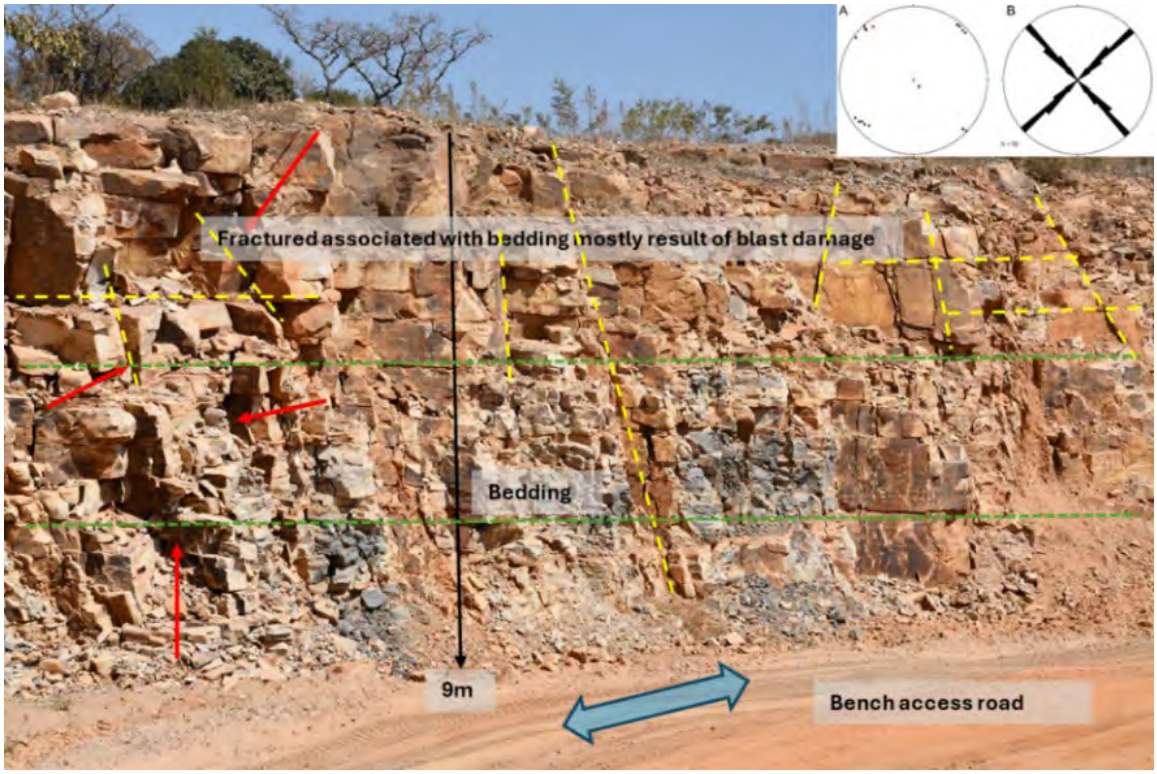

Figure 4-5 (A) Poles of measured faults; (B) rose diagram showing the predominant fault orientation (photograph by van Wyk, 2023).

4.2.4.4 Reactivation potential

Slip and dilation tendency analyses (Morris et al., 1996) were conducted to evaluate the reactivation potential of faults under both normal and strike-slip faulting conditions (Dhansay et al., 2017). The analysis suggests that moderately inclined NW-SE fractures are most likely to reactivate under normal faulting, while steeply inclined NE-SW and NW-SE fractures could reactivate under strike-slip faulting (Figure 4-6).

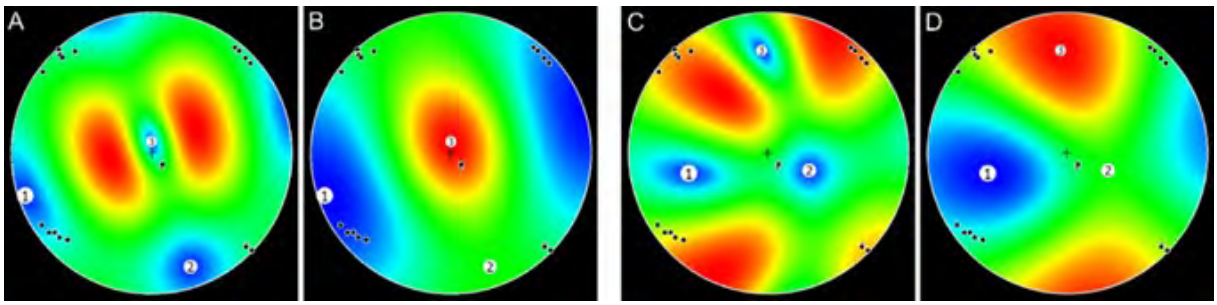

Figure 4-6 Slip and dilation tendency analyses for normal faulting (A, B) and strike-slip faulting (C, D).

4.2.5 Local hydrogeology of the study site

The study area is classified as an intergranular and fractured aquifer system, with borehole yields of 0.5–2.0 L/s (DWS, 1999), as shown in Figure 4-7. The Daspoort Formation has low primary porosity due to its arenitic composition and primarily stores groundwater along structural features such as faults,

fractures, and joints. Vertical joints oriented predominantly NW-SE and NE-SW play a crucial role in groundwater flow across the Bronberg Ridge.

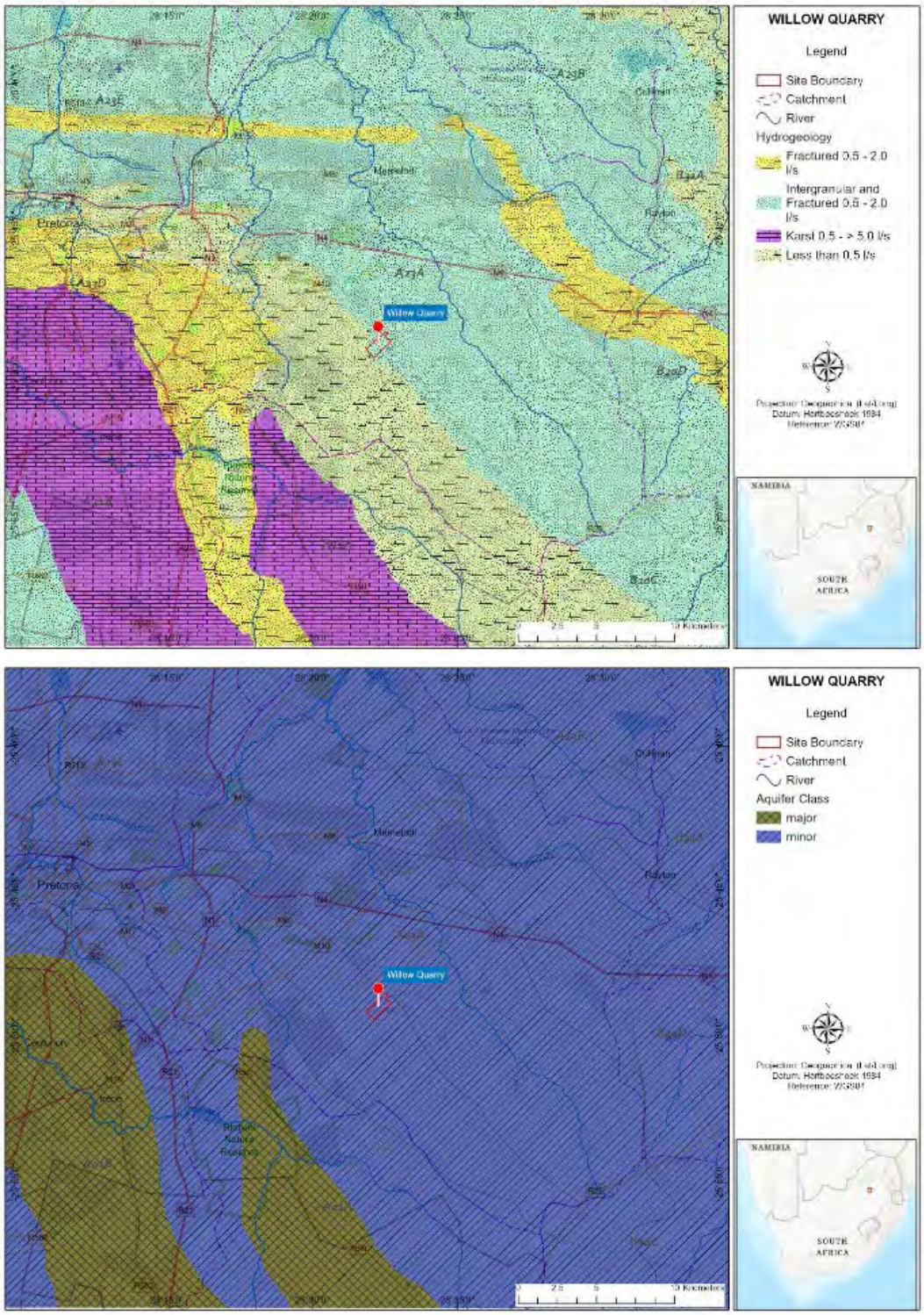

Figure 4-7 Maps showing regional aquifer yield and classification in the study area, based on the 1:500 000 Hydrogeological Map Series (DWS, 1999).

According to Van der Neut (1990), the Daspoort Formation is less than 100 m thick, while the Pretoria Group, which includes the Daspoort Formation, exceeds 2 000 m in thickness. Barnard (2000) does not

classify the Daspoort Formation as a major aquifer, indicating that any associated aquifer would be categorised as a Minor Aquifer according to the South African Aquifer Classification System (Parsons, 1995). A Minor Aquifer refers to geological formations that provide limited groundwater yields, often insufficient for large-scale water supply, but potentially important for local use or ecological functions.

Recharge rates for the study area are estimated at 74.3 mm/a, equivalent to approximately 10.6% of annual rainfall (Vegter, 1995). Groundwater levels fluctuate between 5 m and 25 m below surface, with a clear seasonal pattern driven by rainfall (Figure 4-8).

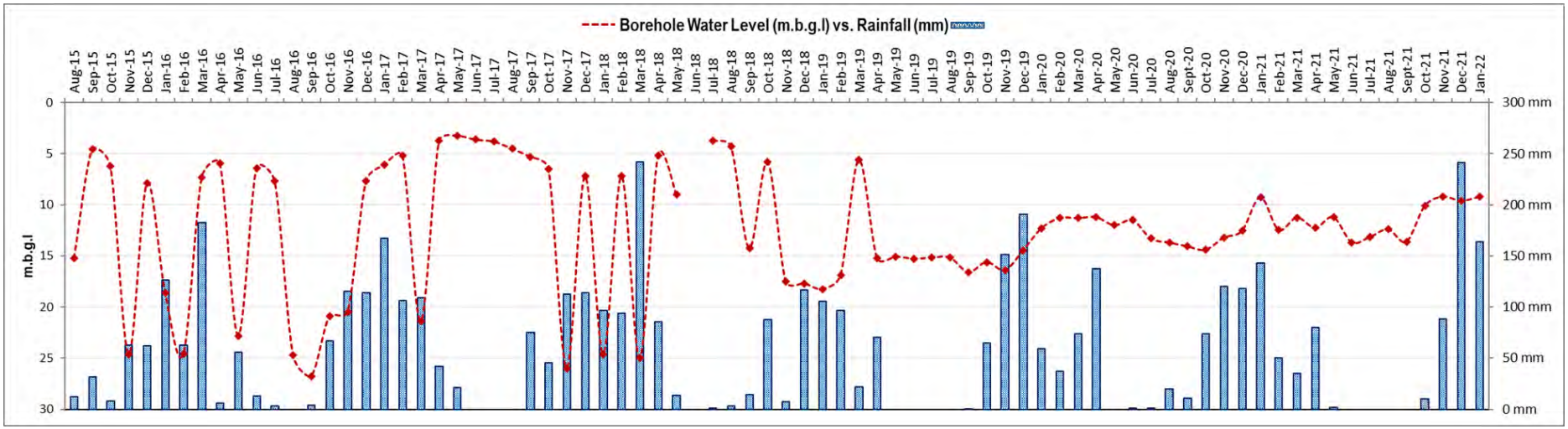

Figure 4-8 Groundwater levels in monitoring borehole WILL-GW-02 and corresponding rainfall data from 2015 to 2021.

4.3 MATERIALS AND METHODS

4.3.1 Sampling strategy

In total, nine samples were collected at the end of the dry season (April to September 2022) and the beginning of the wet season (October 2022) from both quarry pit water and boreholes, excluding tracer samples. The data indicated limited groundwater use in the area, with most boreholes serving private landowners for domestic or livestock purposes.

Groundwater samples were collected from unequipped boreholes using a 2-inch (50 mm) Grundfos MP1 submersible pump (Grundfos South Africa (Pty) Ltd., Johannesburg, South Africa). Each borehole was purged until the physicochemical parameters stabilised. Continuous in situ measurements of temperature, electrical conductivity (normalised to 25 °C), pH, and oxidation-reduction potential were taken using an Aquaread GPS Aquameter (AP-5000) portable multiparameter probe (Aquaread Ltd., Broadstairs, Kent, UK) in a flow-through cell to minimise atmospheric exposure.

Alkalinity was determined on site as $CaCO_3$ (mg/L) with a Hach SL1000 Portable Parallel Analyzer® (PPA) using either low- or high-range total alkalinity Chemkey® reagents (Hach South Africa (Pty) Ltd., Randburg, South Africa). Alkalinity was then converted to HCO_3^- concentrations based on the pH readings. This conversion is reasonable because all samples displayed pH values between 6.5 and 8.2, where bicarbonate is the dominant species contributing to alkalinity (Stumm & Morgan, 1996). Contributions from carbonate (CO_3^{2-}) and carbonic acid (H_2CO_3) were considered negligible within this range.

4.3.2 2.3.2 Analytical methods

4.3.2.1 Analysis of major and minor ions

Water samples were collected using a 60 mL HENKE-JECT® syringe (Henke-Sass, Wolf GmbH, Tuttlingen, Germany), rinsed three times with sample water, and filtered through 0.45 µm cellulose acetate syringe filters into two 60 mL HDPE bottles. The bottle designated for cation analysis was acidified directly in the field to pH ~3 with HNO_3 (Suprapur®, Merck South Africa, Modderfontein, South Africa).

Concentrations of major ions (Cl^-, Na^+, K^+, Mg^{2+}, Ca^{2+}, SO_4^{2-}), as well as bromide (Br^-) and phosphate (PO_4^{3-}), were analysed at Waterlab (Pty) Ltd., Pretoria, in accordance with SANS 241-1:2015, using a Metrohm 930 Compact IC Flex single-channel ion chromatograph (Metrohm SA (Pty) Ltd., Cape Town, South Africa). Anion analysis was performed at 35 °C on a Metrosep A Supp 5-250/4.0 column with a flow rate of 0.7 mL/min, using an eluent of 3.2 mM sodium bicarbonate and 1.0 mM sodium carbonate. Cation analysis was performed at 30 °C on a Metrosep C 6-A150/4.0 column with a flow rate of 0.9 mL/min, using an eluent of 1.7 mM nitric acid and 1.7 mM dipicolinic acid.

The repeatability of the analytical method was within 5%, and precision was ensured through the use of certified reference materials and routine calibration of the instrument. Method precision for major ions, expressed as relative standard deviation (RSD), typically ranged between 2% and 5%, depending on ion concentration, in line with the laboratory's quality control protocols.

4.3.2.2 Sample analysis for stable and radioactive isotopes

Samples were analysed for δ^2H, $\delta^{18}O$, d-excess, and tritium (^3H) content. All $\delta^{18}O$ and δ^2H values are reported relative to Vienna Standard Mean Ocean Water (VSMOW), following Mook (2000). In total, nine water samples were submitted to iThemba LABS (Johannesburg, South Africa) on 30 November 2022 for analysis. The samples were analysed using a Los Gatos Research Liquid Water Isotope Analyzer (Los Gatos Research, a member of the ABB Group, San Jose, California, USA), with analytical precision estimated at 0.5‰ for $\delta^{18}O$ and 1.5‰ for δ^2H. Results are expressed in δ-notation relative to VSMOW.

For tritium analysis, the samples were distilled and subsequently enriched by electrolysis using a specialised set-up consisting of two concentric metal tubes, one made of stainless steel serving as the outer anode and container, and the other made of coated mild steel serving as the inner cathode. After introducing 500 mL of the water sample containing sodium hydroxide into the cell, a direct current of 10–20 A was passed through the cell while the system was cooled to dissipate heat. After several days, the electrolyte volume was reduced to 20 mL, resulting in a 25-fold volume reduction and a corresponding tritium enrichment factor of approximately 20.

To verify enrichment, standard samples of known tritium concentration were included in each batch. For liquid scintillation counting (LSC), samples were prepared by directly distilling the concentrated electrolyte. A mixture of 10 mL of the distilled sample and 11 mL of Ultima Gold scintillation cocktail was placed in a vial and counted using a PerkinElmer Tri-Carb 3170TR/SL Liquid Scintillation Analyzer (PerkinElmer (Pty) Ltd., Midrand, South Africa) for two to three cycles of 4 h each. The detection limit for enriched samples was 0.3 TU.

4.4 RESULTS

4.4.1 Hydrochemical characteristics

Groundwater samples from WILL-GW-01, WILL-GW-02, and FARM-B1 exhibit a calcium-magnesium-bicarbonate facies, indicative of relatively limited chemical alteration. In contrast, the quarry pit water samples WILL-PIT-01 and WILL-PIT-02 show elevated sulphate concentrations. These elevated sulphate concentrations likely result from geochemical interactions within the quarry environment, possibly influenced by mining activities and/or local geological conditions.

The groundwater and quarry pit water sampling points are shown in Figure 2.9, and the Piper diagram representing the hydrochemical facies of the groundwater and quarry pit water samples is presented in Figure 4-9. The contrast in water chemistry between the groundwater and quarry pit water samples emphasises the importance of site-specific water quality assessments in areas affected by anthropogenic disturbance such as quarrying.

Figure 4-9 Map of the study area showing the locations of groundwater and quarry pit water sampling points.

Two distinct hydrochemical facies were identified: a calcium-magnesium-bicarbonate type in most groundwater samples, indicating relatively fresh and shallow groundwater, and a calcium-magnesium-sulphate type in the quarry pit water, likely resulting from the dissolution of sulphide minerals, including pyrite (Figure 4-10). In addition, the presence of an old, now inactive general domestic waste disposal site in the vicinity may also be contributing significantly to the contamination plume, potentially obscuring the effects of pyrite dissolution. Leachate from domestic waste disposal sites is known to introduce a range of contaminants, including nitrate, chloride, sulphate, heavy metals, and organic compounds, which can significantly alter groundwater quality and hydrochemistry (Christensen et al., 2001; Mor et al., 2006; Khan et al., 2022) The influence of such leachate plumes has been widely documented and may produce more complex and persistent contamination signatures than those caused solely by natural geochemical processes such as pyrite oxidation.

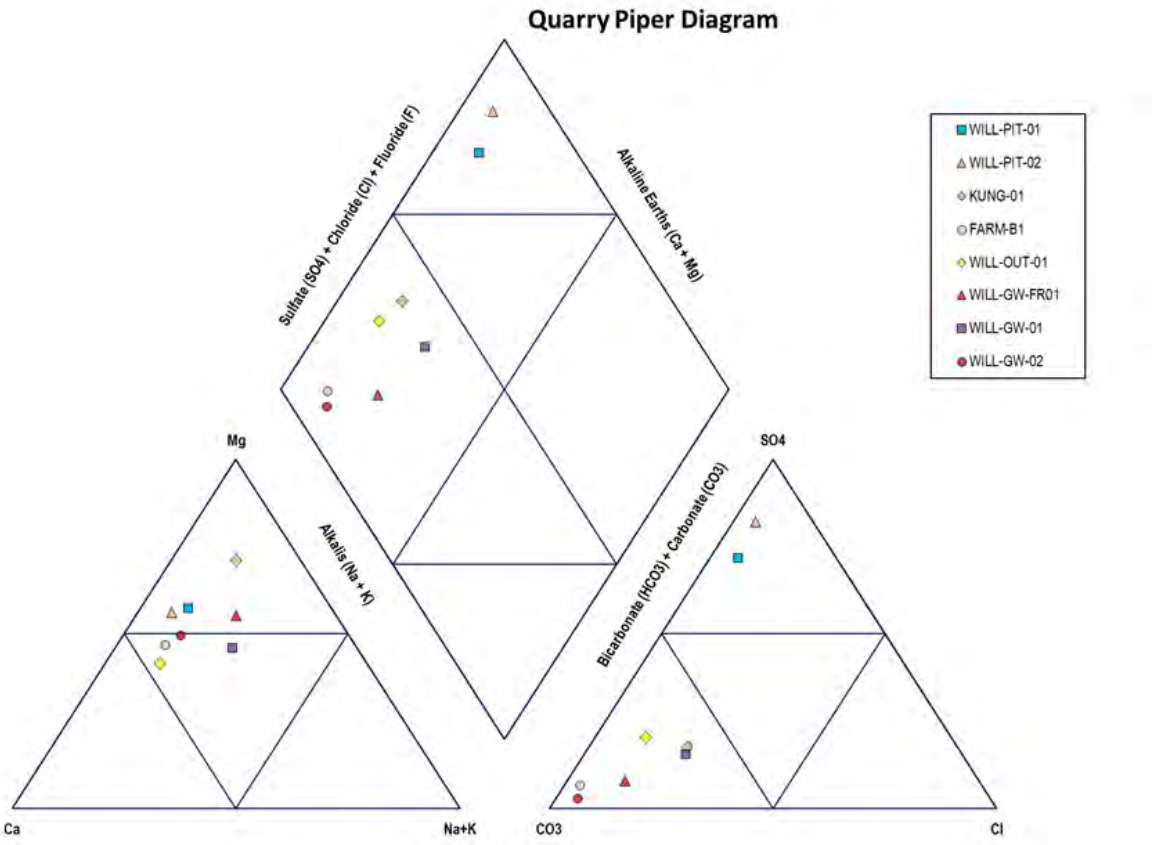

Figure 4-10 Piper diagram representing the hydrochemical facies of quarry pit water and groundwater samples.

4.4.2 Stable isotope analysis

The $\delta^{18}O$ and $\delta^{2}H$ values ranged from -5.40‰ to -1.20‰ and -32.0‰ to -5.80‰, respectively, with mean values of -3.85‰ and -19.20‰, providing a representative isotopic signature for the study area (Table 4-3).

The Global Meteoric Water Line (GMWL) (Craig, 1961) was used as a reference, while the Pretoria Meteoric Water Line (PMWL), derived from the Global Network of Isotopes in Precipitation (GNIP) dataset, was used for local interpretation ($\delta^{2}H = 6.7\delta^{18}O + 7.2‰$). In addition, a Local Evaporation Line (LEL) for the quarry pit water samples was established ($\delta^{2}H = 3.26\delta^{18}O - 1.79‰$).

Samples WILL-GW-01, WILL-GW-02, WILL-GW-FR01, FARM-B1, KUNG-01, and WILL-OUT clustered along the PMWL and GMWL, indicating direct recharge from local rainfall with relatively high d-excess values (mean = 11.6‰), as shown in Figure 4-11**.** In contrast, quarry pit water samples WILL-PIT-01 and WILL-PIT-02 were enriched in $\delta^{2}H$ and $\delta^{18}O$ and showed lower d-excess values, indicating evaporation prior to recharge and/or surface residence. The relatively low slope of the LEL (3.26), calculated from quarry pit water samples that had undergone evaporation, reflects substantial evaporation effects under low-humidity conditions.

Table 4-3 Isotopic signatures for the study area (all dates 2022)

Sample ID	Date	Latitude (DD)	Longitude (DD)	δ ^{2}H‰	δ^{18}O‰	D-Excess‰	TU	±	Elevation (m a.s.l.)
WILL-GW-01	28 Oct	-25.8146667	28.374527	-21.8	-4.21	11.88	0.5	0.2	1425
WILL-GW-02	04 Nov	-25.8143333	28.373777	-21.6	-4.36	13.28	0.4	0.2	1430
WILL-GW-FR01	29 Oct	-25.8166944	28.371666	-22.1	-4.63	14.94	1.0	0.2	1398
FARM-B1	28 Oct	-25.80625	28.372833	-23.0	-4.70	14.67	0.0	0.2	1408
WILL-PIT-01	29 Oct	-25.8161944	28.371333	-5.8	-1.23	4.04	1.1	0.3	1397
WILL-PIT-02	28 Oct	-25.8151389	28.371972	-8.7	-2.12	8.26	1.0	0.3	1423
KUNG-01	04 Nov	-25.8086111	28.374166	-18.2	-3.88	12.84	1.0	0.3	1412
WILL-OUT	28 Oct	-25.8090556	28.376222	-19.6	-4.09	13.12	1.0	0.2	1407
RAINWATER	07 Dec	-25.8150748	28.3738945	-32.0	-5.43	11.44	2.3	0.3	1424
Min				**-32.0**	**-5.40**	**4.00**	**0.0**		
Max				**-5.8**	**-1.2**	**14.9**	**2.3**		
Mean				**-19.2**	**-3.85**	**11.61**	**0.9**		

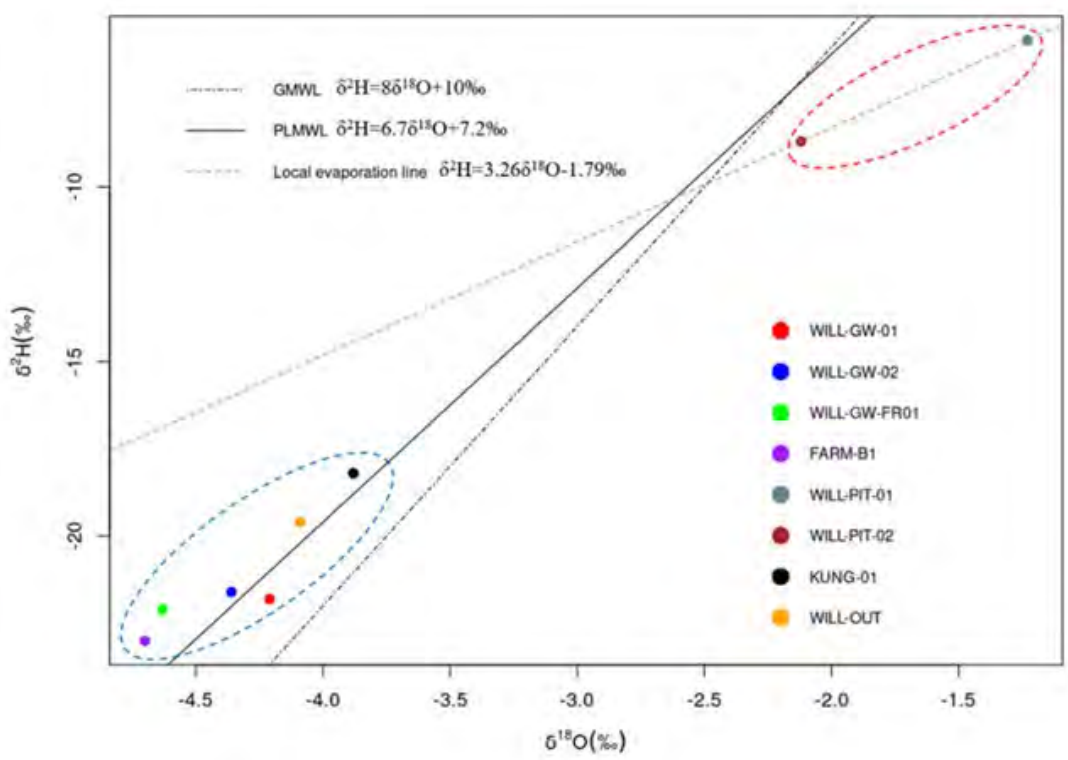

Figure 4-11 δ²H vs. δ¹⁸O plot showing isotopic variation of quarry pit water and groundwater samples relative to the Pretoria Local Meteoric Water Line (PMWL) and the Global Meteoric Water Line (GMWL).

4.4.3 2.4.3 Deuterium excess

Deuterium excess (d-excess) is a second-order isotopic parameter that reflects the difference between the isotopic composition of precipitation and water vapour (Dansgaard, 1964). It is calculated as shown in Equation 4-1

$$d = \delta^2H - 8\delta^{18}O \qquad \textbf{Equation 4-1}$$

High d-excess values, typically above 10‰, may indicate moisture originating from regions affected by high evaporation rates, such as arid environments, or conditions associated with atmospheric recycling (Clark & Fritz, 1997; Bowen & Revenaugh, 2003). The relationship between $\delta^{18}O$ and d-excess is illustrated in Figure 4-12, highlighting the difference in isotopic composition between groundwater and quarry pit water.

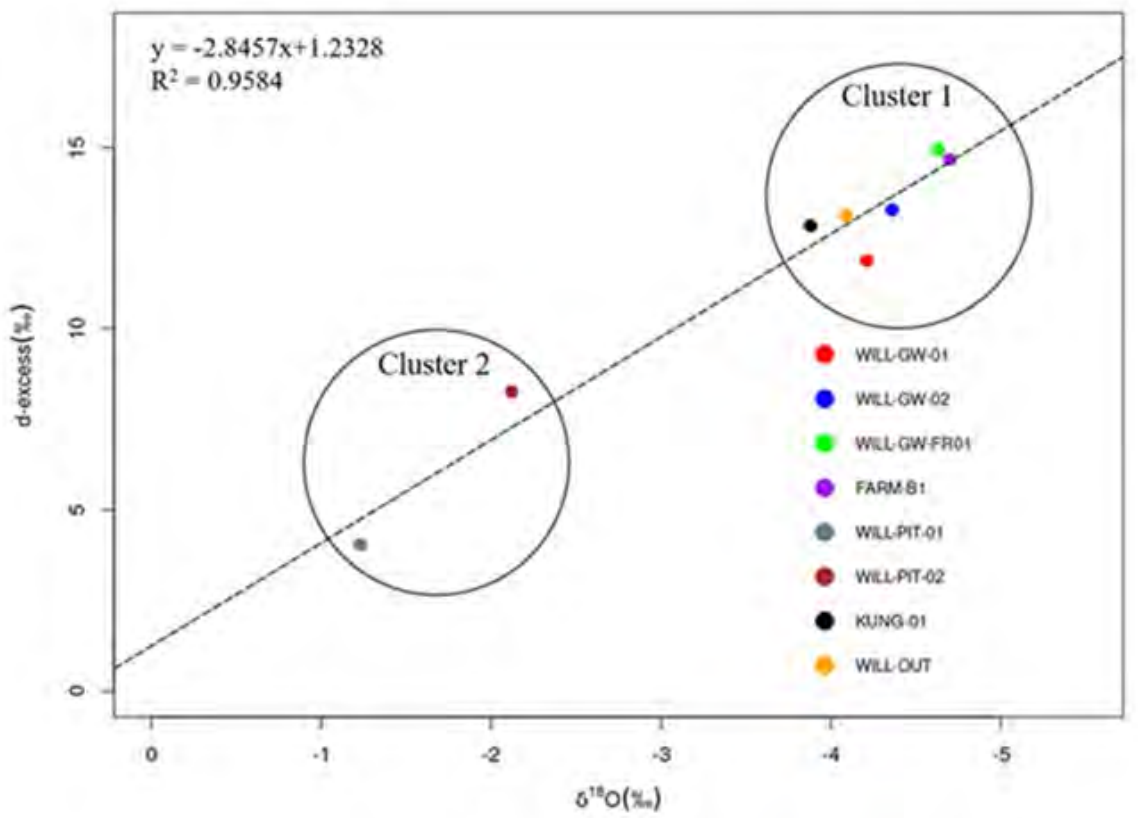

Figure 4-12 Cross-plot of d-excess vs. $\delta^{18}O$ for water samples from the study area.

D-excess values range from 4.04‰ to 14.94‰, with a mean of 11.61‰, suggesting relatively high evaporation at the moisture source. Groundwater samples classified within Cluster I (e.g., WILL-GW-01, WILL-GW-02, WILL-GW-FR01, FARM-B1, and KUNG-01) exhibit comparatively high d-excess values, indicating recharge from rainfall derived from a moisture source affected by evaporative conditions. In contrast, Cluster II quarry pit water samples (e.g., WILL-PIT-01 and WILL-PIT-02) display lower d-excess values, reflecting the influence of evaporation and/or water-rock interaction processes, which likely contribute to the observed enrichment in heavy isotopes (Kendall & McDonnell, 2012). Overall, groundwater samples show higher d-excess values than quarry pit water, a pattern consistent with the low infiltration capacity of the Daspoort Formation.

4.4.4 Tritium analysis

The tritium values of water samples in the study area range from 0.0 to 2.3 TU, with a mean of 0.9 TU. Groundwater samples exhibited tritium concentrations between 0.4 and 1.0 TU, suggesting relatively older groundwater and/or a mixture of older water with recent recharge. Quarry pit water samples (WILL-PIT-01 and WILL-PIT-02) displayed tritium values of 1.0 to 1.1 TU, indicating a stronger component of recent recharge (Figure 4-13).

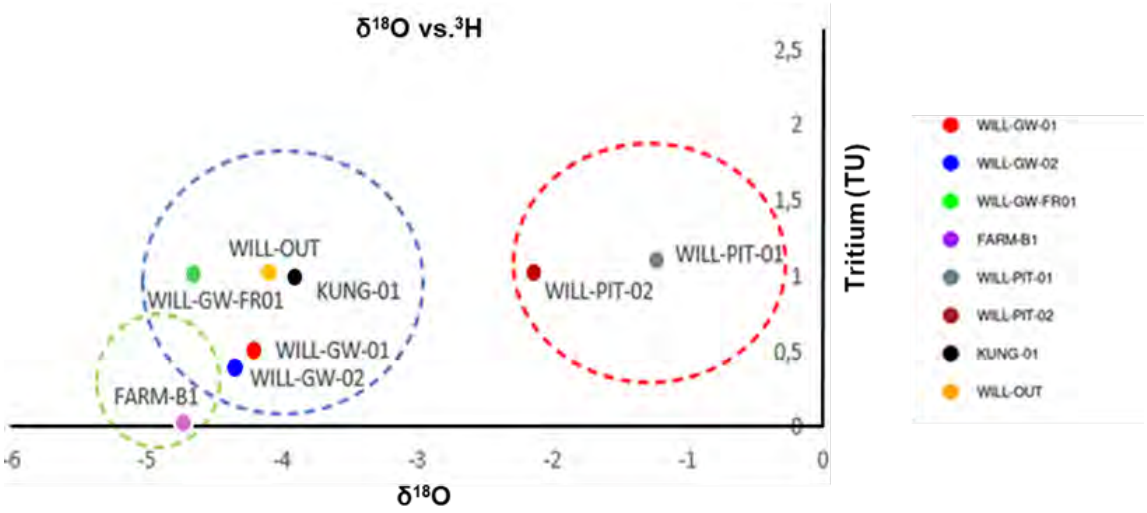

Figure 4-13 Relationship between δ¹⁸O (‰) and tritium (³H, TU) for water samples in the study area.

Overall, the isotopic signatures and d-excess values suggest recharge from local rainfall, while the tritium data indicate that this system includes a component of relatively young, recently recharged water.

4.4.5 Artificial tracers

In February and August 2023, two artificial tracer experiments using fluorescent dyes were carried out at the quarry site. Both experiments used the same injection point (borehole BH.3) and the same monitoring point (M-1), approximately 6 m apart. The M-1 monitoring point was selected as the only natural flow/discharge point (0.9 L/s) in the quarry, located at the contact between quartzite and weathered diabase on the lowest bench of the pit (Figure 4-14). This point was equipped with a GGUN-FL30 fluorometer, providing real-time detection and recording of breakthrough data (Figure 4-15).

The purpose of repeating the experiment was to investigate changes potentially induced by two external factors: (1) hydrological conditions (wet or dry season), and (2) blasting operations that took place in the quarry between the two tracer tests.

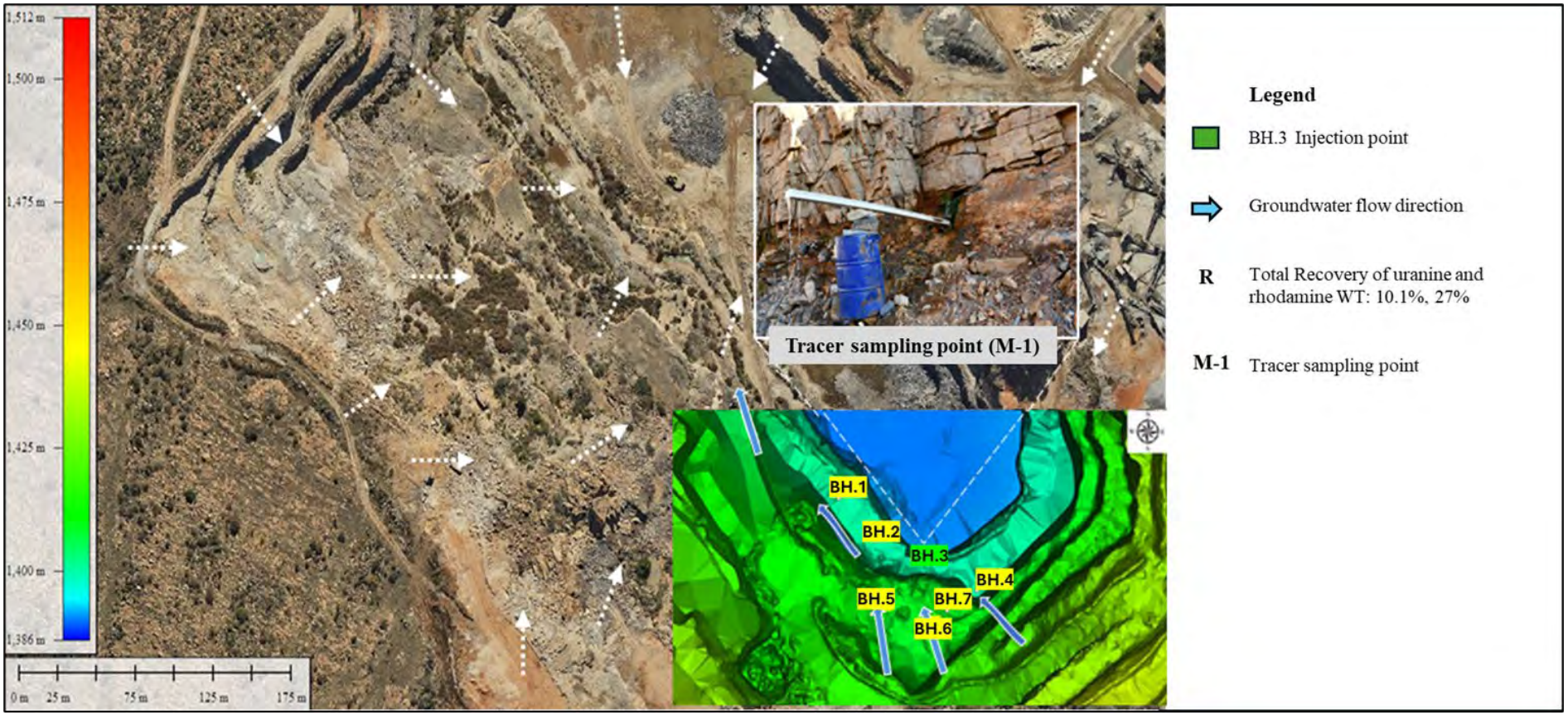

Figure 4-14 Injection points and sampling location used during the tracer tests.

Figure 4-15 Experimental set-up for tracer monitoring using the GGUN-FL30 fluorometer (photographs by van Wyk, 2023).

The first (wet season) tracer test was conducted on 8 February 2023. The water level in borehole BH.3 was 4 m below ground level. Rhodamine WT (4.7 g) was injected into the borehole, followed by 0.5 L of flush fluid. Tracer breakthrough at monitoring point M-1 occurred at 2 488 s, with a dominant flow velocity of 10.8 m/h and a recovery rate of 27%. The breakthrough curve (BTC) displayed multiple peaks, indicating the presence of several flow paths within the fracture network **(Figure 2.16).** Characteristic BTC times and velocities are summarised in Table 4-4**.**

The second (dry season) tracer test was performed on 9 August 2023. The depth to the water level in BH.3 was 5.1 m below ground level. Uranine (2 g) was injected into the borehole followed by 1 L of flush fluid. Initially, no tracer breakthrough was observed. Three additional 85 L flushes were successively applied to mobilise the injected tracer, resulting in a positive breakthrough marked by three concentration peaks **(Figure 2.17).** Despite the three flushes, the overall recovery rate was only 10.1%, substantially lower than in the first experiment. This lower recovery rate is likely due to greater spatial divergence of flows from the injection point, associated with the much higher total flush volume. Characteristic BTC times, corrected for successive flushing times, and associated velocities are summarised in Table 4-4for comparison with the first experiment.

Table 4-4 Summary of tracer tests and results at the quarry site

Test code	Date (2022)	Tracer used	Mass injected (g)	Flushing	Flushing volume (L)	Observation point(s)	Nature of flow	Flow rate (L/s)	Season	Distance to M-1 (m)	t_{max} (s)	t_{mean} (s)	t_{dom} (s)	v_{max} (m/s)	v_{mean} (m/s)	v_{dom} (m/s)	Recovered mass (%)
Test 1	8 Feb	Rhodamine WT	4.7	Yes	0.5	M-1	Natural	0.9	Wet	6.05	2488	2700	2520	0.002	0.002	0.002	27
Test 2a*	9 Aug	Uranine	2.0	Yes	85	M-1	Natural	0.9	Dry	6.05	238	706	526	0.025	0.009	0.012	10.1
Test 2b*	9 Aug	Uranine	0.0	Yes	85	M-1	Natural	0.9	Dry	6.05	1917	2277	2097	0.003	0.003	0.003	7.6
Test 2c*	9 Aug	Uranine	0.0	Yes	85	M-1	Natural	0.9	Dry	6.05	293	643	391	0.021	0.009	0.016	1.8

*Indicates a series of tests stemming from a single tracer injection of uranine, followed by staggered flushes to observe tracer recovery at M-1.

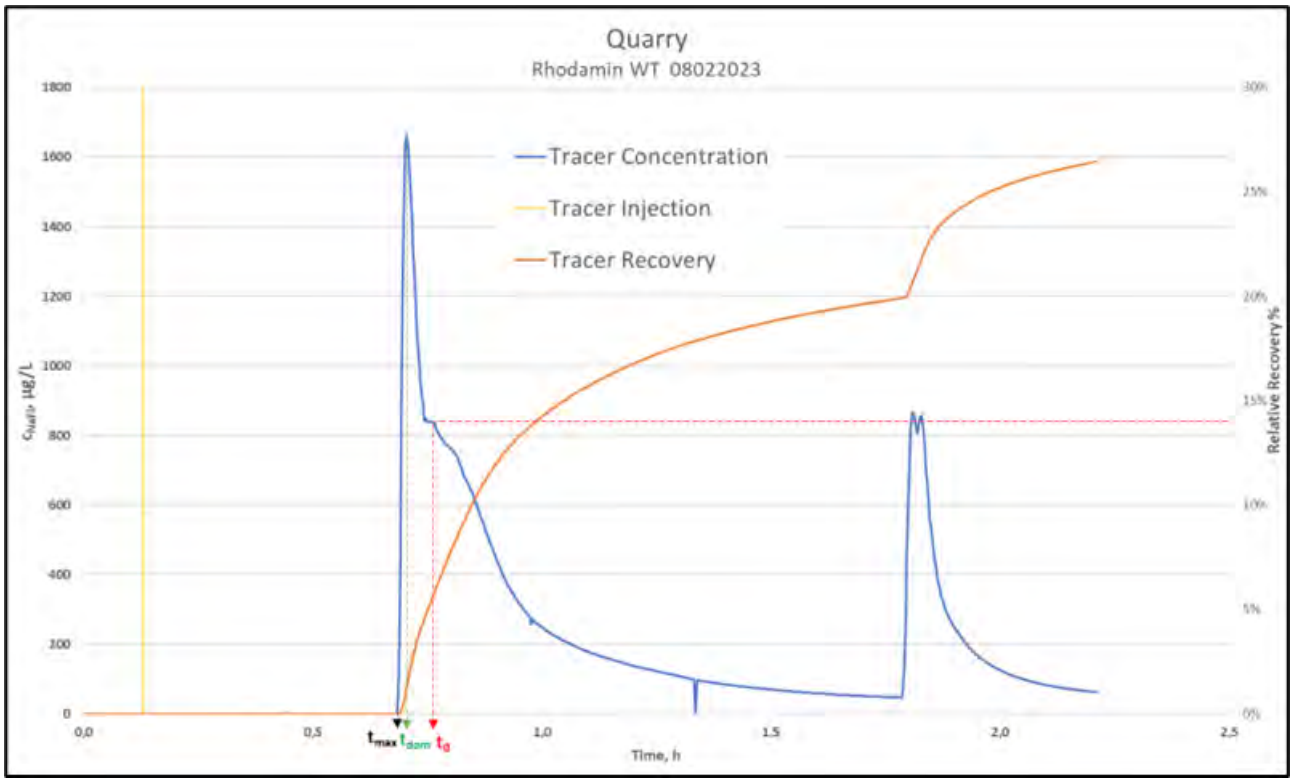

Figure 4-16 Breakthrough and recovery curves for rhodamine WT during the wet season.

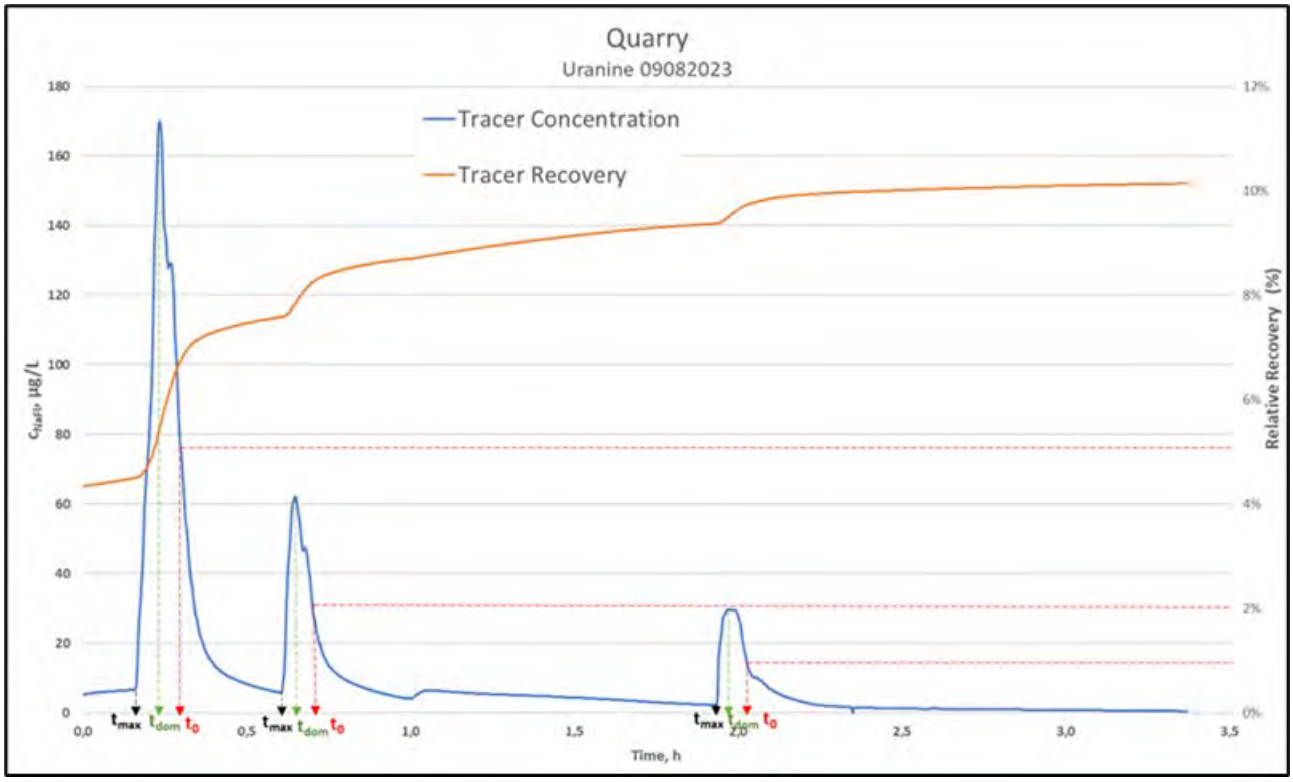

Figure 4-17 Breakthrough and recovery curves for uranine during the dry season.

The data obtained from these tracer tests were further interpreted using analytical modelling. Bodin (2020) developed MFIT (Multi-Flow Inversion of Tracer breakthrough curves), an open-source tool designed for interpreting complex BTCs, including multi-peak and heavy-tailed distributions. The MFIT software models solute transport through discrete one-dimensional channels representing primary flow paths in fractured

systems (Figure 4-18). It applies four analytical models MDMi, MDMed, SFDM, and MDP-2RNE each based on distinct analytical solutions to the advection-dispersion equation (ADE).

Immobile porosity can cause the classical ADE to inadequately predict solute transport; accordingly, dual-domain mass transfer (DDMT) models were developed to represent immobile pathways and zones of low advective velocity (Foster et al., 2021). The MDMi and MDMed models assume that tracer transport occurs via single-porosity, one-dimensional flow paths, whereas the SFDM and MDP-2RNE models incorporate dual-porosity flow paths that simulate mass exchange between mobile and immobile zones. Specifically, the MDP-2RNE model is based on a first-order mass exchange process, whereas the SFDM model assumes a second-order diffusion-based process under a parallel-plate channel geometry. MFIT also integrates PEST for regularised inversion and uncertainty analysis of model parameters (White et al., 2014; Bodin, 2020). The total discharge rate (Q = 3.24 m³/h) was fixed before inversion, while parameters such as tracer mass (M), mean transit time (t_0), Péclet number (Pe), proportion of mobile porosity (Ψ_1), and first-order mass transfer coefficient (ω_1) were optimised to represent tracer transport dynamics.

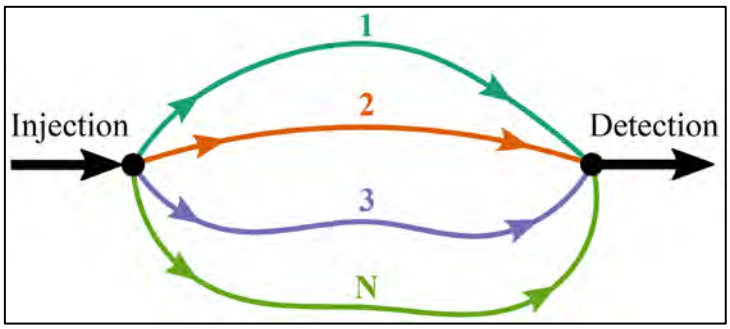

Figure 4-18 Conceptual model of the generic multi-flow modelling approach in MFIT (Bodin, 2020).

As shown in Figure 4-19**,** corresponding to Test 1 in Table 4-4, the inverted BTCs for models with four and 12 flow channels align closely with the experimental data. This fit informs the parameter values listed in Table 4-4**.** Figure 4-19 also presents PHI versus N curves, illustrating the results of the PEST optimisation method for varying channel numbers. Both the MDMi and MDP-2RNE models demonstrate the ability to represent the underlying flow mechanisms.

The optimal number of channels was determined by evaluating the trade-off between model complexity and fit to the observed data. For the MDMi model, the identification of 12 paths is based on a more detailed representation of system heterogeneity, although this choice is not immediately obvious from the PHI(N) curve alone. In the case of the MDP-2RNE model, the four-path configuration provided an adequate fit while maintaining conceptual simplicity. The inflection point on the PHI(N) curve supports this choice, indicating that the four-path model captures the essential flow dynamics without introducing unnecessary complexity. This suggests that the injected mass split into several independent pathways that converged at the output, thereby complicating the fitting of single-flow-path models.

Although the BTCs from both the MDMi and MDP-2RNE models appear almost identical, the underlying conceptual differences between these models are important for interpreting the transport mechanisms. The MDMi model explains tracer transport by representing heterogeneous flow conditions through multiple low-velocity paths. In contrast, the MDP-2RNE model explicitly distinguishes between mobile and stagnant zones, which are not directly represented in the MDMi model. When fewer flow paths are required in MDP-2RNE than in MDMi for the same tracer test, this suggests that the tracer interacted with stagnant or very low-flow zones. In the MDMi model, this behaviour is represented indirectly by introducing additional slow-moving paths. While both models provide similar information regarding the coexistence of fast and slow pathways, the MDP-2RNE model more explicitly reflects the influence of stagnant zones in fractured media.

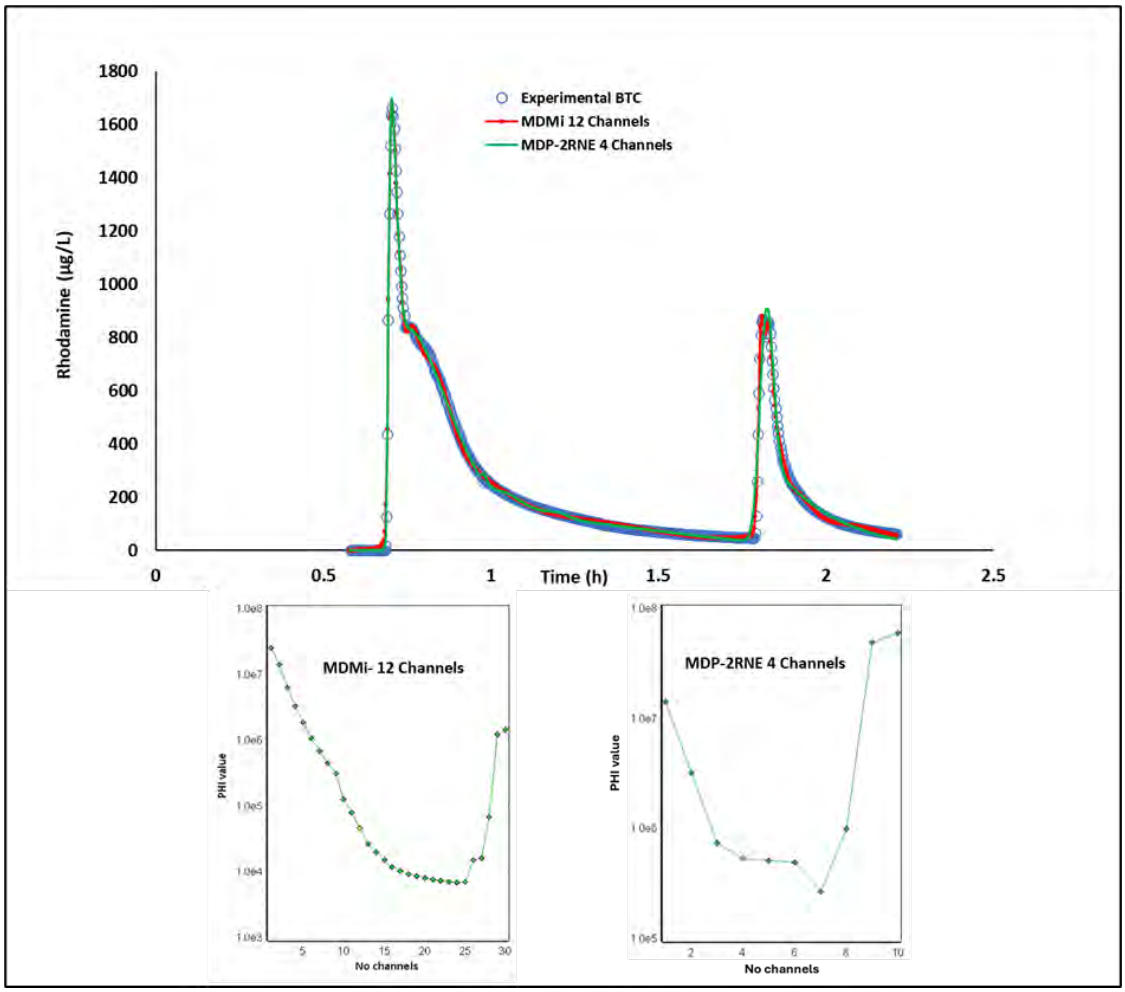

Figure 4-19 Wet season BTC fitting analysis using MDMi and MDP-2RNE models for Test 1 with varying channel numbers (N). PHI represents the fitting error minimised using PEST inversion routines.

For Model 1 (MDMi), mean transit times (t_0) range from approximately 0.698 to 2.043 h, with Pe values indicating a transition from advection-dominated to dispersion-dominated behaviour. For Model 2 (MDP-2RNE), mean transit times vary from 0.689 to 1.821 h, displaying a broader range of Pe values. Both models exhibit similar velocities, averaging approximately 2.0×10^{-3} m/s, while the longitudinal dispersivity (α) indicates a low degree of dispersion, ranging from 1.8×10^{-6} m to 1.7×10^{-1} m. It is important to note that α here refers to longitudinal dispersivity, not to the first-order mass transfer coefficient αj [T^{-1}] discussed by Bodin (2020). Although the SFDM model is not shown in Figure 2.19, it performed comparably to the MDP-2RNE model, which uses a dual-porosity conceptualisation that incorporates stagnant water regions and flowing channels.

Table 4-5Optimised model parameters corresponding to the inverted BTC for the wet season test

Model 1	MDMi (ADE instantaneous injection)							
T_{min}	T_{max}	No. Time Steps	Q (m^3/h)	Distance (m)				
0.58	2.21	500	3.24	6.5				
	Channel *(N)*	Mass (g)	t_0 (h)	Pe	V (m/s)	α (m)	ψ_1	ω_1 (m^{-1})
	1	31732.3	0.698	42701.5	2.6E-03	1.5E-04		

	2	58484.4	0.708	17807.0	2.6E-03	3.7E-04		
	3	70567.8	0.722	6938.3	2.5E-03	9.4E-04		
	4	102820.1	0.754	1591.2	2.4E-03	4.1E-03		
	5	238388.7	0.821	447.8	2.2E-03	1.5E-02		
MDMi	6	184462.7	0.944	151.1	1.9E-03	4.3E-02		
	7	260151.0	1.295	39.1	1.4E-03	1.7E-01		
	8	31209.6	1.805	125457.3	1.0E-03	5.2E-05		
	9	67885.3	1.825	35945.2	9.9E-04	1.8E-04		
	10	47194.5	1.851	13464.3	9.8E-04	4.8E-04		
	11	49088.9	1.905	3293.8	9.5E-04	2.0E-03		
	12	126470.1	2.043	288.9	8.8E-04	2.3E-02		
Model 2								
	1	89620.2	0.689	3581865	2.6E-03	1.8E-06	0.98	0.91
	2	187671.0	0.978	39768.57	1.8E-03	1.6E-04	0.67	0.77
	3	646041.8	0.716	6695.117	2.5E-03	9.7E-04	0.84	0.39
MDP-2RNE	4	21424.5	1.047	3759.173	1.7E-03	1.7E-03	0.92	0.30

For the BTC obtained in the dry season, model fitting focused on the first peak only, since peaks 2 and 3 resulted from the successive flushes and therefore contained no independent transport information. Furthermore, peaks 2 and 3 may have been influenced by previous flushing, which could bias their interpretation. The inverted BTC in Figure 4-20 demonstrates a strong fit to the experimental data, particularly with four flow channels (N = 4). The parameters used for the second tracer simulation are summarised in Table 4-6**.**

The total discharge rate Q was fixed at 3.24 m³/h to facilitate comparison of inverted mass values. Parameters such as tracer mass (M), mean transit time (t_0), Péclet number (Pe), mobile water fraction (Ψ_1), and first-order mass transfer coefficient (ω_1) were optimised.

The last channel is primarily responsible for the tailing observed in the BTC, highlighting delayed tracer transport through specific fracture pathways. These results form the basis for subsequent analysis of transport dynamics under dry-season conditions. Mean transit times ranged from 0.112 to 0.184 h (average: 0.15 h), providing an indication of how rapidly the tracer moved through the primary flow paths of the system. This reflects advective transport conditions, in which the tracer experienced limited interaction with the rock matrix during transit through fractures. Simultaneously, Pe values ranged from 8.7 to 287.6, suggesting varying degrees of advection-dominated transport.

For Model 2 (MDP-2RNE), mean transit times ranged from 0.106 to 0.168 h, with an average of 0.13 h, indicating a similar pattern to Model 1 in which advective transport continued to dominate. The Pe values for this model ranged from 14.6 to 363.0, closely aligning with those of Model 1. Similar to the observations in Model 1, both velocity and dispersivity values showed consistent flow and dispersion behaviour, indicating limited variability between the two models. This finding also suggests minimal exchange between mobile and immobile porosity domains. The first-order mass transfer coefficient (ω_1) was calculated as 0.05 T^{-1}, supporting negligible interaction between mobile and immobile porosity and reinforcing the interpretation that flow occurred primarily within fractures, with limited exchange with the surrounding matrix.

Both models produced similar results, particularly regarding the number of flow channels (N = 4), indicating that tracer transport was primarily confined to fractures with limited interaction with no-flow zones. Although Model 2 (MDP-2RNE) incorporates parameters for dual-porosity exchange, the comparable outcomes suggest that the simpler MDMi model effectively captures the transport dynamics under dry conditions, making it a more efficient and interpretable choice for this dataset.

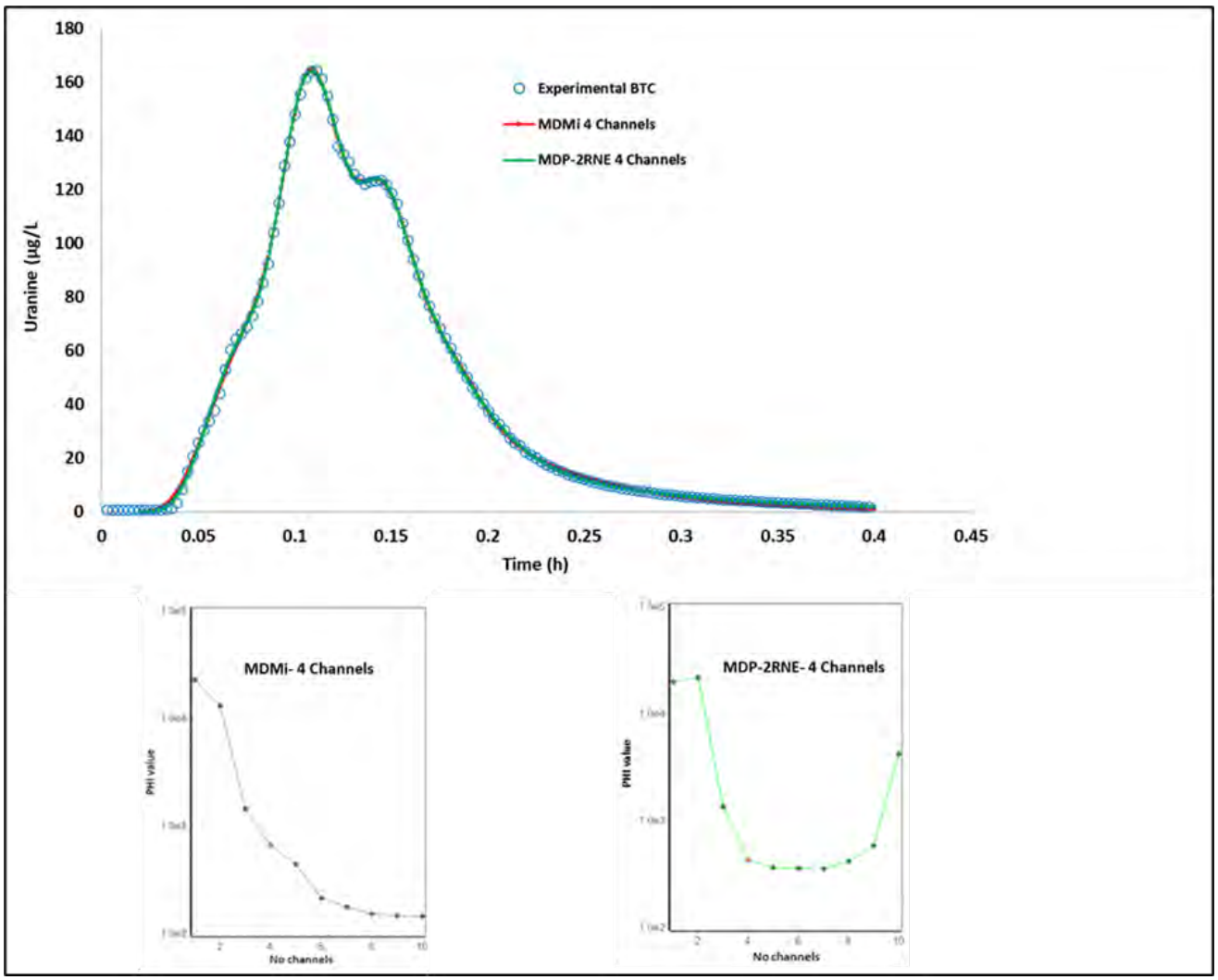

Figure 4-20 Dry season inversion solutions of BTC fitting analysis for tracer Test 2a using MDMi and MDP-2RNE models for varying channel numbers (N).

Table 4-6 Optimised model parameters corresponding to the inverted BTC for the dry season test

Model.1	MDMi (ADE instantaneous injection)							
T_{min}	T_{max}	No. time steps	Q (m^3/h)	Distance (m)				
0.02	0.4	500	3.24	6.5				
	Channel (N)	Mass (g)	T_0 (h)	Pe	V (m/s)	α (m)	ψ_1	ω_1 (m^{-1})
	1	9427.8	0.112	120.7	1.6E-02	5.4E-02		
	2	1956.8	0.184	287.6	9.8E-04	2.3E-02		
MDMi	3	6283.8	0.150	228.4	1.2E-02	2.8E-02		
	4	35431.9	0.140	8.7	1.3E-02	7.5E-01		
Model.2								
	1	23458.2	0.105	14.6	1.7E-02	4.5E-01	0.86	0.05

MDP-2RNE	2	13315.7	0.111	115.6	1.6E-02	5.6E-02	0.96	0.07
	3	3860.7	0.148	363.0	1.2E-02	1.8E-02	0.15	0.05
	4	14050.8	0.168	71.4	1.1E-02	9.10E-02	0.86	0.05

The findings indicate that blasting activities likely altered flow patterns, channel connectivity, and preferential flow pathways within the fractured quarry system. The second tracer test, characterised by N = 4 flow channels, indicated a more clearly defined flow system, demonstrating the potential impact of blasting on flow dynamics. This sequence highlights the way in which anthropogenic activities, specifically blasting, can reconfigure flow pathways and thereby influence the overall hydrodynamics of the system.

While models such as MDMi and MDP-2RNE provide mathematically coherent fits, it is crucial to assess their practical hydrogeological meaning. The ability to obtain a mathematically acceptable fit does not, in itself, guarantee that the model accurately represents the underlying hydrogeological system. Seasonal variations in flow dynamics also influence model complexity. During the wet season, increased rainfall results in higher saturation, which generally enhances hydraulic conductivity and reduces resistance to flow within fractures. At the same time, increased saturation may cause preferential flow paths to shift, necessitating the use of more channels in the model to represent flow interactions across different pathways. In contrast, faster tracer flow rates were observed during the dry season despite lower saturation. This may be due to the larger flushing volume, which temporarily increased the hydraulic head gradient between the injection point and the observation point. This interpretation is also consistent with the lower recovery rate, which may reflect greater flow divergence from the injection point. Alternatively, this apparent anomaly may also be attributed to the mechanical effects of blasting. Blasting may have widened fracture apertures, allowing more efficient flow even under lower saturation conditions, thereby reducing overall resistance and explaining the faster transfer rates observed during the dry-season tracer tests.

Overall, these experiments provided valuable insights into flow rates, fracture pathways, and dispersion characteristics within the altered and fractured environment of the quarry. The results indicate that blasting activities significantly influence these factors by modifying flow rates, directions, and dispersivity. Specifically, blasting can create new pathways and alter the physical properties of fractured rock, leading to changes in subsurface hydrology. With the quarry's closure in November 2023, these findings are especially relevant for informing management strategies related to decanting and other post-closure planning. The comparative analysis of breakthrough curves and tracer transport parameters enhances understanding of the hydrogeological characteristics of the site and emphasises the need to consider the impacts of blasting and active operations on groundwater flow dynamics during closure planning.

4.5 CONCEPTUAL SITE MODEL

The conceptual site model (CSM) provides a framework for understanding the way in which open-cast mining activities have altered the vadose zone and affected groundwater flow at the quarry. Mining operations have created fractures and voids in the subsurface which, once dewatering ceases, may fill with water and form pit lakes (Castro & Moore, 2000). These changes influence groundwater flow and contaminant transport. The CSM provides a simplified representation of the subsurface processes controlling groundwater flow and contaminant transport at the site, focusing on the behaviour of both environmental and artificial tracers within the fractured rock environment.

The model emphasises the geological features, including fracture networks and preferential flow paths, that govern water movement and solute transport. It considers key factors such as tracer sources, transport

mechanisms, and their interactions within the system, thereby providing a more integrated understanding of altered groundwater dynamics.

Environmental tracers such as stable isotopes reveal natural groundwater processes, while artificial tracers such as dye injections provide insight into specific flow paths and transport rates. The contact between the diabase intrusions and Daspoort Formation quartz arenites plays a pivotal role in influencing flow velocity and drainage patterns through the development of preferential flow paths along fractures. The highly heterogeneous nature of these fractures and their extensive networks controls the movement of water through the partially saturated vadose zone. This interaction forms the basis of the hydrogeological conceptual model for the site. Figure 4-21 illustrates the hydrogeological conceptual model for the quarry, showing the influence of subsurface structures on groundwater flow pathways. The fracture network in the quarry exhibits a classic dual-porosity system, characterised by both fast-moving flow channels and stagnant water zones within the fracture network.

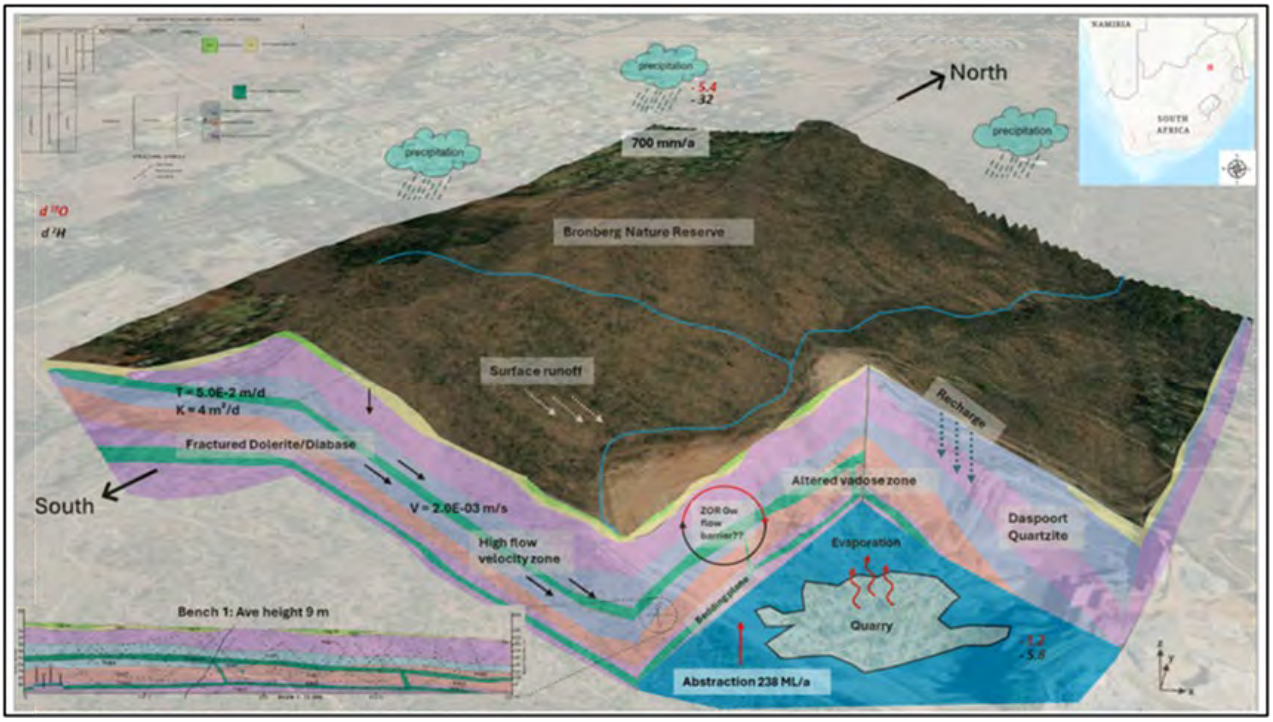

Figure 4-21 Simplified hydrogeological conceptual model illustrating groundwater flow pathways influenced by heterogeneous subsurface structures in an open-pit quarry.

The stagnant zones are particularly important in influencing solute transport and may contribute to delayed tracer breakthrough during wet periods. This behaviour is consistent with the hydrogeological responses observed in the field, where intermittent blasting operations have likely altered fracture geometry through sediment deposition, fracture opening, or erosion. These modifications affect hydraulic behaviour, leading to changes in flow velocities, mixing dynamics, and dispersion characteristics.

4.6 CONCLUSIONS AND RECOMMENDATIONS

This study demonstrates that tracer- and isotope-based techniques, when integrated with structural analysis, provide a powerful means of understanding contaminant transport in an altered vadose zone. The results show that groundwater flow and solute migration are strongly fracture-controlled, shaped by geological structures and further intensified by quarry blasting. This highlights the need to explicitly consider anthropogenic disturbance when conceptualising groundwater systems in similar environments. The application of environmental tracers confirmed active recharge from local rainfall, while artificial tracers revealed variable

flow velocities, recovery patterns, and pathway behaviour under different hydrological and operational conditions. These findings indicate a dynamic and seasonally responsive system in which fault zones, fracture networks, and lithological contacts act as important flow conduits. Beyond hydrogeological characterisation, this work demonstrates the value of multidisciplinary methods in the development of robust, site-specific conceptual models. Such models are essential for predicting post-closure behaviour, informing risk mitigation, and supporting long-term groundwater management.

Future mine closure strategies should incorporate tracer studies, isotope monitoring, and structural mapping as standard components of hydrogeological assessment. This would support adaptive management, facilitate earlier detection of contamination risks, and improve alignment with environmental sustainability objectives.

4.7 FUTURE POSSIBILITIES AND LIMITATIONS

This study has demonstrated the value of combining environmental and artificial tracers with stable isotope analysis to improve understanding of groundwater flow and recharge in an anthropogenically altered vadose zone. While these methods provide a powerful basis for characterising complex flow regimes in fractured media, several limitations remain.

First, the isotope dataset represents only a limited temporal snapshot of recharge conditions. Future work would benefit from multi-seasonal monitoring to capture temporal variability more effectively and refine interpretations of recharge dynamics. Second, although the tracer tests captured key flow characteristics, site-specific heterogeneity and mining-induced disturbance present challenges in extrapolating the findings beyond the immediate study area. Application of these methods to other mined or disturbed environments should therefore be accompanied by detailed hydrogeological and structural characterisation to ensure appropriate contextual interpretation.

Looking ahead, expansion of this work through numerical modelling and longer-term tracer monitoring would improve predictive capability and better support sustainable mine closure and groundwater management strategies. The approach outlined here provides a transferable framework that can be adapted to similar post-mining environments elsewhere, particularly where fractured vadose zones have been influenced by anthropogenic change.

4.8 REFERENCES

Barnard, H. C. (2000). An explanation of the 1:500 000 general hydrogeological map. Pretoria: *Department of Water Affairs and Forestry*.

Bodin, J. (2020). MFIT 1.0. 0: Multi-Flow Inversion of Tracer breakthrough curves in fractured and karst aquifers. *Geoscientific Model Development, 13*(6), 2905-2924.

Bowen, G. J., & Revenaugh, J. (2003). Interpolating the isotopic composition of modern meteoric precipitation. *Water Resources Research, 39*(10), 1299.

Castro, J. M., & Moore, J. N. (2000). Pit lakes: Their characteristics and the potential for their remediation. *Environmental Geology, 39*, 1254-1260.

Christensen, T. H., Kjeldsen, P., Bjerg, P. L., Jensen, D. L., Christensen, J. B., Baun, A., Heron, G. (2001). Biogeochemistry of landfill leachate plumes. *Applied Geochemistry, 16*(7-8), 659-718.

Clark, I., & Fritz, P. (1997). Environmental isotopes in hydrogeology. Boca Raton: CRC Press.

Craig, H. (1961). Isotopic variations in meteoric waters. *Science, 133*(3465), 1702-1703.

Dansgaard, W. (1964). Stable isotopes in precipitation. *Tellus, 16*(4), 436-468.

Dhansay. (2021). Shattered crust: how brittle deformation enables Critical Zone processes beneath southern Africa. *South African Journal of Geology* 2021, 124(2), 519-536.

Dhansay, Musekiwa, C., Ntholi, T., Chevallier, L., Cole, D., & De Wit, M. J. (2017). South Africa's geothermal energy hotspots inferred from subsurface temperature and geology. *South African Journal of Science*, 113(11-12), 1-7.

DWS. (1999). 1:500 000 Hydrogeological Map Series. Pretoria: Department of Water Affairs and Forestry/Department of Water and Sanitation.

Foster, A., Trautz, A. C., Bolster, D., Illangasekare, T., & Singha, K. (2021). Effects of large-scale heterogeneity and temporally varying hydrologic processes on estimating immobile pore space: a mesoscale-laboratory experimental and numerical modeling investigation. *Journal of Contaminant Hydrology, 241*, 103811.

Herold, C., & Bailey, A. (2016). Water Resources of South Africa 2012 Study. Pretoria: *Water Research Commission.*

Kendall, C., & McDonnell, J. J. (2012). Isotope tracers in catchment hydrology. Amsterdam: Elsevier.

Khan, R. A., Khan, N. A., El Morabet, R., Alsubih, M., Qadir, A., Bokhari, A., Manickam, S. (2022). Geospatial distribution and health risk assessment of groundwater contaminated within the industrial areas: an environmental sustainability perspective. *Chemosphere, 303*, 134749.

Mook, W. G. (2000). Environmental isotopes in the hydrological cycle: Principles and applications.

Mor, S., Ravindra, K., Dahiya, R., & Chandra, A. (2006). Leachate characterization and assessment of groundwater pollution near municipal solid waste landfill site. *Environmental monitoring and assessment, 118*(1), 435-456.

Morris, A., Ferrill, D. A., & Henderson, D. B. (1996). Slip-tendency analysis and fault reactivation. *Geology, 24*(3), 275-278.

Parsons, R. (1995). *A* South African aquifer system management classification. WRC Report No. KV 77/95. Pretoria: *Water Research Commission*.

Stumm, W., & Morgan, J. J. (1996). Aquatic chemistry: Chemical equilibria and rates in natural waters (3rd ed.). New York: Wiley.

Van der Neut, M. (1990). Afsettingstoestande van die Pretoria Groep gesteentes in die Pretoria-Bronkhorstspruit-Delmas gebied. MSc thesis, *University of Pretoria.*

van Wyk, Y. (2024). Combined use of environmental and artificial tracers to characterise the anthropogenically altered vadose zone and groundwater system. *University of Pretoria*, Pretoria.

van Wyk, Y., Bodin, J., Witthüser, K., Ubomba-Jaswa, E., Dippenaar, M. A., & Butler, M. (2025). Evaluating contaminant pathways in an altered vadose zone: A multidisciplinary approach in open-pit quarry environments. *Environmental Earth Sciences, 84*(12), 318.

van Wyk, Y., Dippenaar, M. A., & Ubomba-Jaswa, E. (2024). Enhancing hydrological analysis by incorporating environmental and artificial tracers of an altered vadose zone: A systematic review. *Journal of African Earth Sciences, 212*, 105209.

Vegter, J. R. (1995). An explanation of a set of national groundwater maps. Pretoria: Department of Water Affairs and Forestry.

White, J. T., Doherty, J. E., & Hughes, J. D. (2014). Quantifying the predictive consequences of model error with linear subspace analysis. *Water Resources Research*, 50(2), 1152-1173.

CHAPTER 5: ANALYSIS OF UNSATURATED FLOW BEHAVIOUR THROUGH DISCONTINUITIES IN ROCK MASS

Authors: Mampho Maoyi & Louis van Rooy

This comes from the following project-related outcomes:

- Maoyi M. 2026. The use of Infrared Thermography to enhance the characterisation of unsaturated flow through fractured rock mass. PhD (specialising in Engineering Geology) Thesis. University of Pretoria.
- Maoyi M, Bush R, Van Rooy JL, Dippenaar MA (2024). Using rock engineering interaction matrix to assess flow behaviour through discontinuities in the unsaturated zone. In: New Challenges in Rock Mechanics and Rock Engineering–Tomás et al.(eds), © 2024, ISBN 978-1-032-55144-9. New Challenges in Rock Mechanics and Rock Engineering, p.345

5.1 RATIONALE

The background information for this case study can be found in §4.1 and §4.3.

Open pit mining operations are being carried out in the quarry area, with mining benches measuring 8 metres in width and 12 metres in height. The direction of face advancement aligns favourably with the joint orientations, and the overall slope angle of the quarry is 58°. However, a significant challenge arose on the southwestern high wall, with a planar failure between the diabase and quartzite. During quarrying, the removal of overburden stress relief caused the displacement of the overlying quartzite along the contact with the diabase, causing tension cracks on the crest upslope of the open pit. This was during a period of increased rainfall in the area, and because of the natural drainage direction from the ridge, there was increased water ingress into the tension cracks. Due to the impermeable nature of the diabase, interflow occurred along the diabase-quartzite contact and eventually appeared in the pit face; this resulted in a sudden increase in pore pressure and a decrease in effective stress. Geotechnical stability back analysis of slope syn-water ingress indicated that the slope's safety factor decreased to less than 1, with the cohesion on the contact at zero and the friction angle at 17°. Consequently, the shear strength decreased, leading to the failure of the localised planar slope (Figure 5-1).

Figure 5-1 Google Earth image showing localised planar slope failure and geotechnical window mapping location in the quarry pit.

The site conditions described provide an ideal case study for hydrogeological and geotechnical analysis, emphasising the significant impact of geology and ground profile variations in the unsaturated zone. It highlights the crucial role that discontinuities play in influencing the strength, permeability, and stability of surface excavations in rock slopes (Yeh et al. 2020). Therefore, understanding flow behaviour in rock masses requires a thorough understanding of rock mass conditions as well as geometric characteristics of discontinuities such as aperture, roughness, orientation, and persistence, which is critical for practical rock mechanics applications. Subsequently, critical domains for flow behaviour tests were identified by mapping the first bench of the southwestern high wall where there is a natural groundwater seepage zone. The examined wall has a total width of roughly 128 meters, with bench heights averaging 9 metres.

5.2 METHODS

The methodology of this case study entails characterising rock masses and analysing flow behaviour to understand how unsaturated flow occurs through discontinuities in rock masses. The flow chart visually represents the integration of these two fundamental concepts (Figure 5-2), demonstrating the interconnected methods. This framework includes fieldwork for data acquisition, which will be further explained in the subsequent methodology sections.

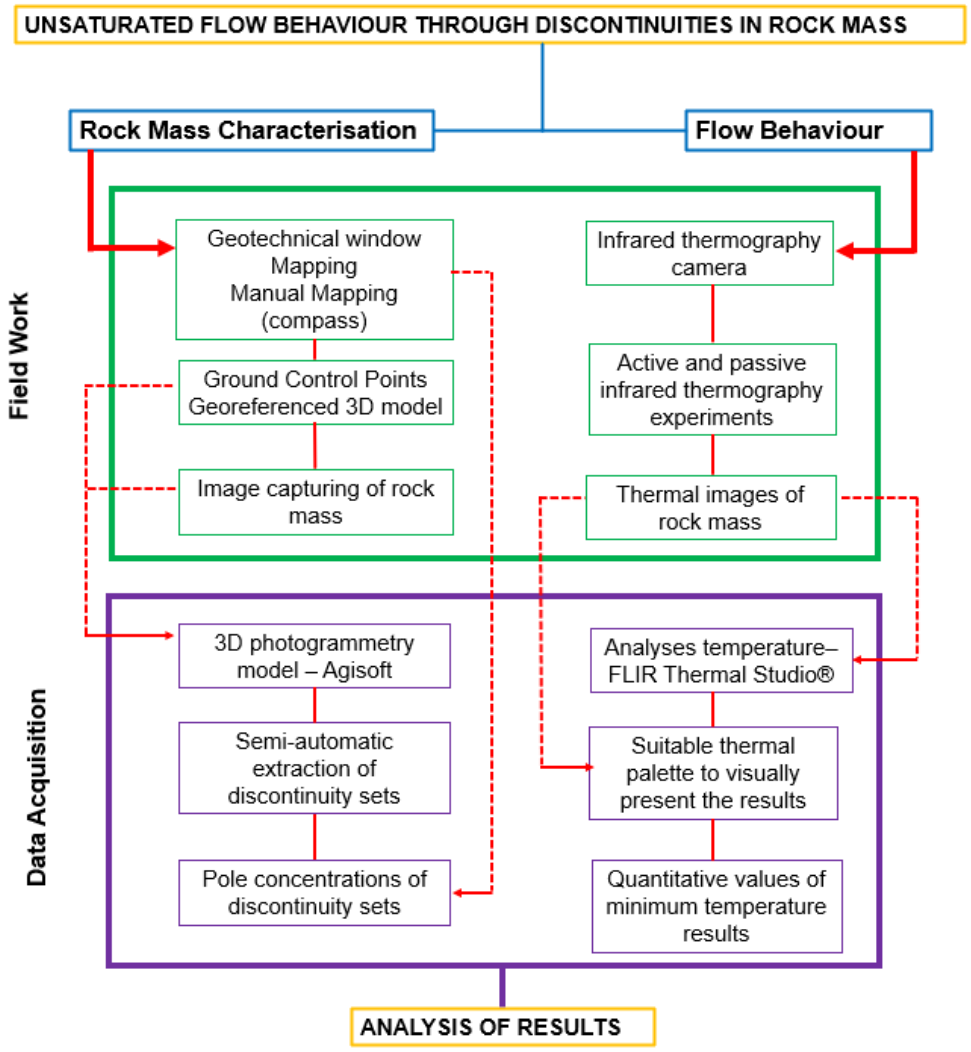

Figure 5-2 Flow chart showing the work process for this case study (Maoyi 2026).

5.2.1 Rock Mass Characterisation

Understanding the geometric properties of rock mass discontinuities is crucial for the comprehensive characterization of rock mass conditions. This process involves the documentation of various factors, including joint orientations, discontinuity set orientations, rock mass weathering, rock hardness, groundwater presence, and overall rock mass conditions (Riquelme et al. 2014). Window mapping was conducted along the first bench from the pit floor, specifically in the geotechnical domains where the seepage zone with natural groundwater was present. The purpose was to identify critical geotechnical domains within this high wall.

Furthermore, the field window mapping method was complemented with photogrammetry to obtain discontinuity data from inaccessible high walls. Ground control points were marked within the sampling window on the high wall (Figure 5-3a). These points were used to georeference the 3D model using Real-time Kinematic positioning, as shown Figure 5-3b (Forlani et al. 2019). Photographs of the high wall were taken with a mobile phone and a digital camera, and the images were processed using Agisoft (Figure 5-3c) . These images must be overlapped, orthorectified, and georeferenced to convert standard image pixels into 3D spatially measurable models (Figure 5-3). Once the model is georeferenced, it allows for an accurate digital geospatial representation of the feature in real-world coordinates. Furthermore, EasyMine™ was used to extract geotechnical features such as discontinuity sets and persistence. The data was further analysed using Rocscience Dips®. The orientation of the discontinuities obtained from the 3D model was further confirmed by the scanline method for joint line surveys using the Breithaupt Cocla® compass (ISRM 1981).

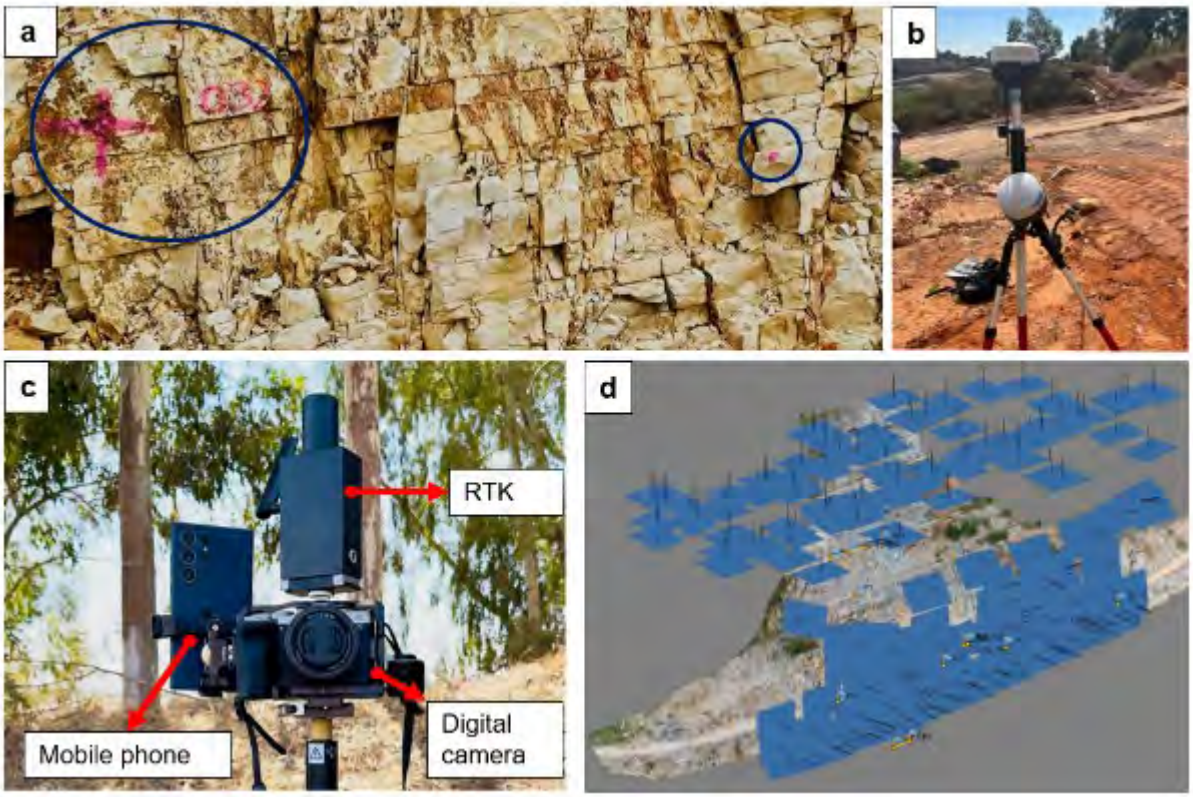

Figure 5-3 (a) Ground control points (GCP) marked on the highwall; (b) Receiver Survey Instruments GPS RTK base and rover; (c) gadgets used to capture images of the highwall (photographed by Maoyi 2024); (d) example of orthographic view of the texture-mapped 3D surface (blue squares depict the camera positions and orientations and the numbered flags indicate the positions of the GCP used for bundle adjustment) (Tung, 2018).

5.2.2 Infrared thermography

The case study used thermal imaging to examine flow behaviour. Thermal images were captured using a FLIR Advanced infrared thermography camera. Before capturing each thermal image, measurements of the emissivity, ambient air temperature, relative humidity and reflected apparent temperature to calibrate temperatures at various acquisition periods were taken. The reflected and atmospheric temperature, relative humidity, and the distance between the rock face and the camera were also defined because the relative humidity and ambient air temperature influence the transmission of infrared radiation.

The field experiments involved both passive and active thermography. Passive thermography uses infrared radiation from the environment, while active thermography requires an external energy source to generate thermal responses for analysis (Hung et al. 2009; Herraiz et al. 2020). During the passive infrared experiments, we captured multiple images of the high wall in the morning at regular intervals. The aim was to assess the thermal camera's ability to identify wet areas on the rock high wall, including the natural groundwater and the surrounding rock mass. For the active thermography, we introduced an additional water source. We drilled a borehole to a depth of 18 meters above the natural seepage zone, with the water level recorded at approximately 5 meters. This borehole is located 3 meters from the high wall and is situated on the haul road that separates bench 1 and bench 2 **(**Figure 5-4**).** The window of interest on the high wall at the groundwater seepage zone, and it was divided into two equal sections, area 1 and area 2, for a comprehensive temperature analysis. During these experiments, we placed an external water source next to the borehole and attached a flow meter with a pipe to record the pumping rates. The borehole was fitted with a pipe extending approximately 0.5 meters to mitigate water gushing, as around 7000 L of cold water (3°C) was injected. Simultaneously, active thermography was employed to capture images of the high wall during the water pumping process.

The thermal images acquired were imported into FLIR Thermal Studio® for post-processing. In the color-scaled image, each pixel corresponds to a distinct temperature value (Mineo and Pappalardo, 2016). This functionality facilitates modifications to the thermal palettes during post-processing, enabling qualitative analysis, such as discerning flow patterns on the high wall, and quantitative analysis of temperature variations during experiments.

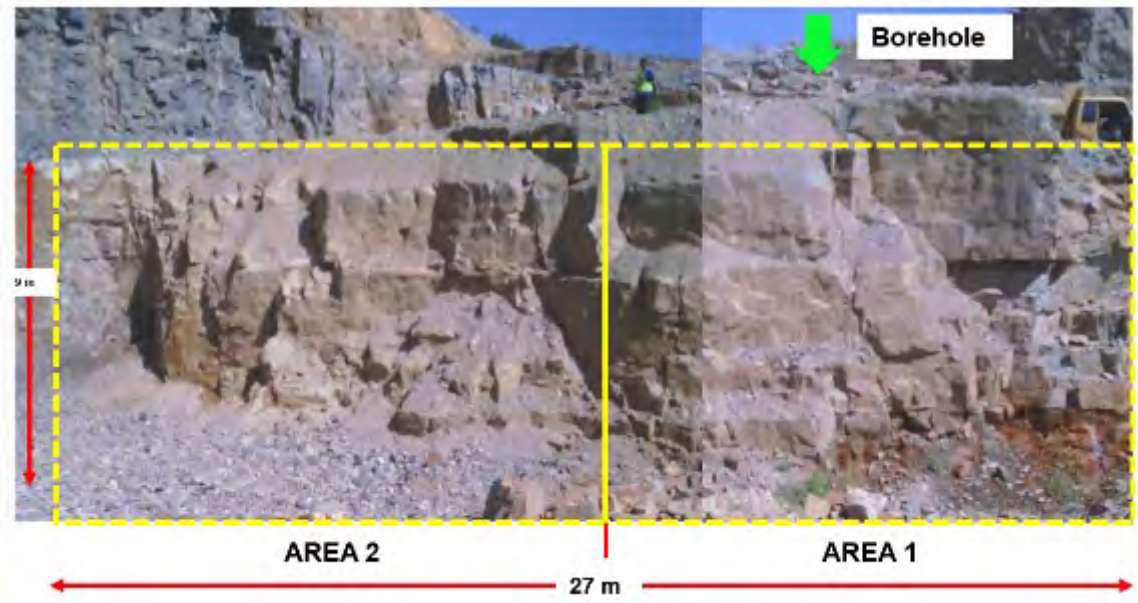

Figure 5-4 Investigated the high wall for infrared flow behaviour experiments.

5.3 RESULTS

5.3.1 Rock Mass Characterisation and Discontinuity mapping

During the window mapping, we examined visible rock face exposures that were safely accessible on the first bench. Based on our geological observations during the window mapping, we have established the following geotechnical classification for the specified areas:

In this region, there are two main geotechnical domains. Geotechnical domain 1 primarily consists of slightly weathered, very hard quartzite, which makes up 98% of the rock mass and shows moderate effects of blasting. Figure 5-5a shows a detailed depiction of this geotechnical zone, highlighting the favourable slope orientation and illustrating the "massive" structure with minimal discontinuities. Only 2% of the rock mass is weak, highly fractured soft rock weathered diabase observed at the slope's top. Furthermore, the groundwater conditions are reported to be dry.

Key characteristics include:

- Discontinuities are not prominent in geotechnical Domain 2.
- Two sub-vertical joints span a 20-meter width and a 3-meter bench height.
- Bedding planes are noticeable throughout the window, particularly in the first 3 meters from the pit's bottom. They become less frequent in the remaining 6 meters of the high wall.

Moreover, there is an abrupt termination zone between domains 2 and 3, indicating a sub-vertical fault zone (Figure 5-5a). This domain features two sub-vertical joints and a bedding plane, which are prominently observed throughout the mapped area. The rock mass in this zone exhibits slight weathering and comprises 95% hard rock (quartzite) and 5% weaker rock (weathered diabase). The boundary between weathered diabase and quartzite is the only place in the pit where continuous water flow is observed. This contact is characterized by ~300 mm wet, yellowish brown, highly fractured, soft rock classified as weathered diabase, which is slightly undulating and is found between the layers of quartzite (Figure 5-5c).

A detailed 3D point cloud was created using a georeferenced photogrammetry model. This model was used to semi-automatically map discontinuities in the bench area where the window mapping for geotechnical classification had been previously conducted. Due to the fractured rock mass resulting from blasting effects, only the most prominent discontinuities were mapped, and microfractures were discarded after analysis. Table 5-1provides the average dip and dip direction values of these discontinuity sets and the persistence of the specific sets. Figure 5-6 shows the representative model of the investigated high wall and the semi-automatic mapping with Joint set 1 denoting the bedding planes and the sub-vertical joint sets 2 and 3. Furthermore, the discontinuity data was integrated with manual mapping, and the poles of the recorded discontinuities were plotted on a stereo net, utilizing equal angle and lower hemisphere projection. The stereo-plot presented also indicates the three major discontinuity sets within this high wall (Figure 5-6b).

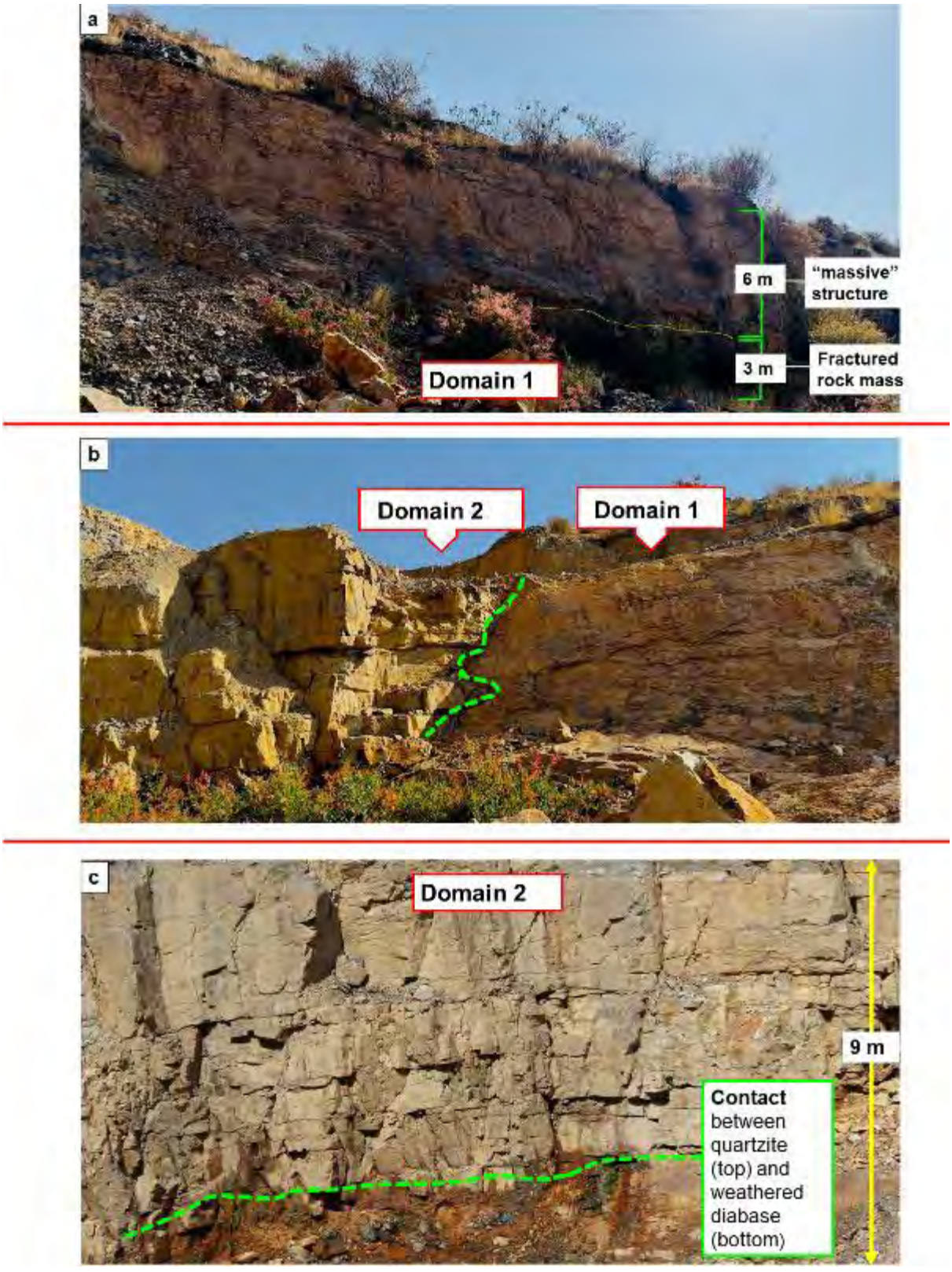

Figure 5-5 Geotechnical domains window mapped in the high wall (a) domain 1 (b) Highly weathered (b) transition between domain 2 and 3 (c) domain 3 with seepage zone between quartzite and diabase (photographed by Maoyi 2024).

Table 5-1 Discontinuity mapping data

Discontinuity Set	1	2	3
Dip (°)	14	86	84
Dip direction (°)	040	322	054
Minimum Persistence (m)	0.61	0.35	0.62
Maximum Persistence (m)	16.34	6.41	3.66

*Average values

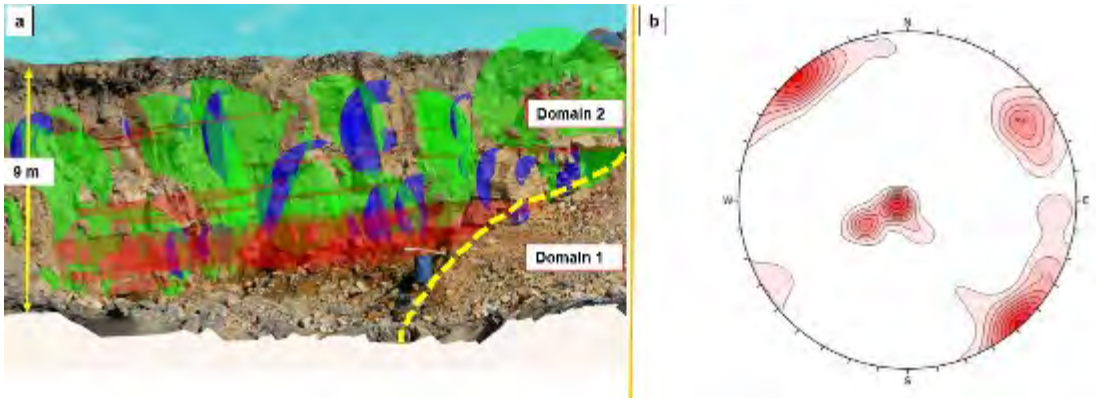

Figure 5-6 (a) 3D Photogrammetric model with the discontinuity sets within the rock mass (b) stereoplot showing the pole concentration of the three major discontinuity sets in the rock mass (Maoyi et al. 2024).

5.3.2 Passive infrared thermography

The following results outline the findings from the passive thermography experiments conducted in the groundwater seepage zone. The rockface exhibited a high emissivity of 0.98, with a reflected atmospheric temperature of 20°C and a relative humidity of 50%. The thermal signatures within a specific image were analysed by setting target points with temperature ranges between a specific minimum of 17.5°C and a maximum of 24.6°C. Additionally, the camera was positioned to capture digital colour images of the precise location, enabling visual comparison of thermal variations at distances ranging from 6 to 15 meters (Figure 5-7a). According to the analysis in Figure 5-7b, it was observed that the warmer red colour is more prominent in the groundwater zone compared to the high wall, where the predominant colour was grey, similar to the atmospheric temperature of 20°C. Furthermore, a spot meter (SP) was utilized to measure temperatures in the thermal image pixel at three different spots on the image. The specific temperatures detected were as follows: SP1 indicated a thermal signature of groundwater at 21.3°C from seepage zone 2, while the high wall exhibited temperatures ranging between 16°C and 19°C, correlating with SP2 and SP3, respectively. These temperature values indicated a distinct difference between the cooler temperatures observed on the high wall and the warmer temperatures at the groundwater flow area.

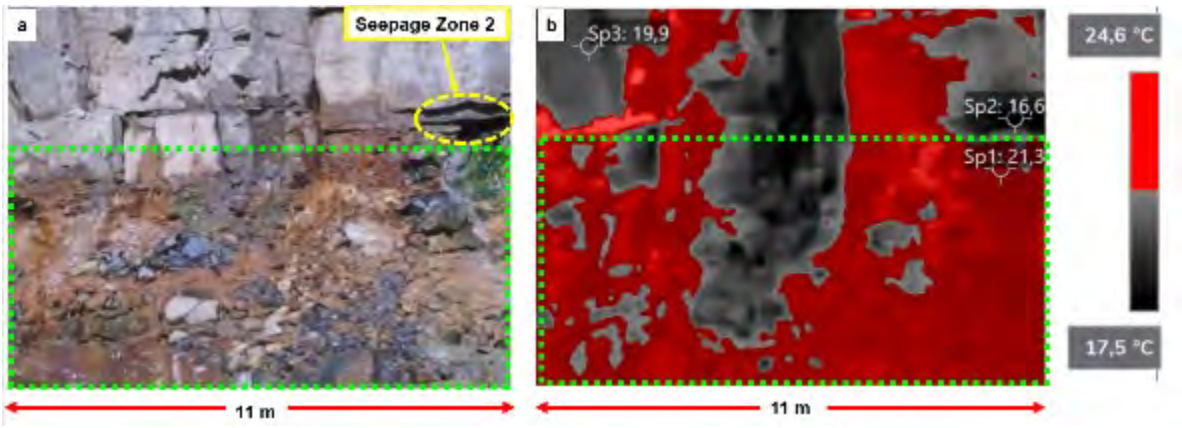

Figure 5-7 (a) Digital picture of the groundwater flow zone on the highwall (b) infrared thermal picture of zone of groundwater flow on the highwall (Maoyi et al. 2024).

5.3.3 Active infrared thermography

In the designated high wall area (Figure 5-4), active thermography was employed to significantly enhance the detection of subsurface anomalies, as outlined by Hung et al. (2009). This innovative method involved the introduction of colder water into the rock mass through a borehole using an external source. The detailed parameters for the infrared thermography experiments can be found in Table 5-2. Notably, each image included a precise temperature scale, ranging from a minimum of 10.0°C for darker colours to a maximum of 53.9°C for lighter colours. Additionally, each image also has a cold spot meter, which detects the coldest spot on the high wall to indicate significant thermal variations from the beginning to the end of the experiment.

Table 5-2 Infrared thermography parameters

Parameters	Values
Emissivity	0.95
Reflected temperature	33°C
Distance	25 m
Atmospheric temperature	33°C
Relative humidity	50%
Reference temperature	0°C

In Area 1, there was a slight variation in temperature, as shown in Figure 5-8. Throughout the experiment, there were minor temperature changes at different times. Although the coldest spot on the high wall (blue dot) moved at various times, indicating detectable temperature variations during the experiment, there were no changes in the flow path within the groundwater zone or the surrounding rock mass. The initial temperature in this area was 22.5°C. After pumping in colder water (approximately 3°C) into the borehole, the temperature of the rock mass decreased. Subsequently, the initial temperature rose to 23.1°C a minute later and then dropped by one degree. After ten minutes, the temperature stabilized at around 22.3°C before reaching a final temperature of 21.3°C.

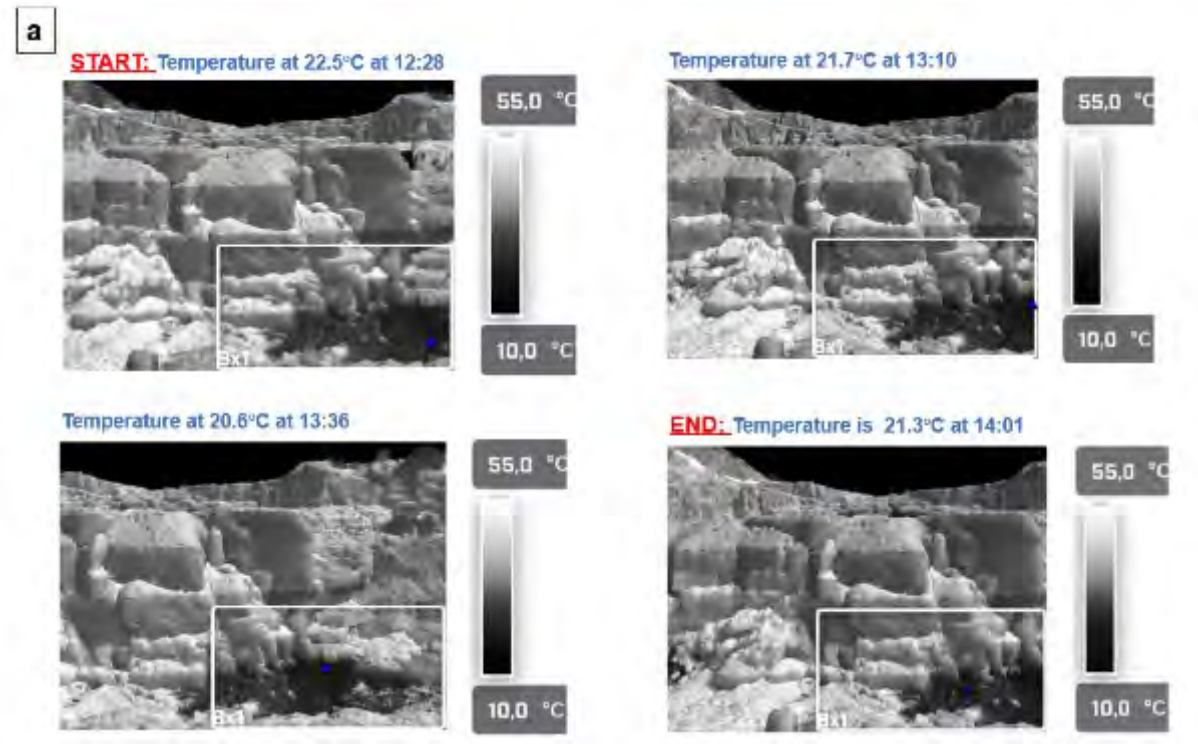

Figure 5-8 (a) Infrared thermography images of area 1 during active thermography experiments: blue spot on the high wall represents the coldest spot on each thermal image (photographed by Lotriet and Maoyi 2024).

In area 2 we observed significant temperature changes about 40 minutes after the start of the experiment. The results presented here focus on the area's notable temperature changes observed from that point onward. Furthermore, Figure 5-9 displays the thermal images corresponding to the temperature graph and indicates the infrared-detected flow behaviour path. These images show distinct thermal changes from the beginning to the end of the experiment, reflected in the temperature variation observed on the high wall. The coldest spot on the high wall (blue dot) indicates a temperature of around 26.7°C; however, it is essential to note that this is only a measurement, as no discernible visual changes in the rock mass were observed. About 4 minutes later (**13:18**), a temperature decreases of 3.9°C was recorded with irregular water spread at the bedding plane of seepage zone 1. Furthermore, by 13:29, the water had extended toward the right side, indicating an expanding wetting front towards area 1. Figure(d) summarises the experiment's conclusion with the constant temperature of 17.8°C with an increased wetted area.

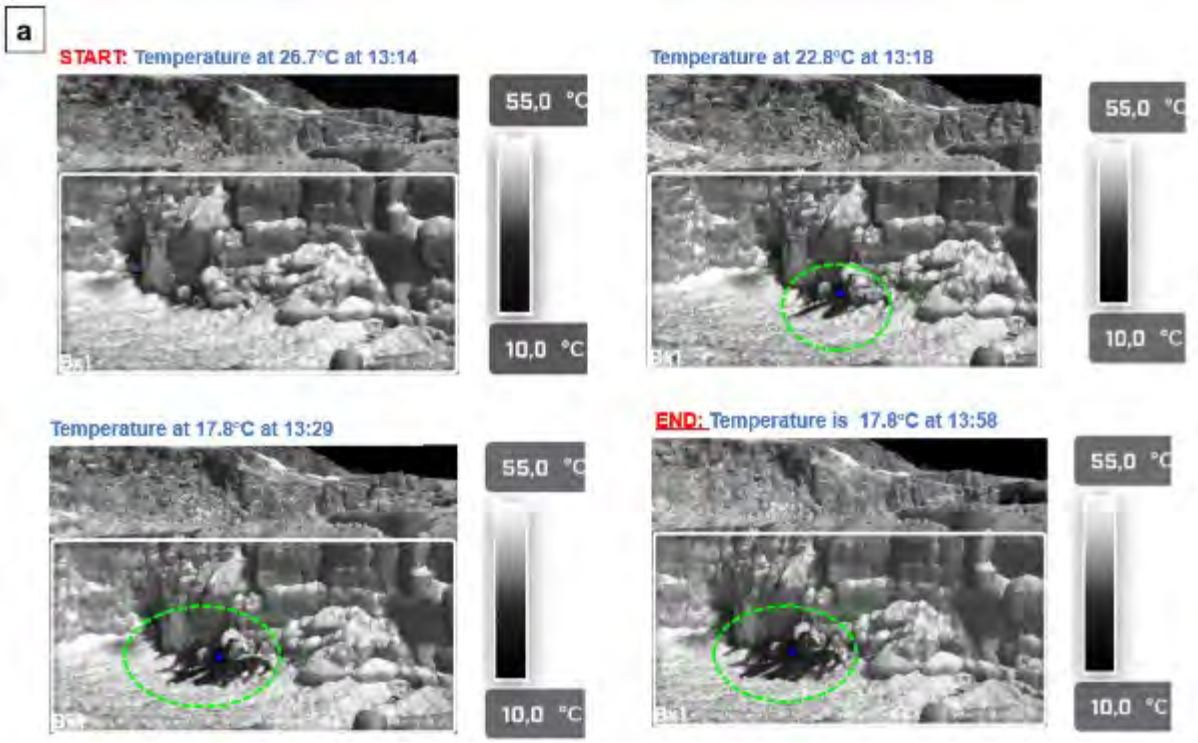

Figure 5-9 (a) Infrared thermography images of area 2 during active thermography experiments: the blue spot on the high wall represents the coldest spot on each thermal image (photographed by Lotriet and Maoyi 2024).

5.4 DISCUSSION

The rock mass in the southwestern high wall of the quarry has been categorised into four distinct domains based on discontinuity sets, geotechnical variances, groundwater flow, and weathering. The quartzite in this high wall is characterized by two sub-vertical joints and a bedding plane. A weak layer (~300 mm) oriented parallel to the bedding plane separates some quartzitic domains is described as a yellowish-brown, highly fractured, soft rock, weathered diabase. The slope orientation of this southwestern high wall is noted as moderately favourable to unfavourable due to discontinuity sets daylighting into the slope excavation.

Furthermore, the process of production blasting has led to the development of blast-induced fractures within the rock mass, thereby resulting in distinct joint spacing characteristics and a blockier configuration of the rock mass. The physical behaviour of a rock mass is primarily influenced by its discontinuities, and the consequences of blasting operations exhibit significant variations based on parameters such as rock mass strength, frequency and nature of discontinuities, type of explosion, as well as the direction and intensity of the stress wave. Consequently, these factors can create flow paths that influence groundwater dynamics and alter groundwater flow patterns due to anthropogenic activities such as blasting (Pusch 2016).

The massive rock mass in domain 1 transitions abruptly to domain 2, where it exhibits a blocky nature; a subvertical fault delineates this transition. Additionally, domain 2 encompasses a notable natural groundwater seepage zone, with groundwater flowing at the interface between the weathered diabase and quartzite. Additionally, the natural groundwater zone is classified as flowing based on rock mass classifications (Bieniaskwi 1979; 1989) and this the only geotechnical domain where there is continuous groundwater flow in the pit. Furthermore, the interstitial region (10 m) of this seepage zones is consistently wet, illustrating the significant influence of geometric complexities on flow anisotropy. Upon exiting the discontinuity, the water creates preferential flow paths, either parallel or perpendicular to the flow direction. Consequently, due to these

preferential flow paths, the water can re-wet existing flow paths, form new ones, or merge existing flow paths as the wetting front on the rock surface increases (Maoyi 2019).

Discontinuity sets can be well-defined, but the quantitative rock mass permeability data needs to be further detailed (backed) by flow path geometry. Subsequently, active and passive thermography techniques were used in the natural groundwater seepage zone and the surrounding rock mass to detect the flow patterns in the high wall. The experimental results indicated that both active and passive thermography techniques could detect saturation on the rock face (i.e., area 1). Furthermore, the natural groundwater seepage zone consistently exhibited a distinct thermal signature that remained identifiable on the rock faces regardless of weather conditions. However, the application of infrared thermography to detect flow paths in the natural groundwater zone proved to be ineffective. This ineffectiveness can be attributed to two primary factors: first, the observed lack of flow paths due to rock mass conditions.

The natural seepage occurs within geotechnical domain 2, which is characterised by a blocky rock mass. The seepage zone exhibits continuous groundwater flow and is adjacent to geotechnical domain 1, characterised by a massive rock mass. The fault delineating these geotechnical domains may act as a flow boundary because the 3D photogrammetric model showed that discontinuity sets in domain 3 do not persist (extend) into domain 2, resulting in no observed flow between these two geotechnical domains. Thus, fluid flow in fractured media may be primarily limited to highly transmissive fracture networks surrounded by a low-permeability rock matrix (Hyman 2020). Secondly, the natural groundwater seepage zone was already cooler than the high wall before starting the active infrared experiments. Therefore, pumping water at a much lower temperature than 3 °C into the borehole may have been necessary to detect this source as it flows out of the discontinuity, as infrared visuals depend on sensitivity.

In addition, while conducting active infrared monitoring of the high wall, an additional outflow location was detected in close proximity to the natural seepage area. The flow pattern was only detected 40 minutes into the experiment, suggesting that water was still finding new paths to flow through the high wall's blasted fracture network. The temperature graph also showed a gradual decrease in this particular area, indicating overall thermal changes in the rock mass. These findings are consistent with the rock mass conditions, which have a blockier structure due to blasting effects but still allow water to exit at a different location from the natural groundwater seepage zone.

It's important to thoroughly understand the rock mass characteristics in this area to accurately compare the thermal analysis findings. The data shows that the rock mass is blocky and relies on specific fractures and the connectivity of the discontinuities. Other factors, like roughness, also affect the flow mechanisms and regimes are important for a more detailed analysis of this research, which is beyond the scope of this case study.

5.5 REFERENCES

Bieniaskwi ZT. (1979). The geomechanics classification in rock engineering applications. Proceedings of the 4th international Conference on Rock Mechanics. Montreux. Balkema. 2: 41-48.

Bieniawski ZT. (1989). Engineering rock mass classifications. John Wiley and Sons, Inc

Forlani G, Diotri F, Cella UM, Roncella R. (2019). Indirect UAV Strip Georeferencing by On-Board GNSS Data under Poor Satellite Coverage. Remote. Sens. 11 :1765.

ISRM [International Society for Rock Mechanics]. (1981). Rock Characterisation, Testing and Monitoring. Brown, E. ed. Pergamon Press.

Herraiz ÁH, Marugán AP, Márquez FPG. (2020). A review on condition monitoring system for solar plants based on thermography. Non-destructive testing and condition monitoring techniques for renewable energy industrial assets. 103-118.

Hung YY, Chen YS, Ng SP, Liu L, Huang YH, Luk BL, Ip RWL, Wu CML, Chung PS. (2009). Review and comparison of shearography and active thermography for nondestructive evaluation. Materials Science and Engineering: R: Reports, 64(5-6):73-112.

Hyman JD. (2020). Flow channeling in fracture networks: characterizing the effect of density on preferential flow path formation. Water Resources Research, 56(9).

Maoyi, M. (2019). Geometric controls on partially saturated flow through natural rock fractures. University of Pretoria (South Africa).

Maoyi M. 2026. The use of Infrared Thermography to enhance the characterisation of unsaturated flow through fractured rock mass. PhD thesis. University of Pretoria

Mineo S, Pappalardo G. (2016). The Use of Infrared Thermography for Porosity Assessment of Intact Rock. Rock Mechanics and Rock Engineering 49: 3027-3039.

Pusch R, Popov V, Adey R, Peratta A. (2016). Rock structure control of groundwater flow and stability–disposal of hazardous waste in abandoned mines. Engineering Geology.

Riquelme AJ, Abellán A, Tomás R, Jaboyedoff M. (2014). A new approach for semi-automatic rock mass joints recognition from 3D point clouds. Computers & Geosciences, 68: pp.38-52.

Tung WY, Nagendran SK, Ismail MAM. (2018). 3D rock slope data acquisition by photogrammetry approach and extraction of geological planes using FACET plugin in CloudCompare. In IOP conference series: earth and environmental science 169 (1): 012051. IOP Publishing.

Yeh PT, Lee KZZ, Chang KT. (2020). 3D Effects of permeability and strength anisotropy on the stability of weakly cemented rock slopes subjected to rainfall infiltration. Engineering Geology (266): 105459.

CHAPTER 6: FRESH ROCK GRANITE WEATHERING RIMS

Author: Leandi Bruyns

This chapter emanates from the following project-related outcomes:

- Bruyns L. 2024. Characterisation of the weathering propagation from joint surfaces in different rock types. MSc (specialising in Engineering Geology) Dissertation. Department of Geology. University of Pretoria.

6.1 RATIONALE

This study delves into the intricate impact of propagating weathering on the adjacent rock material within joints and fractures, and it specifically examines how the progression of weathering induces changes in the hydro-mechanical behaviour of the rock material, and how these transformations may influence the overall engineering response of a rock mass.

The meaningful influence of propagating weathering on the shear strength of discontinuities is important in dictating the natural behaviour of rocks, particularly in terms of stability. An accurate assessment of the shear strength of discontinuities stands as a necessary component in formulating suitable designs for slopes and cavities (Buocz et al., 2014).

Porosity emerges as an important factor in the weathering process that not only wields control over the weathering mechanism, but also subjects it to alteration by the process itself (Ballesteros et al., 2010). This highlights the significance of porosity as a key parameter to scrutinize in this study. The investigation encompasses an exploration into how porosity is impacted by weathering and how this, in turn, leads to consequential changes in other parameters such as adsorption and shear strength.

This study investigates changes in physical, mineralogical, and textural properties of rock with increasing distance from the joint surface into the adjacent parent material. Physical properties were determined using a Schmidt hammer test, providing a rebound number (R-value). Mineralogical and textural analyses employed thin sections, Scanning Electron Microscopy (SEM), X-Ray Fluorescence (XRF), and X-Ray Diffraction (XRD) (Ismail et al., 2019).

The research questions include the following:

- Are the classification systems currently in place satisfactory and accurate as to what it represents in reality?
- Which features dictate the depth to which weathering processes propagate?
- How does propagating weathering influence the hydro-mechanical and engineering properties of the rock material adjacent to joints, fractures, and other exposed surfaces?

The objectives for this study are as follows:

- Understand the process of weathering and determine the extent to which this process can change the hydro-mechanical, chemical, physical, and engineering properties of both rock material and rock masses.
- Study discontinuity properties and how weathering has impacted these properties over time.
- Determine the influence of propagating weathering on the porosity, permeability, and water absorption ability of the rock material adjacent to exposed surfaces.

- Highlight the importance of taking the effects of weathering on rocks and rock masses into account, not only prior to construction but during construction and post-construction as well, since weathering is a constant and inescapable process.

This study proposes that propagating weathering significantly alters the hydro-mechanical and engineering properties of rock material adjacent to joints, fractures, and other exposed surfaces, which emphasises the need to consider weathering effects throughout construction and post-construction phases. Specific geological features such as mineral composition and fracture density are hypothesised to dictate weathering depth. Existing rock classification systems may inadequately represent the complex relationship between weathering processes and rock properties. It is further hypothesised that propagating weathering modifies the properties of rock material near discontinuities, leading to variations in porosity, permeability, and water absorption capacity. Understanding these dynamics is important to improve construction practices and ensure the long-term stability of engineering structures.

6.2 PROBLEM STATEMENT

Weathering remains a very poorly understood concept and lacks in-depth documentation. The propagation of weathering into the adjacent rock material from joints and other discontinuity surfaces has not been well documented, leading to a gap in the Engineering Geology industry. Specifically, how this propagation affects the hydromechanical and other engineering properties of both the adjacent material and the entire rock mass. An important note, raised by Hack (2020), is that the quantity of weathered material adjacent to joints does, in fact, not need to be significantly large to have a major influence on the geotechnical properties of a rock or rock mass. Weathering of rock masses is mainly focused along fractures and other discontinuities present within the rock mass, predominantly due to fluid flow. Discontinuities present in rock masses have a significant influence on the engineering behaviour of a rock mass (Bell, 1992), thus resulting in the necessity to study and understand the changes caused by weathering along these discontinuities (Ismail, et al., 2019).

6.3 METHODOLOGY

The methods were performed during this study with the aim to obtain physical and mineralogical characteristics of the rock samples. The rock samples include the following samples:

1. Quartz-Diorite (Nelspruit Suite)
2. Quartz-Diorite (Nelspruit Suite)
3. Granite (obtained from samples available at the University of Pretoria’s geology storage unit)
4. Shale (Pretoria Group, Silverton Formation).

The methods used during this study include the following:

1. X-Ray Diffraction (XRD)
2. X-Ray Fluorescence (XRF) spectroscopy
3. Weathering Indices (CIA, MIA, CIW, and PIA)
4. Joint Compressive Strength (JCS) and Joint Roughness Coefficient (JRC)
5. Microscopy (thin sections)
6. Scanning Electron Microscopy (SEM).

To provide more details on the methods and the outcomes, only Granite is presented here.

6.4 VISIBLE CHARACTERISTIC OF THE WEATHERED BRIM AND OTHER FEATURES

In Figure 6-1(a) to (d) hand specimen 1 showed a weathering rim of approximately 1.1 cm in depth. The weathering rim can be divided into three weathering zones. Zone 1 is represented by the outer edge of the sample, and this zone was yellowish light brown in colour, and almost white, ranging in thickness from 3 mm to 5 mm. Zone 1 featured a porous to soil-like texture. Zone 2 was approximately 2-3 mm in width and the grains were slightly more cemented compared to those of Zone 1. Zone 2 had a yellowish-orange hue, thus appearing darker than Zone 1. Zone 3 had a reddish-dark brown colour and had a similar texture to the unweathered, central portion of the hand specimen.

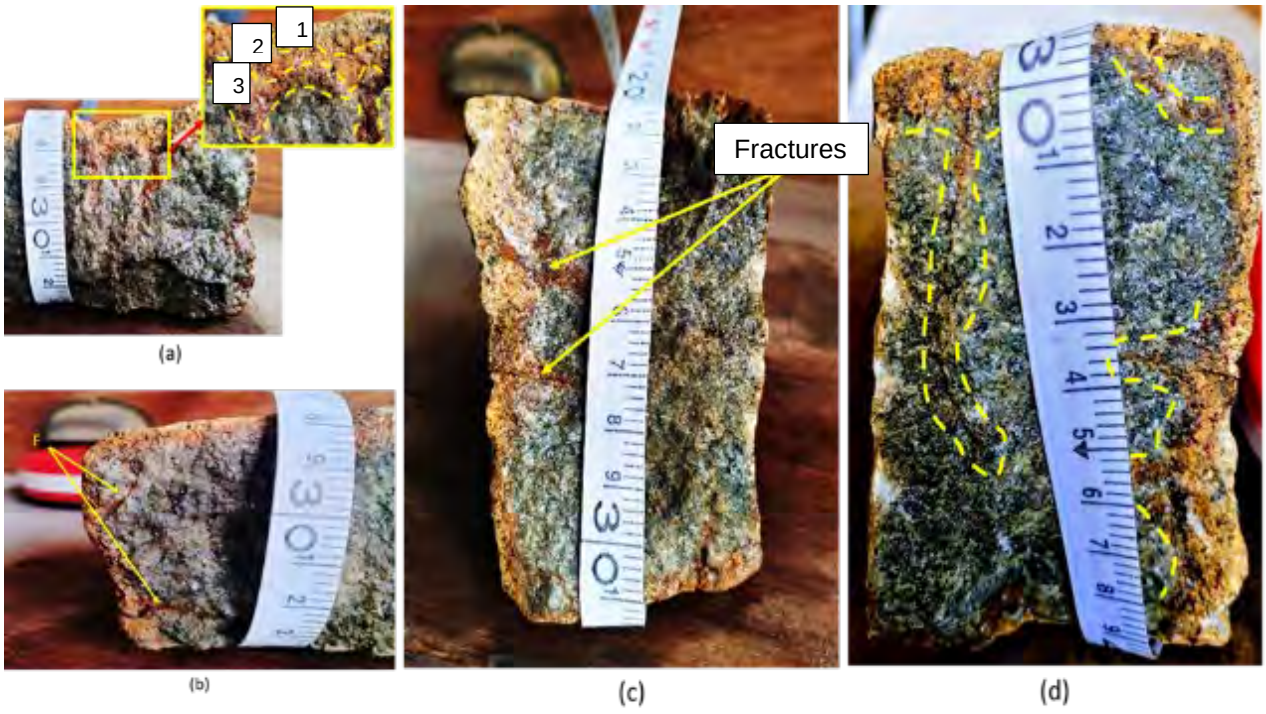

Figure 6-1 Hand specimen 1 showing (a) propagating weathering rim zones; (b and c) visible fracturing starts at the edge of the specimen; and (d) propagation of weathering into rock material adjacent to fractures.

The third zone had a width of approximately 3 mm. Upon further examination, fracturing was observed starting at the surface of the specimen and propagating deeper into the central, unweathered zone of the specimen, shown in Figure 6-1(b-c). The fractures were created as a result of progressive weathering and are responsible for the overlapping of the three weathering zones in some areas of the weathering rim. Propagation of weathering into the adjacent material of the fractures was clearly visible in the form of discolouration as shown in Figure 6-1(d). This discolouration is similar to that of zones two and three of the weathering rim.

6.5 STRENGTH

The results from the Schmidt hammer test can be seen in Table 6-1. The results indicate a recognisable difference between the R-values of the fresh intact rock and the rock material adjacent to the weathered surface.

During the Schmidt hammer test on the unweathered portion of the hand specimen, an average R-value of 29.56 was found. The average R-value for the rock material adjacent to the weathered surface is 14.13. Thus, the R-value or JCS of the rock material is lower, closer to the weathered surface, compared to that of the

unweathered portion of the hand specimen. While performing the Schmidt hammer test, a portion of the hand specimen broke off. This break has taken place along a pre-existing fracture and exposed a part of the hand specimen not previously visible. This newly exposed surface can be seen in Figure 6-2(a-b).

Table 6-1 Schmidt hammer results (R-values) for fresh intact rock and rock material adjacent to the joint

R-Value for fresh/Unweathered Rock	R-Value for rock material adjacent to exposed surface
19.5	11.0
35.0	11.5
27.5	23.0
36.5	17.5
26.0	13.5
29.5	11.0
35.0	15.0
27.5	10.5
Average: 29.56	Average: 14.13

In Figure 6-2 (a) there are four zones visible; however, there was some overlap between these zones. The outer layer, which is labelled as zone 1, is similar in colour and texture to that described previously in Figure 6-2. Zone 2 also possesses similar characteristics to those of zone 2 shown in Figure 6-2 (a). The third zone in Figure 6-2 (a) has a rust-like appearance. This zone (3rd) overlapped with both the 2nd and 4th zones. Zone 4 is dominated by a black-coloured mineral. Upon closer examination, the black mineral was present in zone 3 as well, but to a lesser extent. Fracturing was present in the top-right corner of the sample (Figure 6-2(b)). The fracturing originated at the weathered surface and propagated deeper into the adjacent rock material. The rock material adjacent to these fractures had a similar colour to that of the zone indicated in Figure 6-2(b) (yellow outlining).

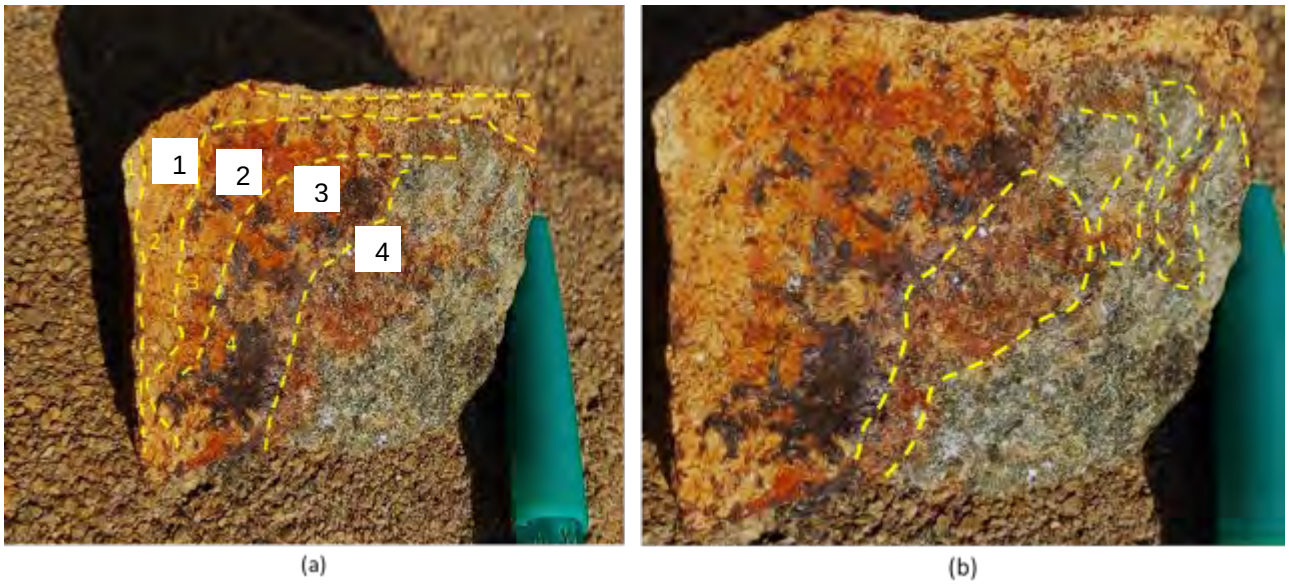

Figure 6-2 (a) Newly exposed surface with 4 zones separated based on colour; (b) fracturing in the top-right corner of the newly exposed surface and a zone similar in colour to the material adjacent to the fracturing.

6.5.1 THIN SECTION ANALYSES

The thin sections were orientated perpendicular to the joint or weathered surfaces of the samples. This allowed for the visibility of propagating weathering into the rock material adjacent to the joint and/or the exposed surface.

6.5.2 Exposed Surface

This section shows images captured at and near the exposed surface of the granite sample. Figure 6-3(a)-(d) show the exposed surface at 2.5 magnification in PPL as follows:

a) Discolouration along the fracture on the right and propagation of alteration originating at the fracture surfaces. Discolouration predominantly affects orthoclase and plagioclase. The darkening of mineral grains is visible on the left side of the thin section. This process originates at the exposed surface of the sample. An open pore space is also visible and has a size of approximately 1001µm.
b) The sizes of the rust-coloured minerals at and near the exposed surface are as follows: 285 µm, 384 µm, and 1482 µm. A large pore space is also visible in this image. Discolouration and staining can be seen around the large reddish-brown mineral. Signs of alteration can also be seen on the left side of the image. Quartz grains show the least amount of change compared to the other minerals present.
c) A large amount of darker coloured minerals is present in the weathered zone of the sample. Discolouration is present along fractures and on the surface of most minerals, with Quartz grains showing the least amount of discolouration and fracturing.
d) This image shows yellow staining along grain boundaries and fractures within the feldspar grains, predominantly. This is a clear sign of alteration at the exposed surface of the sample. Significant fracturing is also visible in this region of the thin section.

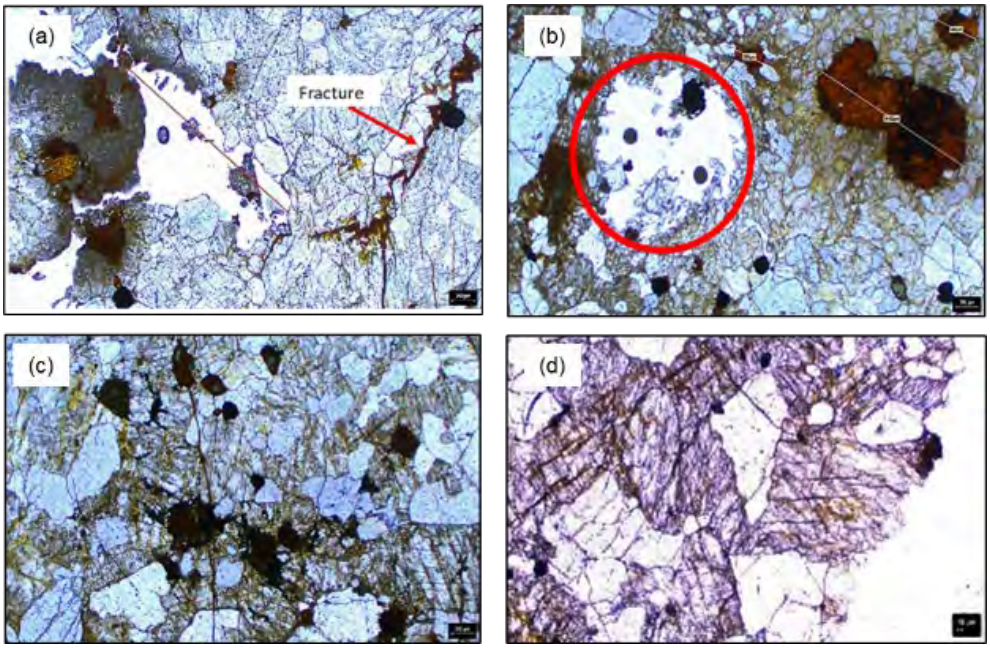

Figure 6-3 Exposed surface of granite.

6.5.3 Transitioning Zone

This section contains the images captured of the transitioning zone between the weathered and fresh portions of granite at x2.5 magnification in PPL (Figure 6-4):

a) The transition from the weathered to less weathered portion is visible in this image with yellow staining present at the bottom of the image and the portion with less yellow staining at the top of the image. Fracturing and discolouration of the darker minerals are still present in the upper portion of the image, which indicates that the lack of a change in colour does not mean that weathering has not affected the visibly unchanged portion of a rock. Thus, proving that discolouration cannot be the deciding factor when determining the degree of weathering.
b) This image shows the transition between weathered and less weathered zones of the thin section. Discolouration (brown) can be seen along fractures and yellow staining is present, predominantly in the lower portion (weathered zone) of the image.
c) This image is taken at the edge of the weathered zone (bottom right). Pore spaces are present in this image; however, these spaces are smaller compared to the pore spaces closer to the exposed surface. Alteration in the upper region of the image can be seen through the discolouration of the darker minerals and along the fracturing. The degree of fracturing is significantly less in the upper (less weathered) portion of the image.

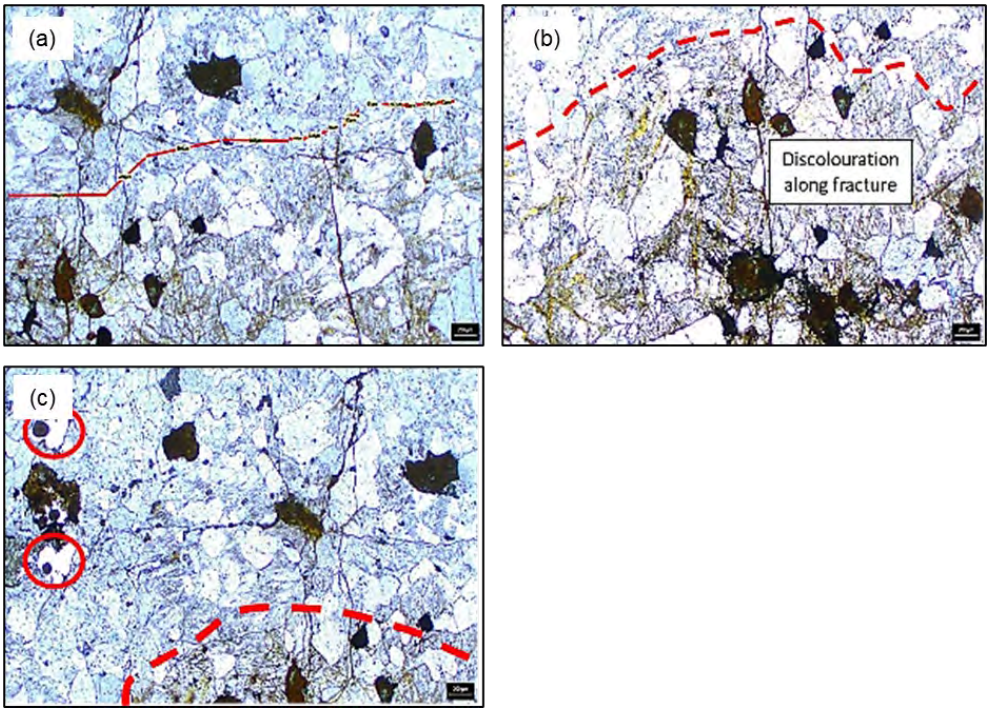

Figure 6-4 Transitioning Zone between weathered and less weathered portion

6.5.3.1 Unexposed Surface

This section contains images captured of the unexposed portion granite. These images can be found in Figure 6-5(a-b).

a) The unexposed surface is shown in this image. Notice the lack of discolouration.
b) The size of the darker minerals closer to fresh surface range from 315µm to 589µm.

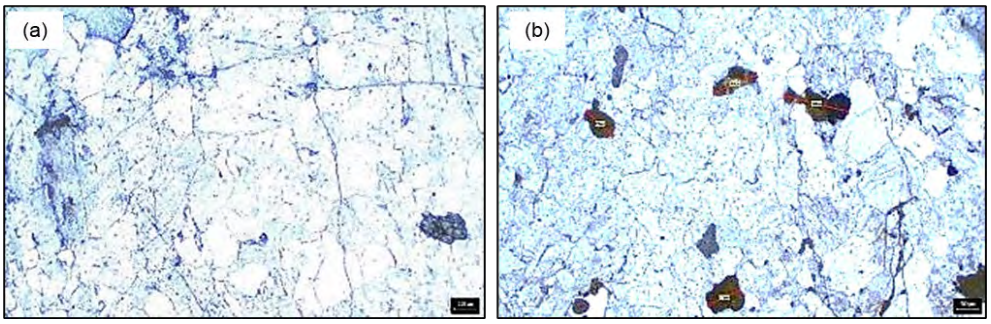

Figure 6-5 Unexposed surface in XPL (a) and PPL (b) at 2.5x magnification.

Figure 6-6(a) to (b) shows the unexposed surface in both XPL (a) and PPL (b) at 2.5x magnification.

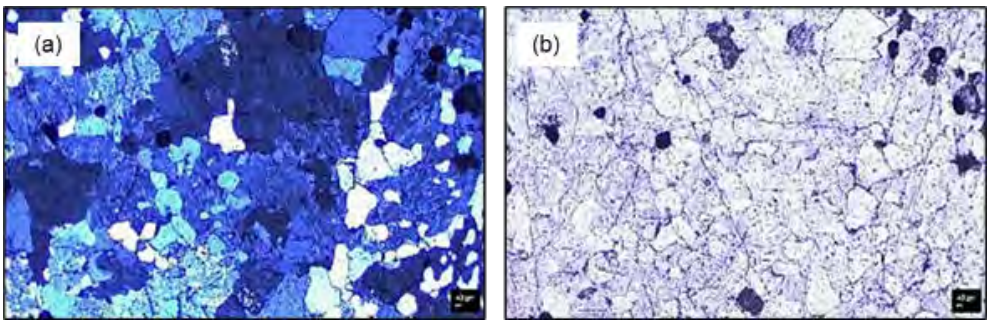

Figure 6-6 Unexposed surface in XPL (a) and PPL (b).

6.6 SEM RESULTS

In preparation for the SEM analysis, the thin sections were carbon coated. In this section, the images captured during the analysis of granite are shown. The exposed surface is shown in Figure 6-7(a) – (b):

(a) This image was taken at 2.00 K magnification. Textural evidence of alteration can be seen. A high degree of fracturing is noted as well as pore spaces within the grains. Iron-Oxide minerals are present on the surface of most of the grains in this image and are concentrated along the boundaries of these mineral grains. Mineral structures have been distorted and changed due to the process of propagating weathering.

(b) Fracturing and alteration along these fractures prevail in the exposed region of the sample. Fracturing takes place within and in between grains. This image was taken at 100 K magnification.

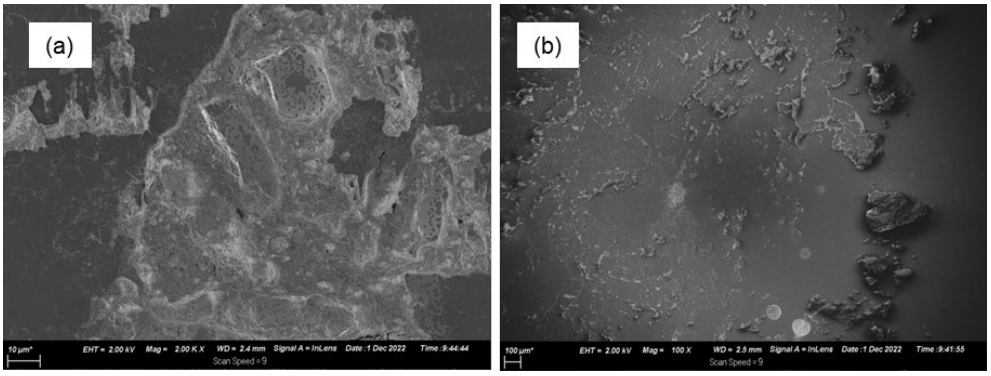

Figure 6-7 SEM images of exposed surface

The unexposed surface is shown in Figure 6-8(a) – (d):

(a) A pore is visible in the upper right corner of the image (left). Alteration can be seen surrounding this pore. A lack of micro-fractures can be seen as the distance from the pore is increased. Slight alteration along grain boundaries can be observed. This image was taken at 7.00 K magnification.
(b) Alteration is present in the form of discolouration and limited fracturing along grain boundaries. This image (left) was taken at 102 K magnification.
(c) Alteration can be seen in the form of discolouration and slight fracturing along grain boundaries. The image on the left has been taken at 100 K magnification.
(d) This image was taken at 100 K magnification. An open pore space is presented in the centre of the image and is surrounded by a rim of altered material. The light-coloured regions indicate the presence of Iron-oxide minerals, which is a sign of weathering taking place in this region.

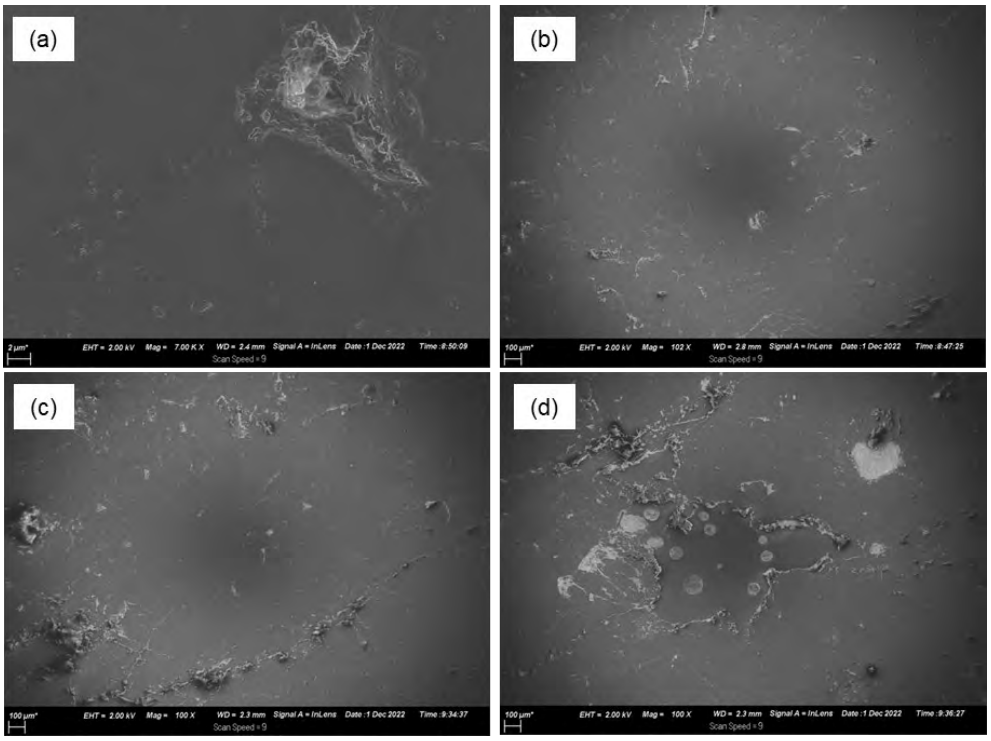

Figure 6-8 SEM images of unexposed surface.

6.7 X-RAY DIFFRACTION RESULTS

The samples were analysed using a PANalytical X'Pert Pro powder diffractometer in θ–θ configuration with an X'Celerator detector and variable divergence- and fixed receiving slits with Fe filtered Co-Kα radiation (λ=1.789Å). The results from the X-Ray Diffraction (XRD) analyses (Table 6-2**.**) shows a summary of the X-Ray Diffraction results for the granite sample.

Table 6-2 Quantitative XRD results

Lab sample code	Rock Type	Quartz (%)	Plagioclase (%)	Orthoclase (%)	Muscovite (%)
LB2	Granite	32.8	31.5	35.8	0.0

Based on the XRD results, LB2 can be characterised as a granite. The QAP- diagram indicating the rock type based on the XRD results is shown in Figure 6-9.

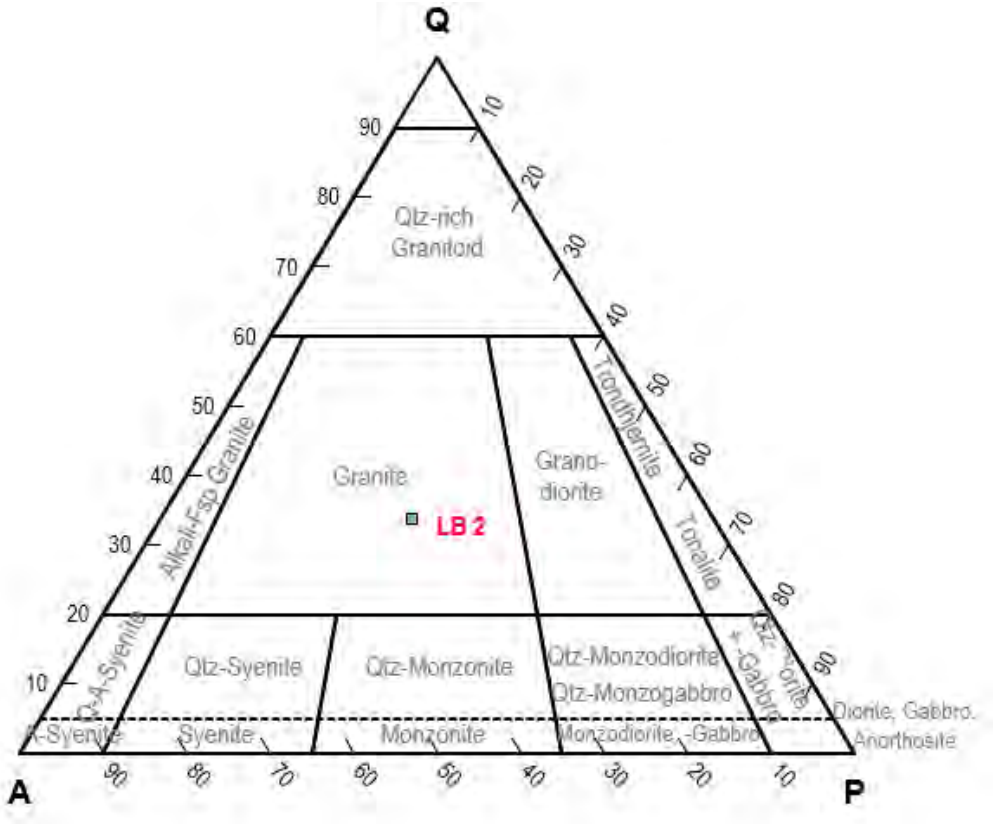

Figure 6-9 QAP plot for Igneous rock sample LB2.

6.8 X-RAY FLUORESCENCE RESULTS

Table 6-3 shows the XRF results for the granite sample. The results are plotted on a graph in Figure 6-10.

Table 6-3 Major element XRF analyses

Elements	Granite
SiO_2	74.41
TiO_2	0.276
$Al2O_3$	11.43
Fe_2O_3	4.2
MnO	0.054
MgO	0.02
CaO	0.615
Na_2O	2.85
K_2O	5.05
P_2O_5	0.01
Cr_2O_3	0.006
L.O.I	0.89
Total	99.78
H_2O^-	0.64

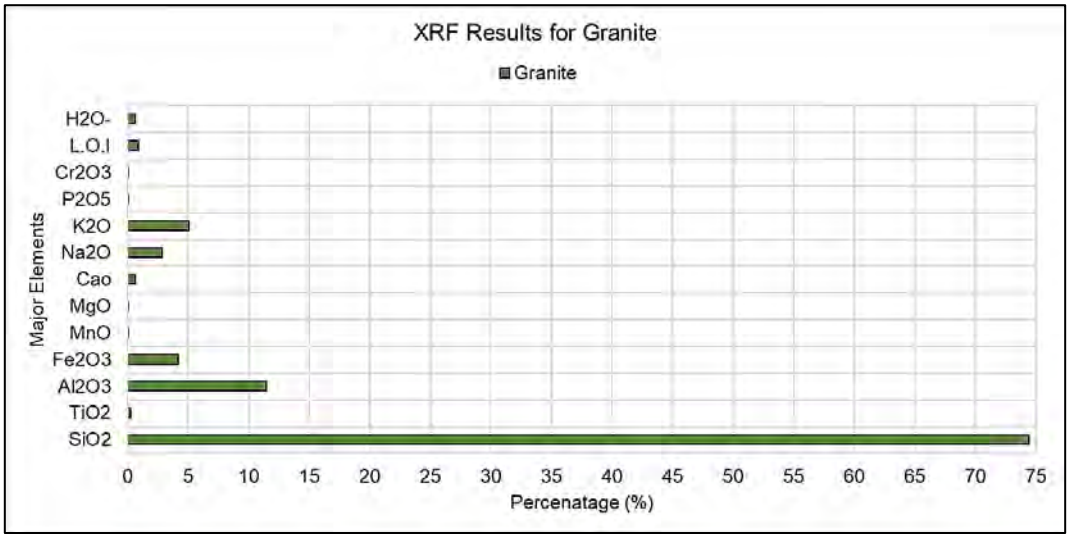

Figure 6-10 Major element percentages for granite.

The correlation between K_2O and Al_2O_3 (Figure 6-11(a)) serves as an indicator of the degree of weathering within the rock sample. Higher K_2O content typically reflects less weathering of feldspar minerals. In contrast, the ratio of Fe_2O_3/SiO_2 vs Al_2O_3/SiO_2 (Figure 6-11(b)) provides insight into the mineralogical composition, particularly highlighting the relative abundance of iron oxides and silicate minerals. These ratios can reveal changes in mineralogical phases and geochemical processes affecting the rock (Alqahtani & Khalil, 2021).

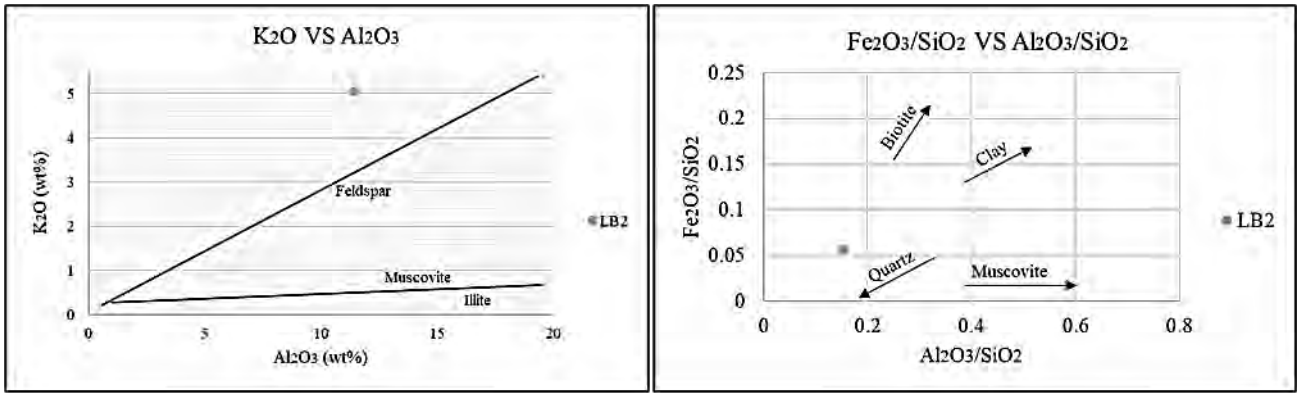

Figure 6-11 (a) K_2O vs Al_2O_3 for LB2 (granite) (Alqahtani & Khalil, 2021).(b) Fe_2O_3/SiO_2 vs Al_2O_3/SiO_2 for LB2 (granite) (Alqahtani & Khalil, 2021).

LB2 plots well within the feldspar region, indicating weak weathering. LB2 contains an exceptionally high proportion of quartz (SiO_2), which makes this sample highly resistant to weathering.

Figure 6-12 indicates the Tertiary diagram of Al_2O_3-(CaO+Na_2O)-K_2O, which was used to establish the degree of weathering LB2, with the CIA shown on the vertical axis. LB2 falls within the weak weathering zone.

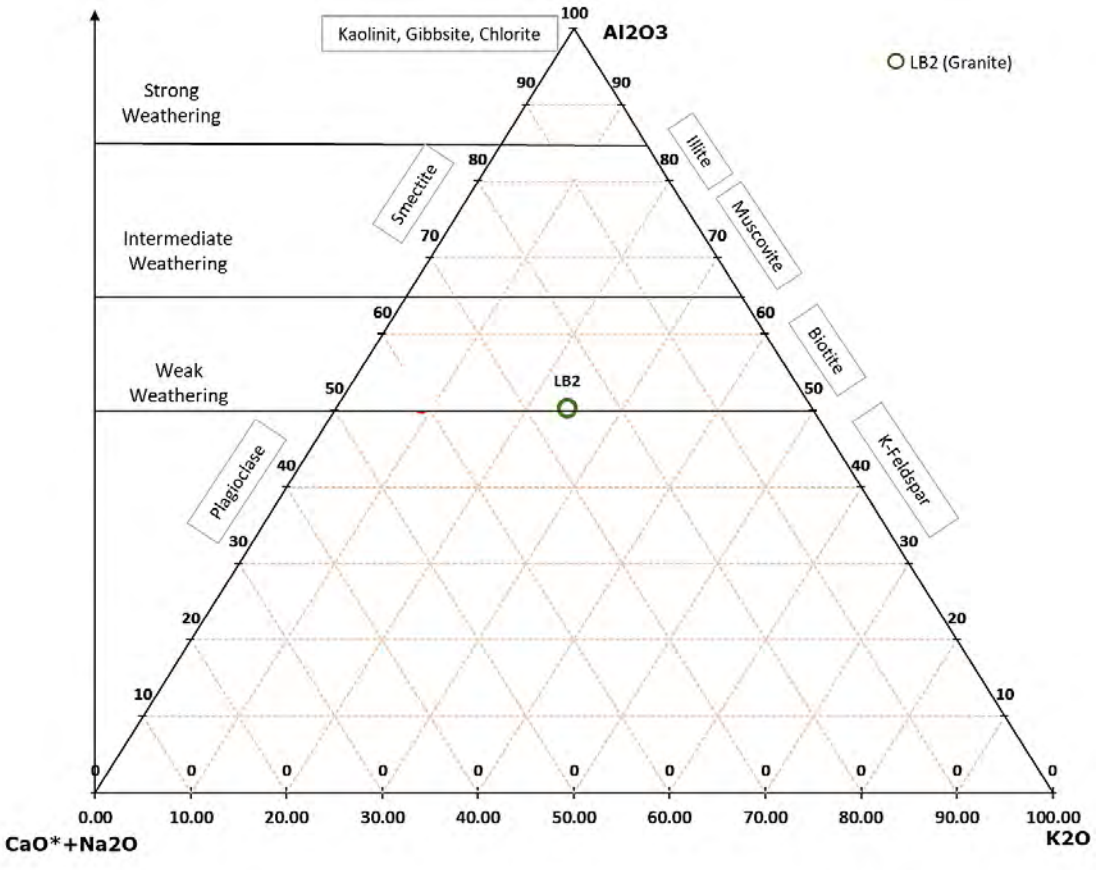

Figure 6-12 Ternary diagram of Al_2O_3-(CaO+Na_2O)-K_2O to obtain the degree of weathering for LB2 with the CIA shown on the vertical axis (Alqahtani & Khalil, 2021).

A summary of all weathering indices results can be found in Table 6-4.

Table 6-4 Calculated CIA, PIA, CIW, MIA percentages for Granite

Parameter	LB2 (Granite)
CIA (%)	50.40
PIA (%)	50.77
CIW (%)	66.40
MIA (%)	0.80

6.9 SUMMARY OF RESULTS

A summary of the results for granite can be found in Table 6-5.

A comparison between the decreased strength and the Chemical Index of Alteration (CIA) for granite is shown in Figure 6-13. A linear relationship can be seen between these parameters.

The relationship between the decreased strength, the chemical composition (SiO_2, Al_2O_3, and Fe_2O_3) and the water content within the granite sample is graphically presented in Figure 6-14. The granite sample showed high SiO_2, which represents the quartz content, and low Al_2O_3, and Fe_2O_3 percentages. This combination resulted in a relatively low, but still significant difference between the unweathered and weathered portions of the sample.

Table 6-5: Summary of results for granite.

Feature	Granite
Depth from surface	N/A
Number of weathering zones	3
Depth of discolouration	1.1cm
Minerals at surface	Fe-Oxides Quartz
Average JCS (fresh) R-Value	29.563
Average JCS (rim) R-Value	14.125
Difference between R-Values	15.438
Degree of Weathering	Slight to Moderate
Average Size of Quartz Grains @Exposed Surface	±600µm
Average Size of Quartz Grains within Unexposed Surface	±1000µm
Average size of open pore spaces @Exposed surface	1001µm
Average size of open pore spaces @Unexposed surface/Transitioning Zone	±300µm
Maximum Size of Fe-Oxides @Exposed Surface	1482µm
Maximum Size of Fe-Oxides @Unexposed Surface	589µm
Signs of Alteration @Exposed surface	Fe-Oxides present. Yellow staining along grain boundaries. Clay/Fe-Oxide minerals withing large fractures.
CIA (%)	50.40
PIA (%)	50.77
CIW (%)	66.40
MIA (%)	0.80
Degree of Fracturing (SEM/Thin section)	Moderate

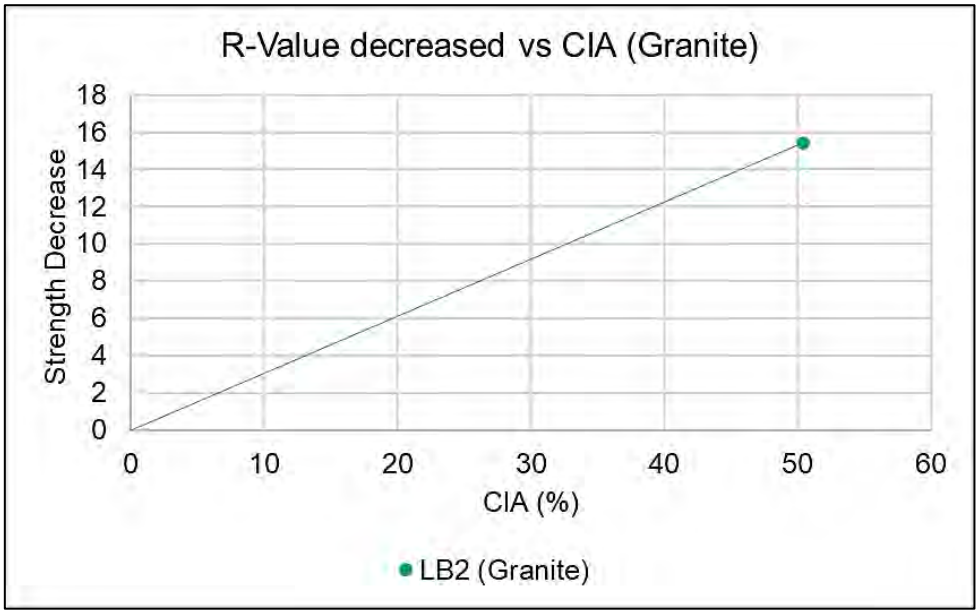

Figure 6-13: Strength decreases and CIA comparison for granite.

A linear relationship can be seen between the CIA and depth of propagating weathering in Figure 6-15.

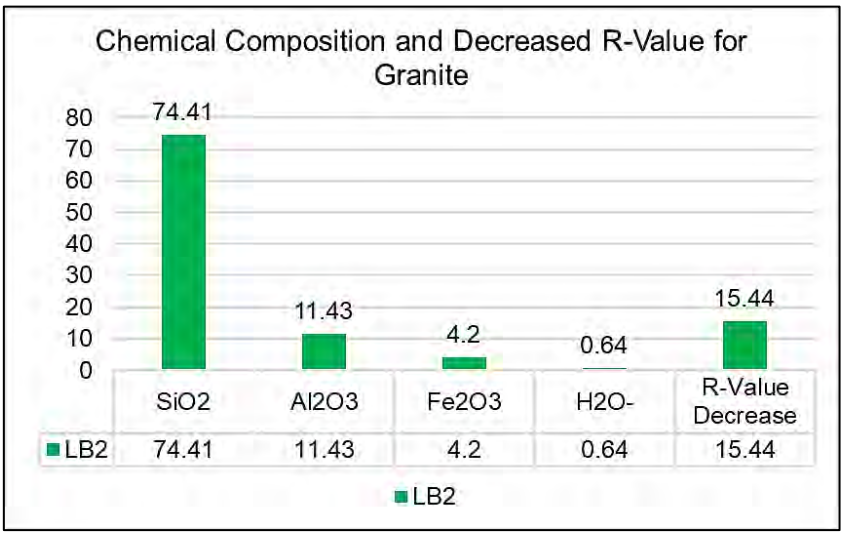

Figure 6-14: Strength decreases compared to water content and chemical composition.

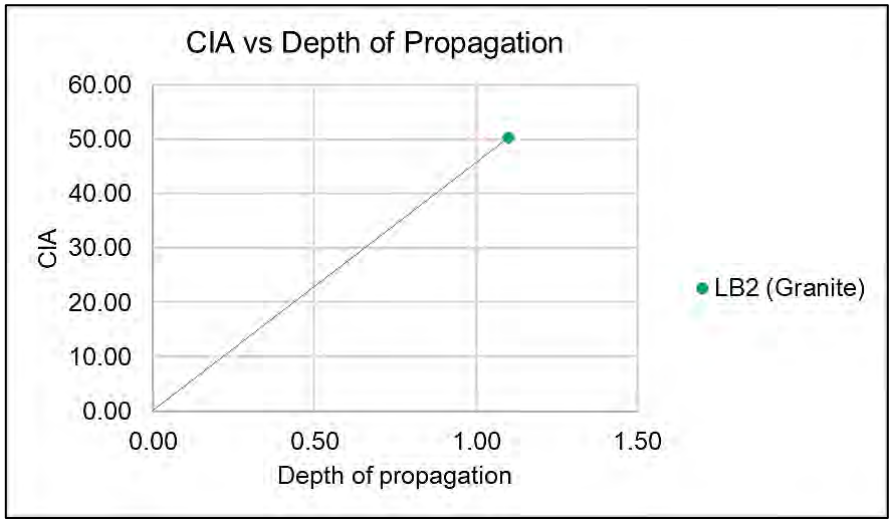

Figure 6-15: Depth of discolouration compared to the CIA for granite.

6.10 OUTCOMES AND WAY FORWARD

Petrographic analysis revealed clear weathering effects at the rim and adjacent rock material of the samples. Fractures, originating at the exposed surfaces, are attributed to weathering processes, with further discoloration and weathering advancing along these fractures, highlighting their role as primary pathways for weathering propagation.

The thin sections indicated a decrease in discolouration as the distance from the exposed surface was increased, but fracturing along grain boundaries and across mineral surfaces remained beyond the point of discolouration. Thus, indicating that the process of weathering had propagated further into the unexposed portion of the rock with no evidence visible to the naked eye.

The weathering indices indicated that Granite experiences little chemical weathering. When comparing the decreased R-values with the amount of quartz (SiO_2) within the sample, it was observed that Granite showed minimal difference between the R-values of the unweathered portion and the rock material adjacent to the exposed surface. This indicates that propagating weathering had little impact on the strength of the material, and the high quartz content aided in this resistance along with the low Al_2O_3 and Fe_2O_3 weight percentages within the granite. A linear relationship was observed between the amount of H_2O and the total decrease in the R-values for LB2 (Granite). Granite showed a linear relationship between the degree of weathering and the depth of visible propagation of weathering.

For the future, the porosity and permeability of the rock material adjacent to an exposed surface need to be studied in more detail through the use of the Capillary Pressure Mercury System (CPMS). A link between the shear strength of a joint and the porosity of the material adjacent to the joint surface could be established in further studies. The effect that propagating weathering from a joint surface has on the flow velocity and flow pattern of fluids also need to be looked at in future works.

6.11 REFERENCES

1. Alqahtani, F. & Khalil, M., 2021. Geochemical analysis for evaluating the paleoweathering, paleoclimate, and depositional environments of the siliciclastic Miocene-Pliocene sequence at Al-

Rehaili area, Northern Jeddah, Saudi Arabia. Arabian Journal of Geosciences, 14, p.239. Available at:< https://doi.org/10.1007/s12517-021-06538-0>.

2. Bell, F.G., 1992. Influence of weathering and discontinuities on the behaviour of rock masses. In: Engineering in Rock Masses. Butterworth-Heinemann Ltd. [online] pp. 27-53. Available at:< http://dx.doi.org/10.1016/B978-0-7506-1965-3.50006-6> [Accessed 17 November 2021].
3. Ismail, M., Mohd-Nordin, M., Hasan, A., Albar, A. and Razali, M., 2019. Shear strength behaviour of rock joint material influenced by different weathering grade. Journal of Physics: Conference Series, [online] 1349, p.012069. Available at:<https://doi.org/10.1088/1742-6596/1349/1/012069> [Accessed 25 March 2021].
4. Hack, G.K., Robert, H., 2020. Weathering, Erosion, and Susceptibility to Weathering. In: Kanji M., He M., Ribeiro e Sousa L. (eds) Soft Rock Mechanics and Engineering. Springer, Cham., Available at: <https://doi.org/10.1007/978-3-030-29477-9_11 > [Accessed 23 October 2021].

CHAPTER 7: URBAN WATER RELATED TO ROODEPLAAT DAM AND HARTBEESPOORT DAM

Authors: Marjuan Visagie & Nelda Smith

This chapter emanates from the following project-related outcomes:

- Visagie ML. 2025. Characterisation of urban surface water quality of two dams and their tributaries impacted with different land uses. MSc (Specialising in Hydrogeology) Dissertation. University of Pretoria.

7.1 SITE DESCRIPTION OF HARTBEESPOORT CATCHMENT AREA

The Hartbeespoort catchment area, located in the Upper Crocodile sub-management area, consists of five quaternary catchments (Figure 7-1): Magalies River (A21F and A21G), Upper Crocodile River (A21D and A21E), Jukskei River (A21C), Hennops River (A21A and A21B), and the incremental Crocodile River catchment near Hartbeespoort Dam (A21H) (Botha, 2015).

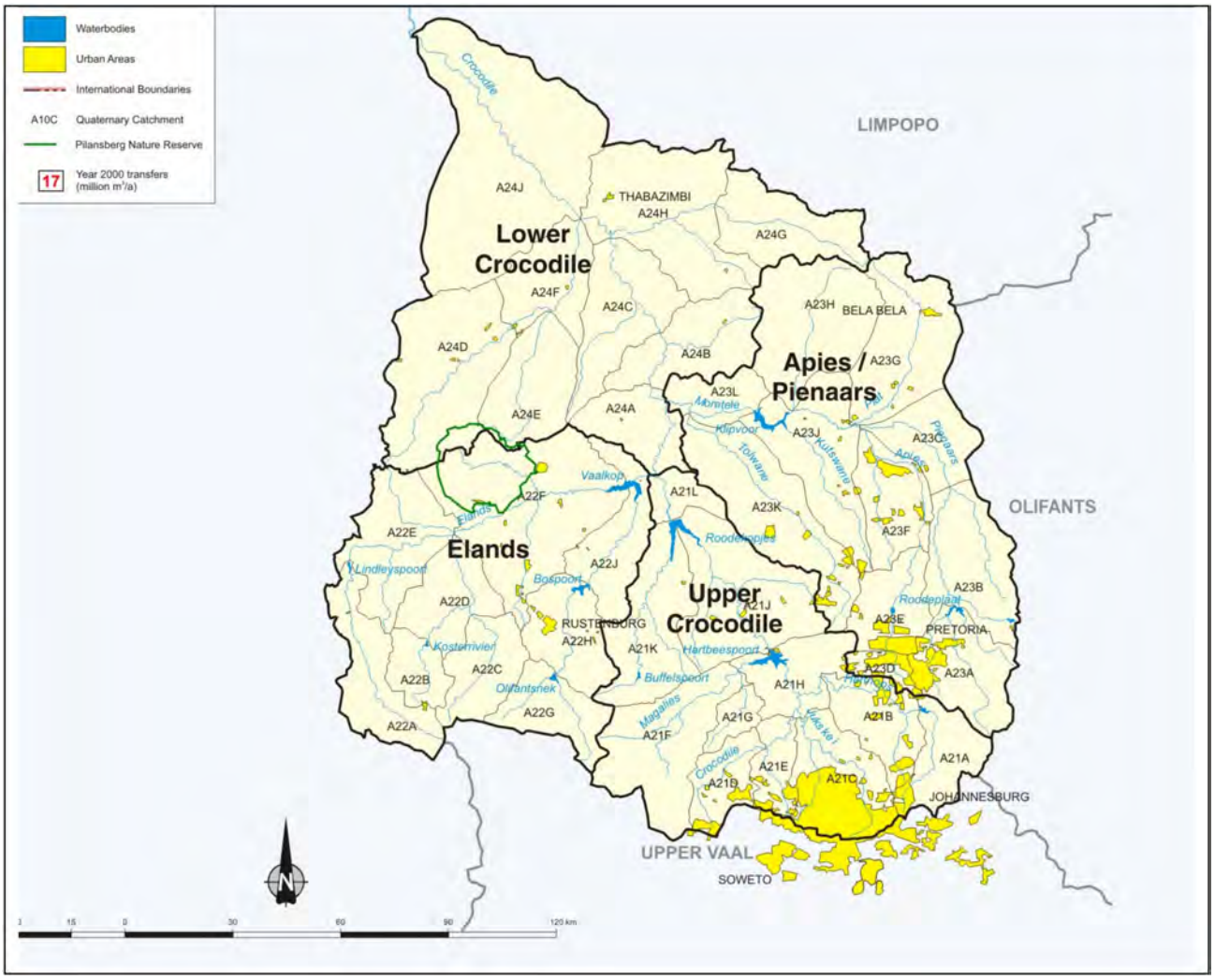

Figure 7-1 Quaternary catchments of the Hartbeespoort catchment area (DWAF, 2008).

7.1.1 Land use within the Upper Crocodile River catchment

The Crocodile River catchment originates from the Witwatersrand Mountain range at an elevation of 1700 m.a.s.l, initially covering a catchment area of 653 km^2 until it reaches the confluence with the Jukskei River. Upon merging with the Jukskei River, the catchment area expands to a total of 2551 km^2 before flowing into Hartbeespoort Dam. The Bloubankspruit is a significant tributary of the Crocodile River before its confluence with the Jukskei River. The Jukskei and Hennops Rivers are the main tributaries feeding into the Crocodile River (Botha, 2015).

The Upper Crocodile River catchment encompasses areas west of Johannesburg, such as Randfontein, Krugersdorp, and Roodepoort. Pollution in the Upper Crocodile River catchment arises from various activities, including gold mining, food processing industries, retail industries, agricultural activities, WWTPs, and urbanisation (Lowies, 2014). However, the main sources of pollution in the catchment are WWTPs, mine drainage, and multiple oxidation ponds situated on farm holdings west of the N24 freeway leading to Pretoria.

Nutrients in the catchment likely originate from the Randfontein and Percy Stewart WWTPs (Dudula, 2007). The Randfontein and Percy Stewart WWTPs are situated adjacent to the upper reaches of the Bloubankspruit and its tributary, the Blougatspruit. The Randfontein WWTP appears to have connections with the nearby Randfontein mine, raising concerns about the impact of its effluent on nitrate, nitrite, and nitrogen levels (Lowies, 2014). Additionally, abandoned gold mines present a risk of acid mine drainage affecting water quality (Botha, 2015). Key establishments along the Crocodile River before the dam include the Pelindaba Nuclear Research Center, Alpha Conference Center, Art Exhibition Center, and Lesedi Cultural Village, with the Pelindaba plant operating a monitored WWTP (Dudula, 2007).

7.1.2 Land use within the Jukskei River catchment

The Jukskei River catchment is one of the largest catchment areas in the Gauteng Province, covering approximately 800 km^2, which primarily includes the City of Johannesburg Metropolitan Municipality, followed by Tshwane and Ekurhuleni Metropolitan Municipalities (Mawasha & Britz, 2022). It encompasses urban areas such as Johannesburg, Midrand, Randburg, and Kempton Park (Botha, 2015). The Jukskei River spans 68 km, originating near Ellis Park stadium in Johannesburg, and flowing into the Crocodile River, which leads to Hartbeespoort Dam and eventually the Indian Ocean (Moeketsi et al., 2022).

The Jukskei River catchment has different land uses, including industrial, commercial, educational, and recreational facilities, tourist destinations, and entertainment venues, all dominated by built-up areas. The catchment is monitored by five gauging stations along with a global weather station (the Climate Forecast System Reanalysis) and two South African weather stations (Mawasha & Britz, 2022). The high-density informal settlements of Alexandra Township increase nutrient, sodium, potassium, and chloride concentrations in the river due to inadequate waste management and effluent runoff (Jardine-Da Silva, 2016). Additionally, a closed landfill north of Alexandra, along with quarrying and construction activities downstream in Midrand and Kyalami, impacts water quality.

The Diepsloot area has numerous activities contributing to the river's pollution, including massive developments in Dainfern and Fourways, Diepsloot Township, compost heaps, and the Northern WWTP. Farming activities downstream of the Diepsloot area include breeding chickens, sheep, and horses. Farming activities in the catchment involve the use of fertilisers and the production of animal manure, resulting in the drainage of nutrients into the Jukskei River. Additionally, lodges and resorts line the river. Like Alexandra Township, the Diepsloot Township lacks adequate stormwater drainage and waste management (Dudula, 2007). The catchment also contains large industries such as the AECI factory and Kelvin Power Station (Botha, 2015).

7.1.3 Land use within the Hennops River catchment

The Hennops River catchment, covering approximately 1010 km^2, is located between Johannesburg and Tshwane, flowing through the City of Johannesburg, Tshwane, and Ekurhuleni municipalities. This urban riverine system experiences significant stress due to severe pollution from domestic waste, industrial effluent, and untreated sewage. The river originates in Kempton Park, flows through Centurion, and eventually joins the Crocodile River before draining into Hartbeespoort Dam.

Rapid urbanisation, informal settlements, industrial developments, and business areas have degraded and diminished the beauty of the Hennops River. The deteriorating water quality is linked to the densely populated informal settlements of Tembisa, Ivory Park, and Rabie Ridge, which lack proper sanitation and waste management facilities, as well as ineffective stormwater drainage (Latcheman, 2023). These informal settlements contribute significant nutrient pollution to the Kaalspruit through overflowing stormwater drains, blocked sewer pipes, and illegal waste dumping along riverbanks (Dudula, 2007). The Kaalspruit, a highly polluted tributary, flows through the densely populated informal settlements of Tembisa and Ivory Park, which merges with the Olifantspruit before entering the Hennops River.

The Hennops River catchment includes several WWTPs, such as the Sunderland Ridge WWTP, which discharges effluent directly into the Hennops River (Latcheman, 2023), and the Olifantsfontein WWTP, which discharges effluent into the Olifantspruit, downstream of the confluence with the Kaalspruit (Hoffmann, 1994). The Hartbeesfontein WWTP releases effluent into the Rietvlei River, which eventually converges with the Hennops River and flows into Rietvlei Dam (Botha, 2015). The riverbanks of the Hennops River are heavily polluted with waste and vegetation debris. The vegetation debris comprises branches and dead trees, while the solid waste debris consists of urban litter such as cans, bottles, plastic bags, clothing, shoes, and tires. The accumulation of urban litter from informal settlements is due to the absence of proper waste collection, handling, and removal services (Latcheman, 2023).

7.1.4 Land use within the Magalies River catchment

The Magalies River catchment, covering approximately 1171 km², primarily consists of agricultural land located south of the Magaliesberg mountain range (Lowies, 2014). The Magalies River originates southwest of the Magaliesburg town, near the majestic Magaliesberg mountain range. The river flows through an agricultural region, where irrigation is practiced along its banks (Botha, 2015). Water is heavily extracted from the river for agricultural use and bottling (Carroll, 2020). The Skeerpoort River is known as the main tributary of the Magalies River (Botha, 2015). The Skeerpoort River flows through the Cradle of Humankind, a World Heritage Site featuring dolomitic caves where fossilised remains of significant hominids have been discovered. As a result, development in the Skeerpoort River catchment is limited to a minimum, with most of the area designated as a nature reserve (Carroll, 2020).

In the Magalies River catchment, where agricultural activities dominate, water quality issues are minimal, despite previously recorded elevated nutrient levels. The main point source of pollution is the Magalies WWTP, while agricultural activities serve as nonpoint sources (Dudula, 2007). The Magalies River catchment is considered the cleanest among the five sub-catchments, facing impacts solely from agriculture and the Magalies WWTP (Botha, 2015).

7.1.5 Land use within the Hartbeespoort Dam catchment

The Hartbeespoort Dam catchment, covering approximately 515 km^2, includes the Swartspruit, Leeuspruit, and the dam itself. The catchment includes three municipalities: Madibeng Local Municipality, Mogale City (West Rand), and the City of Tshwane (Botha, 2015). The catchment is dominated by new developments and

farming activities, with construction activities contributing to the decline in water quality, particularly phosphorus. Despite its low flow rate, the Swartspruit consistently exhibits high nutrient concentrations. The Rietfontein WWTP, situated adjacent to the Swartspruit, discharges effluent directly into the river and is identified as the main point source of pollution, contributing 3.3 tons of phosphorus annually (Dudula, 2007).

7.2 SITE DESCRIPTION OF THE ROODEPLAAT CATCHMENT AREA

The Roodeplaat catchment area, located in the Apies/ Pienaars sub-management area, consists of one quaternary catchment, A23A (Figure 7-1). Its main watercourses are the Pienaars River, Hartbeesspruit, Moreletaspruit, and Edendalespruit (Botha, 2015).

7.2.1 Land use along the Pienaars River

The Pienaars River contributes 43% of the surface inflow to Roodeplaat Dam (Silberbauer & Esterhuyse, 2014) and extends 46 km (Matshali, 2015). It originates in a rural area, flowing through the Mamelodi Township and past the Baviaanspoort WWTP before reaching Roodeplaat Dam (Walmsley and Toerien, 1978). The river drains the largest area in the catchment, covering 357 km^2 (Lomberg, 2010), primarily in the central part. It receives runoff from the Mamelodi Township and biologically treated sewage effluent from the Baviaanspoort WWTP (Bosman and Kempster, 1985). The Baviaanspoort WWTP is identified as the main source of nutrients, specifically phosphates, for Roodeplaat Dam (Lomberg, 2010).

7.2.2 Land use along the Hartbeesspruit/ Moreletaspruit

The Hartbeesspruit, with its major tributary, the Moreletaspruit, drains a section of the Limpopo water system in the eastern part of Pretoria (Modley, 2019). The combined Hartbeesspruit/Moreletaspruit system contributes 27% of the surface inflow to Roodeplaat Dam (Silberbauer & Esterhuyse, 2014). The Hartbeesspruit measures 19 km, while the Moreletaspruit is 23 km long, with both originating in an urban area of Pretoria (Lomberg, 2010). The Hartbeesspruit drains the suburban west part of the catchment and the Silverton industrial area through the Moreletaspruit (Bosman & Kempster, 1985). The combined Hartbeesspruit/Moreletaspruit system drains an area of 161 km^2 (Lomberg, 2010).

The Hartbeesspruit is primarily surrounded by residential holdings of varying cost, extending from Pretoria East to Pretoria South and Mamelodi. Industries primarily surround the upstream southern side, while the northern downstream side is predominantly surrounded by small farms and nature conservation areas (Modley, 2019). The river flows through mixed agricultural land before reaching Roodeplaat Dam. Nutrient enrichment in the Hartbeesspruit results from surface runoff due to excessive fertiliser and livestock feed application, leading to eutrophication and water quality issues (Lomberg, 2010). Additionally, the Hartbeesspruit creates a wetland within the Colbyn Wetland Nature Reserve due to back-flooding (van Aardt et al., 2024).

The Moreletaspruit flows through the eastern suburbs of Pretoria and two nature reserves: Moreleta and Faerie Glen. The Moreletaspruit is situated in the Highveld zone, known for its rocky ridges and grassland biomes. The river is mainly surrounded by residential holdings, along with land used for industrial, commercial, and business purposes, but to a lesser extent (Modley, 2019).

7.2.3 Land use along the Edendalespruit

The Edendalespruit contributes 8% of the surface inflow to Roodeplaat Dam (Silberbauer & Esterhuyse, 2014) and stretches 28 km (Matshali, 2015). It drains the smallest area in the catchment, covering 129 km^2, primarily in the eastern part dominated by agricultural land and grassland. Agricultural activities along the

Edendalespruit include dryland farming and numerous plantations near the impoundment inlet (Lomberg, 2010).

The downstream northern side is dominated by woodlands, while the upstream southern side is dominated by grasslands (Lomberg, 2010). Small farms and residential holdings surround the river, with the Mamelodi Township on the western side characterised by informal settlements (Modley, 2019). The Leeuwfontein estate, also on the western side, developed without legal property subdivision, rezoning, or planning. Residents of the estate have expressed concerns about the lack of basic services. Although Leeuwfontein may initially appear attractive with its large houses and high boundary walls, it is, in reality, an extensive informal settlement constructed from bricks and mortar (Mabona, 2023).

The proximity of the Edendale lead mine to the Edendalespruit has raised concerns about hazardous concentrations of lead leaching into the river (Modley, 2019). Nutrient enrichment in the Edendalespruit is caused by excessive fertiliser application, the presence of livestock facilities, and plantations. This enrichment will lead to eutrophication and subsequently affect the water quality (Lomberg, 2010).

7.3 GEOLOGY

The general geology of the Hartbeespoort region consists of the Chuniespoort Group at the base, overlain unconformably by the Pretoria Group, and ultimately intruded by the Bushveld Complex (Figure 7-2) (Davis, 2017). Similarly, the Roodeplaat area contains the Chuniespoort Group at the base, unconformably overlain by the Pretoria Group, and finally intruded by the Bushveld Complex. Additionally, it features intrusions of the Pienaars River Alkaline Complex or Roodeplaat Complex, which postdate the Bushveld Complex (Figure 7-3) (Lomberg, 2010).

7.4 SAMPLING LOCATIONS

The sampling locations for the Roodeplaat catchment area in Figure 7-4 and for the Hartbeespoort catchment area are shown in Figure 7-5.

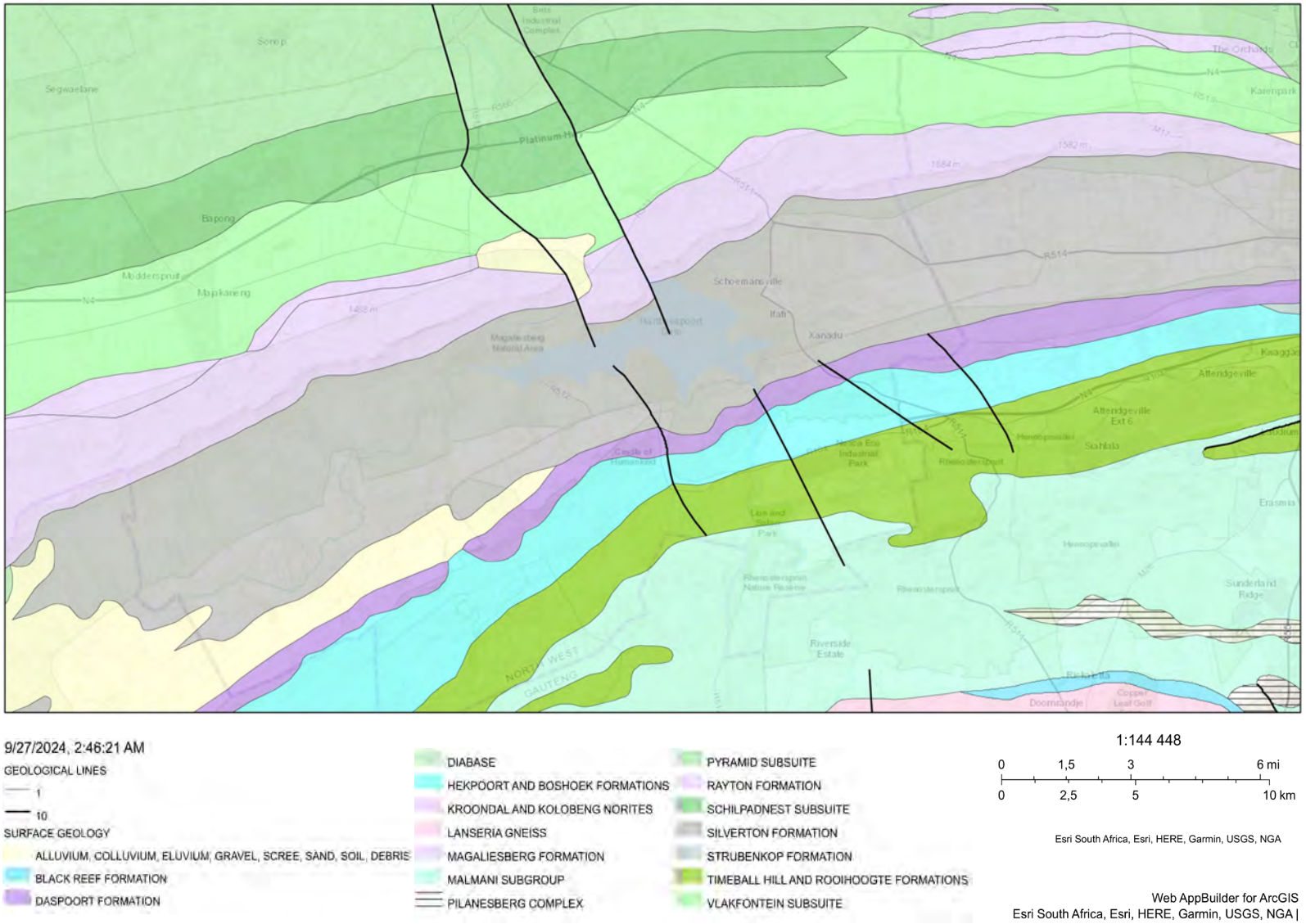

Figure 7-2 Transparent geological map constructed in the Council of Geoscience Data Management Portal showing the geology and faults in the Hartbeespoort Dam region

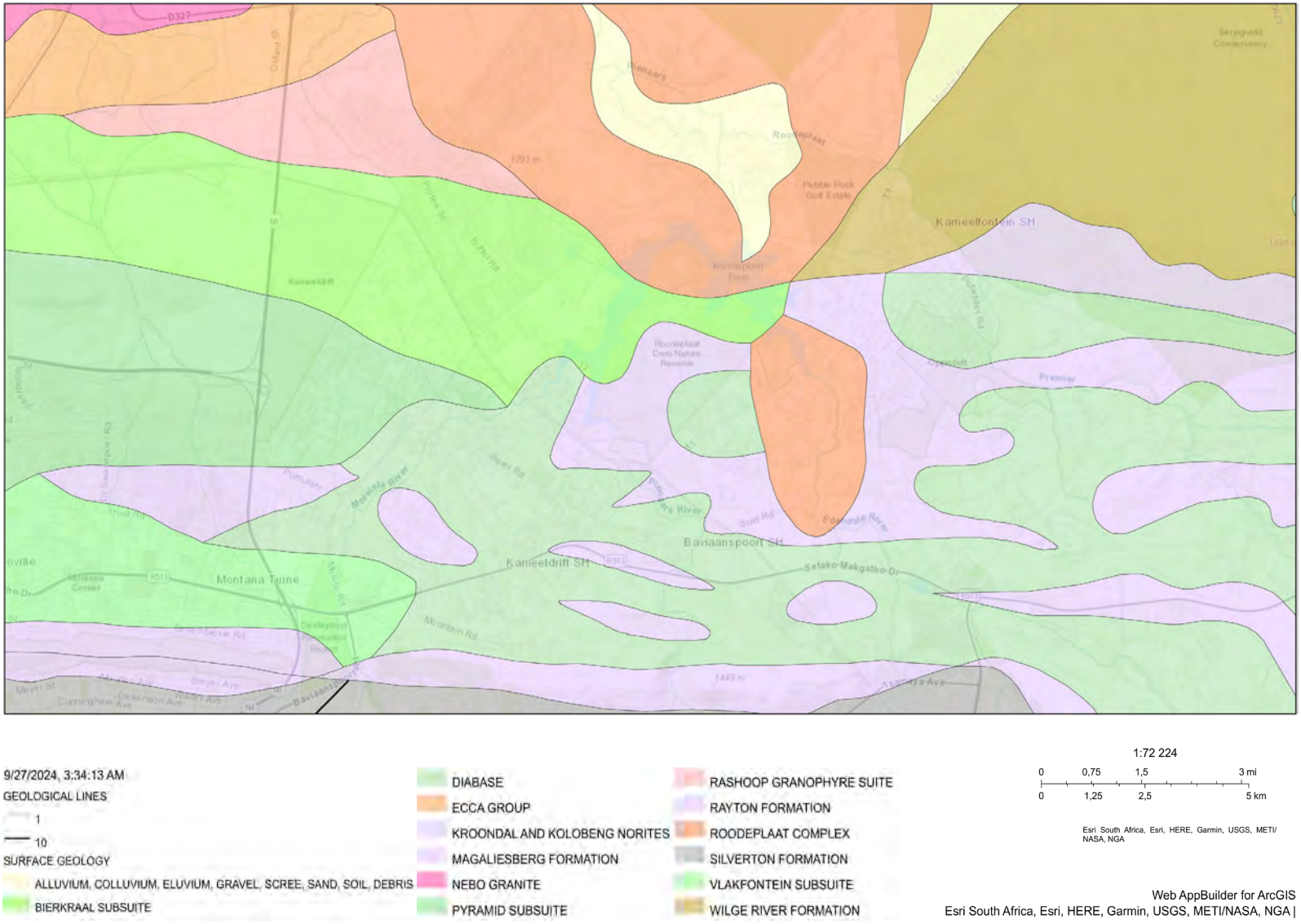

Figure 7-3 Transparent geological map constructed in the Council of Geoscience Data Management Portal showing the geology and faults in the Roodeplaat Dam region.

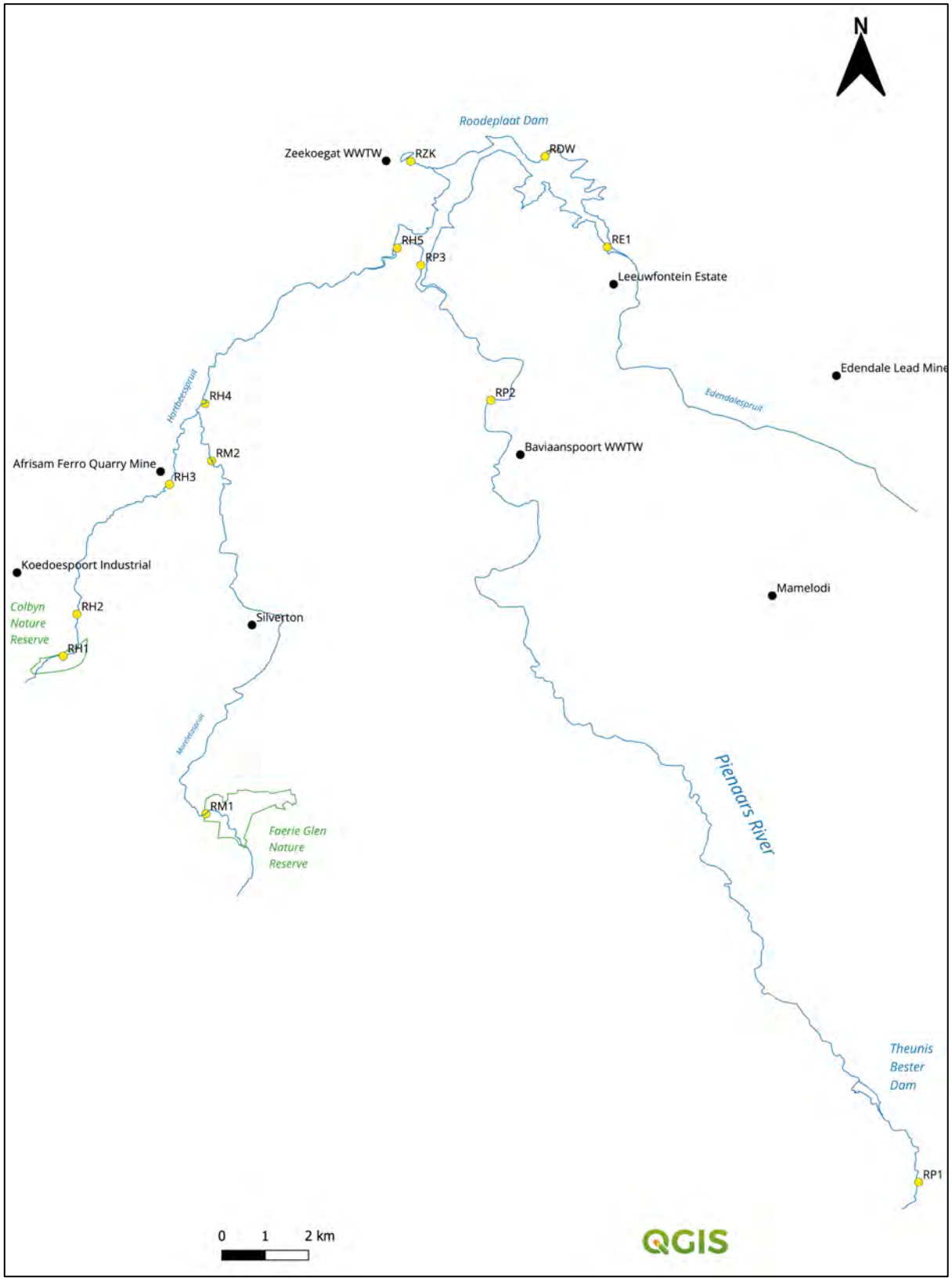

Figure 7-4 Map constructed in QGIS depicting the Roodeplaat catchment area, illustrating the rivers and their primary tributaries feeding into the dam. It also highlights various land use activities within the catchment and indicates the locations of the selected sampling sites.

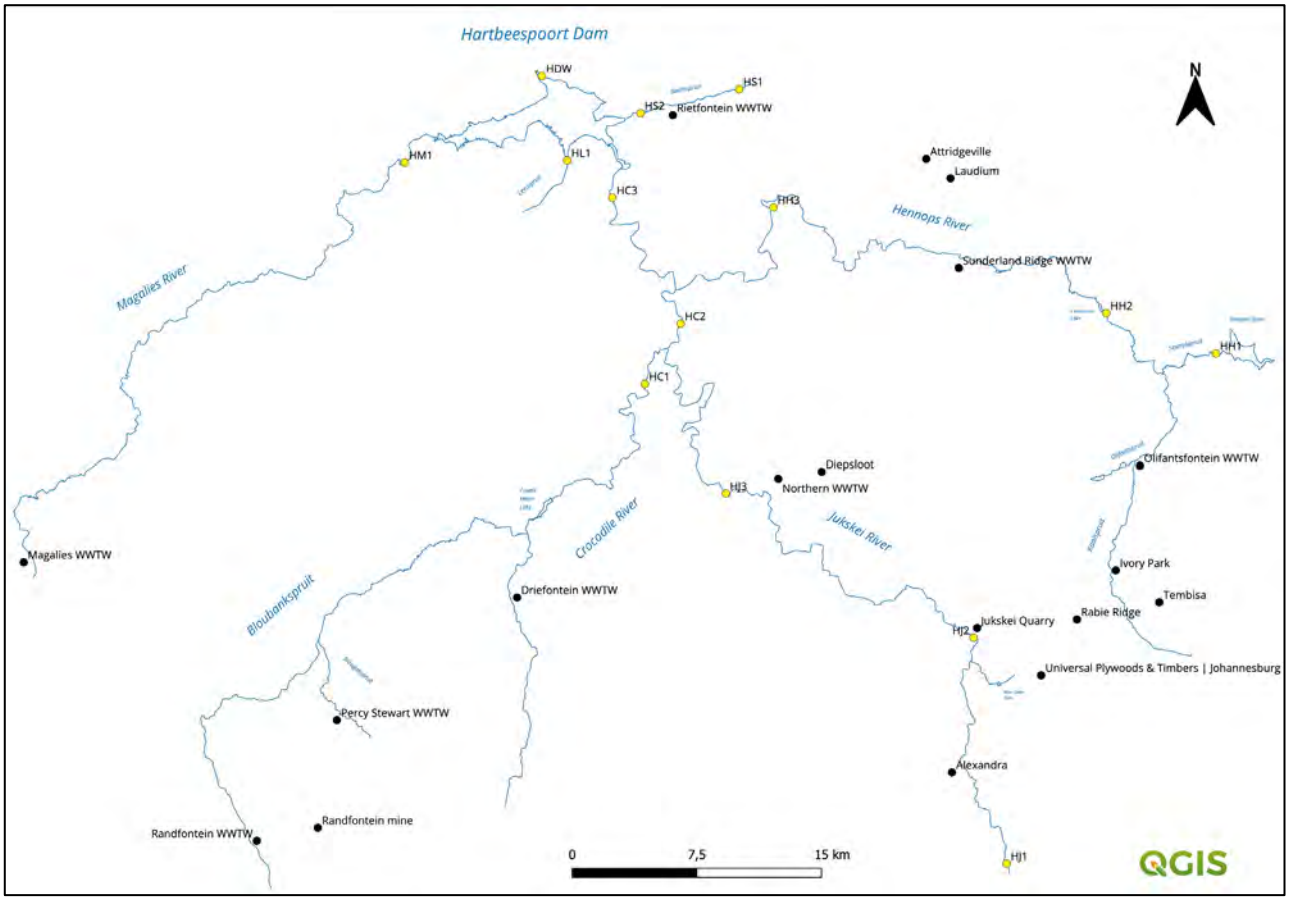

Figure 7-5 Map constructed in QGIS depicting the Hartbeespoort catchment area, illustrating the rivers and their primary tributaries feeding into the dam. It also highlights various land use activities within the catchment and indicates the locations of the selected sampling sites

7.5 HARTBEESPOORT CATCHMENT RESULTS

All the water quality results for the Hartbeespoort Catchment are shown in Table 7-1.

Table 7-1 Physical water quality parameters of the sites selected along the Crocodile River, Hennops River, Jukskei River, Magalies River, Swartspruit and Leeuspruit, as well as at the dam wall, during June 2024.

Parameter	HC1	HC2	HC3	HH1	HH2	HH3	HJ1	HJ2	HJ3	HM1	HS1	HS2	HL1	HDW
Physical Water Quality														
EC (mS/m)	105	78.0	78.7	42.9	69.0	74.6	40.0	56.3	71.9	35.7	62.6	73.2	59.8	59.2
TDS (mg/ℓ)	816	434	438	274	390	392	212	356	422	258	404	512	398	392
TDS (mg/ℓ)	<4.5	19	14	9.0	93	13	<4.5	48	<4.5	9.0	<4.5	10.0	8.0	<4.5
T (˚C)	20.0	20.0	19.9	20.0	20.0	20.0	18.8	19.4	19.4	20.0	20.0	19.7	20.0	19.9
Microbiological Water Quality														
Total Coliforms (CFU/100 mℓ)	470	>100000	85000	240	>100000	48000	11000	>100000	>100000	180	2	310	890	4600
Faecal Coliforms (CFU/100 mℓ)	105	73000	8600	12	>100000	9000	3600	25000	42000	39	1	70	400	490
***E. Coli* (CFU/100 mℓ)**	60	68000	8000	10	>100000	7000	3400	21000	36000	33	1	60	400	430
Chemical Water Quality Parameters														
Nitrite (mg/ℓ)	0.351	0.576	0.638	0.355	0.105	0.235	0.268	0.503	0.439	0.087	0.078	0.073	0.852	0.817
Nitrate (mg/ℓ)	4.96	2.02	2.04	1.48	0.364	1.13	1.02	2.00	0.631	1.08	0.301	0.270	3.80	4.20
Un-ionised Ammonia (mg/ℓ)	0.031	0.544	0.621	0.182	0.333	0.419	0.210	0.118	0.407	0.005	0.005	<0.005	0.022	<0.005
Ammonium (mg/ℓ)	0.643	17.8	20.3	4.77	21.3	17.1	6.41	9.52	26.1	0.122	0.096	0.230	3.57	0.654
Orthophosphate (mg/ℓ)	0.574	1.52	2.35	1.19	2.51	2.40	0.390	0.605	1.85	<0.009	<0.009	<0.009	1.23	0.957
Chloride (mg/ℓ)	58.1	60.2	61.9	44.9	68.5	61.6	36.4	47.6	72.5	6.81	12.4	50.8	57.6	56.3
Sulphate (mg/ℓ)	385	134	92.7	40.8	68.2	51.3	42.4	57.2	52.5	12.1	21.7	68.6	74.9	76.3
Total Alkalinity	129	177	206	146	242	246	127	164	225	189	336	268	137	126

Parameter	HC1	HC2	HC3	HH1	HH2	HH3	HJ1	HJ2	HJ3	HM1	HS1	HS2	HL1	HDW
(mg $CaCO_3$/ℓ)														
Calcium (mg/ℓ)	125	58.6	52.7	36.2	42.3	46.5	36.0	46.2	41.2	39.9	54.5	59.7	48.2	48.0
Magnesium (mg/ℓ)	45.8	22.2	21.6	17.6	18.2	21.5	17.3	18.4	15.0	26.3	44.5	37.6	20.1	19.2
Sodium (mg/ℓ)	57.0	56.9	57.7	44.5	73.8	58.9	27.6	42.9	65.5	6.68	26.9	53.2	49.5	49.7
Potassium (mg/ℓ)	6.32	9.52	10.2	8.71	12.7	10.9	5.23	7.80	11.8	0.028	1.60	8.03	6.03	8.66
Fluoride (mg/ℓ)	<0.263	<0.263	0.269	<0.263	<0.263	<0.263	<0.263	<0.263	0.328	<0.263	0.716	0.597	<0.263	<0.263
Aluminium (mg/ℓ)	0.039	0.046	0.024	0.054	0.068	0.015	0.003	0.020	0.022	0.033	<0.002	0.012	0.020	<0.002
Iron (mg/ℓ)	<0.004	0.056	0.111	0.075	0.292	0.292	0.030	0.033	0.082	<0.004	<0.004	0.019	<0.004	<0.004
Lead (mg/ℓ)	<0.004	<0.004	<0.004	<0.004	<0.004	<0.004	<0.004	<0.004	<0.004	<0.004	<0.004	<0.004	<0.004	<0.004
Zinc (mg/ℓ)	<0.002	<0.002	<0.002	<0.002	<0.002	<0.002	0.002	0.004	0.017	<0.002	<0.002	<0.002	<0.002	<0.002
Cadmium (mg/ℓ)	<0.002	<0.002	<0.002	<0.002	<0.002	<0.002	<0.002	<0.002	<0.002	<0.002	<0.002	<0.002	<0.002	<0.002
Arsenic (mg/ℓ)	<0.006	<0.006	<0.006	<0.006	<0.006	<0.006	<0.006	<0.006	<0.006	<0.006	<0.006	<0.006	<0.006	<0.006
Microcystin (µg/ℓ)	<0.5	<0.5	<0.5	<0.5	<0.5	<0.5	<0.5	<0.5	<0.5	<0.5	<0.5	<0.5	<0.5	<0.5
Total Organic Carbon (mg/ℓ)	5.64	8.13	8.10	9.35	11.7	8.99	7.05	9.52	10.0	2.93	5.90	7.76	7.91	8.20

7.6 HARTBEESPOORT CATCHMENT DISCUSSION

7.6.1 Jukskei River

Alexandra Township significantly increased the total suspended solids (TSS) concentration and decreased the dissolved oxygen (DO) concentration. The low DO concentration may result from bacteria consuming oxygen while decomposing organic material released from the township. The township also contributed to the rise in nitrate, ammonium, orthophosphate, and total organic carbon (TOC) concentrations in the river. Moreover, the township significantly increased the microbial counts (total coliforms, faecal coliforms, and *E. coli*) in the river. Moreover, the Universal Plywoods & Timbers manufacturing plant in Johannesburg is likely a source of nitrate pollution to the Jukskei River. Additionally, the Jukskei Quarry may also contribute to nitrate concentrations in the river due to its use of explosives.

The Northern WWTP and Diepsloot Township did not increase the TSS concentration in the river. This may result from a reduction in the river's flow velocity, which allows suspended solids to settle, or from the Northern WWTP effectively removing suspended solids, leading to the discharge of effluent with low TSS concentrations into the river. A low DO concentration was recorded downstream of the Northern WWTP and Diepsloot Township. This low DO concentration may result from bacteria consuming oxygen while decomposing organic material released from the Northern WWTP and Diepsloot Township. Additionally, the Northern WWTP and Diepsloot Township may contribute to the rise in orthophosphate and TOC concentrations in the river.

The Northern WWTP is primarily responsible for the significant increase in ammonium concentration in the river. The decrease in nitrate concentration, coupled with the increase in ammonium concentration, suggests that the Northern WWTP is likely not performing the nitrification process adequately. The Diepsloot Township may also contribute to the increase in ammonium concentration but to a lesser extent. Additionally, the Northern WWTP is mainly responsible for the rise in microbial counts, indicating that it did not perform the disinfection process. The Diepsloot Township may also contribute to the increase in microbial counts but to a lesser degree.

7.6.2 Hennops River

The Olifantsfontein WWTP is primarily responsible for the substantial increase in TSS concentration in the river, indicating that it did not effectively remove suspended solids, leading to the discharge of effluent with high TSS concentrations. The densely populated informal settlements of Ivory Park, Tembisa, and Rabie Ridge may also contribute to the rise in TSS concentration but to a lesser extent. The DO concentration decreased downstream of the informal settlements and Olifantsfontein WWTP. The low DO concentration may result from bacteria consuming oxygen while decomposing organic material released from the informal settlements and Olifantsfontein WWTP. Additionally, the informal settlements and Olifantsfontein WWTP may be responsible for the rise in orthophosphate and TOC concentrations in the river.

The Olifantsfontein WWTP is mainly responsible for the substantial increase in ammonium concentration in the river. The decrease in nitrate concentration, along with the rise in ammonium concentration, suggests that the Olifantsfontein WWTP is probably not performing the nitrification process adequately. The informal settlements may also contribute to the increase in ammonium concentration but to a lesser degree. Furthermore, the Olifantsfontein WWTP is primarily responsible for the significant increase in microbial counts, indicating inadequate disinfection. The informal settlements may also contribute to the increase in microbial counts but to a lesser degree.

The Sunderland Ridge WWTP, Atteridgeville, and Laudium Townships decreased the TSS concentration in the river. This may be due to either a reduction in the river's flow velocity, allowing suspended solids to settle, or the Sunderland Ridge WWTP effectively removing suspended solids, leading to the discharge of effluent with low TSS concentrations into the river. The increase in DO concentration downstream of the Sunderland

Ridge WWTP, Atteridgeville, and Laudium Townships may be due to turbulent water flow. Additionally, the Sunderland Ridge WWTP, Atteridgeville, and Laudium Townships did not increase the orthophosphate and TOC concentrations in the river.

The Sunderland Ridge WWTP is primarily responsible for the significant rise in nitrate concentration in the river. The decrease in ammonium concentration, coupled with the increase in nitrate concentration, suggests that the Sunderland Ridge WWTP is likely performing the nitrification process adequately. The townships could also contribute to the increase in nitrate concentration but to a lesser extent. Moreover, the microbial counts decreased downstream of the Sunderland Ridge WWTP, Attridgeville, and Laudium Townships, indicating that the Sunderland Ridge WWTP effectively carried out the disinfection process, while the townships did not significantly elevate microbial counts.

7.6.3 Crocodile River

The Randfontein, Percy Stewart, and Driefontein WWTPs may be responsible for the low TSS concentration recorded at HC1, as they may have effectively removed suspended solids, resulting in the discharge of effluent with low TSS concentrations into the river. These WWTPs contributed high nitrate and low ammonium concentrations to the Crocodile River, suggesting they likely performed the nitrification process adequately. Mining activities at the Randfontein mine, located along the Bloubankspruit, may be responsible for the elevated sulphate and calcium concentrations recorded at HC1. Literature indicates that the Randfontein WWTP is connected to the nearby Randfontein mine (Lowies, 2014).

The Jukskei River contributed higher concentrations of TSS, ammonium, orthophosphate, and TOC, along with elevated microbial counts, to the Crocodile River. Alexandra Township is the main source of TSS, while the Northern WWTP is the primary source of ammonium to the Jukskei River. The Alexandra and Diepsloot Townships also contribute ammonium but to a lesser degree. The Northern WWTP, Alexandra, and Diepsloot Townships are sources of both orthophosphate and TOC. The Alexandra Township is the main source of microbial counts, with the Northern WWTP and Diepsloot Township also contributing but to a lesser degree.

The Hennops River contributed higher concentrations of nitrate and DO to the Crocodile River. The Sunderland Ridge WWTP is the main source of nitrate, while the Atteridgeville, and Laudium Townships contribute nitrate to a lesser extent. Additionally, turbulent water flow contributed to higher DO concentrations in the Hennops River.

7.6.4 Swartspruit

The Rietfontein WWTP is primarily responsible for the increase in TSS concentration in the river, indicating that it did not effectively remove suspended solids, resulting in the discharge of effluent with elevated TSS concentrations. The DO concentration decreased downstream of the Rietfontein WWTP. The relatively low DO concentration may result from bacteria consuming oxygen while decomposing organic material released from the Rietfontein WWTP. The Rietfontein WWTP may be responsible for the rise in TOC concentration in the river.

Although the ammonium concentration increased and the nitrate concentration decreased after passing the Rietfontein WWTP, both remained low. However, the nitrate concentration at HS2 is still higher than the ammonium concentration. As a result, any effluent discharged into the river by this WWTP is likely compliant with the national standards, as no significant impact is observed at HS2.

Additionally, the rise in microbial counts after passing the Rietfontein WWTP is not significantly high, with counts similar to those recorded at the upstream sites of the Crocodile River and Hennops River. The increase may be attributed to the faecal impact of animals.

7.6.5 Leeuspruit

The low TSS concentration recorded at HL1 may be due to a lack of turbulence, allowing the suspended solids to settle more easily. The relatively high DO concentration may be due to aquatic plants, such as hyacinth, photosynthesising and generating oxygen, possibly increasing the DO concentration. A high TOC concentration was measured at HL1, possibly due to the runoff of herbicides and/ or pesticides from agricultural land. Relatively low ammonium and high nitrate concentrations were measured at HL1, likely resulting from rural runoff of over-fertilised agricultural land. The relatively low microbial counts recorded at this site may be due to a lack of re-suspension, as the turbulence is low at HL1.

7.6.6 Magalies River

The low TSS concentration recorded at HM1 may be due to reduced river flow, which causes solids to settle out of the water. Additionally, the Magalies WWTP may be effectively removing suspended solids, leading to the discharge of effluent with low TSS concentrations into the river. The high DO concentration recorded at this site may be due to the turbulent water flow.

The Magalies WWTP may be responsible for the relatively high nitrate concentration. The low ammonium concentration, along with the relatively high nitrate concentration, suggests that the Magalies WWTP is likely performing the nitrification process adequately. The relatively high nitrate concentration may also result from agricultural activities. The low microbial counts indicate that the Magalies WWTP did not add significantly to the microbial load of the river.

7.6.7 Hartbeespoort Dam wall

The low TSS concentration, below the detection limit, recorded at HDW may be due to particles settling out of the water, as water flow typically slows down in this area, allowing suspended solids to settle more easily. The relatively low DO concentration may be due to the lack of turbulent water flow and the limited presence of aquatic plants, such as hyacinth, at this site. HDW recorded a high nitrate concentration and a low ammonium concentration. This may be due to water being exposed to oxygen for a longer period than the water upstream, leading to the oxidation of ammonium to nitrate. HDW recorded a relatively low orthophosphate concentration and a relatively high TOC concentration. This may be due to the mix of rivers with high and low concentrations of these parameters flowing into the dam. HDW recorded relatively low microbial counts. This may be due to sedimentation and die-off of microbes as they travel further away from their sources. Also, this can be due to a lack of re-suspension, as the turbulence is low at this site.

7.7 ROODEPLAAT CATCHMENT RESULTS

All the water quality results for the Roodeplaat Catchment are shown in Table 7-2.

Table 7-2 Physical water quality parameters of the sites selected along the Pienaars River, Moreletaspruit, Hartbeesspruit and Edendalespruit, as well as at the Zeekoegat canal and dam wall, during June 2024.

Parameter	RP1	RP2	RP3	RM1	RM2	RH1	RH2	RH3	RH4	RH5	RE1	RZK	RDW
Physical Water Quality													
Electrical Conductivity (mS/m)	33.2	77.1	52.3	30.6	34.5	44.8	39.5	32.6	34.3	48.1	48.0	76.7	48.2
Total Dissolved Solids (mg/ℓ)	200	520	438	186	176	272	224	274	264	394	420	498	390
Total Suspended Solids (mg/ℓ)	<4.5	50	33	<4.5	<4.5	<4.5	<4.5	<4.5	<4.5	8.0	<4.5	51	<4.5
Temperature (˚C)	18.6	18.8	18.0	18.4	18.5	18.5	18.5	17.9	17.9	18.0	18.1	19.0	17.5
Microbiological Water Quality													
Total Coliforms (CFU/100 mℓ)	15	>100000	1090	3800	27000	390	410	<1	12000	7300	1090	>100000	2700
Faecal Coliforms (CFU/100 mℓ)	13	60000	40	2700	3460	110	60	<1	4000	720	270	>100000	950
E. Coli (CFU/100 mℓ)	8	52000	30	2200	3300	83	60	<1	3000	700	230	>100000	300
Chemical Water Quality Parameters													
pH	8.23	7.75	7.95	8.17	8.08	7.97	8.15	8.13	8.18	8.15	7.91	7.33	7.71
Dissolved Oxygen (mg/ℓ)	9.75	5.14	5.97	9.72	9.68	9.29	8.64	8.94	9.34	8.46	6.07	6.09	5.06
Nitrite (mg/ℓ)	0.195	0.264	0.213	0.087	0.197	0.070	0.080	0.206	0.165	0.207	0.216	<0.065	0.159
Nitrate (mg/ℓ)	0.465	0.744	0.428	1.05	1.92	0.553	0.818	1.09	1.77	0.543	0.313	0.235	<0.194
Un-ionised Ammonia (mg/ℓ)	0.012	0.558	0.369	0.012	0.023	<0.005	<0.005	0.012	0.014	0.417	0.304	0.279	0.156
Ammonium (mg/ℓ)	0.229	33.4	11.3	0.228	0.567	0.120	0.107	0.302	0.282	8.19	11.6	35.3	9.36
Orthophosphate (mg/ℓ)	<0.009	3.13	<0.009	<0.009	0.067	<0.009	<0.009	<0.009	<0.009	<0.009	<0.009	<0.009	<0.009
Chloride (mg/ℓ)	10.9	63.2	46.3	21.5	28.3	62.1	35.6	27.2	30.0	44.3	42.2	65.5	43.0
Sulphate (mg/ℓ)	21.6	66.6	41.3	21.3	26.3	28.7	27.3	26.0	27.8	38.0	35.2	43.2	35.5

Parameter	RP1	RP2	RP3	RM1	RM2	RH1	RH2	RH3	RH4	RH5	RE1	RZK	RDW
Total Alkalinity (mg CaCO3/ℓ)	167	259	197	127	129	131	153	136	139	183	189	269	190
Calcium (mg/ℓ)	37.2	34.8	36.3	36.2	35.1	47.3	48.0	34.7	36.3	36.3	36.9	34.8	36.1
Magnesium (mg/ℓ)	22.8	22.1	20.3	17.5	19.1	21.5	22.7	20.7	21.1	20.5	20.7	16.6	20.4
Sodium (mg/ℓ)	18.4	69.9	43.9	14.8	21.9	30.2	18.6	17.5	21.0	40.3	39.4	64.2	39.4
Potassium (mg/ℓ)	1.38	13.5	9.41	2.61	3.47	3.60	2.71	3.09	3.05	8.41	8.71	14.5	8.58
Fluoride (mg/ℓ)	<0.263	<0.263	<0.263	<0.263	<0.263	0.407	<0.263	<0.263	<0.263	0.418	<0.263	0.535	<0.263
Aluminium (mg/ℓ)	0.006	0.025	0.034	<0.002	0.003	<0.002	<0.002	0.010	0.017	0.013	0.008	0.024	0.003
Iron (mg/ℓ)	<0.004	0.146	0.032	<0.004	<0.004	<0.004	0.026	0.034	0.011	0.017	<0.004	0.126	<0.004
Lead (mg/ℓ)	<0.004	<0.004	<0.004	<0.004	<0.004	<0.004	<0.004	<0.004	<0.004	<0.004	<0.004	<0.004	<0.004
Zinc (mg/ℓ)	<0.002	0.004	0.010	0.002	0.006	0.006	<0.002	0.006	0.005	0.005	0.003	0.014	0.003
Cadmium (mg/ℓ)	<0.002	<0.002	<0.002	<0.002	<0.002	<0.002	<0.002	<0.002	<0.002	<0.002	<0.002	<0.002	<0.002
Arsenic (mg/ℓ)	<0.006	<0.006	<0.006	<0.006	<0.006	<0.006	<0.006	<0.006	<0.006	<0.006	<0.006	<0.006	<0.006
Microcystin (µg/ℓ)	<0.5	<0.5	2.50	<0.5	<0.5	<0.5	<0.5	<0.5	<0.5	5.00	<0.5	<0.5	<0.5
Total Organic Carbon (mg/ℓ)	3.26	9.84	8.65	4.19	5.25	5.42	4.42	5.02	3.88	7.41	7.46	12.4	7.45

7.8 ROODEPLAAT CATCHMENT DISCUSSION

7.8.1 Pienaars River

The Baviaanspoort WWTP is primarily responsible for the significant increase in total suspended solids (TSS) concentration in the river, indicating that it did not effectively remove suspended solids, leading to the discharge of effluent with high TSS concentrations. The Mamelodi Township may also contribute to the rise in TSS concentration but to a lesser extent. The dissolved oxygen (DO) concentration decreased downstream of the Baviaanspoort WWTP and Mamelodi Township. The low DO concentration may result from bacteria consuming oxygen while decomposing organic material released from the Baviaanspoort WWTP and Mamelodi Township. The Baviaanspoort WWTP is mainly responsible for the substantial increase in orthophosphate concentration in the river, as this WWTP is considered the main source of phosphate to Roodeplaat Dam (Lomberg, 2010). The Mamelodi Township may also contribute to the rise in orthophosphate concentration but to a lesser extent. The Baviaanspoort WWTP and Mamelodi Township may be responsible for the significant increase in total organic carbon (TOC) concentration in the river.

The Baviaanspoort WWTP is mainly responsible for the significant increase in ammonium concentration in the river. Although the nitrate concentration also increased between RP1 and RP2, the increase was not as significant compared to ammonium, suggesting that the Baviaanspoort WWTP likely did not perform the nitrification process adequately. The Mamelodi Township may also contribute to the increase in ammonium concentration but to a lesser extent. Furthermore, the Baviaanspoort WWTP is mainly responsible for the significant increase in microbial counts, indicating that it did not perform the disinfection process adequately. The Mamelodi Township may also contribute to the increase in microbial counts but to a lesser degree. The concentrations of TSS, nitrate, ammonium, orthophosphate, and TOC, along with the microbial counts (total coliforms, faecal coliforms, and *E. coli*), decreased, while only the DO concentration increased as it approached the dam at RP3.

7.8.2 Hartbeesspruit/ Moreletaspruit

Low TSS concentrations, below the detection limit, were recorded at all the sites along the Moreletaspruit as well as at the majority of sites along the Hartbeesspruit. Only the downstream site of the Hartbeesspruit, where the river flows into the dam, recorded a concentration above the detection limit, which may be attributed to rural runoff from agricultural land. The DO concentration slightly decreased after passing the Silverton Industrial area, which may be due to water flowing laminar at RM2. The DO concentration decreased after flowing out of the Colbyn Nature Reserve at RH2. The concentration slightly increased after passing the Koedoespoort Industrial area and Afrisam Ferro Quarry Mine. The concentration further increased after the Moreletaspruit confluence, indicating that the Moreletaspruit increased the DO concentration of the Hartbeesspruit. The concentration decreased downstream towards entering the dam, which may be due to a reduction in turbulence as the river flows into the dam at this point.

The Silverton Industrial area may be responsible for the increase in nitrate concentration between RM1 and RM2. The nitrate concentration increased after flowing out of the Colbyn Nature Reserve at RH2. The concentration increased further after passing the Koedoespoort Industrial area and Afrisam Ferro Quarry Mine, suggesting that they are sources of nitrate to the Hartbeesspruit. Similar to the Jukskei Quarry in the Hartbeespoort catchment area, the Afrisam Ferro Quarry mine also increases nitrate concentrations due to its use of explosives. The concentration rose again after the Moreletaspruit confluence, indicating that the Moreletaspruit increased the nitrate concentration of the Hartbeesspruit. The concentration decreased upon entering the dam at RH5.

The Silverton Industrial area may be responsible for the rise in ammonium concentration between RM1 and RM2. The ammonium concentration decreased after flowing out of the Colbyn Nature Reserve at RH2. The concentration increased after passing the Koedoespoort Industrial area and Afrisam Ferro Quarry Mine, suggesting that they are sources of ammonium to the Hartbeesspruit. The concentration decreased after the Moreletaspruit confluence and increased significantly towards entering the dam at RH5. Rural runoff from over-fertilised agricultural land may be responsible for the significant increase in ammonium concentration between RH4 and RH5. The Silverton Industrial area may be responsible for the rise in orthophosphate concentration between RM1 and RM2. All the sites along the Hartbeesspruit recorded orthophosphate concentrations below the detection limit.

The Silverton Industrial area may be responsible for the rise in TOC concentration between RM1 and RM2. The TOC concentration decreased after flowing out of the Colbyn Nature Reserve at RH2. The concentration slightly increased after passing the Koedoespoort Industrial area and Afrisam Ferro Quarry Mine. The concentration decreased after the Moreletaspruit confluence and significantly increased towards entering the dam at RH5. Runoff of herbicides and/ or pesticides from agricultural land may be responsible for the significant increase in TOC concentration between RH4 and RH5.

The Silverton Industrial area may be responsible for the increase in microbial counts between RM1 and RM2. The total coliform increased while the faecal coliform and E. coli counts decreased after flowing out of the Colbyn Nature Reserve at RH2. The microbial counts decreased to below the detection limit after passing the Koedoespoort Industrial area and Afrisam Ferro Quarry Mine. The counts increased after the Moreletaspruit confluence, indicating that the Moreletaspruit increased the microbial counts of the Hartbeesspruit. The microbial counts decreased towards entering the dam at RH5.

7.8.3 Edendalespruit

A low TSS concentration, below the detection limit, was recorded at RE1, likely due to reduced river flow, which allows solids to settle out of the water column. This site recorded a relatively low DO concentration, which may be attributed to the absence of aquatic plants, such as hyacinth, and the lack of turbulence in the river, as this is the point where the river flows into the dam. RE1 measured a low nitrate and high ammonium concentration. The Mamelodi Township, Leeuwfontein estate, and agricultural activities may be responsible for the elevated ammonium concentration recorded at this site.

Concerns about the Edendale Lead Mine releasing hazardous concentrations of lead into the river were previously raised. However, lead concentrations below the detection limit were recorded at this site. RE1 measured an orthophosphate concentration below the detection limit and a relatively high TOC concentration. The Mamelodi Township, Leeuwfontein estate, and agricultural activities may be responsible for the high TOC concentration at this site. The Mamelodi Township, Leeuwfontein estate, and agricultural activities may also be responsible for the relatively low microbial counts recorded at this site.

7.8.4 Zeekoegat canal

The Zeekoegat WWTP is mainly responsible for the significantly high TSS concentration recorded at RZK, indicating that it did not effectively remove suspended solids, leading to the discharge of effluent with high TSS concentrations. This site recorded a relatively low DO concentration. Although the water flowed turbulently at this site, the relatively low DO concentration may result from bacteria consuming oxygen while decomposing organic material released from the Zeekoegat WWTP. Additionally, this site recorded an orthophosphate concentration below the detection limit and a substantially high TOC concentration. The Zeekoegat WWTP may be responsible for the significantly high TOC concentration.

The Zeekoegat WWTP is primarily responsible for the significant ammonium concentration recorded at RZK. The substantially low nitrate concentration, along with the significantly high ammonium concentration,

suggests that the Zeekoegat WWTP is likely not performing the nitrification process adequately. Moreover, the Zeekoegat WWTP is mainly responsible for the significantly high microbial counts, which exceed the detection limit, indicating it did not perform the disinfection process adequately.

7.8.5 Roodeplaat dam wall

The low TSS concentration, below the detection limit, recorded at RDW may be due to particles settling out of the water, as water flow typically slows down in this area, allowing suspended solids to settle more easily. The low DO concentration may be due to the lack of turbulent water flow and the limited presence of aquatic plants, such as hyacinth, at this site. RDW recorded a nitrate concentration below the detection limit and a relatively high ammonium concentration. This situation seems unusual, as it would be expected that the nitrate concentration exceeds the ammonium concentration. The water at the dam wall was exposed to oxygen for a longer period than the water upstream, resulting in the oxidation of ammonium to nitrate. RDW recorded an orthophosphate concentration below the detection limit and a relatively high TOC concentration. This may be due to the mix of rivers with high and low concentrations of these parameters flowing into the dam. RDW recorded relatively low microbial counts. This may be due to sedimentation and die-off of microbes as they travel further away from their sources. Also, this can be due to a lack of re-suspension, as the turbulence is low at this site.

7.9 PIPER DIAGRAMS

Most samples in the Hartbeespoort catchment area plot in the recently recharged field, characterised by Ca-Mg-HCO_3 ions (Figure 7-6). Notably, HJ3 and HH2 are plotting near the boundary of the Na-K-HCO_3 field. However, they primarily plot within the Ca-Mg-HCO_3 field. In contrast, HC2, HL1, and HDW show a Ca-Mg-Cl-SO_4 composition (Figure 6). This composition is associated with pollution from multiple sources, specifically mining and urbanisation (Masindi & Abiye, 2018). HC1 is an outlier with the same polluted composition.

Similarly, most samples in the Roodeplaat catchment area plot in the recently recharged field, characterised by a Ca-Mg-HCO_3 composition (Figure 7-7). RP2 plots near the Na-K-HCO_3 boundary but mainly falls in the Ca-Mg-HCO_3 field, while RZK primarily falls in the Na-K-HCO_3 field with some overlap in the Ca-Mg-HCO_3 field.

It is evident from the Piper diagrams that anthropogenic activities have a greater impact on the Hartbeespoort catchment area compared to the Roodeplaat catchment, as most samples plot higher in the diamond and anion triangle of the Hartbeespoort diagram.

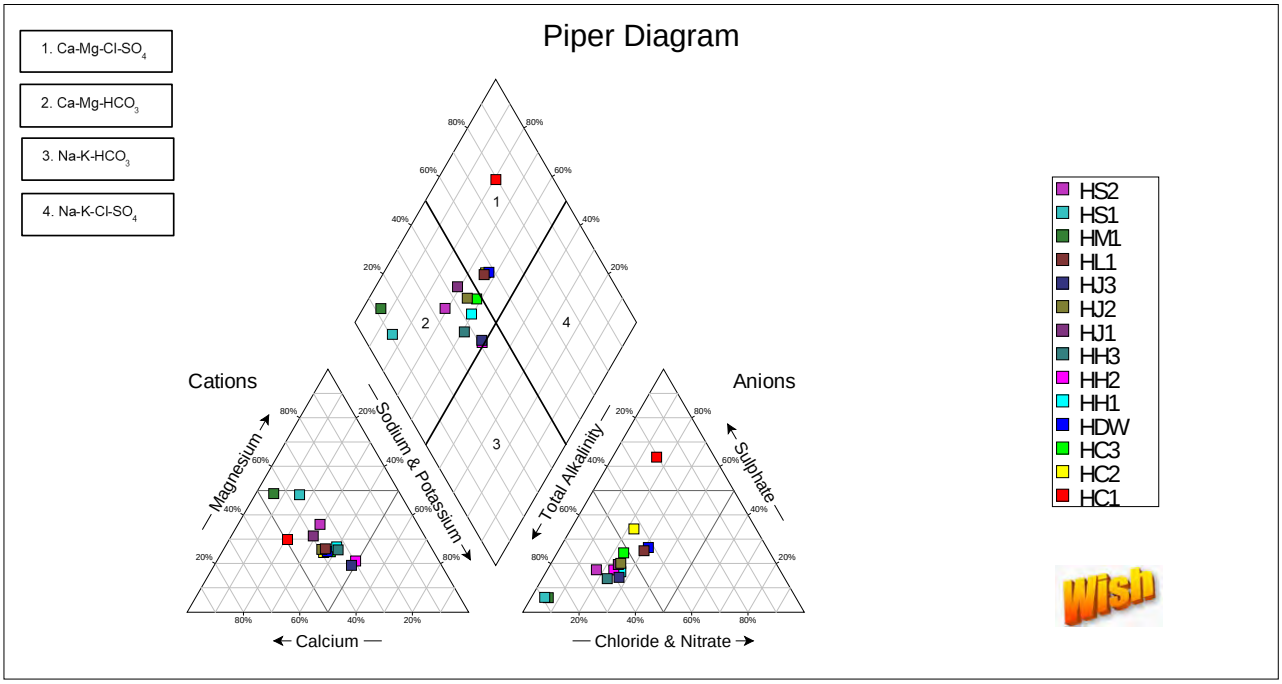

Figure 7-6 Piper diagram, constructed in WISH, of the selected sites in the Hartbeespoort catchment area.

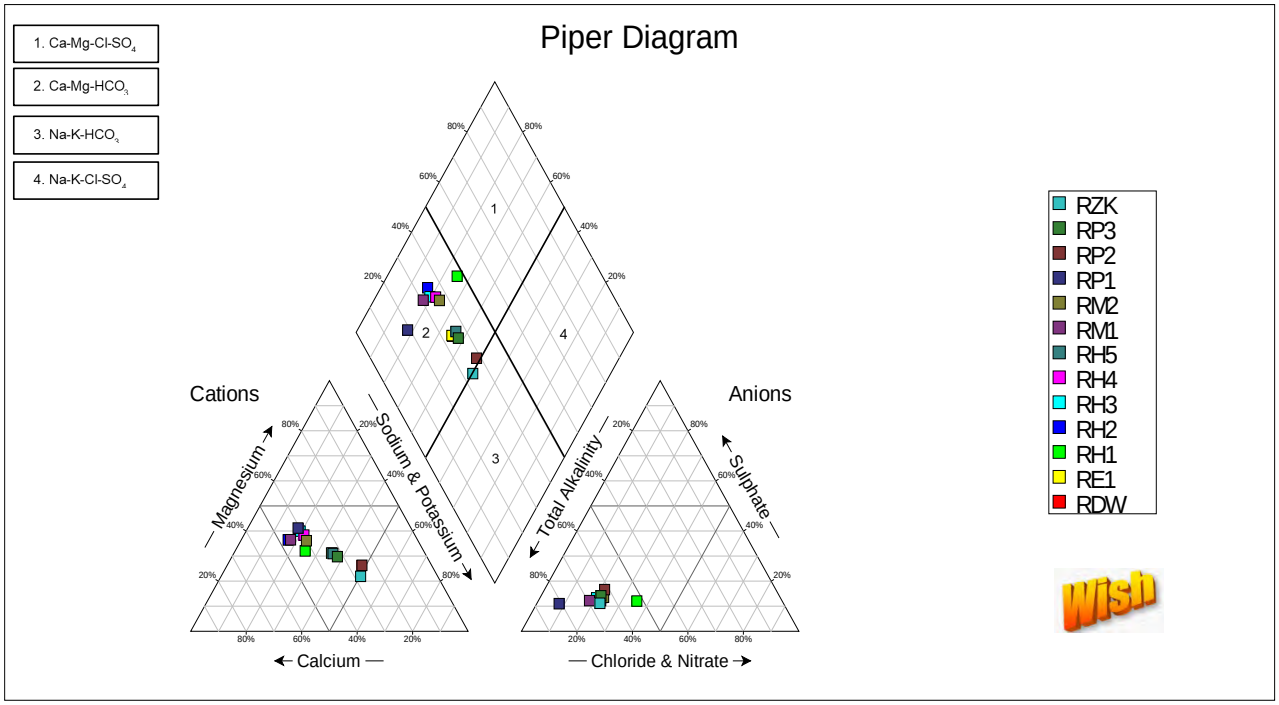

Figure 7-7 Piper diagram, constructed in WISH, of the selected sites in the Roodeplaat catchment area.

7.10 OUTCOMES AND FINDINGS

Urban water quality is influenced by a mix of land uses, including agriculture, formal and informal residential areas, and industrial activities within the catchment areas. These combined land uses collectively affect water

in the study regions. The data indicates that the most significant impact comes from malfunctioning WWTPs, with population density further pressuring these facilities and infrastructure. If the WWTPs operate optimally, water quality and aquatic health in the catchments are expected to improve substantially. Informal settlements also contribute to poor water quality due to inadequate sanitation, poor waste management, and ineffective stormwater drainage. While agricultural activities also affect water quality, their impact is smaller, as the catchment areas are primarily urban.

7.11 REFERENCES

Bosman, H.H. and Kempster, P.L. (1985). Precipitation chemistry of Roodeplaat Dam catchment. Water SA. 11(3): 157–164.

Botha, F.J. (2015). Nutrient reduction options in Hartbeespoort Dam catchments to lower in-dam eutrophication status. MSc dissertation, North-West University, North-West, South Africa, 1-130pp.

Carroll, A. (2020). A re-analysis of nutrient mass balances in the Hartbeespoort Dam. MSc dissertation, University of Witwatersrand, Johannesburg, South Africa, 1-115pp.

Davis, A. (2017). Hydrogeological Characteristics of Hartbeespoort Dam. MSc dissertation, University of Witwatersrand, Johannesburg, South Africa, 1-74pp.

Dudula, M.Z. (2007). A situation analysis of the water quality in the Hartbeespoort dam catchment: nutrients and other pollutants' assessment on rivers entering the dam. MSc dissertation, University of Witwatersrand, Johannesburg, South Africa, 1-146pp.

DWAF (Department of Water Affairs and Forestry). (2008). The development of a reconciliation strategy for the Crocodile (West) water supply system: Summary of previous and current studies. Report No. P WMA 03/000/00/3408, Prepared by BKS (Pty) Ltd and Arcus Gibb (Pty) Ltd. May 2008. DWAF.

Hoffman, J.R. (1994). Non-point source pollution in the Hennops River valley. Water Research Commission, Report number: 518/1/95.

Jardine-Da Silva, J.M. (2016). A case study on the historical water quality trends pertaining to the Jukskei River in the Gauteng Province, South Africa. MSc dissertation, University of Johannesburg, Johannesburg, South Africa, 1-87pp.

Latcheman, D.D.S. (2023). An assessment of land-based activities as inputs of microplastic pollution in South Africa's aquatic environment: a case study of Durban Bay harbour and the Hennops River. MSc dissertation, University of Witwatersrand, Johannesburg, South Africa, 1-95pp.

Lowies, M.L. (2014). A comparative study of chemical and physical water quality along the Crocodile River in the Gauteng and North West Provinces, South Africa. MSc dissertation, University of Johannesburg, Johannesburg, South Africa, 1-632pp.

Mabona, W. (2023). Tshwane's illegal suburb leaves residents stuck without services. GroundUp News. Available from: https://www.groundup.org.za/article/leeuwfontein-tshwanes-illegal-suburb-leaves-residents-stuck-without-basic-services/. (Accessed: 08 November 2023).

Masindi, K. and Abiye, T. (2018). Assessment of natural and anthropogenic influences on regional groundwater chemistry in a highly industrialized and urbanized region: a case study of the Vaal River Basin, South Africa. Environmental Earth Sciences. 77(20): 1–14.

Mawasha, T. and Britz, W. (2022). Detecting land use and land cover change for a 28-year period using multi-temporal Landsat satellite images in the Jukskei River catchment, Gauteng, South Africa. South African Journal of Geomatics, 11(1): 13–29.

Moeketsi, P., Nkhonjera, G.K. and Alowo, R. (2022). Changes in land use land cover within the Jukskei River Basin and its implications on the water availability. IOP Conference Series: Earth and Environmental Science, 1087(1): 1–9.

Mtshali, S. (2015). Surface hydrology report for the proposed Transnet Koedoespoort hazardous landfill stormwater design. July 2015.

Silberbauer, M.J. and Esterhuyse, C.M. Parallel drainages – the urban hydrology of the Moreletaspruit. In 17th SANCIAHS National Hydrology Symposium, UWC. SANCIAHS.

van Aardt, A.C., Scott, L., Grundling, P.-L., Grundling, A.T. and Woodborne, S. (2024). Revisiting past savanna environments: Pollen analysis of the COLBYN wetland on the Southern African Central Plateau. Review of Palaeobotany and Palynology. 331: 1–8.

Walmsley, R.D. and Toerien, D.F. (1978). The chemical composition of the waters flowing into Roodeplaat Dam. Water SA. 4(4): 192–202.

CHAPTER 8: TIMBAVATI GROUNDWATER AND SURFACE WATER QUALITY

→ Author: Kirsten Raible ←

This chapter emanates from the following project-related outcomes:

- Raible K. (2024). Hydrochemistry, hydrogen and oxygen isotopes, and radon in waters of the greater Timbavati catchment, South Africa. MSc (Specialising in Hydrogeology) Dissertation. University of Pretoria.
- Raible K, Diamond RE, Dippenaar MA (2025). Hydrochemistry, stable isotopes, and radon in waters of the Greater Timbavati catchment, South Africa. Hydrogeology Journal. 33:2003-2021. https://dx.doi.org/10.1007/s10040-025-02953-9

8.1 STUDY AREA DESCRIPTION

8.1.1 Locality and prevailing conditions / land use

The location of the study area can be seen in Figure 8-1**.** The location of the sample sites and underlying geology can be seen in Figure 8-2. The study area is within the Lowveld region of South Africa in both the Mpumalanga and Limpopo provinces. It initially consisted of a 10 km radius around the Hans Hoheisen Wildlife Research Station, located adjacent to the Orpen Gate of the Kruger National Park, but was then expanded to include the B73E and B73F quaternary catchments of the Lower Olifants catchment and the X40C quaternary catchment of the Sabie-Sand River Catchment. Most of the study area consists of game and wilderness reserves. There are, however, also the communities of Welverdiend and Acornhoek in the southwestern section of the study area. The land in these communities has been developed to an extent, and they also use large areas of land for grazing cattle and other livestock as well as growing the occasional crop.

8.1.2 Geology

There are two principal types of gneisses in the Lowveld, south of the Murchison Greenstone Belt: the layered composite Makhutswi Gneiss and the homogeneous Klaserie Gneiss (Robb et al., 2006). These are Palaeoarchaean intrusions formed around 3600-3200 million years ago. Approximately 1106-1112 million years ago, large-scale magmatism led to the emplacement of over 2 million km³ of mantle-derived magma into the Palaeoarchaean to Mesoproterozoic formations and cratonic basement rocks on the Kaapvaal Craton. This group, known as the Umkondo Igneous Province, includes intrusions such as the Timbavati Gabbro (Allsopp et al., 1989; Anhaeusser, 2006; Hanson et al., 2004a; Hanson et al., 2004b).

The Makhutswi Gneiss occurs in two sections, covered by Karoo and Transvaal Supergroup rocks in the east and west, respectively. It is light grey, fine to medium-grained, with alternating leucosome bands up to 15 cm thick, and is complexly folded (Robb et al., 2006; Schutte, 1986; Walraven, 1989). The major minerals found in this rock are plagioclase, microcline, quartz, and biotite, with hornblende and pyroxene present only occasionally. Limited geochemical data suggest that the Makhutswi Gneiss is tonalitic to granodioritic in composition. Remnants of ultramafic, amphibolite, metaquartzite, and calc-silicate rocks are also found within the Makhutswi Gneiss (Schutte, 1986; Robb, Brandl, Anhaeusser, & Poujol, 2006). Poujol et al. (1996) estimated the age of the Makhutswi Gneiss at around 3228±12 Ma near the Murchison Greenstone Belt, while Barton (1984) found it to be around 3268±113 Ma in the Phalaborwa area. A younger tonalitic, unmigmatised biotite gneiss is locally intruded as dyke or stock-like bodies, with an age estimated at around 3112±5 to 3078±6 Ma (Robb et al., 2006).

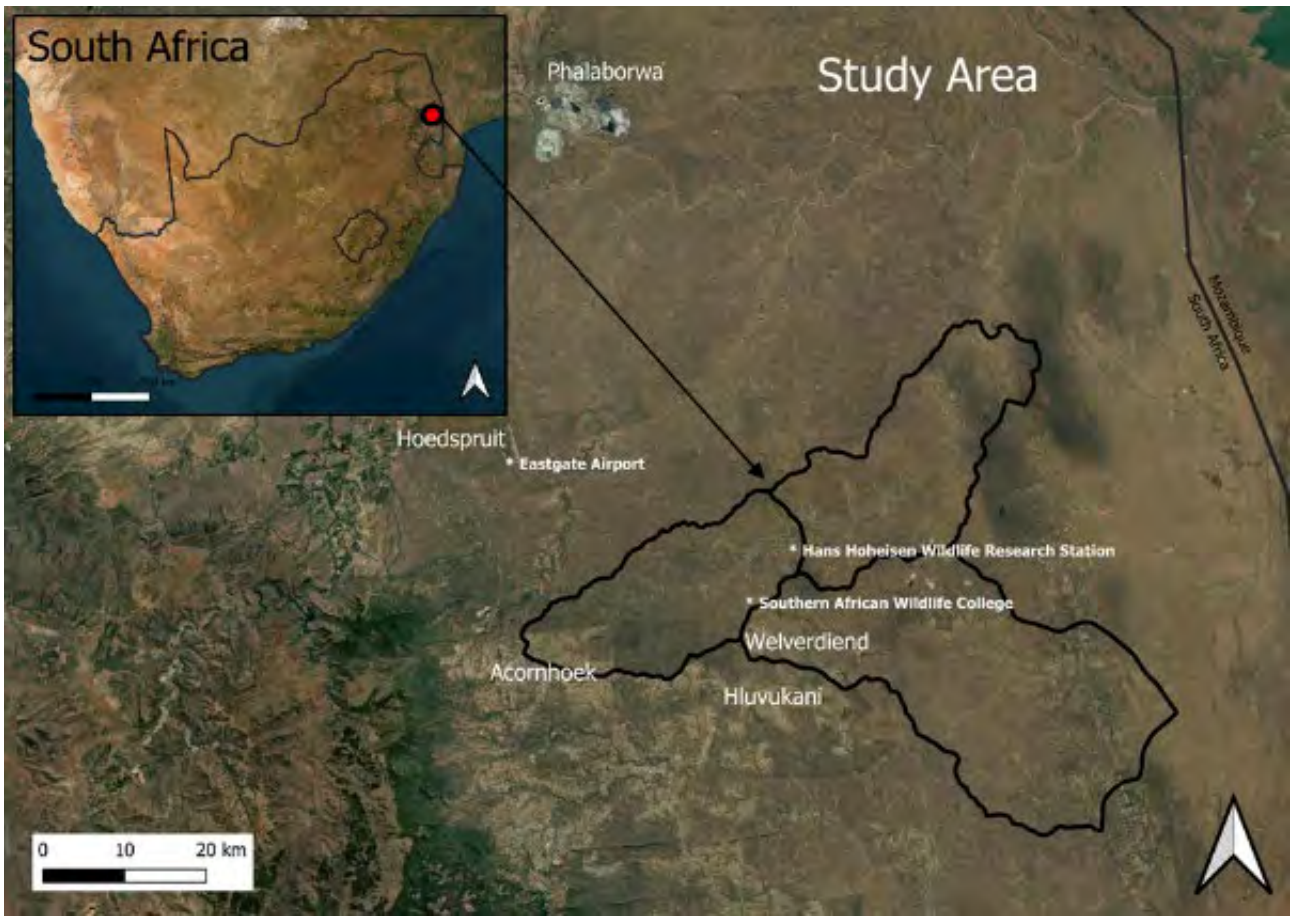

Figure 8-1 Regional locality and catchment boundaries.

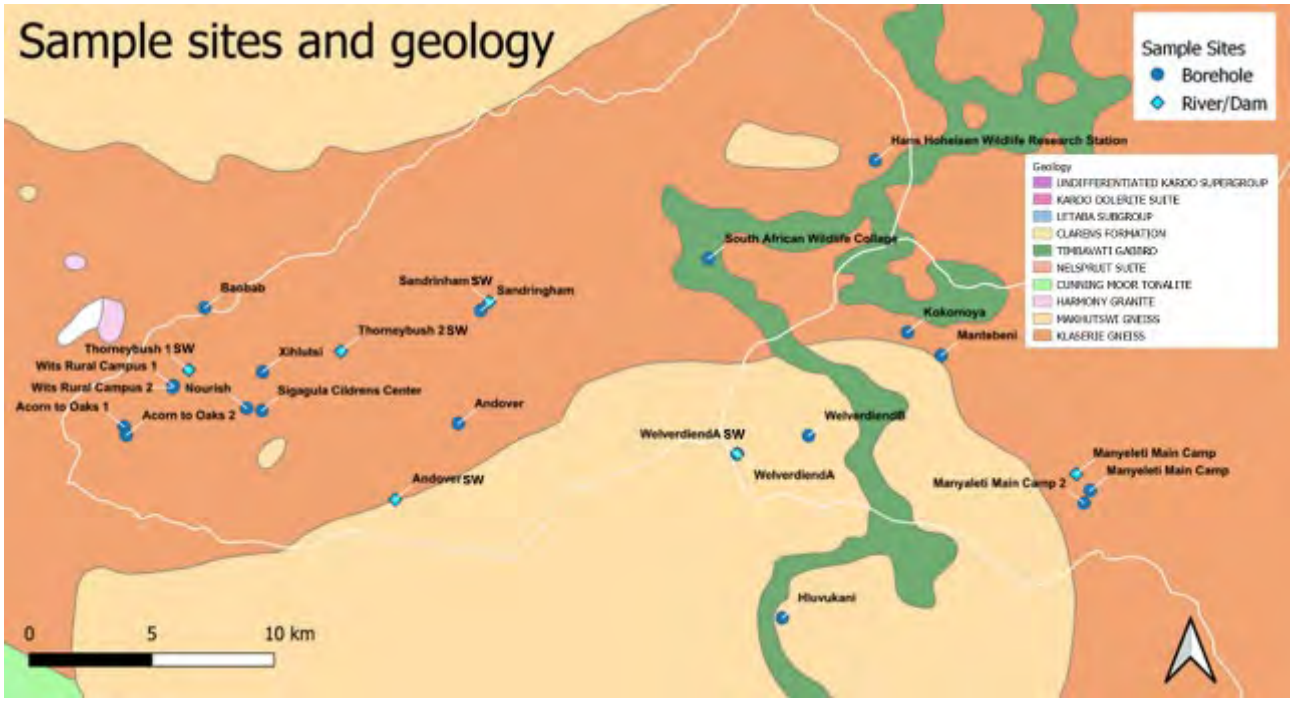

Figure 8-2 Sampling positions in relation to the geology in the catchments (Raible et al., 2025).

The Klaserie Gneiss is located between the two sections of Makhutswi Gneiss and contacts the Nelspruit Suite and Cunning Moor Tonalite body. It has a mineralogy similar to that of the Makhutswi Gneiss but is coarse-

grained, well-foliated, and not migmatised (Robb et al., 2006; Walraven, 1989). The Klaserie Gneiss is believed to post-date the Makhutswi Gneiss, but no radiometric ages are currently available (Robb et al., 2006).

The Timbavati Gabbro consists of mafic to ultramafic rocks intruding various older granites, gneisses, and magmatic Archaean basement rocks of the Mpumalanga Lowveld. Discontinuous outcrops occur as a series of small hills and ridges, following a roughly zigzag pattern in the western half of Kruger National Park (Anhaeusser, 2006; Brandl, 1985a; Saggerson and Logan, 1970; Walraven, 1986, 1989a; Walraven and Hartzer, 1986). These intrusions appear sill-like, dipping between 20 and 30 degrees towards the east (Schutte, 1986). The emplacement of the Timbavati Gabbro was influenced by pre-existing structures in the basement granitoids, such as faulting, jointing, and regional foliation (Anhaeusser, 2006; Bristow et al., 1982). Mapping by Michaluk (1983) showed that the sill outcrop pattern formed a series of connected arched segments, suggesting that the Timbavati Gabbro was emplaced along a series of north-south linked conical fractures (Walraven, 1983; Walraven, 1986). In the Orpen area, the sills are believed to be about 200 m wide (Gordon-Welsh, 1980), while in the Pretoriuskop area, they range between 300 and 480 m (Clubley-Armstrong, 1979). A chill margin is present at the contact between the host rocks and the gabbro, with the host rock showing varying degrees of recrystallisation (Schutte, 1986). A geochemical study by Walraven (1984) concluded that the magma of the Timbavati Gabbro resulted from several separate intrusive pulses rather than a single differentiated intrusion, leading to at least three different types of gabbro (Anhaeusser, 2006; Walraven, 1986).

The geology of the area includes the Makhutswi and Klaserie Gneiss, primarily composed of plagioclase ($NaAlSi_3O_8$ – $CaAl_2Si_2O_8$), microcline ($KAlSi_3O_8$), quartz (SiO_2), and biotite ($K(Mg,Fe)_3AlSi_3O_{10}(F,OH)_2$) (Schutte, 1986; Robb et al., 2006). The Timbavati Gabbro consists mainly of olivine ($(Mg,Fe)_2SiO_4$), clinopyroxene ($Ca(Mg,Fe)Si_2O_6$), orthopyroxene ($(Mg,Fe,Ca)(Mg,Fe,Al)(Si,Al)_2O_6$), and plagioclase ($NaAlSi_3O_8$ – $CaAl_2Si_2O_8$) (Walraven, 1986).

8.1.3 Hydrology and hydrogeology

The study area is located within the B73E and B73F quaternary catchments of the Lower Olifants catchment, within the Olifants Water Management Area, as well as the X40C quaternary catchment of the Sabie-Sand River Catchment, within the Inkomati Water Management Area. The Timbavati River is the main river in the study area. It is perennial and flows towards the northeast. The Lower Olifants catchment represents the catchment of the Olifants River between the Steelpoort confluence and the Mozambique border. According to the *Olifants Water Management Area Internal Strategic Perspective* compiled by DWAF (2004), the area is characterised by having large agricultural developments, including irrigation and wide tracts of game management areas, including the western portion of the Kruger National Park. There is, however, little groundwater development.

The average mean annual precipitation in the catchment is less than 500 mm but can reach 1000 mm along the escarpment. Aquifers are confined to weathered and fractured rock zones and boreholes are between 30 to 80 m deep with water levels between 5 and 15 mbgl. While the groundwater quality is generally good, there are isolated areas with elevated nitrate concentrations. The main use of groundwater is for domestic use and stock watering. Boreholes generally yield between 0.5 ℓ/s and 2 ℓ/s, in areas east of Hoedspruit, it can increase to 5 ℓ/s. Groundwater recharge is between 25-37 mm/a in the westernmost section of the B73E quaternary catchment and decreases to 10-15 mm/a in the B73F quaternary catchment. TDS values within the B73E and B73F quaternary catchments are between 500 and 2000 mg/ℓ, with the western half of B73E and the eastern section of B73F generally having the lower values (Department of Water Affairs and Forestry, 2004). The average mean annual precipitation in the catchment is less than 500 mm but can reach 1000 mm along the escarpment. Aquifers are confined to weathered and fractured rock zones and boreholes are between 30 to 80 m deep with water levels between 5 and 15 mbgl. While the groundwater quality is generally good, there are isolated areas with elevated nitrate concentrations. The main use of groundwater is for domestic use and

stock watering. Boreholes generally yield between 0.5 ℓ/s and 2 ℓ/s, in areas east of Hoedspruit, it can increase to 5 l/s. Groundwater recharge is between 25-37 mm/a in the westernmost section of the B73E quaternary catchment and decreases to 10-15 mm/a in the B73F quaternary catchment. TDS values within the B73E and B73F quaternary catchments are between 500 and 2000 mg/ℓ, with the western half of B73E and the eastern section of B73F generally having the lower values (Department of Water Affairs and Forestry, 2004).

8.1.4 Weather/climate

The lowveld climate is known for having a hot and humid summer with a mild and dry winter. The climate of southern Africa is influenced by anticyclonic systems that are semi-rhythmically moving from east to west (Venter and Gertenbach, 1986). Based on the Köppen climate classification system, the study area has a Cwa subtropical climate.

8.2 METHODS

8.2.1 Desktop Study

A desktop study was conducted by reviewing existing data and available literature for the study area, such as the climate, geology, hydrology, and hydrogeology. Secondary data was also obtained in the form of GIS data sets. These included land use from the European Space Agency Climate Change Initiative Land Cover project, a digital elevation model from USGS Earth Explorer and geology from the Council for Geoscience.

8.2.2 Field work

An initial hydrocensus was conducted in September 2021 before sampling took place and additional data was added to the hydrocensus as more sample sites were identified on later site visits. Landowners and managers as well as community leaders in the Timbavati Catchment area were contacted directly to acquire access to the boreholes and surface water bodies. The following data was recorded for boreholes during the hydrocensus: the owner, the coordinates, date and time of recording, its use, the pump type, the power supply to the pump, borehole construction material, the collar height, the protection, when the borehole was last pumped, and a photograph of the borehole. When possible, the borehole depth, pump depth and water level were also recorded.

From the boreholes and surface water bodies identified in the hydrocensus, 25 sampling points were chosen based on their accessibility. These 25 sites consist of six surface water sample points and 19 groundwater sample points. While most of the sampling sites were located within game reserves, a few were also located on land belonging to community outreach centres and communal land. For security reasons, when sampling in the reserves a game ranger was always present. The locations of the sampling points can be seen Figure 8-2.

All sampling was done in accordance with SABS ISO 5667 guidelines. Five sampling rounds were conducted over a two-year period to obtain data that reflected seasonal variations in the water chemistry as shown in Table 8-1. A total of 100 samples were collected during the dry and wet seasons and the data that was recorded when sampling include the sample ID, reason for sampling, location of sampling point, nature of sampling point, date, time, sample method, sample appearance, details of preservation techniques, details of sample storage method employed, possible source of sampling bias, name of sample collector, and a photograph of the sample site. Rainwater was collected and rainfall (mm) was recorded at two sites, namely Hans Hoheisen Wildlife Research Station and Manyeleti Main Camp for isotope analysis.

Table 8-1 Sampling schedule

Round of Sampling	Dates of Sampling	Notes
First	14/09/2021 to 15/09/2021 26/10/2021 to 28/10/2021	Minimal sampling was done during this time as sites were still being identified
Second	21/02/2022 to 25/02/2022	
Third	30/05/2022 to 03/06/2022	
Fourth	29/08/2022 to 02/09/2022	Samples were taken for chemical analysis
Fifth	21/11/2022 to 25/11/2022	

Equipment was cleaned and calibrated the night before sampling took place. As all the boreholes being sampled were equipped with pumps, taps or pipes were opened to allow access to the borehole water as close to the pump as possible and before water entered a tank. If the borehole was not currently in use, it was switched on and allowed to run for 10 minutes before the sample was taken. The sample bottles, containers, and Aquaread AP-5000 were all rinsed in the water from the borehole before the samples were taken. Groundwater samples were collected in 2 PET bottles and into the Aquaread AP-5000 calibration cup. Sample bottles were then sealed and labelled with the sample name and date of sampling; no preservation techniques were used. The Aquaread AP-5000 was then lowered into the calibration cup and the analysis run. The reason for the on-site analysis being done in the calibration cup rather than by lowering the Aquaread AP-5000 down the borehole is that all the boreholes had pumps installed. The equipment was cleaned and dried before being packed away.

The sampling procedure for surface water bodies was mostly the same as that for the borehole samples, except that the water was collected from the larger surface water bodies using a bailer before being transferred to the sample bottles and containers. Samples were collected using a bailer as it was not safe to put the PVC bottles directly in the water due to the presence of crocodiles and hippopotami. Rainwater was collected in a rain gauge and rainfall volumes were recorded every morning at 08h00 against the previous day's date. Rainwater was then poured into a 5ℓ bottle, and the lid was tightly sealed to prevent evaporation. At the end of the month, the 5ℓ bottle was shaken to ensure the water was well mixed, including the water droplets on the side of the bottles. The water was then poured into 2 smaller 50 mℓ bottles, to the top if possible, and the lid tightly sealed to prevent evaporation. The bottle was then labelled with the respective month and location.

8.3 WATER QUALITY AND LABORATORY RESULTS

8.3.1 TDS, ORP, DO and pH

The relationship between TDS, ORP, DO, and pH concentrations was analysed across five rounds of sampling (Figure 8-3). pH values in groundwater samples ranged from 6.97 to 8.40, with a mean value of 7.48, while surface water samples ranged from 7.47 to 9.3, with a mean value of 8.30. Most groundwater samples and all surface water samples were found to be alkaline. Groundwater TDS values ranged from 540 to 3 580 mg/ℓ, with a mean value of 1 220 mg/ℓ, whereas surface water samples ranged from 140 to 620 mg/L, with a mean value of 330 mg/ℓ. Although there appeared to be a trend of decreasing TDS with increasing pH, the Pearson correlation coefficient (r) values indicated no correlation for groundwater samples (r = -0.15) and minimal correlation for surface water samples (r = -0.5). ORP values in groundwater samples ranged from 19 to 200 mV, with a mean of 99 mV, while surface water samples had ORP values ranging from 35 to 196 mV, with an average of 91 mV. Pearson's r values indicated a minimal correlation between ORP and pH in surface water samples (r = 0.45), while no correlation was observed in groundwater samples (r = 0.20). DO concentrations in groundwater samples ranged from 2.65 to 8.60 mg/ℓ, with a mean of 5.33 mg/ℓ. Surface water samples had DO concentrations ranging from 6.26 to 12.66 mg/ℓ, with a mean of 8.22 mg/ℓ. No correlation was found

between DO and pH in both groundwater and surface water samples, with Pearson's r values of 0.06 and 0.13, respectively.

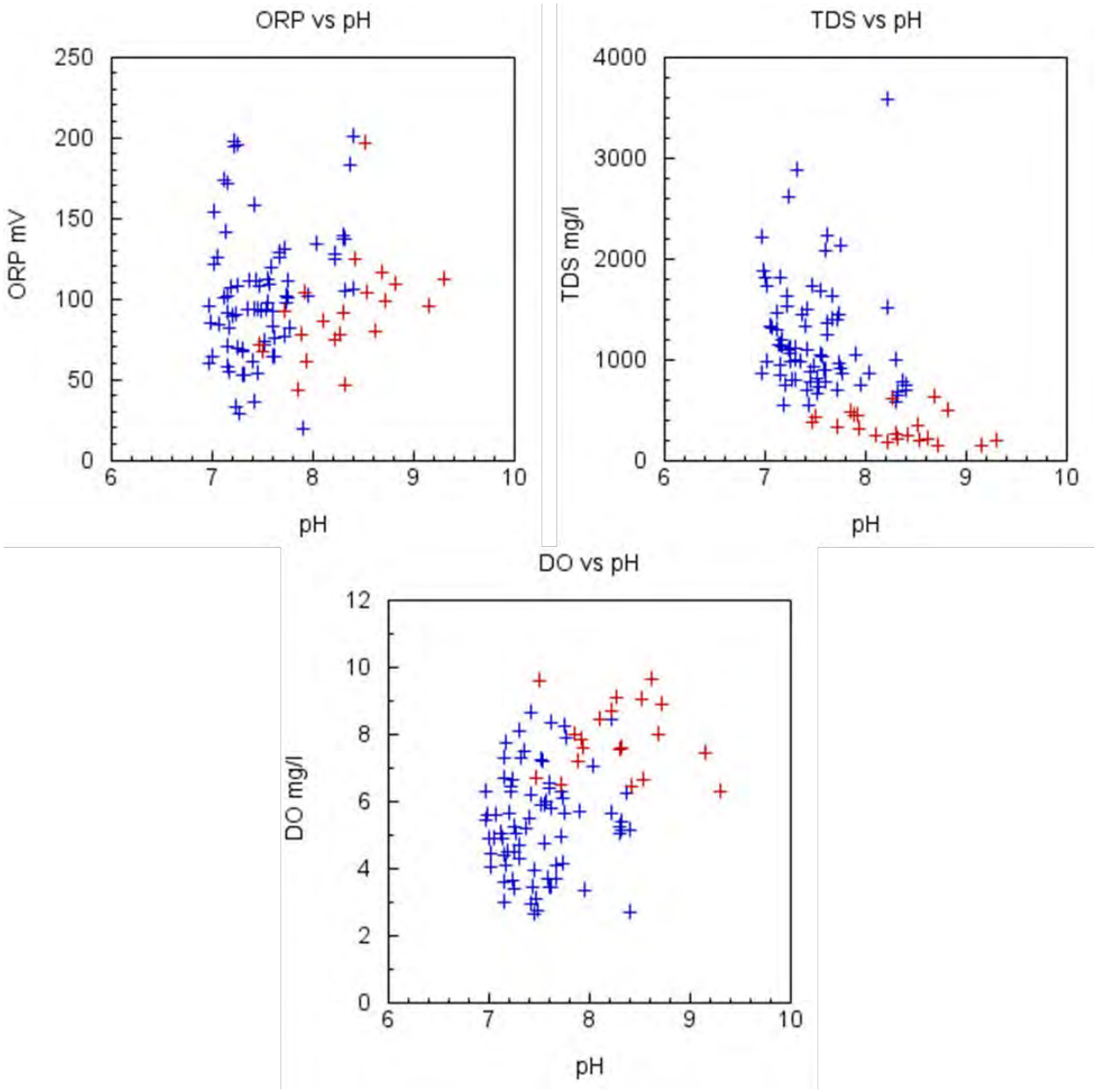

Figure 8-3 Graphs showing the relationship between TDS, DO and ORP versus pH respectively for all the groundwater (blue) and surface water (red) samples taken during the 5 rounds of sampling (Raible et al. 2025).

8.3.2 Cations and Anions

Analysis of the cation and anion compositions showed that most water samples were within mixed cation and anion facies, except for WelA, HLU, and UPCell. (Table 8-2 and Figure 8-4) The predominant cation composition in most samples was $Na^+ + K^+$ (49%-76%), followed by Mg^{2+} (12%-29%) and Ca^{2+} (7%-30%). Anion compositions ranged from HCO_3^- (48%-80%) to Cl^- (17%-49%) and SO_4^{2-} (1%-9%). Cation and anion concentrations were generally higher in groundwater than in surface water samples, except for UPCell, which had a unique magnesium bicarbonate-type composition. WelA and HLU samples were characterised as chloride types, with higher chloride concentrations compared to other samples.

Table 8-2 Cation and anion compositions for water samples taken during the fourth round of sampling

Locality	Date	pH	Ca (mg/ℓ)	Mg (mg/ℓ)	Na (mg/ℓ)	K (mg/ℓ)	HCO_3 (mg/ℓ)	Cl (mg/ℓ)	SO_4 (mg/ℓ)
60SCC	29-Aug-2022	7.66	33.7	18.3	141.0	0.541	372	71.7	16.3
61NOR	29-Aug-2022	8.06	44.2	23.0	164.0	1.38	416	151	8.51
62A201	29-Aug-2022	8.49	46.3	22.9	177.0	0,309	407	207	4.75
63A202	29-Aug-2022	7.54	43.6	16.0	173.0	0.911	429	166	4.39
64SAN	30-Aug-2022	7.41	59.5	43.7	195.0	142	788	98.3	25.6
65SANSW	30-Aug-2022	7.59	16.5	9.22	48.1	4.46	167	42.4	4.71
66AND	30-Aug-2022	7.48	44.9	23.5	181.0	3.34	446	155	11.7
67ANDSW	30-Aug-2022	7.37	6.45	4.07	24.6	16.9	85,7	27.1	7.83
68WITS1	30-Aug-2022	7.29	48.6	19.5	102.0	0.442	352	96.5	29.7
69WITS2	30-Aug-2022	7.53	49.5	18.8	126.0	1.59	467	78.3	24.7
70WELA	31-Aug-2022	7.73	125.0	93.8	224.0	9.3	465	461	42.8
71WELASW	31-Aug-2022	7.72	24.6	10.9	27.2	31.3	211	42,7	6.78
72HLU	31-Aug-2022	7.43	192.0	136.0	314.0	11.7	641	761	98.3
73THORSW1	31-Aug-2022	7.66	28.3	18.3	112.0	0.264	243	145	10.4
74Xih	31-Aug-2022	7.72	45.7	34.6	265.0	1.2	526	287	24
75MANM1	01-Sep-2022	7.86	24.5	35.6	299.0	1.96	740	226	13.7
76MANM2	01-Sep-2022	7.62	45.5	50.3	200.0	1.84	743	136	19.0
77MANSW	01-Sep-2022	7.75	7.35	4.88	18.8	9.44	70,3	21.2	8.57
78MANT	01-Sep-2022	7.25	91.9	88.7	292.0	10.9	943	406	17
79KM	01-Sep-2022	7.45	61.0	53.1	289.0	7.39	803	276	14.5
80UPCell	02-Sep-2022	7.47	50.9	138.0	70.05	5.28	769	151	38
81BA0	22-Sep-2022	7.37	53.7	14.4	127.0	1.61	364	81.4	20.3

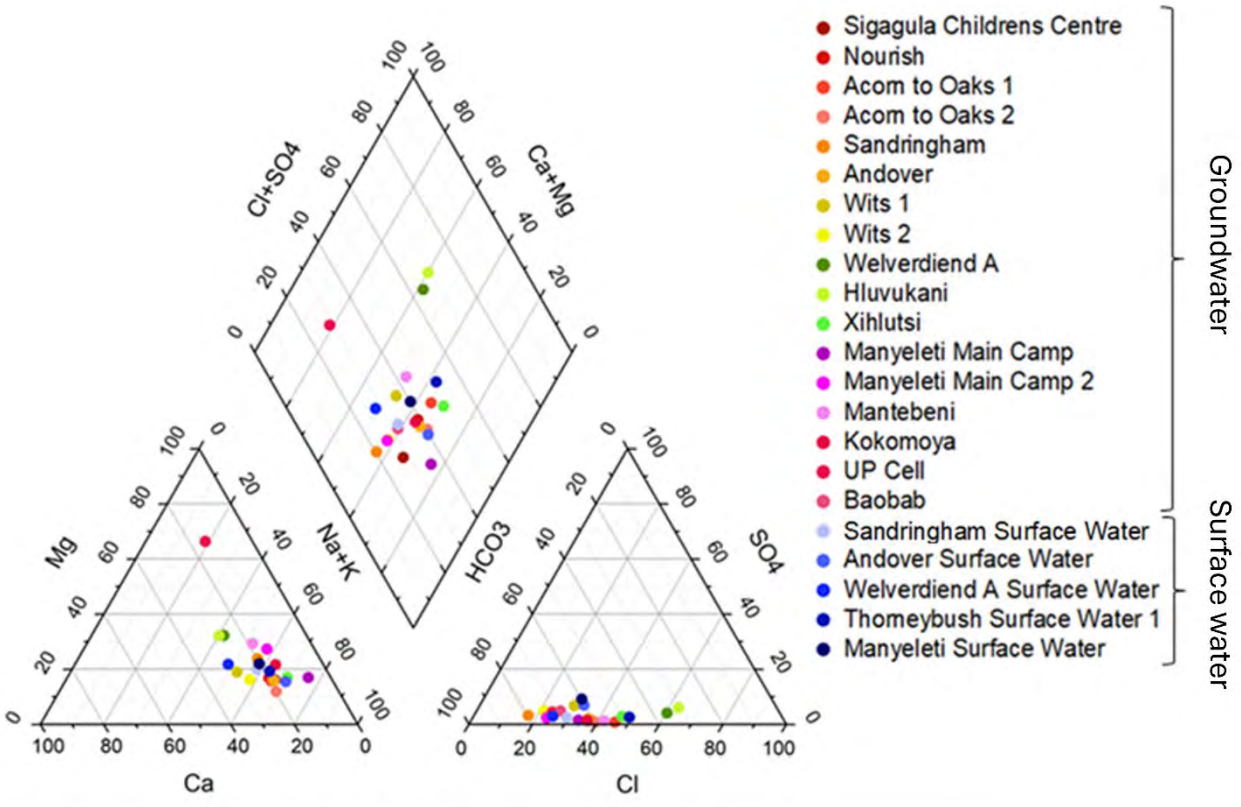

Figure 8-4 Piper plot of the cation and anion facies for water samples taken during the fourth round of sampling (Raible et al. 2025).

Further analysis showed that, except for WelA, HLU, and UPCell, groundwater samples followed similar compositional trends, with lower Na^+ concentrations in UPCell and higher Cl^- concentrations in WelA and HLU. Surface water samples generally had lower ion concentrations compared to groundwater samples, except for potassium, which was higher in surface waters. Groundwater samples such as SCC, NOR, A2O2, AND, Wits1, Wits2, and BAO, along with surface water samples like SANSW, ANDSW, WelASW, and MANSW, exhibited compositions of $Na^+ + K^+ > HCO_3^- > Cl^- > Ca^{2+} > Mg^{2+} > SO_4^{2-}$. Other samples, including MANM, MANT, and KM, displayed a similar but slightly varied composition. Unique trends were observed in specific samples, such as high chloride levels in WelA and HLU and high magnesium levels in UPCell.

8.3.3 ICP Metal Scan

Results from the ICP-Metal scan revealed that elements such as lithium, boron, aluminium, silicon, scandium, titanium, vanadium, manganese, iron, cobalt, nickel, copper, zinc, arsenic, rubidium, strontium, rhodium, caesium, barium, and europium were present in at least one sample with concentrations of 0.001 mg/ℓ or above.

8.3.4 Nitrates

NH_4, NO_3^-, and TDS concentrations were analysed over five rounds of sampling, with results showing consistently higher nitrate levels in more urbanised areas (Table 8-3 and Figure 8-5). NH_4 concentrations in groundwater ranged from 0.01 to 0.75 mg/ℓ with a mean of 0.20 mg/ℓ, while surface water concentrations ranged from 0.02 to 1.7 mg/ℓ with a mean of 0.34 mg/ℓ. A minimal correlation was observed between NH_4 and TDS in groundwater (Pearson's r = 0.47), with no significant correlation in surface water (r = 0.19). NO_3^- concentrations in groundwater ranged from 0.28 to 1350 mg/ℓ with a mean of 83.1 mg/ℓ, while surface water concentrations ranged from 1.59 to 10.4 mg/ℓ with a mean of 5.56 mg/ℓ. Surface water samples showed no correlation between nitrate and TDS (r = -0.19), whereas groundwater samples exhibited a moderate correlation (r = 0.59).

Table 8-3 Summary of nitrate concentrations from water samples taken during all 5 rounds of sampling (Raible et al. 2025).

Round of Sampling	Average NO_3^- (mg/ℓ)			
	Surface water	Groundwater: all	Groundwater: without Welverdiend A, Welverdiend B and Hluvukani	Groundwater: just Welverdiend A, Welverdiend B and Hluvukani
September and October 2021	1.49	38.5	12.3	169.4
February 2022	6.30	71.8	18.2	339.6
May and June 2022	5.63	51.3	14.0	331.3
August and September 2022	5.76	81.8	18.3	526.1
November 2022	5.76	148.0	12.9	1092.0
All Rounds	5.56	83.1	15.6	508.7

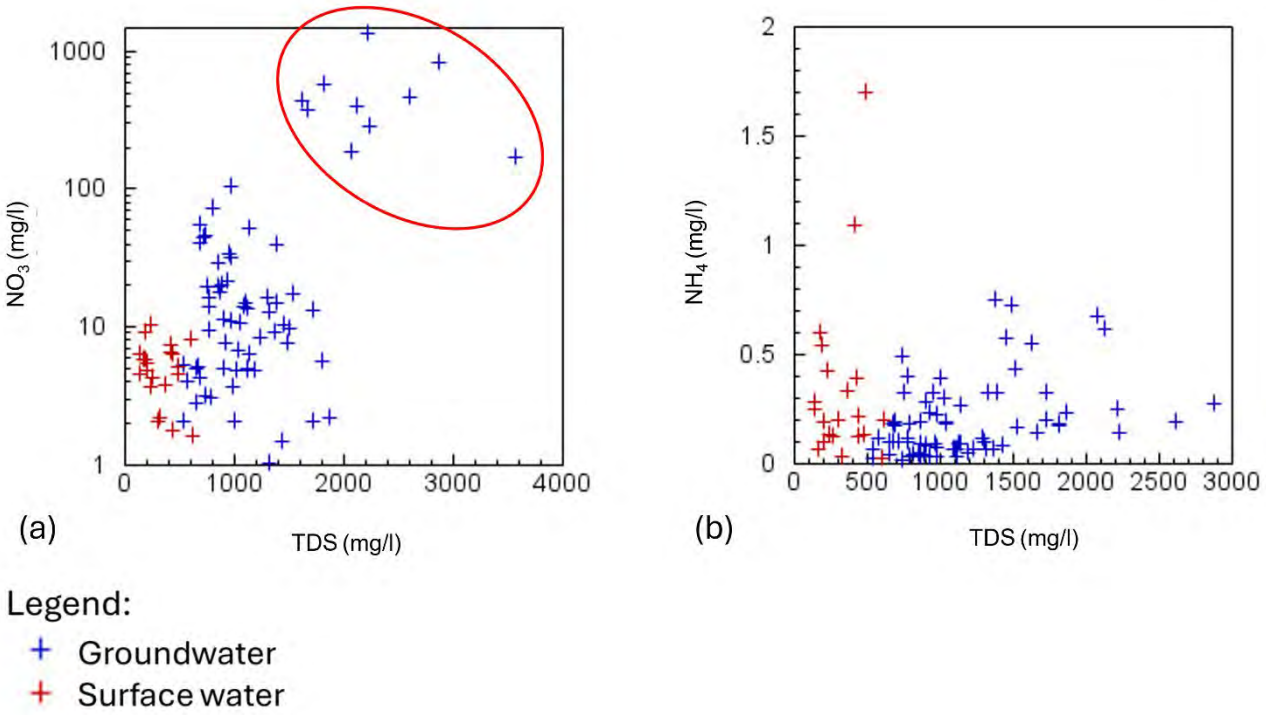

Figure 8-5 Nitrate and ammonium concentrations from water samples taken during all 5 rounds of sampling. Circled in red are the groundwater samples taken from Welverdiend A, Welverdiend B and Hluvukani (Raible et al. 2025).

8.3.5 Hydrogen and Oxygen Isotopes

The variation between the mean isotope compositions of groundwater and surface water samples is -32.7‰ for δD and -6.1‰ for δ18O. Surface water samples were used to calculate the equation for the local evaporation line: δD = 5.1 δ18O + 0.3. The weighted regression equation for the local meteoric water line is δD = 6.2 δ18O + 8.3, while the regression line for groundwater samples is δD = 4.9 δ18O - 1.7. Groundwater samples consistently show a lighter isotopic composition compared to surface water samples. Additionally, the months with the lowest rainfall had the heaviest isotopic compositions. The minimum, maximum, and mean isotopic compositions for groundwater and surface water are provided for reference (Table 8-4 and Figure 8-6).

Table 8-4 Summary of hydrogen and oxygen isotopes concentrations from water samples taken during all 5 rounds of sampling as well as rainwater samples collected over entire study period.

	Min		Max		Mean	
	δD (‰)	**$\delta^{18}O$ (‰)**	**δD (‰)**	**$\delta^{18}O$ (‰)**	**δD (‰)**	**$\delta^{18}O$ (‰)**
Groundwater	-27.7	-0.8	-5.0	1.3	-20.5	-3.8
Surface water	-14.2	-2.2	41.9	7.5	12.2	2.3
Rain	-24.9	-4.8	33.1	5.4	-2.76	-1.9

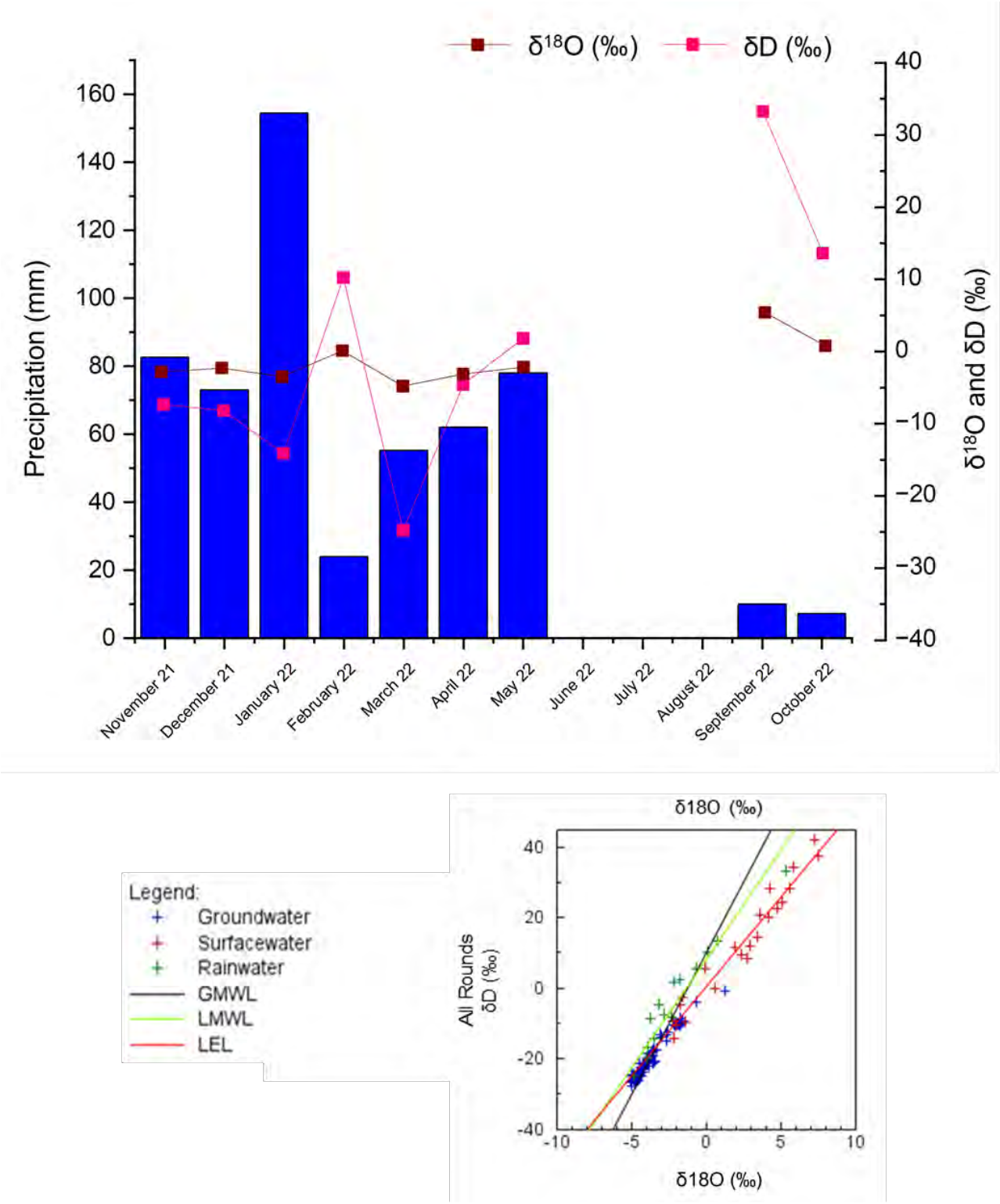

Figure 8-6 Monthly precipitation and corresponding hydrogen and oxygen isotope concentrations (top), and hydrogen and oxygen isotope concentrations from water samples taken during all 5 rounds of sampling as well as rainwater samples collected over entire study period (bottom) (Raible et al. 2025).

8.3.6 Radon

The RAD7 printout provides the arithmetic mean of radon concentrations, along with the highest and lowest values and the standard deviation of the readings taken during each run. Mean surface water radon

concentrations ranged from 0 to 522 Bq/m³, with an average of 119 Bq/m³. In contrast, mean groundwater concentrations ranged from 188 to 51,400 Bq/m³, with an average of 16,900 Bq/m³ (Table 8-5 and Figure 8-7). The data were analysed to examine the relationship between mean radon and pH concentrations over five sampling rounds, as well as changes in average radon concentrations for combined surface water and groundwater samples across each sampling round. Additionally, mean radon concentrations were compared with the underlying geology of the study area to identify potential links between geology and radon levels.

Table 8-5 Summary of radon concentrations from water samples taken during all 5 rounds of sampling

Site name	Radon (Bq/m³)				Geology
	Mean	High	Low	SD	
Baobab	4000	5000	3000	800	Klaserie Gneiss
Thorneybush - Xihlutsi	6000	7000	6000	600	Klaserie Gneiss
South African Wildlife College	7000	8000	6000	1000	Klaserie Gneiss
Manyeleti Main Camp 1	8000	9000	7000	700	Klaserie Gneiss
WelverdiendA	8000	9000	8000	600	Makhutswi Gneiss
Hluvukani	9000	10000	8000	1000	Makhutswi Gneiss
Wits Rural Campus 2	9000	10000	8000	800	Klaserie Gneiss
Sigagula Childrens Centre	9000	10000	8000	1000	Klaserie Gneiss
Manyeleti Main Camp 2	15000	17000	13000	1000	Klaserie Gneiss
Andover	15000	17000	13000	2000	Klaserie Gneiss
Wits Rural Campus 1	20000	22000	18000	2000	Timbavati Gabbro
UPCell	22000	25000	20000	2000	Klaserie Gneiss/Timbavati Gabbro
Kokomoya	24000	26000	22000	5000	Klaserie Gneiss
Sandringham	24000	26000	22000	2000	Klaserie Gneiss
Mantebeni	25000	28000	23000	2000	Klaserie Gneiss
Nourish	25000	27000	23000	2000	Klaserie Gneiss
Acorn to Oaks 1	26000	27000	24000	2000	Klaserie Gneiss
Acorn to Oaks 2	34000	38000	31000	3000	Klaserie Gneiss

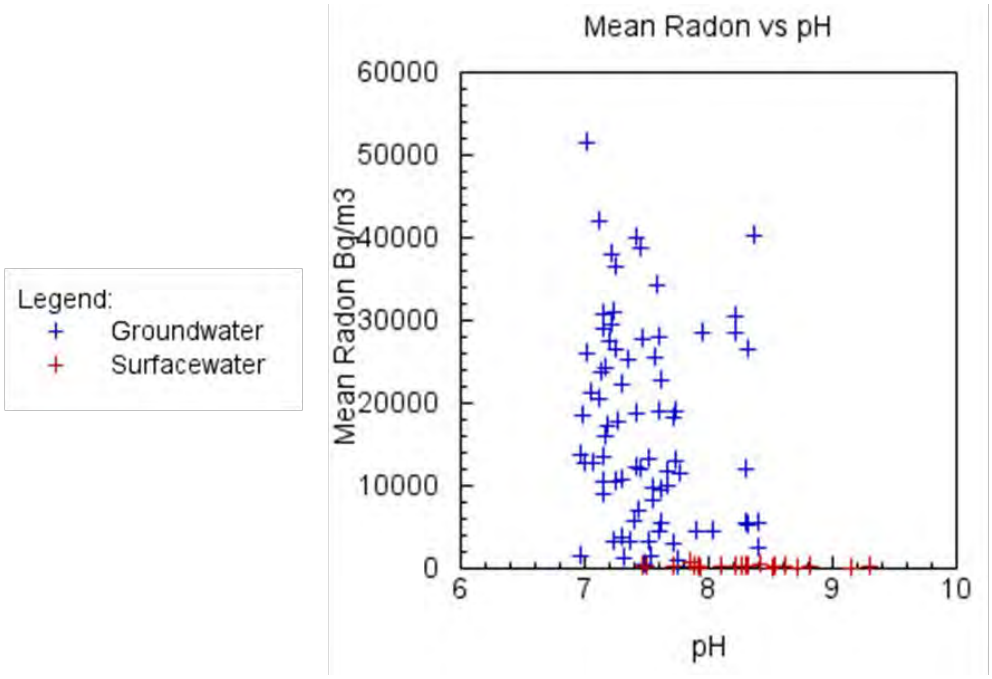

Figure 8-7 Radon concentrations from water samples taken during all 5 rounds of sampling.

8.4 DISCUSSION

8.4.1 Water Quality

Several water samples from the Timbavati region exceeded recommended guidelines for various contaminants, highlighting significant water quality issues as shown in Table 8-6. Sodium levels in samples WelA, HLU, Xih, MANM2, MANT, and KM were above SABS aesthetic guidelines, while potassium concentrations in MANT, HLU, ANDSW, and WelASW surpassed WHO recommendations. Fluoride levels in BAO and Xih exceeded the WHO guideline of 1.5 mg/L, increasing the risk of fluorosis, a condition that causes skeletal deformations. Heavy metals, particularly arsenic and nickel, were found at toxic levels, with samples HLU, WelA, MANT, KM, Xih, and UPCell exceeding WHO and SABS limits. These elevated levels are likely due to both natural sources, such as weathering of arsenic-bearing rocks, and anthropogenic activities like agricultural runoff and industrial discharge. Aluminum concentrations were higher than WHO guidelines in surface water samples WELASW, SANDSW, ANDSW, and MANMSW, likely due to atmospheric deposition. Iron was present above SABS taste guidelines in all samples, with elevated levels in WelA, HLU, MANM2, MANT, KM, and UPCell exceeding health standards, contributing to poor taste and potential health concerns. Nickel concentrations exceeded WHO standards in one sample, reflecting conditions typical of groundwater in arid regions with high arsenic levels and reduced oxygen environments.

Table 8-6 Water samples from the Timbavati region exceeded recommended guidelines for various contaminants, highlighting significant water quality issues.

Constituent	Unit	Min	Max	Mean	WHO Guideline	SABS Guideline
pH	-/-	6.97	8.4	7.5		5 to 9.7
		7.47	9.3	8.34		
Total Dissolved Solids	mg/ℓ	541	3580	1216	≤1000 (Aesthetic)	≤1200 (Aesthetic)
		139	622	326		
Ammonium (NH_4^+)	mg/ℓ	0.03	0.75	0.20	≤35 (Aesthetic)	
		0.02	1.7	0.36		
Chloride (Cl^-)	mg/ℓ	4.4	98	28	≤250 (Aesthetic)	
		4.7	10	7.7		
Sulphate (SO_4^{2-})	mg/ℓ	4.4	98.3	24.3	≤250 (Aesthetic)	≤250 (Aesthetic) 500 (Health)
		4.7	10.4	7.7		
Fluoride (F^-)	mg/ℓ	0	2.0	0.94	≤1.5	≤1.5
		0.29	0.37	0.13		
Calcium (Ca^{2+})	mg/ℓ	25	190	62	≤200	
		6.5	28	17		
Magnesium (Mg^{2+})	mg/ℓ	14	140	49	≤150	
		4.1	18	9.5		
Potassium (K^+)	mg/ℓ	0.31	12	3.6	≤10	
		0.26	31	12		
Sodium (Na^+)	mg/ℓ	100	314	196		≤200 (Aesthetic)
		19	48	46		
Iron (Fe^{2+})	mg/ℓ	0.04	7.6	2.4	≤0.3 (Aesthetic)	≤0.3(Aesthetic) ≤2(Health)
		0.61	1.7	0.96		
Manganese (Mn^{2+})	mg/ℓ	0.003	0.026	0.002	≤0.4	≤0.1 (Aesthetic) ≤0.4 (Health)
		0	0	0		
Boron (B^{3+})	mg/ℓ	0	0.64	0.14	≤2.4	≤2.4
		0	0	0		
Aluminium (Al^{3+})	mg/ℓ	0	0.0076	0.0008	≤0.2	≤0.3
		0	0.60	0.37		
Nickel (Ni^{2+})	mg/ℓ	0	0.10	0.01	≤0.07	≤0.07
		0	0	0		
Copper (Cu)	mg/ℓ	0	0.009	0.001	≤2	≤2
		0	0	0		
Arsenic (As^{3+})	mg/ℓ	0.0007	0.16	0.02	≤0.01	≤0.01
		0.0006	0.005	0.002		
Barium (Ba^{2+})	mg/ℓ	0.003	0.18	0.05	≤1.3	≤0.7
		0.06	0.22	0.1		

8.4.2 Water Chemistry

The Olifants Water Management Area Internal Strategic Perspective (DWA, 2004) reported that TDS values in the B73E and B73F quaternary catchments range between 500 and 2,000 mg/L, aligning with data collected during sampling. Higher TDS values are found in groundwater samples, which also exhibit the lowest $\delta^{18}O$ values, indicating a lighter isotopic composition. This suggests that minimal evaporation has occurred, as lighter isotopes, such as $^1H_2{}^{16}O$, evaporate first, leaving behind water enriched in heavier isotopes. Lower TDS values are observed in surface water samples, which have a heavier isotopic composition due to evaporation, indicating that the solutes primarily originate from weathering and water-rock interactions rather than evaporation processes.

Based on cation and anion concentrations, groundwater samples can be categorised into three groups as shown in Table 8-7. Surface water samples generally have lower ion concentrations compared to groundwater, consistent with their lower TDS values. All surface water samples, except THORSW1, exhibit ion compositions similar to Group 1, while THORSW1 aligns with Group 2.

Table 8-7 Groups based on cations and anions with the relevant geological lithology and samples

Group	Geology	Samples	Cations	Anions
Group 1	Klaserie gneiss	SCC, NOR, A201, A202, SAN, AND, Xih, MANT, KM, WITS1, WITS2, BAO, MANM1, and MANM2	$Na^+ + K^+$	HCO_3^-
Group 2	Makhutswi Gneiss	WELA and HLU	$Na^+ + K^+$	Cl^-
Group 3	Timbavati Gabbro	UPCell	Mg^{2+}	HCO_3^-

The high sodium concentrations in Groups 1 and 2 groundwater samples likely result from the weathering of albite, with potassium sourced from the weathering of microcline and biotite, and calcium derived from the weathering of anorthite in the gneisses. High magnesium levels in the UPCell sample are attributed to the weathering of olivines and pyroxenes, while calcium and sodium ions are sourced from plagioclase in the Timbavati Gabbro. Elevated bicarbonate (HCO_3^-) concentrations in groundwater are byproducts of silicate weathering, where carbonic acid (H_2CO_3), formed by CO_2 dissolving in water, reacts to form clay minerals such as kaolinite and bicarbonate (Appelo and Postma, 2005). WELA and HLU, though similar in cation composition to Group 1 samples, are distinguished by higher chloride levels, averaging 611 mg/ℓ compared to Group 1's 174 mg/ℓ, indicating potential pollution (Hunt et al., 2012). Potassium and aluminum in these samples likely originate from microcline and biotite, with magnesium and iron also derived from biotite.

8.4.3 Nitrates

Nitrate concentrations in groundwater samples, particularly from Welverdiend A, Welverdiend B, and Hluvukani, were significantly higher compared to surface water samples and other groundwater locations, likely due to the higher population density and urbanization in these areas. These three locations exhibited a marked increase in nitrate levels over time, likely due to on-site sanitation as a primary source of contamination, consistent with Tredoux et al.'s (2009) findings. Surface water nitrate concentrations remained relatively stable, while groundwater concentrations, excluding the three urbanized sites, showed an alternating pattern without a clear seasonal trend. Nitrate levels were measured using the Aquaread AP-5000 Nitrate ISE electrode, and when compared to WHO (2017) and SABS (2022) guidelines, concentrations above the permissible levels were found in samples from HLU, SCC, BAO, WelA, and WelB. A comparison between Aquaread probe and laboratory analysis showed a consistent discrepancy, with Aquaread readings being approximately 0.5 times higher, likely due to the timing of sample analysis rather than ion interference. Additionally, trace levels of nitrite were detected in some samples, indicating ongoing denitrification processes.

8.4.4 Hydrogen and Oxygen Isotopes

The study area experiences a lowveld climate with summer rainfall, but unusual patterns were observed in 2022, with heavy rainfall in April and May and very little in September and October. A weighted meteoric water regression line was used to better characterize the local rainfall, considering heavier rainfall events while minimizing evaporation effects. The local meteoric water line (LMWL) has a shallower gradient compared to the global meteoric water line (GMWL), typical in warmer regions. Months with the lowest rainfall, such as February, September, and October, had the heaviest isotopic compositions, illustrating the "amount effect," where heavier rainfall events result in lighter isotope compositions. The high δD values in September were likely due to low humidity following the dry winter, leading to increased evaporation of lighter isotopes during precipitation. Higher d-excess values in April and May 2022 suggest evaporation occurred under less humid conditions at the moisture source, while the negative d-excess value in September indicates non-equilibrium conditions during evaporation.

Groundwater samples showed lighter isotopic compositions, plotting near the lower half of the GMWL, likely due to recharge during heavy rainfall when lighter isotopes condense and precipitate. The groundwater samples also plot along the lower end of the local evaporation line (LEL) with some evidence of pre-aquifer evaporation. Throughout the sampling period, groundwater isotopic compositions remained relatively constant, though one sample from September/October 2021 plotted closer to surface water, possibly due to inadequate borehole purging. Surface water samples were enriched in heavier isotopes compared to groundwater, with seasonal variations indicating enrichment through evaporation. However, the lack of a correlation between increased TDS and δ18O suggests that evaporation may not be the sole cause. In some cases, surface and groundwater samples shared overlapping isotopic compositions, indicating possible surface water-groundwater interactions. By the final sampling round in November 2022, only large dams at Manyeleti, Andover, and Sandringham retained water, with the largest dams showing the most enrichment due to evaporation. The presence of vegetation, particularly water lilies, in Sandringham may have reduced evaporation in this dam.

8.4.5 Radon

ANDS, WelASW, SANSW, and THORSW1 were the only surface water samples consistently containing radon throughout all sampling rounds. However, during August/September 2022, radon was present in all surface water samples. The presence of radon in surface water, along with overlapping pH, TDS, ORP, and DO values with groundwater, suggests potential groundwater discharge into rivers and dams. THORSW2 was the only surface water sample with radon concentrations comparable to groundwater levels during the May/June 2022 sampling. BAO had the lowest average radon concentration at 4190 Bq/m³, while Acorn to Oaks 2 had the highest at 34200 Bq/m³. Despite uranium concentrations in groundwater samples being below the detection limit of 0.015 mg/ℓ, making it impossible to assess any correlation with radon, no clear relationships were observed between radon concentrations and pH, DO, EC, TDS, SAL, or ORP, aligning with Cho & Choo (2029), who noted that radon tends to behave independently of most geochemical parameters.

8.5 OUTCOMES AND WAY FORWARD

There was some overlap between the groundwater and surface water samples regarding pH, TDS, ORP, and DO; however, the two groups generally plotted separately. Based on the relationship between TDS and δ18O, the high TDS values in the groundwater are attributed to weathering and water-rock interactions rather than evaporation. The differences in groundwater and surface water chemistry are therefore due to the addition of ions and other chemical constituents from the weathering of rocks and minerals.

The groundwater samples can be divided into three groups based on their chemistry.

The SAWC site could not be sampled during the detailed chemical analysis in August and September 2022 due to inaccessibility. It would be interesting to see if SAWC shares the same ion composition as UPCell since it is also located on the Timbavati Gabbro.

Nitrate concentrations were generally higher in the groundwater samples, with a mean value of 83.1 mg/ℓ, reaching as high as 1350 mg/ℓ in WelA during the final round of sampling. In contrast, the surface water samples had a mean value of 5.56 mg/ℓ, with a maximum of 10.4 mg/ℓ in WelASW. The highest nitrate concentrations were found in the communities of Welverdiend, Hluvukani, and Acornhoek, indicating that the source of nitrate contamination is likely human, animal, and agricultural waste. Additionally, some boreholes in these areas were located downslope from pit latrines and cattle kraals. An analysis of nitrogen isotopes could provide a clearer picture of the exact source of nitrate contamination.

Groundwater samples exhibited a lighter mean isotopic composition of -20.5 δD‰ and -3.8 δ18O‰, compared to mean surface water values of 12.2 δD‰ and 2.3 δ18O‰, and mean rainwater composition of -2.76 δD‰ and -1.9 δ18O‰. The lighter isotopic composition in groundwater is due to recharge from heavy rainfall events and the amount effect. However, the similarity in gradients between the regression equation for groundwater samples and the Local Evaporation Line (LEL) suggests some evaporation occurs before recharge. There is also a possibility that evaporation alone does not fully explain the heavier isotopic composition of the surface water samples, as indicated by the lack of an increase in TDS with an increase in δ18O.

There was no distinct correlation between radon concentrations and geology, nor any clear relationships between pH, DO, EC, TDS, SAL, ORP, and radon concentrations. However, radon was detected in surface water samples ANDSW, WelASW, SANSW, and THORSW1. The presence of radon in these samples, along with occasional overlap in pH, TDS, ORP, and DO values with groundwater samples, may indicate groundwater discharge into rivers and dams.

This study advanced the understanding of the hydrochemistry in the greater Timbavati area and highlights the complex interconnectivity of hydrology, hydrogeology, geography, and geology. The analysis of environmental isotopes provided insights into recharge processes and water sources, as well as identified seasonal variations in the area's hydrochemistry. The detection of radon in certain surface water and groundwater samples, coupled with the overlap in pH, TDS, DO, and ORP, suggests potential groundwater-surface water interactions, demonstrating the interconnectivity of hydrology and hydrogeology in the area.

The characterization of groundwater and surface water chemistry revealed distinct patterns and relationships between water geochemistry and quality with the local geology and geography. Piper plots, Stiff diagrams, and Schoeller diagrams identified three main groups of groundwater samples, each characterized by unique cation-anion compositions associated with specific underlying geology. Elevated nitrate concentrations and heavy metals in certain groundwater samples highlight the impact of anthropogenic activities on water quality. These findings have significant implications for water resource planning and management, emphasizing the need for integrated approaches to safeguard water quality and sustainability in the greater Timbavati area.

8.6 REFERENCES

Abiye TA, Demlie MB, Mengistu H (2021) An overview of aquifer physiognomies and the δ18O and δ2H distribution in the South African groundwaters. Hydrology 8:68, https://doi.org/10.3390/hydrology8020068

Allsopp HL, Kramers JD, Jones DL & Erlank AJ (1989) The age of the Umkondo Group, eastern Zimbabwe, and implications for palaeomagnetic correlations. South African journal of geology 92:11–19

C. R. Anhaeusser (2006) Ultramafic and Mafic Intrusions of the Kaapvaal Craton, In: M. R. Johnson, C. R. Anhaeusser, R. J. Tomas, Eds., The Geology of South Africa, Council for Geosciences, 2006, Pretoria. pp. 95-134

Appelo CAJ, Postma D (2005) Geochemistry, groundwater and pollution, 2nd edn. CRC Press, Amsterdam

Baskaran M (2016) Radon: A tracer for geological, geophysical and geochemical studies. Springer, https://doi.org/10.1007/978-3-319-21329-3

Brandl G (1985) 1:25000 Geological Series map (2330 Tzaneen). Geological Survey of South Africa

Clark I (2015) Groundwater Geochemistry and Isotopes. 1st edition. CRC Press, Boca Raton

Department of Water Affairs and Forestry (2004) Olifants Water Management Area: Internal Strategic Perspective. Prepared by GMKS, Tlou and Matji and WMB on behalf of the Directorate: National Water Resource Planning. DWAF Report No P WMA 04/000/00/0304. South Africa

Diamond E (2022) Stable Isotope Hydrology, 1st edition. The Groundwater Project, Ontario

Diamond RE, Harris C (2019) Stable isotope constraints on hydrostratigraphy and aquifer connectivity in the Table Mountain Group. South African Journal of Geology 2019 122:317–330, https://doi.org/10.25131/sajg.122.0021

Ding Z, Ma J, Zhao W, et al (2013) Profiles of geochemical and isotopic signatures from the Helan Mountains to the eastern Tengger Desert, northwestern China. J Arid Environ 90:77–87, https://doi.org/10.1016/j.jaridenv.2012.10.01

Graham JP, Polizzotto ML (2013) Pit latrines and their impacts on groundwater quality: a systematic review. Environ Health Perspect 121:521–530, https://doi.org/10.1289/ehp.1206028

Grolander S (2009) Radon as a groundwater tracer in Forsmark and Laxemar. (SKB-R--09-47). Sweden

Hanson RE, Gose WA, Crowley JL, et al (2004) Paleoproterozoic intraplate magmatism and basin development on the Kaapvaal Craton: Age, paleomagnetism and geochemistry of~ 1.93 to~ 1.87 Ga post-Waterberg dolerites. South African Journal of Geology 107:233–254, https://doi.org/10.2113/107.1-2.233

Hao S, Li F, Li Y, et al (2019) Stable isotope evidence for identifying the recharge mechanisms of precipitation, surface water, and groundwater in the Ebinur Lake basin. Science of the Total Environment 657:1041–1050, https://doi.org/10.1016/j.scitotenv.2018.12.102

Harkness JS, Swana K, Eymold WK, et al (2018) Pre-drill groundwater geochemistry in the Karoo Basin, South Africa. Groundwater 56:187–203, https://doi.org/10.1111/gwat.12635

Hughes CE, Crawford J (2012) A new precipitation weighted method for determining the meteoric water line for hydrological applications demonstrated using Australian and global GNIP data. J Hydrol (Amst) 464:344–351, https://doi.org/10.1016/j.jhydrol.2012.07.029

Lachassagne P, Dewandel B, Wyns R (2021) Hydrogeology of weathered crystalline/hard-rock aquifers—guidelines for the operational survey and management of their groundwater resources. Hydrogeol J 29:2561–2594, https://doi.org/10.1007/s10040-021-02339-7

Liu Y, Yamanaka T (2012) Tracing groundwater recharge sources in a mountain–plain transitional area using stable isotopes and hydrochemistry. J Hydrol (Amst) 464:116–126, https://doi.org/10.1016/j.jhydrol.2012.06.053

McGill BM, Altchenko Y, Hamilton SK, et al (2019) Complex interactions between climate change, sanitation, and groundwater quality: a case study from Ramotswa, Botswana. Hydrogeol J 27:997–1015, https://doi.org/10.1007/s10040-018-1901-4

Peng T-R, Huang C-C, Zhan W-J, Wang C-H (2016) Assessing groundwater sources and their association with reservoir water using stable hydrogen and oxygen isotopes: a case study of the Taipei Basin, northern Taiwan. Environ Earth Sci 75:1–13, https://doi.org/10.3390/geosciences8030084

Petersen RM, Nel JM, Strydom T, et al (2023) The use of stable isotopes to identify surface water–groundwater interaction in the Kruger National Park, South Africa. Water SA 49:96–102, http://dx.doi.org/10.17159/wsa/2023.v49.i2.3992

Putman AL, Fiorella RP, Bowen GJ, Cai Z (2019) A global perspective on local meteoric water lines: Meta-analytic insight into fundamental controls and practical constraints. Water Resour Res 55:6896–6910, https://doi.org/10.1029/2019WR025181

Saggerson EP, Logan CT (1970) Distribution controls of layered and differentiated mafic intrusions in the Lebombo volcanic sub-province. Special Publication Geological Society of South Africa 1:721–733

Schutte IC (1986) The general geology of the Kruger National Park. Koedoe 29:13–37

Tommasino L (2005) Radon. J Chem Educ 82:32–44

Tredoux G, Engelbrecht P, Israel S (2009) Nitrate in Groundwater: Why is it a hazard and how to control it? WRC Report No. TT 410/09, Water Research Commission, Stellenbosch

Walraven F (1986) The Timbavati Gabbro of the Kruger National Park. Koedoe 29:69–84

Walraven F (1989) The geology of the Pilgrim's Rest area. https://api.semanticscholar.org/CorpusID:127896541

Walraven F, Hartzer FJ (1986) Sheet 2530 Barberton (1: 250 000 Geological Series). Geol Surv S Afr

West AG, February EC, Bowen GJ (2014) Spatial analysis of hydrogen and oxygen stable isotopes ("isoscapes") in ground water and tap water across South Africa. J Geochem Explor 145:213–222, https://doi.org/10.1016/j.gexplo.2014.06.009

Wright EP (1992) The hydrogeology of crystalline basement aquifers in Africa. Geological Society, London, Special Publications 66:1–27, https://doi.org/10.1144/GSL.SP.1992.066.01.01

Yeh H-F, Lee C-H, Hsu K-C (2011) Oxygen and hydrogen isotopes for the characteristics of groundwater recharge: a case study from the Chih-Pen Creek basin, Taiwan. Environ Earth Sci 62:393–402, https://doi.org/10.1007/s12665-010-0534-2

Yeh H-F, Lee J-W (2018) Stable hydrogen and oxygen isotopes for groundwater sources of Penghu Islands, Taiwan. Geosciences 8:84, https://doi.org/10.3390/geosciences8030084

Zhu S, Zhang F, Zhang Z, et al (2019) Hydrogen and Oxygen Isotope Composition and Water Quality Evaluation for Different Water Bodies in the Ebinur Lake Watershed, Northwestern China. Water 11:1–35, https://doi.org/10.3390/w11102067